THE UNIVERSITY *of* EDINBURGH

Simulation of dense suspensions with discrete element method and a coupled lattice Boltzmann method

---

Tim Najuch

21st November 2018

The University of Edinburgh

School of Engineering
Institute for Infrastructure and Environment
Granular Mechanics and Industrial Infrastructure Group

A thesis submitted for the degree of Doctor of Philosophy

Simulation of dense suspensions with discrete element method and a coupled lattice Boltzmann method

Tim Najuch

External reviewer Prof. Jos Derksen
School of Engineering
University of Aberdeen

Internal reviewer Dr. Kevin Hanley
Institute for Infrastructure and Environment
The University of Edinburgh

Supervisor Dr. Jin Sun

21st November 2018

Tim Najuch

Simulation of dense suspensions with discrete element method and a coupled lattice Boltzmann method

A thesis submitted for the degree of Doctor of Philosophy, 21st November 2018
Reviewers: Prof. Jos Derksen and Dr. Kevin Hanley
Supervisor: Dr. Jin Sun

The University of Edinburgh
Granular Mechanics and Industrial Infrastructure Group
Institute for Infrastructure and Environment
School of Engineering
Thomas Bayes Road, Alexander Graham Bell Building, The King's Buildings
EH9 3FG Edinburgh

Declaration

I declare that this thesis has been composed solely by myself and that it has not been submitted, in whole or in part, in any previous application for a degree. Except where states otherwise by reference or acknowledgment, the work presented is entirely my own.

Edinburgh, 21st November 2018

Tim Najuch

Abstract

Suspensions, mixtures of a fluid and particles, are widespread in nature and industry. A better understanding of suspension flow physics could be gained by accurate simulations and hence, many different simulation techniques for fluid-solid flows have been proposed. The intention of this thesis is to establish an accurate, high-fidelity methodology to simulate sheared dense suspensions on microscale which allow for extraction of reliable data for macroscale models and better understanding of underlying physical processes. Therefore, two partially saturated coupled lattice Boltzmann discrete element methods (LBDEM) are analysed and evaluated with regard to the stresslet computation of suspension flow under simple shear at first. Simulation results for a single sphere, two spheres, and several hundred spheres, immersed in a sheared fluid show that a commonly used partially saturated method based on the non-equilibrium bounce-back lead to non-satisfactory results. But an alternative superposition method, which is mostly neglected in the literature, can result in accurate stresslet calculations. Furthermore, an ideal single relaxation parameter range for the fluid phase to reduce slip velocity effects is determined. Based on the stresslet study outcome, the superposition method is used to simulate two particle collisions in the second part of this work. Thereby, a careful assessment of the partially saturated LBDEM capabilities to resolve lubrication interactions between particles, which are important in suspension flows, is achieved. Moreover, a popular lubrication correction model, which is applied for very small gap distances between particles which cannot be resolved by the lattice size, is slightly modified and calibrated to be suitable when used with the partially saturated coupling method. In the third part of this thesis, a comparison between the expensive LBDEM coupling and a tremendously cheaper discrete element method (DEM) with a model for lubricated particle-particle interactions is carried out. It is shown that for low Reynolds number sheared suspensions, with intermediate to dense solid packing fractions, the differences between both aforementioned LBDEM and DEM approaches can be minor. Thus, it is demonstrated that a DEM with a lubrication model can be effectively used to simulate microscale processes of dense suspension under simple shear in a low Reynolds number regime for a significant lower fraction of the computational expenses necessary for LBDEM simulations. Hence, in the last part of this thesis, only a DEM with a lubrication model is employed to study particle-particle contact and lubrication interactions as well as the underlying dissipation mechanism in dense sheared suspensions on microscale. Thereby, providing evidence that the suspension bulk viscosity divergence is caused by

the lubricated dissipative interactions while mechanical particle-particle contact is the stress dominating contribution for high solid fractions close to jamming.

Layperson summary

Mixtures of a fluid and particles, described as suspensions, are common in nature and industry, for example coastal erosions or $3D$-printing. The physics of fluid-particle flows are however complex and to gain a better understanding of the physics, simulations can be a helpful tool in addition to experiments. Various methods to simulate fluid-particle flows have been proposed. One class of methods aims on simulating fluid-particle flows by capturing the motion of every single particle and resolving the fluid flow around the particles in great detail. The focus in the first part of this thesis is set on analysis and evaluation of a method which allows for detailed simulation of fluid-particle flows. It is shown that a commonly used method results in inaccurate interactions between fluid and particles and thereby leading to wrong viscosity values of the overall fluid-particle mixture. However, it is also shown that a slightly alternative approach, which is mostly neglected in the literature, can result in correct fluid-particle interactions and viscosities. The alternative approach is furthermore shown to model sufficiently so called lubrication forces which are fluid forces arising due to particles moving with different velocities in close distance to each other. Methods which simulate the fluid flow around the particles are computationally very expensive. Therefore, it is shown in the third part of this thesis that a simple lubrication force model can be used as an appropriate substitution for the fluid phase. Thereby, leading to tremendous cheaper (and simplified) simulations. In the last part, the simplified lubrication force model is used to investigate interactions between particles immersed in a fluid. The obtained results provide a possible explanation for very fast growing viscosities with increasing amount of particles in a suspension.

Acknowledgements

This thesis would have not seen the light of the day without my supervisor Jin Sun. I am extremely grateful for giving me the opportunity to complete my PhD studies under his guidance and providing constant support and encouragement during this PhD project and beyond.

I would like to thank Jos Derksen and Kevin Hanley for serving as examiners of my thesis.

The LBM world had been unknown to me before I started this project. Fortunately, I could benefit from helpful advice. Therefore, I would like to thank Philippe Seil for support and advice using his open-source Palabos-LIGGGHTS coupling as well as for fruitful LBM discussions. Furthermore, I would like to also thank Timm Krüger and Oliver Henrich for very helpful discussions and pointing out that the re-written superposition method of the partially saturated cell method resembles a Kupershtokh force. Moreover, Jonas Latt's advice with regard to my implementation of Lees-Edwards boundary conditions into Palabos is highly acknowledged.

I am grateful that Rangarajan Radhakrishnan looked into the details of the lubricated particle interaction model in LAMMPS and my first implementation of the grand resistance matrix. The many productive discussions about modelling of lubricated particle interactions and the resulting collaborative work on the implementation of lubrication models into LAMMPS/LIGGGHTS is highly acknowledged.

This PhD project was part of a larger European research network on granular materials. Therefore, I am thankful that I had the possibility for a secondment at Johnson Matthey (thank you Michele Marigo et al.) and at DCS Computing (thank you Christoph Kloss). Moreover, I would like to thank all other PhD students, post-docs, and supervisors of the T-MAPPP research network for mutual support and the very "family like" atmosphere. It was a great and valuable experience which provided not only subject specific research training, but will have a lasting impact on my future. All this would have not been possible without the European Union which provided the funding for this European Union's Seventh Framework Programme for research, technological development and demonstration under grant agreement no ITN607453.

Contents

List of Figures

List of Tables

Nomenclature

Abbreviations

BB method	Non-equilibrium bounce-back method
BGK	Bhatnagar-Gross-Krook model
CFD	Computational fluid dynamics
DEM	Discrete element method
DLM/FD	Distributed Lagrangian Marker / Fictitious Domain
FDM	Finite difference method
FVM	Finite volume method
IBM	Immersed boundary method
LB / LBM	Lattice Boltzmann / Lattice Boltzmann method
LBDEM	Coupled lattice Boltzmann discrete element method
LEbc	Lees-Edwards boundary condition
MRT	Multiple relaxation time model
PDF	Partially saturated cell method
SBM	Suspension balance model
SGR	Subgrid resolution
SP method	Superposition method
TRT	Two relaxation time model

Calligraphic letters

$\mathcal{M}$	Mobility matrix

$\boldsymbol{\mathcal{R}}$	Grand resistance matrix

Greek letters

$\boldsymbol{\alpha}$	Angular particle acceleration
β_{ij}	Interphase momentum transfer coefficient
γ	Particle size ratio
γ_n	Damping coefficient for collision in normal direction
γ_t	Damping coefficient for collision in tangential direction
$\dot{\gamma}$	Shear rate
δ	Particle overlap
$\delta_{c,i}$	Inner cut-off for lubrication DEM model
$\delta_{c,o}$	Outer cut-off for lubrication DEM model
δ_{cut}	LBDEM lubrication cut-off calibration parameter
ϵ_s	Solid fraction on lattice node
ε	Porosity in suspension system
ε_r	Coefficient of restitution
ε_{eff}	Effective coefficient of restitution
η_f	Dynamic fluid viscosity
η_r	Relative suspension viscosity
$[\eta]$	Intrinsic viscosity
λ	Mean free path
μ_r	Coefficient of friction
μ_{eff}	Effective friction coefficient
ν_f	Kinematic fluid viscosity
$\boldsymbol{\xi}$	Velocity in (Boltzmann) velocity space
ρ	Density in Boltzmann method
ρ_f	Fluid density
ρ_p	Particle density

ρ_s	Solid density
Σ^p	Particle stress
$\boldsymbol{\sigma}_f$	Stress tensor of fluid phase
$\boldsymbol{\sigma}_s$	Stress tensor of solid phase
τ	Relaxation time
ϕ	Solid fraction in suspension system
ψ	Independent variable
Ω_i^f	Discrete lattice Boltzmann collision model for the fluid phase
Ω_i^s	Discrete lattice Boltzmann collision model for the solid phase
ω^∞	Fluid vorticity
ω_i	Lattice weighting function in lattice Boltzmann method
$\boldsymbol{\omega}$	Angular velocity

Latin letters

$B(\mathbf{x}, \tau)$	Weighting function for solid fraction on lattice node $\mathbf{x}$
B_{ij}	Particle-specific friction coefficients
$\mathbf{c}_i$	Velocity vector of discrete particle distribution function
c_s	Speed of sound in the lattice Boltzmann system
d_p	Particle diameter
d_{eff}	Effective particle diameter
$\mathbf{E}$	Strain rate tensor
$\mathbf{F}^B$	Force due to Brownian motion
$\mathbf{F}^C$	Contact force
$\mathbf{F}^H$	Hydrodynamic force
$\mathbf{F}^L$	Lubrication force
$\mathbf{F}_{fp,d}$	Fluid-solid drag force
$\mathbf{F}_{fp}$	Fluid-solid interaction force
$f(\mathbf{x}, t)$	Particle distribution function

$f^{eq}(\mathbf{x}, \mathbf{u}, t)$	Equilibrium particle distribution function
f_i	Discrete particle distribution function
f_i^{eq}	Discrete equilibrium particle distribution function
f_{-i}	Discrete particle distribution function in opposite direction of i
f_{-i}^{eq}	Discrete equilibrium particle distribution function in opposite direction of i
h_{gap}	Particle-particle gap distance
$\mathbf{J}$	Moment of inertia
k^*	Non-dimensionalised spring stiffness
k_B	Boltzmann constant
k_n	Spring stiffness in normal direction of collision
k_t	Spring stiffness in tangential direction of collision
Kn	Knudsen number
m	Mass
Ma	Mach number
N	Number of lattice cells over a particle diameter
p	Pressure
p_f	Fluid pressure
p_s	Solid phase pressure
R	Gas constant
r_p	Particle radius
r_{eff}	Effective radius
Re	Reynolds number
$\mathbf{S}$	Stresslet
St	Stokes number
$\mathbf{T}^C$	Contact torque
$\mathbf{T}^H$	Hydrodynamic torque

$\mathbf{T}^L$	Lubrication torque
T	Temperature
t	Time
$\mathbf{u}_b$	Boundary velocity
V	Total volume of void spaces and solid body
V_p	Particle volume
w_i	Discrete weighting function for the lattice Boltzmann directions
$\mathbf{x}_l$	Lagrangian marker point
$\mathbf{x}_{p,c}$	Particle centre of mass

1 Introduction

1.1 Motivation - suspensions in nature and industry

Suspensions, mixtures of a fluid and particles, behave very differently to Newtonian fluids such as water. The presence of particles suspended in a fluid, including Newtonian fluids, leads to many non-Newtonian characteristics of the overall suspension mixture. An example is an increased viscosity in comparison to a Newtonian fluid depending on the solid fraction and even leading to a possibly jammed state when too many particles are suspended. Other common characteristics are shear thinning, which means that the viscosity decreases for increasing shear rate, or shear thickening, which leads to an increasing viscosity with increasing shear rate. More effects and aforementioned suspension behaviour have been subject in a plethora of research activities because suspensions are ubiquitous in nature and are a critical part in many important industrial applications.

In nature, suspensions can be found in form of destructive mudslides or landslides and volcanic flows. Prediction of mudslides and landslides could lead to precautions avoiding fatalities and infrastructural damages. Such infrastructural damages do not only lead to local socio-economic disruptions, but can have geographically widespread implications as exemplarily discussed by Winter et al. (2016) for landslide events in Scotland. Costs caused by mudslides and landslides accumulate to billion dollars as illustrated in figure 1.1. Further losses, related to suspension flow in nature, are caused by sediment erosion in river beds and coastlines. For example, the European Commision (2009) reports the tremendous cost of 15.8 billion € in total expenses spent on coastal protections against flooding and erosion over the period 1998-2015.

Apart from phenomena in nature, understanding of suspension flows is crucial in industrial applications. Endeavours to generate electricity from “green” sources, such as wind power or solar power, is undertaken by many governments to reduce the human carbon footprint as agreed by a majority of nations in the global Paris climate agreement from 2015. A major issue with “green” energy sources is the inherent unreliability and volatility of power generation. However, a remedy could be efficient power storage by constructing either pumped-storage plants or giant batteries. The latter solution could be realised by fluid-solid Redox batteries which pump anode and cathode material, suspended as particles in an electrolyte, through a membrane allowing only for electron exchange as described by Duduta et al. (2011), Chalamala et al. (2014) and Hatzell et al. (2015).

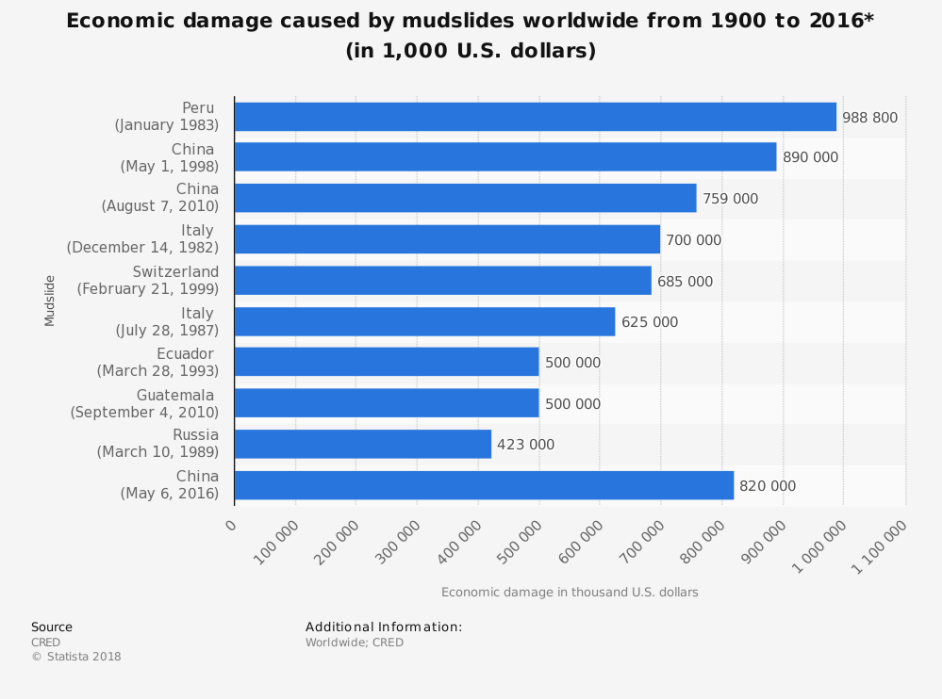

Fig. 1.1.: Worldwide economic damage caused by mudslides according to and adopted from CRED (n.d.).

An advantage of flow batteries is the possibility to scale the capable power storage by changing correspondingly the tank sizes containing the cathode and anode materials. This is especially advantageous to common Lithium batteries when the required power storage capabilities are very large, cf. Chalamala et al. (2014).

Further knowledge about suspension flow behaviour is necessary in the production process for Lithium battery packs which is described, for example, by Tagawa and Brodd (2009). During the Lithium battery production the electrode materials are mixed into a fluid and the resulting slurry is coated onto a current collector sheet. The coated sheets are subsequently exposed to a drying process to evaporate the fluid and thereby yielding the final electrode material which can be cut and compressed to battery cells. For efficient batteries, knowledge about suspension handling is of high importance to achieve an optimal coating surface.

The coating step in the battery production process is similar to an extrusion process. Extrusion processes are the most popular technique in additive manufacturing, commonly known as $3D$-printing, according to Gibson et al. (2015). From the variety of additive manufacturing techniques, extrusion processes squeeze either dry granular materials, molten materials, or suspensions through a nozzle to form layer by layer the requested structural shape.

1.2 Fluid-solid flow modelling approaches

Despite the enormous impact of suspension flows, or more generally expressed as fluid-solid or multiphase flows, a whole understanding is far from completeness. Although much research has been performed to gain a better insight into multiphase flow processes (cf. Hoef et al. (2008)), some knowledge gaps remain such as occurence of turbulence in fluid flows, let alone turbulence in multiphase flows. Besides experimental investigations, numerical methods are exceptionally useful and have become an exceedingly helpful tool due to a steady development of computational resources. However, fluid-solid flow effects are complex due to the vast range of length and time-scales involved. Therefore, numerical investigations of fluid-solid flows require a fine resolution of the different length and time scales (microscale) and result in a tremendous computational effort unless multiphase models are applied which allow for a coarser resolution of fluid-solid flow structures (meso- or macroscale). Yet, development of reliable multiphase flow models is hindered because of the very different scales. Construction of multiphase models has suffered under strict assumptions and thus complex processes have been inadequately described (cf. Enwald et al. (1996), Hoef et al. (2008) and Hoef et al. (2006)).

Thus, various numerical approaches resolving different scales of fluid-solid flows exist and can be classified into two basic groups: Eulerian and Lagrangian.

1.2.1 Fluid phase

According to Hoef et al. (2006), the choice of modelling approach in case of the fluid phase is determined by the Knudsen number

$$Kn = \frac{\lambda}{L}\,, \tag{1.1}$$

where L is a characteristic length scale of the fluid flow and λ is the mean free path which describes the average travelled distance of molecules between collisions. The mean free path can be determined with the molecule density n (number of molecules per volume) and the scattering cross-section σ_{SCS} as $\lambda = \frac{1}{\sqrt{2}n\sigma_{SCS}}$ according to Gombosi (1994).

Very small Knudsen numbers $Kn < 0.01$ allow the application of continuum approaches, i.e. the application of the common mass/momentum/energy conservation equations in fluid mechanics. An increase of the free mean path of the molecules to $0.01 < Kn < 0.1$ leads to potential slip boundary conditions on the fluid-solid interface in contrast to the $Kn < 0.01$ region where no-slip boundary conditions on the interface are fulfilled. Yet, the momentum conservation, i.e. the Navier-Stokes equations, are still valid. However, continuum assumptions are not legitimate for large Knudsen numbers $Kn > 0.1$ and

therefore the fluid is described by the fundamental Boltzmann equation, representing the kinetic theory of molecular gases. Speaking in terms of Eulerian and Lagrangian, the Eulerian approach represents the continuum approach and the Lagrangian approach confines molecular models.

1.2.2 Solid phase

In case of the solid phase, the Eulerian approach represents a continuum description similar to the continuum approach for the fluid phase. E.g. Anderson and Jackson (1967) derived averaged continuum equations for the solid phase which are similar to the commonly known mass conservation and Navier-Stokes equations. In the Lagrangian approach however, the solid phase is described by discrete solid particles whose motions are determined by Newton's second law for motion.

1.2.3 Fluid-solid interaction modelling

Both the fluid phase and solid phase interact with each other and additionally solid-solid interactions are common. The degree of necessary coupling in a model is described by the solid volume fraction $\phi = \frac{\sum V_p}{V}$ which is the ratio of the total particle volume $\sum V_p$ to the total volume V covered by particles and fluid (cf. Hoef et al. (2006)). For $\phi < 10^{-6}$, only a so called one-way coupling is necessary, i.e. the solid volume fraction is low enough to consider only a fluid influence on the particles and to neglect a reciprocal particle influence as well as particle-particle interactions. Higher solid volume fractions $10^{-6} < \phi < 10^{-3}$ require consideration of the particle influence on the fluid flow in addition to the impact of fluid flow on the particle motion. However, the particle-particle collisions are still neglected in this two-way coupling approach. In four-way coupled systems, which are highly relevant for industrial processes, particle-particle interactions are, besides a mutual fluid-particle coupling, significant in systems of $\phi > 10^{-3}$.

1.3 Multiscale models

In the previous section, the two different general modelling approaches, Eulerian and Lagrangian, for solid and fluid phase are elucidated. In fluid-solid flows, the approaches for the phases do not have to be the same and can be chosen in different combinations. However, phases interact with each other and formulation of the interactions depends strongly of the chosen combination of modelling approaches.

The most fundamental modelling approach is a combination of Lagrangian-Lagrangian models (cf. Hoef et al. (2008)), i.e. suspended solid phase and fluid phase are represented by particles. This leads to a molecular description of the fluid flow. The flow of both

phases is determined by solution of Newton's second law for motion for each particle and the interaction between both phases is a result of the particle collisions. An extremely fine resolution of the multiphase flow processes is obtained by the Lagrangian-Lagrangian approach. In fact, according to Hoef et al. (2008), the resolved scales are so fine in the Lagrangian-Lagrangian approach that it is only relevant in cases of a strong influence of thermal fluctuations of the fluid phase on the motion of the solid particles.

Description of fluid-solid flows on a slightly larger scale leads to the so called resolved Eulerian-Lagrangian approach (cf. Hoef et al. (2008)). In this kind of direct numerical simulation, the fluid flow is determined on a numerical mesh (Eulerian viewpoint) with cell sizes smaller than the actual solid particle sizes, whereas the solid particles are tracked by the Lagrangian approach. The interaction between the phases is achieved by a no-slip boundary condition of the fluid on the particle surfaces.

Direct numerical simulations (DNS), which resolve all fluid structures, allow for validation and development of multiphase models, e.g. Derksen and Sundaresan (2007) used this technique to evaluate two-fluid model closures. Furthermore, DNSs are helpful for investigations of physical phenomena or processes on microscale, e.g. sediment erosion (cf. Kidanemariam and Uhlmann (2014)) or heat transfer in fluid-particle flows (cf. Deen et al. (2012), Deen and Kuipers (2014)). However, DNSs require tremendous computational efforts and are thus not feasible for engineering applications. Yet, DNSs are an invaluable technique to construct models on a larger scale (cf. Deen and Kuipers (2014)).

Models on a larger scale include unresolved Eulerian-Lagrangian approaches and Eulerian-Eulerian approaches (cf. Hoef et al. (2008)). The former approach is similar to the resolved Eulerian-Lagrangian approach, but differs in that the mesh cell size of the Eulerian grid is larger than the particle sizes and therefore confines several particles in one cell. This leads to an averaged fluid flow field. The particles are described by a Lagrangian approach. On this basis, the coupling between fluid and particles is performed by closure terms (e.g. drag closure). These unresolved Eulerian-Lagrangian approaches are computational less costly than direct numerical simulations, but are still rather applied to laboratory scale experiments than full-scale engineering tasks (cf. Hoef et al. (2008)).

Eulerian-Eulerian approaches known as two-fluid models are useful to simulate engineering fluid-solid flow problems. In a fluid-particle flow, both phases are modelled as separate continua whose interactions have to be considered not only in a fluid-solid closure, but also in a solid-solid closure. The advantage of such an approach is the requirement of much less computational power than more detailed approaches. However, one drawbacks is the necessity of an adequately developed and calibrated model for the

investigating problem. Moreover, only a narrow range of physical parameters and effects can be considered due to limited closure modelling capabilities.

1.4 Aim & structure of thesis

The aim of this thesis is on one hand to study and develop the capabilities of the discrete element method and partially saturated lattice Boltzmann method couplings to simulate dense suspensions. On the other hand, this thesis aims to show how aforementioned methodologies can be be used to investigate physical microscale processes affecting the bulk behaviour of dense suspensions. Therefore, the following chapter 2 discusses the necessary fundamentals - micro-macro-scale transition, simulation methods on microscale, and modelling approaches on macroscale. The subsequent result chapters 3-6 of this thesis are written in article form for publication reasons in journals. Hence, the chapters contain separate introduction, methodology, and conclusion sections. In chapter 3, two partially saturated lattice Boltzmann methods to simulate suspensions are theoretically and numerically evaluated with regard to the stresslet computation and its effect on the bulk viscosity of suspensions. In chapter 4, the partially saturated lattice Boltzmann method is evaluated and calibrated in terms of simulation capabilities of lubrication forces between two particles. Thereafter, sheared simulations of dense suspensions are conducted with a discrete element method, employing a lubrication force model, and the previous evaluated coupled lattice Boltzmann discrete element method. A comparison between both simulation approaches is performed showing that dense suspensions can be also simulated by a discrete element method with additional lubrication force modelling. In the last results chapter, the DEM with lubrication force modelling is employed to study and explain the viscosity divergence for increasing solid fraction in dense suspensions and thereby also demonstrating its usefulness to simulate dense suspensions. The thesis finishes with a summary and conclusion chapter which is followed by recommendations for possible future work.

2 Fundamentals & literature review

2.1 Coarse graining

In general, reducing the degrees of freedom of a system is described as coarse graining. In fluid-solid flows, the various Lagrangian and Eulerian methods, described in the previous sections, resolve the fluid and solid phases on different length scales. Bridging the different scales for modelling purposes or combining different methods to hybrid methods can be achieved by coarse-graining of flow parameters, i.e. transferring properties from a fine resolved scale (microscale) to a coarse resolved scale (meso- or macroscale).

2.1.1 Averaging techniques

Coarse-graining requires the averaging of variables. An overview of averaging techniques is provided by, for instance, Drew (1983), Enwald et al. (1996) and Pope (2000), and a recap is given here.

A volume average of a variable $f(\mathbf{x}, t)$ at location $\mathbf{x}$ and time t is defined as:

$$\langle f \rangle_V(\mathbf{x}, t) = \frac{1}{V} \int_V f(\mathbf{x}, t)\, dV\,, \tag{2.1}$$

where the averaging process takes place at a time t around the location $\mathbf{x}$ in the volume V. The dimensions of averaging volume V should be between the characteristic length scales of the phases and the length scales of the system.

Similar, a time average at a location $\mathbf{x}$ over a time interval Δt reads

$$\langle f \rangle_t(\mathbf{x}, t) = \frac{1}{\Delta t} \int_{t-\Delta t/2}^{t+\Delta t/2} f(\mathbf{x}, t)\, dt\,. \tag{2.2}$$

Additionally, there is the possibility to apply an ensemble average:

$$\langle f \rangle_E(\mathbf{x}, t) = \lim_{N\to\infty} \frac{1}{N} \sum_{n=1}^{N} f^{(n)}(\mathbf{x}, t)\,, \tag{2.3}$$

which yields the average of N conducted experiments with regard to the variable $f(\mathbf{x}, t)$ at location $\mathbf{x}$ and time t.

Furthermore, a weighted averaging can be performed. Explained by Anderson and Jackson (1967) and Drew (1983), a weighting function $g(r)$ is therefore introduced. $g(r)$ is a monotonically decreasing function as well as it is always $g(r) > 0$ for all $r > 0$. Moreover, it holds

$$\int_V g(r)dV = 1\,. \tag{2.4}$$

The integration process in equation (2.4) is performed over the whole system volume. Introduction of the aforementioned function $g(r)$ with $r = |\mathbf{x} - \mathbf{y}|$ allows the formulation of a weighted average in volume V_y subject to a spatial coordinate y and can be written as:

$$\langle f \rangle_w(\mathbf{x}, t) = \int_{V_y} f(\mathbf{y}, t) g(|\mathbf{x} - \mathbf{y}|) dV_y\,. \tag{2.5}$$

In statistics an expected value of a variable f, also known as mean, is obtained by:

$$\langle f \rangle_e = \int_{-\infty}^{\infty} \psi p_f(\psi)\, d\psi\,, \tag{2.6}$$

where $p_f(\psi)$ represents a probability density function where ψ is an independent variable which corresponds to the variable f. The obtained averaged variable in equation (2.6) is also called a moment of first order. The mean values of

$$\langle f^n \rangle_e(\mathbf{x}, t) = \int_{-\infty}^{\infty} \psi^n p_f(\psi, \mathbf{x}, t)\, d\psi\,, \tag{2.7}$$

are called a moment of n-th order.

Mathematical details about arithmetic operations between different averaged variables as well as Reynolds decomposition are not explained here and the interested reader is referred to the works by Drew (1983), Enwald et al. (1996) and Pope (2000).

2.1.2 Coarse-graining in fluid-solid flows

The necessary micro-meso-macro transition, i.e. up-scaling from the microscale to larger scale, for fluid-solid flows can be performed by employing above averaging procedures. For example, the porosity ε in a fluid-solid system can be obtained according to Anderson and Jackson (1967) by evaluating (2.5) so that:

$$\varepsilon = \int_{V_y} g(|\mathbf{x} - \mathbf{y}|) dV_y\,, \tag{2.8}$$

where $\mathbf{y}$ is a coordinate in space. Similarly, other quantities can be evaluated, such as the fluid momentum density

$$\varepsilon \langle \mathbf{u} \rangle_f = \int_{V_{fluid}} \mathbf{u}_f(\mathbf{y}) g(|\mathbf{x} - \mathbf{y}|) dV_y\,, \tag{2.9}$$

where $\mathbf{u}_f$ is the fluid velocity at position $\mathbf{y}$, or solid fluid momentum density

$$\varepsilon\langle\mathbf{u}\rangle_s = \int_{V_{particles}} \mathbf{u}_s(\mathbf{y}) g(|\mathbf{x}-\mathbf{y}|) dV_y \,, \tag{2.10}$$

Hitherto, the discussion about coarse-graining has included the whole simulation domain. However, in some cases it is required to average only over specific volume elements, e.g. separate volumes close to walls to filter out wall effects or for coupled Eulerian-Lagrangian methods for which the numerical mesh might define fluid volume elements. Therefore, different coarse-graining methods for fluid-solid flows have been developed. E.g. Sun and Xiao (2015) discuss, mostly for unresolved Eulerian-Lagrange simulations, popular coarse-graining methods for the particle phase, such as the particle centroid method, the divided particle volume method, the two-grid formulation, the statistical kernel method, and the diffusion-based coarse graining method. All methods should fulfil to some extent the following criteria: Conserve physical quantities such as particle mass or particle momenta, flawless coarse graining near boundaries, mesh-independent results, simple implementation into numerical solvers, and achieve smooth coarse grained fields. The first two criteria are of highest importance in order to reproduce correctly all physical properties. The remaining criteria are preferably also fulfilled to achieve an overall excellent coarse-graining method, albeit achievement is not a strict necessity to obtain a physical correct method.

2.2 Microscale

2.2.1 Particle dynamics

Popular methods to investigate the solid phase characteristics on microscale are inelastic hard-sphere models, also referred to as event-driven method, and soft-sphere models according to Herrmann and Luding (1998), Luding (2004), Pöschel and Schwager (2005) and Andreotti et al. (2013). The former method is based on instantaneous collisions between rigid particles. The particle momentum exchange occurs for only two particles in contact and hence the hard-sphere model is used for dilute particle systems. In soft-sphere models, contact forces between spheres are determined from the particle-particle overlap. A soft-sphere model requires therefore a fine time-step resolution leading to extensive computational overhead. Although not recommendable to simulate dilute particle systems, the soft-sphere model is widely used to simulate multi-particle contacts as they are found in for example dense suspensions. Hence, the hard-sphere model is described only very briefly in contrast to the soft-sphere model in the remainder of this section.

2.2.1.1. Hard-sphere method

As above mentioned, collisions with the event-driven method occur instantly and the momentum between particles is exchanged instantly at contact. For a particle-wall collision in direction of the wall normal vector, a coefficient of restitution ε_r can be defined which describes the rebound of the particle from the wall by setting the normal post-collision velocity of a particle $\mathbf{u}_{p,n}^{'}$ in relation to the normal pre-collision velocity $\mathbf{u}_{p,n}$:

$$\varepsilon_r = \frac{\mathbf{u}_{p,n}^{'}}{\mathbf{u}_{p,n}} \, . \tag{2.11}$$

Similarly, the post-velocities of particles with same diameter and mass for collisions along the particle centre-to-centre line can be determined:

$$\mathbf{u}_{p,1/2,n}^{'} = \mathbf{u}_{p,1/2,n} \mp \frac{1+\varepsilon_r}{2} \left(\mathbf{u}_{p,1,n} - \mathbf{u}_{p,2,n} \right) \, . \tag{2.12}$$

Differences in physical and geometrical properties of the particles, rotation, and oblique collisions, which require also modelling of tangential forces, can be considered in hard-sphere models and the interested reader is referred to the works of Herrmann and Luding (1998) and Pöschel and Schwager (2005) for more details.

2.2.1.2. Soft-sphere method

Soft-sphere modelling was introduced by Cundall and Strack (1979) and is widely known as discrete element method (DEM). The theory is based on Newton's equations for motion in translational,

$$m_i \frac{\partial \mathbf{x}_i^2}{\partial^2 t} = \mathbf{F}_i = \sum_i \mathbf{F}_i^C + \sum_i \mathbf{F}_i^L \, , \tag{2.13}$$

and rotational motion,

$$\mathbf{J}_i \frac{\partial \boldsymbol{\omega}_i}{\partial t} = \mathbf{T}_i = \sum_i \mathbf{T}_i^C + \sum_i \mathbf{T}_i^L \, , \tag{2.14}$$

where mass, position, moment of inertia and angular velocity of particle i are described by m_i, $\mathbf{x}_i$, $\mathbf{J}_i$ and $\boldsymbol{\omega}_i$, respectively. Both equations are applicable to particles of any shape. The total force and torque is a superposition between various contributions, such as particle-particle contacts $\sum_i \mathbf{F}_i^C / \sum_i \mathbf{T}_i^C$ or lubrication interactions between particles $\sum_i \mathbf{F}_i^L / \sum_i \mathbf{T}_i^L$. Lubrication theory is succinctly described in the next section 2.2.2 and lubrication modelling in DEM is discussed in chapter 5.

Contact modelling for overlapping particles is an essential part in DEM simulations and different models have been proposed. The most widely used models are a Hooke and Hertz model as described by Luding (1998) and Herrmann and Luding (1998). In normal

direction of the collision, which is along the particle centre-to-centre line, the Hooke model relates the particle overlap δ to a linear spring force with the spring stiffness k_n and relates the relative collision velocity to a dashpot model with the damping coefficient γ_n. In tangential direction, forces are analogously with a spring k_t and dashpot γ_t model constructed leading to the final expression:

$$\mathbf{F}^C_{Hooke} = (k_n \boldsymbol{\delta}_n + \gamma_n \mathbf{u}_{p,rel,n}) - (k_t \boldsymbol{\delta}_t + \gamma_t \mathbf{u}_{p,rel,t}) \ . \tag{2.15}$$

The Hertz model modifies the Hooke model to a non-linear model by multiplication of $\sqrt{\delta_n r_{eff}}$, i.e.

$$\mathbf{F}^C_{Hertz} = \sqrt{\frac{\delta_n}{r_{eff}}} \mathbf{F}_{C,Hooke} \ , \tag{2.16}$$

where the effective particle radius is $r_{eff} = \frac{r_i r_j}{r_i + r_j}$. Schäfer et al. (1996) investigated the spring stiffnesses choice on the collision dynamics and by analysis of the oscillation periods showed that the tangential stiffness is ideally chosen as a function of the normal spring stiffness according to an optimal relation $k_t = \frac{2}{7} k_n$ which leads to similar oscillations in normal and tangential direction. The relation $k_t = \frac{2}{7} k_n$ might not be the ideal choice as recently shown by Thornton et al. (2011), but is commonly used in the DEM literature.

A key component to simulate realistic behaviour of granular materials is consideration of static friction between particles by an additional Coulomb friction criterion:

$$|\mathbf{F}^C_t| \leq |\mu_r \mathbf{F}^C_n| \ . \tag{2.17}$$

The tangential contact force $\mathbf{F}^C_t$ is thereby limited by the product of coefficient of friction μ_r and absolute contact normal force. However, the literature differs in which force contributions are considered for the normal and tangential forces in the Coulomb criterion. Cundall and Strack (1979) evaluate the normal force in the Coulomb criterion (2.17) as the normal spring force $\mathbf{F}^C_n = k_n \boldsymbol{\delta}_n$ and make similarly use of the tangential spring force for the tangential force $\mathbf{F}^C_t = min(k_t \boldsymbol{\delta}_t, \mu_r \mathbf{F}^C_n)$. Slightly different, Herrmann and Luding (1998) suggest to evaluate the Coulomb criteria based on the normal force comprising spring and dashpot force, i.e. $\mathbf{F}^C_n = k_n \boldsymbol{\delta}_n + \gamma_n \mathbf{u}_{p,rel,n}$, but consider only the tangential spring force, i.e. $\mathbf{F}_{k,t} = k_t \boldsymbol{\delta}_t$. Although the aforementioned different Coulomb criterion proposals are exemplarily discussed for the Hooke model, the very same separation of spring and dashpot force contributions for the normal and tangential forces applies for the Hertz model.

Besides the above described contact models, many additional force models to include different physical effects have been proposed. In this work, the particle interactions are limited to mechanical contact and lubrication forces. Hence, a detailed discussion is not carried out here and only the major models are mentioned here for reference purposes. In

simulations carried out in this work, particles are of spherical shape. However, in reality particles are found to have all kind of complex forms. In DEM, non-sphericity of particles can be either modelled by introduction of rolling friction models while using spherical particles as discussed by Ai et al. (2011) or by modelling the complex non-spherical shape. Therefore, non-spherical particle shape can be modelled by polygons according to Cundall (1988) or superquadrics according to Williams and Pentland (1992), or the non-spherical particles are constructed from multiple spherical particles as suggested by Favier et al. (1999) and Jensen et al. (1999). Further modelling approaches for non-spherical particles are possible and discussed in a review by Lu et al. (2015). Apart from particle shape effects in granular flows, the contact between particles can be more complex than previously described. Particles can undergo adhesive, elastic-plastic collisions and contact models capturing such behaviour have been proposed, e.g. by Luding (2005) and Thakur et al. (2014). Furthermore, other non-contact interaction forces relevant for cohesion, e.g. van-der-Walls forces, electrostatic forces, liquid bridge forces, can be considered in simulations and are discussed by Zhu et al. (2007). Although many different geometrical and physical properties can be considered between particles, the caveat of DEM simulations is careful calibration of the various model parameters to obtain correct bulk scale quantities as discussed in a calibration review for DEM by Coetzee (2017).

2.2.2 Lubricated particle interactions & Stokesian Dynamics

Two surfaces separated by a fluid, for example in lubricated bearings, experience a motion resisting force when squeezed together due to an increased pressure build up in the fluid. Similarly, particles in close contact affect each others' kinematics due to indirect interactions through an interstitial fluid. Lubrication interactions are a fundamental part of suspension flows and hence, have been research subject for decades.

Theoretical analysis to derive expressions for lubrication interactions have been undertaken for smooth, rigid, spherical particles in low Reynolds number flows so that the Navier-Stokes equations could be considerable simplified. Solutions for the Stokes equations / creeping flow equations can be determined by series expansion techniques, such as asymptotic expansion or multipole expansion. Brenner (1961) deduced thereby the hydrodynamic interaction force on a sphere while steadily moving aforementioned sphere towards or from a wall or free surface. Solutions for parallel motion of a sphere along a planar wall with regard to translational and rotational motion as well as expressions for hydrodynamic force and torque were found by O'Neill and Stewartson (1967) and Goldman et al. (1967a). The theory derived by Goldman et al. (1967a) also shows that with the above assumptions the moving sphere cannot touch the wall. Furthermore, Goldman et al. (1967b) extended the solutions for a wall undergoing shearing motion. Cox and Brenner (1967) determined more accurate solutions for the hydrodynamic force

on a sphere approaching a wall for very small gap distances by dividing the expansion calculations into an “inner” and “outer” region, depending on the wall-particle distance. Hydrodynamic forces on two particles, of which one is fixed, were analysed by Cooley and O’Neill (1969). Hansford (1970) studied the hydrodynamic forces for two equally sized spheres approaching each other with the same velocities along the centre-to-centre particle line by dividing expansion techniques into an inner and outer regime as introduced by Cox and Brenner (1967). Jeffrey (1982) determined accurately higher order solutions for the hydrodynamic forces on two bi-disperse sized spheres which approach each other with equal velocities. Moreover, Jeffrey (1982) compared derived expressions to previous numerical calculations for different particle size ratios to find numerical values for constant terms in the expanded solutions.

Brenner and O‘Neill (1972) introduced a general formulation to determine hydrodynamic forces and particle velocities for multi-particle systems. Therefore, a grand resistance matrix $\boldsymbol{\mathcal{R}}$ for determination of hydrodynamic forces in dependency of the particle velocities and fluid background shear velocity were developed. Furthermore, a shear resistance matrix, or also so called mobility matrix, which is the inverse of the grand resistance matrix, $\boldsymbol{\mathcal{M}} = \boldsymbol{\mathcal{R}}^{-1}$ to determine particle velocities in dependency of the hydrodynamic forces was introduced. The hydrodynamic forces can be in the simplest form expressed as:

$$\mathbf{F} = \boldsymbol{\mathcal{R}} \cdot \mathbf{U} \, , \tag{2.18}$$

where the force matrix on the left-hand side and the velocity matrix on the right-hand side have N force and velocity vectors for N particles. The grand resistance matrix has thus $N \times N$ elements. The torque is analogously determined.

Further work with regard to the resistance matrix formulation and calculation of matrix elements was conducted by Majumdar and O‘Neill (1972),Cox (1974), and Batchelor (1976) who tried to merge previous literature in terms of the grand resistance matrix formulation. Jeffrey and Onishi (1984) provide an overview of the grand resistance matrix formulation for hydrodynamic forces and torques as well as for the mobility matrix for translational and angular particle velocities with detailed calculations of the matrix elements for bi-disperse two particle pair interactions. Jeffrey (1992) extended the previous work on the resistance and mobility matrix formulation to incorporate strain rate effects and expressions for the stresslet values in a two particle system. For the interested reader the very detailed and comprehensive overview of lubrication interactions, their derivations and general formulation in grand resistance matrix formulation by Kim and Karrila (2005) is strongly recommended. In chapter 5, the idea and details of the grand-resistance matrix formulation are revisited to simulate dense suspensions through the means of a DEM.

In Stokesian dynamics, developed by Bossis and Brady (1984) and Brady and Bossis (1988), the grand-resistance matrix for pairwise particle-particle interactions is used to

determine the motion of inertialess particles. The particle motion can be described by Newton's second law, i.e.

$$\mathbf{m}\frac{\partial \mathbf{x}^2}{\partial^2 t} = \mathbf{F}^H + \mathbf{F}^C + \mathbf{F}^B \ . \tag{2.19}$$

Besides hydrodynamic forces $\mathbf{F}^H$, contact forces $\mathbf{F}^C$ for colliding particles and forces from Brownian motion $\mathbf{F}^B$ can be considered. For inertialess particles, valid for low Reynolds number flows, the left-hand side vanishes and Eq. (2.19) can be re-written by substitution of Eq. (2.18) to:

$$0 = \boldsymbol{\mathcal{R}} \cdot \mathbf{U} + \mathbf{F}^C + \mathbf{F}^B \ , \tag{2.20}$$

which leads to the following expression for the particle velocities:

$$\mathbf{U} = -\boldsymbol{\mathcal{R}}^{-1} \cdot \left(\mathbf{F}^C + \mathbf{F}^B\right) \ . \tag{2.21}$$

The particle positions are updated for every timestep from Eq. (2.21). However, the Stokesian dynamics method requires computation of the inverse grand resistance matrix at every single timestep due to its dependency of the geometrical relations, distance and size ratio, between particles.

The above discussion about lubrication forces is based on the assumption of smooth particles. In reality however, particles exhibit a surface roughness and the surface asperities are commonly of the size 10^{-2} to 10^{-3} of a particle radii according to measurements of Smart and Leighton Jr. (1989). Such particle asperities can lead to changed interactions between particles and thereby to changed particle trajectories as shown by Da Cunha and Hinch (1996). Thus, changed particle interactions due to surface roughness lead to a change in suspension rheology with normal stress differences not found for smooth particles and reduced suspension viscosities for increased surface roughness according to Davis et al. (2003). However, Tanner and Dai (2016) reported in contrast to Davis et al. (2003) increased suspension viscosities for rough particles. The opposing results could be possibly explained by different friction conditions. The friction is unchanged for changed asperity sizes in the analysis conducted by Davis et al. (2003) whereas the friction coefficients of the particles used in the experiments by Tanner and Dai (2016) are not measured and hence not stated. However, Tanner and Dai (2016) mention in the introduction that an increased roughness could be related to increased friction which could explain the different findings to Davis et al. (2003).

Besides surface roughness, particle inertia affects particle-particle collisions within a fluid. Previous work on particles colliding with a wall immersed in a fluid, e.g. numerical work by Davis et al. (1986) and experiments conducted by Joseph et al. (2001) and Gondret et al. (2002), shows that the collision and particle rebounce depend only to some weak extent on the particle material and that it can be classified according to a Stokes number $St = \frac{m_p U_0}{6\pi\mu_f r_p^2}$ where m_p is the particle mass, U_0 is the approaching velocity, μ_f the fluid

viscosity, and r_p is the particle radius. For Stokes numbers below a value of around ten, the rebound of a sphere is strongly affected by the fluid leading to no observable rebound. For Stokes numbers larger than ten, the fluid influence on the rebound starts to decrease. An effective coefficient of restitution $\varepsilon_{eff} = \frac{\varepsilon_{wet}}{\varepsilon_{dry}}$ can be defined where the coefficient of restitution is defined as the ratio of impact velocity U_{impact} and rebound velocity $U_{rebound}$, i.e. $\varepsilon = \frac{U_{rebound}}{U_{impact}}$. For increasing Stokes numbers the effective coefficient of restitution increases and asymptotically converges towards $\varepsilon_{eff} = 1$ for very large Stokes number $St > \mathcal{O}(1000)$, i.e. the fluid influence is irrelevant as the rebounce cannot be differentiated to dry collisions. The altered collision behaviour and the influence of particle surface roughness on the collision is attempted to be described in changed collision models obeying elastohydrodynamic lubrication theory, e.g. Yang (2006) and references therein.

2.2.3 Lattice-Boltzmann Method (LBM)

2.2.3.1. Basic theory

A fundamental approach to describe fluids are lattice-gas models / lattice-gas automaton (LGA). In LGAs the fluid molecules are represented by fictitious molecules, called discrete Boolean elements, with discrete locations and velocities. The single Boolean elements are placed on nodes of a lattice (cf. figure 2.1). As described by Frisch et al. (1986), the LGA procedure consists of two repeating steps: Propagation and collision. In the propagation step the discrete elements are moved along the node connections into the direction of their velocity vectors. In the following collision step, the collisions between discrete elements, which are located on the same node, are computed. The number of discrete elements and the corresponding momentum are conserved during the collision processes.

Simulations with LGA are very detailed and applying LGA on larger scales is not viable. However, instead of using discrete Boolean elements, the discrete Boolean elements can be statistically summarised in particle distribution functions, as elucidated by McNamara and Zanetti (1988). Therefore, the molecules of the fluid are ensemble averaged, and the evolution of the particle distribution function in space and time can be described by the Boltzmann equation:

$$\frac{\partial f}{\partial t} + \boldsymbol{\xi} \cdot \frac{\partial f}{\partial \mathbf{x}} + \frac{\mathbf{F}}{m} \cdot \frac{\partial f}{\partial \boldsymbol{\xi}} = \left(\frac{\partial f}{\partial t}\right)_{coll} . \tag{2.22}$$

This fundamental gas-kinetic transport equation was derived by Boltzmann (1872) where the left-hand side represents the substantial derivative of the particle distribution function f and a collision term is found on the right-hand side.

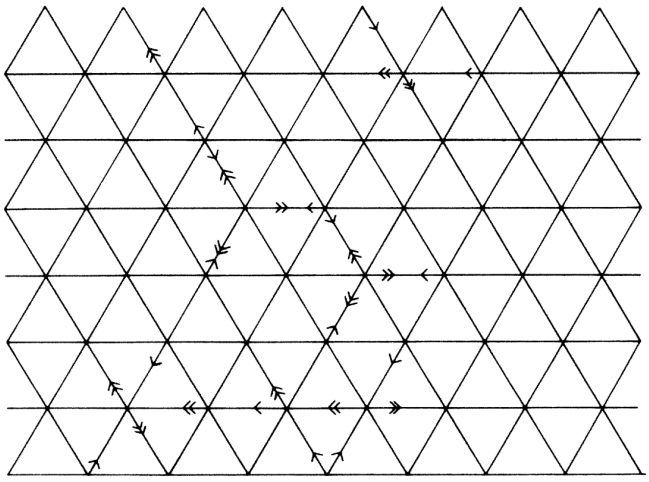

Fig. 2.1.: Lattice for a lattice-gas automata. Elements with a single arrow represent the actual time step, whereas elements with a double arrow are the following timestep. Adopted from Frisch et al. (1986).

The particle distribution function $f(\mathbf{x}, \boldsymbol{\xi}, t)$ in the Boltzmann equation provides information about the mass of molecules with velocity $\boldsymbol{\xi}$ at location $\mathbf{x}$ at time t, i.e. the distribution function has in a three-dimensional physical space and three-dimensional velocity space the units $[f] = \frac{mass}{length^3 \times (length/time)^3} = \frac{mass \times time^3}{length^6}$. This means that an integration over the whole physical space $\mathbf{x}$ and velocity space $\boldsymbol{\xi}$ yields the mass m of molecules in the system:

$$m = \int_{\boldsymbol{\xi}} \int_{\mathbf{x}} f(\boldsymbol{\xi}, \mathbf{x}, t)\, d\mathbf{x}\, d\boldsymbol{\xi}\,. \tag{2.23}$$

As one is usually more interested in quantities on the macroscale than on the microscale, equation (2.23) can be generalised by taking moments of the particle distribution function according to equation (2.7). Thereby, the macroscopic density

$$\rho(\mathbf{x}, t) = \int \boldsymbol{\xi}^0 f(\mathbf{x}, \boldsymbol{\xi}, t) d\boldsymbol{\xi} \tag{2.24}$$

or the macroscopic momentum

$$\rho(\mathbf{x}, t)\mathbf{u}(\mathbf{x}, t) = \int \boldsymbol{\xi}^1 f(\mathbf{x}, \boldsymbol{\xi}, t) d\boldsymbol{\xi} \tag{2.25}$$

can be evaluated.

In LGA the collisions occur between single molecules, whereas in the Boltzmann equation, the collision process between molecules results in a change of the particle distribution function $f(\mathbf{x}, \mathbf{c}, t)$. A change in the distribution function due to collision is expressed in the collision term on the right-hand side of the Boltzmann equation and has to be modelled. The approach to model the collision term suggested by Boltzmann (1872) is based on the collision between two elastic particles which are uncorrelated before collision. The derivation can be either found in Boltzmann (1872) or Lieberman and

Lichtenberg (2005) and the final collision integral can be written according to Lieberman and Lichtenberg (2005) as:

$$\left(\frac{\partial f}{\partial t}\right)_{coll} = \int d^3v_2 \int_0^{2\pi} d\phi_1 \int_0^{\pi} (f_1' f_2' - f_1 f_2)|\mathbf{v_1} - \mathbf{v_2}| I sin\theta_1 d\theta_1 \tag{2.26}$$

where the particles have the relative velocity $|\mathbf{v_1} - \mathbf{v_2}|$ and the particle distribution function of the colliding particles after the collision is given by f_1' and f_2' and before the collision by f_1 and f_2. However, evaluation of the collision integral (2.26) is difficult and simpler collision term models have been suggested. Different collision terms are discussed in the later subsection 2.2.3.6, but for the sake of elucidating the Chapman-Enskog expansion in section 2.2.3.3, a common simplified expression for the collision term is introduced here. The widely known Bhatnagar-Gross-Krook (BGK) model proposed by Bhatnagar et al. (1954) which reads:

$$\left(\frac{\partial f}{\partial t}\right)_{coll} = \frac{f^{eq} - f}{\tau(v)}\,, \tag{2.27}$$

where the particle distribution function f is relaxed towards a local equilibrium f^{eq} over a collision relaxation time τ. The equilibrium function f^{eq} can be determined by the solution of the Boltzmann equation in the special case of thermodynamic equilibrium and has for mono-atomic collisions a Maxwell distribution:

$$f^{eq}(\mathbf{x}, |\mathbf{v}|, t) = \rho \left(\frac{1}{2\pi RT}\right)^{3/2} e^{-|v|^2/(2RT)}\,, \tag{2.28}$$

where R and T are the gas constant and the temperature, respectively.

2.2.3.2. Discretised Boltzmann equation

The Boltzmann equation in continuous form, i.e. Eq. (2.22), is difficult to evaluate because the particle distribution function spans over seven dimensions. However, it is simpler to solve the equation numerically and therefore, discretisation in velocity space, physical space, and time are required. The procedure to discretise the Boltzmann equation has been extensively elucidated in the literature, e.g. Wolf-Gladrow (2000), Succi (2001) and Krüger et al. (2017), and instead of reiterating all the details, only the key points are provided here. The discretisation of the velocity space follows basically the following points:

1. Non-dimensionialise the Boltzmann equation (2.22)

2. An equilibrium function can be determined from the Boltzmann equation for an equilibrated system, resulting in a Maxwell distribution

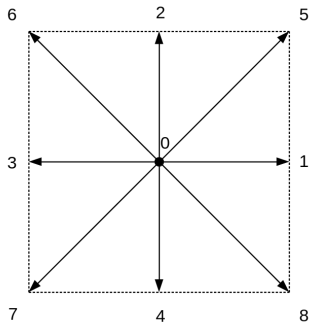

Fig. 2.2.: Two dimensional lattice arrangement with 9 velocities (D2Q9).

3. Simplify the equilibrium distribution by applying Hermite polynomials up to second order

4. Discretise the velocity space by Hermite-Gauss quadrature

5. Apply Hermite expansion and Hermite-Gauss quadrature also to the distribution function

6. Rescale velocities by $1/\sqrt{3}$ to remove irrational factors

Alternatively, the discretisation in velocity space can be achieved by a Taylor expansion about the Mach number and can lead to correct mass and momentum conservation (i.e. Navier-Stokes equations) on macroscale. However, a difference for higher orders, i.e. on the energy balance level, is found compared to a Hermite expansion. In either way, the focus is here on isothermic adiabatic fluids which leads to the velocity-discretised equilibrium function:

$$f^{eq}(\mathbf{x}, v_i, t) = w_i \rho \left(1 + \frac{c_{i_\alpha} u_\alpha}{c_s^2} + \frac{u_\alpha u_\beta (c_{i_\alpha} c_{i_\beta} - c_s^2 \delta_{\alpha\beta})}{2 c_s^4} \right) . \tag{2.29}$$

The weighting function w_i depends on the number and arrangement of lattice velocities c_i. The lattice velocities have to be determined so that the correct macroscale values are obtained. For example, in figure 2.2 is a common velocity set for a two dimensional system illustrated. This lattice arrangement is abbreviated as $D2Q9$ system indicating two dimensions ($D2$) and nine velocity directions ($Q9$). The corresponding weighting functions are then for the different populations $w_0 = 4/9$, $w_{1/2/3/4} = 1/9$, and $w_{5/6/7/8} = 1/36$. For other lattice structures, the weighting functions change so that macroscale values, such as momentum or stresses, are correctly obtained. The dimensionless and velocity-discretised Boltzmann equation reads then:

$$\frac{\partial f_i}{\partial t} + \mathbf{c}_i \cdot \frac{\partial f_i}{\partial \mathbf{x}} = \Omega_i + F_i \, , \tag{2.30}$$

where the index i represents a specific particle distribution function between $i = [0...Q-1]$. The terms Ω_i and F_i represent a collision term and external forcing term, respectively.

Besides the velocity space discretisation, a discretisation in space and time is necessary. Therefore, common numerical discretisation schemes, as for instance comprehensively described by Ferziger and Perić (2002), can be applied to discretise equation (2.30). If, for example, a first order explicit forward Euler discretisation in time and space is applied, the resulting discretised Boltzmann equation can be expressed as:

$$f_i(\mathbf{x} + \mathbf{c}_i \Delta t, t + \Delta t) - f_i(\mathbf{x}, t) = \Delta t(\Omega_i + F_i) + \mathcal{O}\left(\Delta t^2\right) . \tag{2.31}$$

Equation (2.31) is known as the lattice Boltzmann equation. Similar to LGA, the distribution functions undergo two sequential steps on the numerical mesh, method specifically called lattice, to solve the LB Eq. (2.31): A collison and propagation step. The collision step is locally performed by evaluation of the Ω_i term on each lattice node. During the propagation step, the distribution functions are moved along the chosen lattice arrangement, e.g. $D2Q9$ in figure 2.2, to adjacent lattice nodes.

2.2.3.3. Chapman-Enskog analysis

As mentioned briefly in section 2.2.3.1, construction of adequate moments yields macroscopic values such as the fluid momentum. Similarly, the moments of the discrete distribution functions lead to the macroscopic values, i.e. $\sum f_i = \rho$ and $\sum f_i \mathbf{c}_i = \rho \mathbf{u}$. Mass conservation and momentum equation can be derived by a Chapman-Enskog analysis. This analysis is relevant in the later chapter 3. Here, the focus is on the Chapman-Enskog analysis of the LB equation without an external force, i.e.

$$\frac{\partial f_i}{\partial t} + \mathbf{c}_i \cdot \frac{\partial f_i}{\partial \mathbf{x}} = \Omega_i . \tag{2.32}$$

The Chapman-Enskog analysis is essentially a perturbation ansatz for the particle distribution function in Eq. (2.32). The particle distribution function is perturbed around a small value ϵ to $f = f^{(0)} + \epsilon f^{(1)} + \epsilon^2 f^{(2)} + ...$ and the spatial gradient is perturbed to $\nabla f = \epsilon \nabla f^{(1)}$. In addition to the perturbed distribution function, the time derivative is split into time derivatives of order $\mathcal{O}\left(\epsilon^{(1)}\right)$ and $\mathcal{O}\left(\epsilon^{(2)}\right)$, i.e. $\frac{\partial}{\partial t} = \epsilon \frac{\partial}{\partial t_1} f^{(1)} + \epsilon^2 \frac{\partial}{\partial t_2} f^{(2)}$. Higher order expansions of the perturbed time derivative have to be considered because a viscous stress tensor does not appear otherwise in the macroscale momentum equations and would thereby lead only to the Euler equations, but not the Navier-Stokes equations.

By Taylor expanding (2.32), it can be written:

$$\Delta t(\partial_t + \mathbf{c}_i\nabla)f_i + \mathcal{O}(\Delta t^3) = -\frac{\Delta t}{\tau}f_i^{neq} + \Delta t(\partial_t + \mathbf{c}_i\nabla)\frac{\Delta t}{2\tau}f_i^{neq} \,, \tag{2.33}$$

Applying the aforementioned perturbation ansatz to equation (2.33) and sorting terms with regard to their perturbation order, leads to:

$$\mathcal{O}\left(\epsilon^{(0)}\right) : \; f_i^{(0)} = f_i^{eq}(\mathbf{u}_f) \,, \tag{2.34}$$

$$\mathcal{O}\left(\epsilon^{(1)}\right) : \; \Delta t(\partial_t^{(1)} + \mathbf{c}_i\nabla^{(1)})f_i^{eq} = -\frac{\Delta t}{\tau}f^{(1)} \,, \tag{2.35}$$

and

$$\mathcal{O}\left(\epsilon^{(2)}\right) : \; \Delta t(\partial_t^{(2)})f_i^{eq} = -\frac{\Delta t}{\tau}f^{(2)} - \Delta t(\partial_t^{(1)} + \mathbf{c}_i\nabla^{(1)})\left[1 - \frac{\Delta t}{2\tau}\right]f_i^{(1)} \,. \tag{2.36}$$

From the non-equilibrium function, the constraints $\sum f_i^{(k)} = 0$ and $\sum f_i^{(k)}\mathbf{c}_i = 0$ for $k > 0$ can be deduced.

Taking the zeroth moment of equations (2.35) and (2.36), combination of the resulting equations and reversing the perturbation ansatz, a mass conservation equation on macroscale can be found:

$$(\partial_t + \nabla)\rho\mathbf{u} = 0 \,. \tag{2.37}$$

Similarly a momentum conservation equation can be obtained by taking the first moment of equations (2.35) and (2.36):

$$\partial_t(\rho\mathbf{u}) + \nabla\cdot\Pi = 0 \,, \tag{2.38}$$

where $\Pi = \sum_i c_{i,\alpha}c_{i,\beta}\left[f_i^{eq} + \left(1 - \frac{1}{2\tau}\right)f_i^{(1)}\right]$ is the momentum flux tensor. The first term can be evaluated to $\Pi^{(0)} = \sum_i c_{i,\alpha}c_{i,\beta}f_i^{eq} = p\delta_{\alpha\beta} + \rho u_\alpha u_\beta$ where $p = \rho/3$. The second term $\Pi^{(1)} = \sum_i \left(1 - \frac{1}{2\tau}\right)f_i^{(1)}$ can be determined by taking the second moment of equation (2.35) which leads to $\Pi^{(1)} = \nu(\nabla_\alpha(\rho u_\beta) + \nabla_\beta(\rho u_\alpha))$ where $\nu = (\tau - 1/2)c_s^2$ with the speed of sound $c_s = 1/\sqrt{3}$. Substitution into Eq. (2.38) leads to the incompressible Navier-Stokes equations:

$$\partial_t(\rho\mathbf{u}) + (\mathbf{u}\cdot\nabla)(\rho\mathbf{u}) = -\nabla p + \nu\nabla^2(\rho\mathbf{u}) \,. \tag{2.39}$$

2.2.3.4. Boundary conditions

Important in numerical simulations are appropriate formulation of boundary conditions on the fringe and within the simulation domain as the very dynamics in fluid flows are subject to the boundary conditions. In common computational fluid dynamics (CFD)

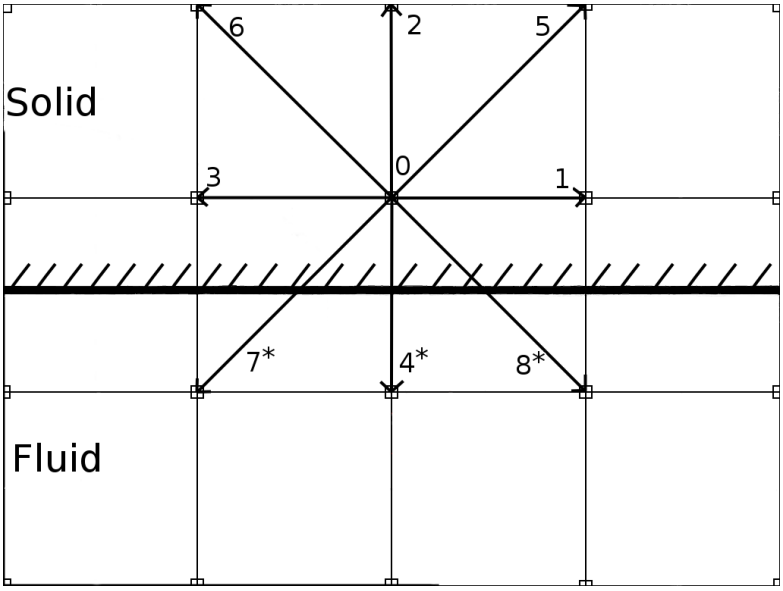

Fig. 2.3.: Sketch of bounce-back boundary condition.

methods, such as finite difference methods (FDM) or finite volume methods (FVM) to solve the macroscopic conservation equations, the boundaries can be straightforward imposed by setting macroscopic conditions on the boundary and corresponding ghost nodes, e.g. definition of a no-slip condition on walls can be achieved by ad-hoc definition of the macroscopic velocity values on the boundary nodes. Boundary conditions for the LBM are somewhat more complex due to solving for the Boltzmann equation, which describes the fluid on a mesoscale by the particle distribution function, in contrast to the conservation equations on macroscale. Therefore, the particle distribution functions on or close to boundaries need to be adequately manipulated or expressed as a function of macroscopic quantities.

Boundary conditions for walls can be basically grouped into two categories: Link-wise and wet-node boundaries. For the first type, the boundary lies in-between the fluid and the solid node as exemplary depicted in figure 2.3. The latter type defines the boundary condition on the solid node. In both cases, part of the particle distribution functions are known due to being streamed from adjacent fluid nodes onto the solid nodes. However, other distribution functions, e.g. f_4^*, f_7^*, and f_8^* in figure 2.3 for a top wall boundary condition in a D2Q9 system, are unknown. The unknown particle distribution functions have to be set or determined so that the required macroscopic boundary conditions are achieved.

The link-wise boundary conditions can be distinguished into a full-way and half-way bounce back. During a full-way bounce back, explained by e.g. He et al. (1997) and Chen and Doolen (1998), the distribution functions undergo the usual propagation step. But the unknown populations at the wall are determined during the collision step by assigning the values of the known distribution functions which would propagate out

of the simulation domain, i.e. $f_{-i} = f_i$ where the subscript $-i$ represents the opposite distribution function of i (e.g. $f_4 = f_2$ in a $D2Q9$ system). For half-way bounce back conditions, the unknown distribution functions at the current collision step are assigned the values of the opposite particle distribution functions from the previous collision step. Thereafter, the propagation step is performed.

Wet-node boundaries incorporate macroscopic quantities, such as density or velocity, to find expressions for the particle distribution functions interaction with solid nodes. A common wet-node boundary was proposed by Zou and He (1997) who basically evaluate mass and momentum according to $\rho = \sum_i f_i$ and $\rho\mathbf{u} = \sum f_i \mathbf{c}_i$, respectively, on the boundary nodes to find expressions for the unknown particle distribution functions. The resulting system of equations requires however closure which is achieved by assumption of a non-equilibrium bounce back. Thereby, the unknown particle distribution functions are expressed in dependence of the known particle distribution function and macroscopic densities and velocities. The non-equilibrium bounce back boundary can be used to define either a velocity or pressure Dirichlet boundary condition. Furthermore, this boundary condition can be not only used to obtain a no-slip condition on a fixed or moving wall, but can also be used as an inlet or outlet condition. More wet-node boundary conditions were developed, e.g. Skordos (1993) tries to increase the accuracy by considering fluid velocity gradients in the equilibrium function or Inamuro et al. (1995) who replace the unknown populations by an equilibrium function which includes a counter slip velocity to impose the correct wall velocity. A comparison between common boundary conditions, including the aforementioned ones, was conducted by Latt et al. (2008) for boundaries which are aligned to the lattice structure. Latt et al. (2008) found that there is no generally advised optimal boundary choice as the choice depends on the simulation geometry and on a competing influence between stability and accuracy.

Apart from the above described boundary conditions, periodic boundary conditions are easily implemented in LB simulations. Therefore, the particle distribution functions which leave the simulation domain are re-inserted on the opposite simulation domain boundary. Based on periodic boundaries, Wagner and Pagonabarraga (2002) introduced Lees-Edwards boundary conditions (LEbc), orignally developed by Lees and Edwards (1972) for molecular dynamic simulations, into the LBM. LEbc allow for study of systems under simple shear without any wall influence. The LEbc can be helpful to study fundamental rheology of suspensions. LEbc are realised by two additional modifications to the distribution functions which cross periodic boundaries in direction of the shearing gradient: A Galilean velocity transformation and a shift of the particle distribution position in shearing direction. The Galilean transformation is

$$f_i^G(\mathbf{x}, t) = f_i(\mathbf{x}, t) + f_i^{eq}(\mathbf{x}, \mathbf{u} + \mathbf{U}_{boundary}, t) - f_i^e q(\mathbf{x}, \mathbf{u}, t) \tag{2.40}$$

and the shift in position is

$$f_i(\mathbf{x}^{\pm}, t) = (1 - d_x^R) f_i^G(\mathbf{x} + d_x^I, t) + d_x^R f_i^G(\mathbf{x} + d_x^I \pm 1, t) \; . \tag{2.41}$$

The shifting procedure of the distribution function has to be interpolated between the discrete lattice nodes as the resulting shifted position does not necessarily have to lie on a lattice node. Therefore, the shifted distance $d_x = t\Delta \mathbf{U}_{boundary,x}$ is split into an integer d_x^I and real part $0 \leq d_x^R < 1$.

Despite the multitude of proposed boundary conditions, the final expressions are relatively simple and often straightforward to implement. Hence, the LBM is popular for simulations with complex geometries, such as fluid flows through porous media. E.g. simulations of flow through static assemblies of particles to obtain precise drag force correlations, which can be then useful for meso- or macro-scale multiphase modelling using CFD-DEM techniques (cf. Hoef et al. (2005), Beetstra et al. (2007c) and Beetstra et al. (2007a), and references therein).

2.2.3.5. External forcing

In equation (2.31) two terms are found on the right side. The first is a fluid collision term, which was only briefly discussed and more details are given in the next section 2.2.3.6, and the other is a term for consideration of external forces. In the most simple approach introduced by He et al. (1997), the external force term in Eq. (2.31) is expressed as:

$$F_i = \frac{w_i \mathbf{c}_i \mathbf{F}}{c_s^2} \; . \tag{2.42}$$

However, Guo et al. (2002) showed by theoretical analysis that additional error terms appear on the macroscale when an external force as in Eq. (2.42) is included in the LB algorithm. Guo et al. (2002) suggested modifications to the external forcing so that the imposed external force is expressed as

$$F_i = \left(1 - \frac{1}{2\tau}\right) w_i \left[\frac{\mathbf{c}_i - \mathbf{u}}{c_s^2} + \frac{(\mathbf{c}_i \cdot \mathbf{u})}{c_s^4} \mathbf{c}_i\right] \cdot \mathbf{F} \tag{2.43}$$

and moreover, the velocity calculation is updated to

$$\rho \mathbf{u} = \rho \mathbf{u}^* + \frac{\Delta t}{2} \mathbf{F} \; , \tag{2.44}$$

where $\rho \mathbf{u}^* = \sum_i f_i \mathbf{c}_i$. Thereby, error terms due to external forcing are removed on the macroscale leading to more accurate results.

Another forcing scheme was introduced by Kupershtokh et al. (2009) who wrote the external force as

$$F_i = f_i^{eq}(\mathbf{u} + \Delta\mathbf{u}) - f_i^{eq}(\mathbf{u}) \; . \tag{2.45}$$

The velocity difference in the first equilibrium term is determined from the imposed force $\mathbf{F}$, i.e. $\Delta\mathbf{u} = \frac{\mathbf{F}\Delta t}{\rho}$. The equilibrium velocities are computed according to $\rho\mathbf{u}^{eq} = \sum_i f_i\mathbf{c}_i$ and differ from the real velocities $\rho\mathbf{u} = \sum_i f_i\mathbf{c}_i + \frac{\mathbf{F}\Delta t}{2}$. Kupershtokh et al. (2009) introduced this forcing scheme to simulate two fluid flows which interact via an additional force term in the LB equation.

In contrast to the above forcing term suggestions, Shan and Chen (1993) set the external forcing term to $F_i = 0$ and incorporate forces by modification of the equilibrium velocity in the fluid collision term leading to

$$\rho\mathbf{u}^{eq} = \sum_i f_i\mathbf{c}_i + \frac{\mathbf{F}\tau}{\rho} \; . \tag{2.46}$$

Similar to boundary conditions in LB, a variety of suggestions to consider external forces exist. A review and comparison by theoretical analysis and numerical simulations of external forcing schemes was conducted by Huang et al. (2011). Based on a theoretical analysis, Huang et al. (2011) group the various external forcing schemes in two different groups depending on similarities in the macroscale error terms. For numerical simulations of single-phase Taylor-Green vortices, all forcing schemes lead to nearly same accuracies. However, simulations of two-fluid multiphase flow show discrepancies between the forcing schemes of which all obtained results have to some extent a dependency on the relaxation parameter choice and different accuracies and stabilities are obtained for different schemes, leading to no clear given recommendation by Huang et al. (2011).

2.2.3.6. Collision terms

In section 2.2.3.1, the BGK collision model, Eq. (2.27), introduced into LBM by Qian et al. (1992), is briefly discussed. However, He et al. (1997) showed that the BGK model leads to slip velocities in Poiseuille flows. The slip velocities are dependent on the relaxation parameter τ, effectively the viscosity, and the employed boundary condition. Yet, the BGK model is only one possible collision term model and other collision models can be a remedy to enforce the no-slip condition for changing viscosities.

As the BGK model has only one relaxation parameter which is linked to the viscosity, introduction of multiple relaxation parameters is the logical conclusion. Multiple relaxation time (MRT) models were introduced by Lallemand and Luo (2000) and D'Humières et al. (2002). The difference to the BGK model is not only the number of relaxation parameters, but that rather the moments on macroscale are relaxed instead of the distribution

functions. For that purpose, the particle distribution functions have to be transformed into the moment space by $m_k = \sum_{i=0}^{q-1} M_{ki} f_i$ where M_{ki} is a transformation matrix. After the collision in moment space, i.e. $\mathbf{S}[\mathbf{m}(\mathbf{x},t) - \mathbf{m}^{eq}(\mathbf{x},t)]$ where $\mathbf{S} = \omega_i \mathbf{I}$ contains several relaxation parameters ω_i, a transformation back to the distribution function space by multiplication of $\mathbf{M}^{-1}$ has to be performed. The transformation matrix can be related to different moments by $m_k = \sum_{i=0}^{q-1} M_{ki} f_i$. For example, the first row leads to $m_0 = \rho = \sum f_i = \sum M_{0i} f_i \rightarrow M_{0i} = 1$. Some relaxation parameters are related to physical quantities, shear and bulk viscosity for example, and other relaxation parameters are not and can be therefore freely chosen. The free parameters can be chosen so that a no-slip condition is fulfilled when the viscosity is changed. Moreover, fine tuning of the free parameters can lead to increased stability of the simulations, which is especially relevant for high Reynolds number flows.

However, choosing the free relaxation parameters is not straightforward or trivial. Somewhat simpler than the MRT scheme is a two relaxation time (TRT) model, suggested by Ginzburg (2005), which consists of only two relaxation parameters. One of the relaxation parameters is related to the viscosity and the other parameter can be freely chosen to improve the accuracy of the simulations.

In both cases, MRT and TRT, the free relaxation parameter(s) have to be determined. For MRT schemes, Lallemand and Luo (2000) and D'Humières et al. (2002) provide relaxation parameter sets based on linear analysis. Another approach is to derive by theoretical analysis the macroscopic slip velocities for Couette or Poiseuille flow in dependence of the relaxation parameters. Therefore, the velocity momentum is computed according to $\rho \mathbf{u} = \sum_i f_i \mathbf{c}_i$ at the wall in form of a general expression which includes the relaxation parameters. The obtained expression of the fluid velocity at the wall can be compared to the known analytical solution to obtain an expression for the slip velocity which in turn can be used to find correlations between the freely chosen relaxation parameters and relaxation parameters which describe physical quantities, such as the viscosity, to improve the no-slip condition. He et al. (1997) found thereby expressions for the slip velocities in dependency of lattice resolution and single relaxation parameter τ. For immersed boundary methods using TRT or MRT, Lu et al. (2012) and Seta et al. (2014) derived analytically expressions for the free parameters in Coutte and Poiseuille flow. They found by numerical simulations that slip velocities cannot be completely circumvented, but the improvement in obtained slip velocities is acceptable where a TRT scheme can be as effective as a MRT scheme. Alternatively, D'Humières and Ginzburg (2009) deduced recurrence equations from the LB evolution equation with a TRT model in steady-state. The recurrence equations are basically a set of equations which result from a combination of the evaluated LB equation, i.e. all possible LB propagation steps are written out in explicit forms and combined to recurrence equations (equations which depend recursively on previous values). The obtained general recurrence equations were analysed for bounce-back boundary conditions. D'Humières

and Ginzburg (2009) found an optimal combination between the two relaxation times which can lead to reduced constant slip velocities when properly "calibrated" with regard to the employed boundary conditions. Furthermore, free parameters have been attempted to be empirically determined by conducting simulations and varying the parameters to find optimal parameters sets with regard to stability and accuracy, e.g. Pan et al. (2004) and Pan et al. (2006). However, the caveat of determining parameter sets for one specific case, e.g. Poiseuille flow, is the narrow range of its validity. For a changed setup, e.g. coupled fluid-particle flows, a different parameter set might prove more reliable, as stated by D'Humières and Ginzburg (2009), i.e. ideally parameter sets have to be individually determined as they do not apply in general.

2.2.3.7. Fluid-solid couplings

Despite the multitude of boundary conditions in LBM, complex geometries can be simulated relatively straightforward, especially when compared to common CFD techniques such as FDM or FVM. Thus, LBM is predestined to simulate flow through porous media or multiphase flow as the bulk of literature in this fields, summarised by Chen and Doolen (1998) and Aidun and Clausen (2010), shows.

Pioneering work to simulate fluid-solid multiphase flow with a LBM was done by Ladd (1994a), Ladd (1994b) and Ladd and Verberg (2001) and has been widely used since then. The coupling between the solid particle and the fluid is based on local momentum transfer between distribution functions, which are inside and outside the particle volume, on the particle surface realised by bounce back of the distribution functions. The distribution functions colliding with the particle surface are modified by

$$f_{-i}(\mathbf{x}, t+\Delta) = f_i(\mathbf{x}, t) - 2w_i\rho\mathbf{u}_b \cdot \mathbf{c}_i \tag{2.47a}$$

$$f_i(\mathbf{x}, t+\Delta) = f_{-i}(\mathbf{x}, t) + 2w_i\rho\mathbf{u}_b \cdot \mathbf{c}_i \ , \tag{2.47b}$$

where Eqs. (2.47a) and (2.47b) describe the modifications of the outside and inside distribution functions, respectively. The opposing distribution function of f_i is expressed as f_{-i} and the particle boundary velocity is determined through consideration of translational particle velocity $\mathbf{u}_p$ and angular particle velocity Ω_p in relation to the particle centre of mass $\mathbf{x}_{p,c}$ as $\mathbf{u}_b = \mathbf{u}_p + \Omega_p \times (\mathbf{x} + \frac{1}{2}\mathbf{c}_i - \mathbf{x}_{p,c})$. The hydrodynamic force and torque from the fluid on the particle can be computed from the momentum exchange between the distribution functions. Therefore, the local forces on the boundary nodes,

$$F_{H,LBM,node}(\mathbf{x} + \frac{1}{2}\mathbf{c}_i) = 2\left[f_i(\mathbf{x}, t) - f_{-i}(\mathbf{x} + \mathbf{c}_i, t) - 2w_i\rho\mathbf{u}_b \cdot \mathbf{c}_i\right]\mathbf{c}_i \ , \tag{2.48}$$

have to be summed up: $\mathbf{F}_H = \sum F_{H,LBM,node}(\mathbf{x} + \frac{1}{2}\mathbf{c}_i)$ and $\mathbf{T}_H = \sum(\mathbf{x} + \frac{1}{2}\mathbf{c}_i) \times F_{H,LBM,node}(\mathbf{x} + \frac{1}{2}\mathbf{c}_i)$. Aidun et al. (1998) removed the fluid within particles to mitigate the restriction of particles having a much larger density than the fluid and being able to set the particle density to similar values as the fluid density. However, the fluid removal within particle volume leads to local violations of the mass conservation. The bounce back method to couple fluid and solid phase can be used to simulate the rheology of suspensions in shear flow realised by two parallel sheared wall as was shown by Hyväluoma et al. (2005). A simple shear setup between two sheared walls was used by Kulkarni and Morris (2008) and Haddadi and Morris (2014) to study the suspension rheology with regard to viscosity, normal stress differences, pressure, mircostructure, and radial distribution functions. However, for simple shear realised by Lees-Edwards boundary conditions, Lorenz et al. (2009a) showed that neither the method by Ladd (1994a) nor by Aidun et al. (1998) conserve the particle momentum for a particle crossing Lees-Edwards boundary conditions. Lorenz et al. (2009a) introduced therefore a correction leading to the correct momentum conservation. Lorenz et al. (2009b) showed that sheared simulations with Lees-Edwards boundary conditions to compute bulk viscosities can be possible with the suggested momentum correction.

Another approach to couple fluid-solid flows is the immersed boundary method (IBM) introduced in LBM by Feng and Michaelides (2004) and Feng and Michaelides (2005). Based on the IBM proposed by Peskin (2002), Lagrangian marker points are placed on the particle surface. The coupling to the fluid, simulated by LBM on an Eulerian background lattice, is achieved by introduction of an additional forcing term F_i in the LB equation:

$$f_i(\mathbf{x} + \mathbf{c}_i\Delta t, t + \Delta t) = f_i(\mathbf{x}, t) + \Omega_i^f + F_i \ . \tag{2.49}$$

The forcing term is determined from the no-slip condition on the particle surface. Therefore, the fluid velocities have to be interpolated from the Eulerian lattice points $\mathbf{x}_f$ to the Lagrangian marker points $\mathbf{x}_l$ by

$$\mathbf{u}(\mathbf{x}_l, t) = \sum_f \mathbf{u}(\mathbf{x}_f, t) D(\mathbf{x}_f - \mathbf{x}_l)\Delta x^3 \ , \tag{2.50}$$

where

$$D(\mathbf{x}_f - \mathbf{x}_l) = \delta(x_f - x_l)\delta(y_f - y_l)\delta(z_f - z_l) \tag{2.51}$$

and

$$\delta(r) = \begin{cases} \frac{1}{4}\left(1 + cos\left(\frac{\pi|r|}{2}\right)\right) & , \ |r| \leq 2 \\ 0 & , \ |r| > 2 \end{cases} \ . \tag{2.52}$$

The force density at the Lagrangian points $\mathbf{G}(\mathbf{x}_l, t)$,

$$\mathbf{G}(\mathbf{x}_l, t) = \frac{\mathbf{u}_p(\mathbf{x}_l, t) - \mathbf{u}(\mathbf{x}_l, t)}{\Delta t} \ , \tag{2.53}$$

has to be spread to the Eulerian points,

$$\mathbf{G}(\mathbf{x}_f, t) = \sum_{l}^{N} \mathbf{G}(\mathbf{x}_l, t) D(\mathbf{x}_f - \mathbf{x}_l) \Delta A \ , \tag{2.54}$$

where ΔA is the surface area of the corresponding boundary point. The external forcing term in Eq. (2.49) can be then expressed as:

$$F_i = \frac{3\rho w_i}{c^2} \mathbf{G} \cdot \mathbf{c}_i \ . \tag{2.55}$$

Many different suggestions for combination of fluid collision term and calculation of the forcing term have been investigated by Lu et al. (2012) and Seta et al. (2014). As described in the previous section 2.2.3.6, Seta et al. (2014) found that a TRT scheme can be as effective as a MRT scheme to reduce slip velocity effects. However, the slip velocities cannot be completely avoided and Seta et al. (2014) show that slip velocities depend not only on the fluid collision scheme, but also on the smoothing function δ when an IBM is used.

Besides the fluid-solid couplings which are based on the bounce back rule and the IBM, partially saturated cell methods (PSM) can couple fluid and solid phase. As very detailed analyses of the PSM is performed in chapters 3 and 4, the basic concept is discussed here only very briefly. In a PSM, developed by Noble and Torcyznski (1998), the particle overlaps with an Eulerian lattice. Each overlap is considered by a collision term for the solid phase Ω_i^s in addition to the fluid phase collision Ω_i^f so that the LB equation is written as:

$$f_i(\mathbf{x} + \Delta t \mathbf{c}_i, t + \Delta t) = f_i(\mathbf{x}, t) + \left[1 - B(\mathbf{x}, \tau)\right] \Omega_i^f + B(\mathbf{x}, \tau) \Omega_i^s \ , \tag{2.56}$$

where $B(\mathbf{x}, \tau)$ is a weighting function to take the particle overlap with the lattice node at $\mathbf{x}$ into account. Noble and Torcyznski (1998) suggested two solid phase collision models Ω_i^s of which the first, and most popular, is inspired by the non-equilibrium bounce-back boundary condition,

$$\Omega_i^s = f_{-i}(\mathbf{x}, t) - f_i(\mathbf{x}, t) + f_i^{eq}(\rho, \mathbf{U}_s) - f_{-i}^{eq}(\rho, \mathbf{u}) \ , \tag{2.57}$$

and a second suggestion, named superposition method,

$$\Omega_i^s = f_i^{eq}(\rho, \mathbf{U}_s) - f_i(\mathbf{x}, t) + \left(1 - \frac{\Delta t}{\tau}\right) \left[f_i(\mathbf{x}, t) - f_{-i}^{eq}(\rho, \mathbf{u})\right] \ . \tag{2.58}$$

Holdych (2003) slightly modified the solid collision term (2.57) by substituting the fluid velocity by the particle velocity:

$$\Omega_i^s = f_{-i}(\mathbf{x}, t) - f_i(\mathbf{x}, t) + f_i^{eq}(\rho, \mathbf{U}_s) - f_{-i}^{eq}(\rho, \mathbf{U}_s) \ . \tag{2.59}$$

Furthermore, the weighting function $B(\mathbf{x}, \tau)$ can assume different forms. Noble and Torcyznski (1998) proposed a linear weighting function of the lattice solid fraction,

$$B(\mathbf{x}, \tau) = \varepsilon_s \ , \tag{2.60}$$

and a non-linear function,

$$B(\mathbf{x}, \tau) = \frac{\varepsilon_s(\tau/\Delta - 1/2)}{(1-\varepsilon_s) + (\tau/\Delta t - 1/2)} \ . \tag{2.61}$$

The solid fraction ε_s on the lattice nodes has to be accurately determined for the PSM. Owen et al. (2011) discuss different approaches to evaluate the solid fraction and group them into three different categories, viz. exact closed-form solution, cell decomposition, and polygonal approximation. For the first method, exact closed-form solution, the solid fraction for a lattice node covered by a particle is computed exactly. In contrast, the second approach is a brute force method and used in later chapters (cf. also Fig. 3.1). Basically, the lattice cells are decomposed into smaller cells, a subgrid, and the number of sub-cells inside the particle volume are used to compute the solid fraction. This method is universally applicable and straightforward to implement, but comes with drastically increasing computational overhead for increasing subgrid resolution. Methods in the third category evaluate the lattice node solid fraction from polygon (2D) and polyhedra (3D) approximations of the particle surface. In contrast to determining the solid fraction, Zhou et al. (2011) replaced the solid fraction ε_s in the above weighting functions by a normalised shortest distance D_s, ranging between [0,1], between lattice node and particle surface, i.e. $D_s = 1 - \frac{d_s}{d_{max}}$ where d_s is the shortest distance between lattice node and particle surface and $d_{max} = \sqrt{2}/2$ is the maximum value of d_s (here in a 2D system).

All above described fluid-solid couplings have in common that the Eulerian lattice cell size is smaller than the particle size, i.e. the fluid flow around the particles is resolved to a length scale comparable to the lattice cell size. For particles in close contact, when the gap distance is below one lattice cell size, the fluid flow cannot be determined. However, for high solid fractions, as for dense suspensions, close range lubrication forces between particles are important. Thus, Nguyen and Ladd (2002) and Ding and Aidun (2003) introduced for small gap distances, which cannot be resolved, a lubrication force correction. Nguyen and Ladd (2002) compute lubrication force corrections on basis of the grand-resistance matrix (cf. section 2.2.2) which requires only particle properties, such as particle velocities and sizes, and a gap distance based on the difference between actual particle gap distances and minimal resolvable gap distance (of the order of one lattice cell). In comparison, Ding and Aidun (2003) compute a lubrication force correction between particles for paired lattice nodes (links) whose separation is smaller than the minimal resolvable limit. The total lubrication interaction on a particle is obtained by summation of corrections applied on all lattice nodes. Although more cumbersome to

evaluate, the proposed correction of Ding and Aidun (2003) could be possibly also used for non-spherical particles in contrast to the suggestion by Nguyen and Ladd (2002) due to its formulation being based on the GRM which is only valid for spherical particles.

2.2.4 Navier-Stokes solvers

The simulation of fluid flows has a long history of development efforts and the LBM is a rather new technique. In fact, finite difference methods (FDM), finite volume methods (FVM), or finite element method (FEM), which solve for mass conservation and Navier-Stokes equations directly instead of solving the Boltzmann equation, are well established and widely used in academia and industry - especially being the standard CFD tool in industry. Instead of discussing FDM and FVM, a very basic overview of existing fluid-solid couplings for Navier-Stokes solvers are given here and the interested reader is directed to the extensive and comprehensive discussion on FDM and FVM techniques by Ferziger and Perić (2002).

Fluid-solid couplings can be classified into two major groups, namely conforming and non-conforming methods. In conforming methods the numerical mesh conforms to the particle shape leading to tremendous computational costs for moving particles due to frequent mesh movement or remeshing when the numerical mesh becomes too skewed as shown by Haeri and Shrimpton (2012). In contrast, non-conforming methods are based on a fixed Eulerian background mesh. Particles overlap with the Eulerian mesh and a coupling between fluid and solid phase is most commonly obtained by use of an immersed boundary method (IBM), very similar to the IBM discussed in the previous section 2.2.3.7, or a distributed Lagrange multiplier / fictitious domain method (DLM/FD). A very comprehensive overview of possible IBM and DLM/FD methods is given by Haeri and Shrimpton (2012). In essence, coupling of the different phases is obtained by a no-slip condition on the particle surfaces. Therefore, in the DLM/FD approach, firstly developed for rigid particles by Glowinski et al. (1998) and Glowinski et al. (1999), Lagrange marker points are placed over the whole volume of the particles in contrast to the Lagrange force points distributed only on the particle surfaces in the IBM which was originally developed by Peskin (2002) to simulate blood flow through a heart.

In the DLM/FD framework, a strong and weak coupling can be used. For a strong coupling, a fluid-particle mixture equation in form of a Navier-Stokes equation and a DEM for the particle phase are solved. The hydrodynamic forces and torques between particles and fluid have to be determined for the strong coupling. In contrast, a weak coupling does not require determination of hydrodynamic interactions because the motion equations for fluid and particle phase are summarised to a resulting total momentum equation which does not contain hydrodynamic force and torque terms. The detailed derivation process can be found in Glowinski et al. (1999). Glowinski et al. (1999) show that

the DLM/FD can be used for accurate direct numerical simulations of suspensions by validating the method to the settling behaviour of two particles and several hundred circular discs. The DLM/FD method allows also for simulation of non-spherical particles, e.g. Wachs (2009) simulated sedimentation processes for circular, rectangular, and triangular particles. Therefore, Wachs (2009) also introduced additionally a soft-sphere contact model capable to model contact forces of arbitrarily convex shaped particles in normal and tangential direction of a collision.

IBMs, as above mentioned, have Lagrangian marker points placed only on the particle surface. The Navier-Stokes equation for the fluid reads

$$\frac{\partial \mathbf{u}}{\partial t} + (\mathbf{u} \cdot \nabla)\mathbf{u} = -\frac{1}{\rho}\nabla p + \nu \nabla^2 \mathbf{u} + \mathbf{f}_i \ , \tag{2.62}$$

where the term $\mathbf{f}_i$ represents a force expression between particle i and fluid. A variety of methods exist to determine the forcing term. In essence, the procedure is similar to IBMs in LBM as discussed in section 2.2.3.7, i.e. the no-slip condition on the particle surfaces is achieved by interpolating the fluid velocities to the Lagrange force points and determining the force term at each Lagrangian point by considering the velocity difference between fluid and particle surface. The particle velocities are evaluated by Newton's second law for motion in which also other forces, such as gravitation or collision forces, can be considered (cf. equations (2.13) and (2.14)). The results for the forcing term are interpolated back to the Eulerian grid, to be included into the Navier-Stokes equations (2.62). A popular and efficient direct forcing approach for moving particles was proposed by Uhlmann (2005). According to Uhlmann (2005), a discrete volume is associated to each Lagrangian force point resulting in a fluid-solid interaction volume force term, which is obtained by the aforementioned interpolation procedure, rather than a single interaction force acting on each Lagrangian point. Thereby, every particle is surrounded by a layer of volume forces. The proposed method by Uhlmann (2005) leads to smooth particle motions and less restrictive time-step choices. The efficiency of the IBM is demonstrated, for instance, in direct numerical simulations of turbulent open channel flows to study sediment erosion effects with over 260000 particles by Kidanemariam and Uhlmann (2014).

2.3 Macroscale

2.3.1 Governing equations

Fluid-solid flows can be described on macroscale by an Eulerian-Eulerian approach, such as a two-fluid model (TFM) approach. Both phases, fluid and solid phase, are not fully resolved continua described by averaged conservation equations. The averaged conservation equations (mass, momentum, energy) are deduced for each phase

separately by applying averaging processes (cf. section 2.1.1), such as volume, time-volume and weighted time-volume averaging methods, to the local instantaneous balance equations.

2.3.1.1. Averaged equations

The derivation of averaged two-fluid equations have been extensively studied by many research groups, e.g. Anderson and Jackson (1967) and Nott et al. (2011). The final set of averaged two-fluid equations for a single fluid and single solid phase, whose stepwise deduction can be found for example in Anderson and Jackson (1967), are obtained by applying a weighted averaging technique, such as Eq. (2.5), on point mass and momentum conservation equations and can be written with an external volume force (e.g. gravity) $\rho \mathbf{g}$ as:

$$\frac{\partial \varepsilon}{\partial t} + \nabla \cdot (\langle \varepsilon \mathbf{u}_f \rangle) = \mathbf{0}\,, \tag{2.63}$$

for the averaged fluid mass conservation and

$$\varepsilon \rho_f \left[\frac{\partial}{\partial t} (\langle \mathbf{u}_f \rangle) + (\langle \mathbf{u}_f \rangle \cdot \nabla) \langle \mathbf{u}_f \rangle \right] = \nabla \cdot \langle \sigma_f \rangle - \mathbf{F}_{fp} + \varepsilon \rho_f \mathbf{g}\,, \tag{2.64}$$

for the averaged fluid momentum conservation. Similar averaged equations are found for the solid phase. The averaged mass conservation equation for the solid phase is

$$\frac{\partial \phi}{\partial t} + \nabla \cdot (\langle \phi \mathbf{u}_s \rangle) = \mathbf{0}\,, \tag{2.65}$$

and the averaged momentum conservation equation for the solid phase reads

$$\phi \rho_s \left[\frac{\partial}{\partial t} (\langle \mathbf{u}_s \rangle) + (\langle \mathbf{u}_s \rangle \cdot \nabla) \langle \mathbf{u}_s \rangle \right] = -\nabla \cdot \langle \sigma_s \rangle + \mathbf{F}_{fp} + \mathbf{F}_{ss} + \phi \rho_s \mathbf{g}\,. \tag{2.66}$$

Each phase has its own velocity, $\mathbf{u}_f$ and $\mathbf{u}_s$, which is weighted by porosity ε and solid fraction $\phi = \varepsilon - 1$ for the fluid and solid phase, respectively. The momentum equations contain furthermore separate stress tensors for fluid and solid phase, σ_f and σ_s, which require adequate modelling which is discussed in subsequent sections. Moreover, interaction between the fluid and solid phase is considered by the interaction force term $\mathbf{F}_{fp}$ and similarly interactions between different solid phases can be considered by a solid-solid interaction term $\mathbf{F}_{ss}$.

Very similar to the above TFM, the suspension balance model (SBM) describes the suspension behaviour on macroscale by mass and momentum conservation equations for fluid, particle, and suspension mixture. The main difference is consideration of particle migration due to stress gradients in the SBM. Two of the three phase equations (fluid,particle, suspension mixture) are necessary to evaluate and according to Nott et al.

(2011), the suspension momentum and particle momentum balance equations with particle volume V_p and particle number per volume element n can be written as

$$\frac{\partial}{\partial t}\langle\rho\mathbf{u}\rangle + \boldsymbol{\nabla}\cdot\langle\rho\mathbf{u}\mathbf{u}\rangle = \boldsymbol{\nabla}\cdot[\varepsilon\langle\boldsymbol{\sigma}_f\rangle + \phi\langle\boldsymbol{\sigma}_s\rangle] + \langle\mathbf{F}\rangle \tag{2.67}$$

and

$$\rho_p V_p\left[\frac{\partial}{\partial t}(n\langle\mathbf{u}_p\rangle) + \boldsymbol{\nabla}\cdot(n\langle\mathbf{u}_p\mathbf{u}_p\rangle)\right] = nV_p\langle\mathbf{F}_{ext,p}\rangle + n\langle\mathbf{F}_p\rangle\,, \tag{2.68}$$

respectively. $\mathbf{F}_{ext,p}$ is an external force term, such as gravity, and $\mathbf{F}_p$ is the particle phase force, which can include terms such as the drag force or force terms due to hydrodynamic stress. The force term $\mathbf{F}$ in Eq. (2.67) is a net body force and for example, consists a gravity and interphase force. The corresponding mass conservation equations read for the suspension

$$\boldsymbol{\nabla}\cdot\langle\mathbf{u}\rangle = 0 \tag{2.69}$$

and for the particle phase

$$\frac{\partial\phi}{\partial t} + \boldsymbol{\nabla}\cdot\langle\phi\mathbf{u}_p\rangle = 0\,. \tag{2.70}$$

2.3.1.2. Closure laws

The obtained averaged set of equations require closures. Enwald et al. (1996) elucidate that three types of closure are necessary, viz. topological, constitutive and transfer closures. Topological closures are needed for description of spatial distribution of flow variables. Physical properties for each phase are covered in corresponding constitutive closures and interactions between the phases, such as drag, lift, or buoyancy forces, are summarised in transfer closures.

2.3.2 Transfer closures

The fluid-particle interaction force $\mathbf{F_{fp}}$ is, in contrast to microscale simulations, volume averaged over single fluid-particle forces $\mathbf{F_{fp}} = \frac{1}{V}\sum\mathbf{f}_{f_i}$ (cf. Hoef et al. (2008), Xiao and Sun (2011)) and consists of several different parts: Buoyancy force, drag force, Basset force, lift force, Saffmann force, and Magnus force. Considering only buoyancy and drag force $\mathbf{F}_{ip,d}$, the fluid-particle interaction force is

$$\mathbf{F}_{ip} = -\phi\nabla p + \mathbf{F}_{ip,d}\,, \tag{2.71}$$

where $\mathbf{F}_{ip,d} = \beta(\mathbf{u}_f - \mathbf{u}_s)$ is the drag force connecting the relative velocity between fluid and solid phase through an interphase momentum transfer coefficient, or sometimes also called friction coefficient, β.

The simplest drag correlation is the Stokes drag force, which is valid for a single sphere in a low Reynolds number flow, and it follows for the inter-phase momentum exchange coefficient:

$$\beta = 6\pi\eta_f r_p \,. \tag{2.72}$$

2.3.2.1. Monodisperse drag models

A common drag force modelling approach is based on the results of Ergun (1952). Ergun determined the pressure drop of a flow through a static assembly of spheres and thereby obtained an expression for the drag force valid for dense particle systems. For monodisperse dilute systems, Wen and Yu (1966) proposed a drag model. Commonly, both drag models by Ergun (1952) and Wen and Yu (1966) are combined to capture the vast range of solid fractions in monodisperse systems, i.e.:

$$\beta = \begin{cases} 150\frac{\phi^2}{\varepsilon}\frac{\eta_f}{d_p^2} + 1.75\phi\frac{\rho_f}{d_p}|u_f - u_s| & , \quad \phi \geq 0.2 \\ \frac{3}{4}C_d\frac{\varepsilon\phi}{d_p}\rho_f|u_f - u_s|\varepsilon^{-2.65} & , \quad \phi < 0.2 \end{cases} \,. \tag{2.73a}$$

$$C_D(Re) = \begin{cases} \frac{24}{Re}(1 + 0.15Re^{0.687}) & , \quad Re < 1000 \\ 0.44 & , \quad Re \geq 1000 \end{cases} \,. \tag{2.73b}$$

$$Re = \frac{\varepsilon\rho_f|u_f - u_s|d_p}{\eta_f} \tag{2.73c}$$

However, the transition in force between the dense and dilute system is not smooth which is shown by Beetstra et al. (2007c).

Similar studies of flow through static assemblies of particles to obtain drag force correlations, however on numerical basis, were conducted, e.g. by Hill et al. (2001), Benyahia et al. (2006), Hoef et al. (2005) and Beetstra et al. (2007a). Hill et al. (2001) derived a drag model for solid fractions ranging close to the maximum packing fraction of static monodisperse particle assemblies and for Reynolds number to the order of $Re \approx \mathcal{O}(100)$. The model was extended for void fractions and Reynolds numbers, which are typically found in fluidised beds, by Benyahia et al. (2006). Hoef et al. (2005) and Beetstra et al. (2007a) extended drag correlations to larger Reynolds numbers and considered moreover bidisperse particles (cf. next section).

Drag models can be also deduced by studying the sedimentation of particles. Thereby, Syamlal et al. (1993) derived a popular drag model.

Di Felice (1994) found a way to express the drag force on multiple particles by multiplying the drag force of a single particle with a voidage function to consider influences of neighbouring particles.

The aforementioned models are appropriate for only specific applications. Consideration of further influential parameters (e.g. polydisperse particles, non-spherical particles, segregation processes, aggregation and breakage processes, heat transfer) requires modifications and extensions of existing models as well as calibration of corresponding modelling parameters or development of a complete new model.

2.3.2.2. Polydisperse drag models

LBDEM simulations of flow through static mono- and bidisperse particle assemblies for solid fractions ranging to close-packing of the assemblies, i.e. $\phi_{max} \geq 0.6$, were conducted by Hoef et al. (2005) for low-Reynolds number flows, $Re << 1$, and by Beetstra et al. (2007a) who extended the investigated Reynolds number regime to the order of $Re \approx \mathcal{O}(1000)$. Large deviations between monodisperse drag force expressions and actual drag forces in bidisperse systems are found. The obtained LBDEM data resulted in the construction of an improved drag model for bidisperse system. The newly derived (and corrected; cf. Beetstra et al. (2007b)) drag model is based on a monodisperse drag model extended by a correction factor to incorporate the bidispersity and can be written in the simplest case in dimensionless form as follows:

$$F_{ip,d} = (\varepsilon y_i + (1-\varepsilon) y_i^2) F_{ip,d,mono}(\varepsilon, \langle Re \rangle)\,, \tag{2.74}$$

where $F_{ip,d,mono}(\varepsilon, \langle Re \rangle)$ is the corresponding monodisperse drag force for the same porosity as in the polydisperse case. The model parameters are defined as $y_i = \frac{d_i}{\langle d \rangle}$, $\langle Re \rangle = \frac{\rho_F U \langle d \rangle}{\eta_f}$ and $\frac{1}{\langle d \rangle} = \sum_i \frac{\kappa_i}{d_i}$. Furthermore it is demonstrated that bidisperse drag force modelling is crucial because of high deviations between bidisperse simulation results and the monodisperse drag force models. For higher packing fractions $\phi > 0.5$, Beetstra et al. (2007a) conclude that the particle assembly indicates some ordering. Therefore, the drag force is dependent on the flow direction for large Reynolds numbers and thus, data was averaged over simulations with different directions.

Sarkar et al. (2009) investigated by LBDEM simulations fluid flow through fixed polydisperse particle assemblies. Two types of random particle assemblies were investigated: Gaussian and log-normal size distribution. It is found that the influence of the different size distributions on the drag force can be neglected.

2.3.2.3. Particle-particle drag

Particles in a suspension affect each other in its motion by transmitting forces through the fluid due to sheer presence or relative velocities. Therefore, Yin and Sundaresan (2009a) studied equally sized particle assemblies with two different imposed velocity values on two types of particles in a low Reynolds number and high Stokes number regime. On this basis, Yin and Sundaresan (2009a) introduced, similar to the grand-resistance matrix notation for particle-particle lubrication forces, a particle-particle drag law for particles with relative velocities to each other:

$$\mathbf{F}_{ip,d} = \begin{cases} \mathbf{F}_{ip,d1} = -B_{11}\Delta\mathbf{U}_1 - B_{12}\Delta\mathbf{U}_2 \\ \mathbf{F}_{ip,d2} = -B_{21}\Delta\mathbf{U}_1 - B_{22}\Delta\mathbf{U}_2 \end{cases}, \tag{2.75}$$

where the particle-specific friction coefficients B_{ij} are determined from simulations. Lubrication forces between particles affect the hydrodynamic particle-particle drag and Yin and Sundaresan (2009a) elucidate that the particle-particle drag influence on fluid-particle drag can be important. Therefore, Yin and Sundaresan (2009a) compared their drag law to the combined drag correlation given in equations (2.73) and found that particle-particle drag is important to be considered and it could have a large influence on simulations of segregation phenomena. Extension of the particle-particle drag law towards particles of different sizes was undertaken by Yin and Sundaresan (2009b) and modification to include inertial effects due to higher Reynolds numbers were considered by Holloway et al. (2010).

2.3.3 Constitutive closures

Evaluation of the above described TFM and SBM require also closure expressions for the unknown stress terms for the fluid phase σ_f and solid phase σ_s, i.e. constitutive closures. Closures for the stress terms are of paramount importance because the whole physical behaviour of one phase is mirrored in the stress closures.

2.3.3.1. Suspension stress - theory

An approach for suspensions to relate the microscale to macroscale was proposed by Batchelor (1970) who derived a general formulation for the computation of bulk stress in a suspension. According to Batchelor (1970), the bulk stress can be computed as:

$$\Sigma_{ij} = \frac{1}{V}\int(\sigma_{ij} - \rho u_i^{'} u_j^{'})dV \tag{2.76}$$

where V is the averaging volume. For an incompressible Newtonian fluid, equation (2.76) can be written as:

$$\Sigma_{ij} = \frac{1}{V}\int_{V-\sum V_p}\left[-p_f\delta_{ij} + \eta_f\left(\frac{\partial u_i}{\partial x_j} + \frac{\partial u_j}{\partial xi}\right)\right]dV + \frac{1}{V}\sum\int_{V_p}\sigma_{ij}dV - \frac{1}{V}\int\rho u_i^{'}u_j^{'}dV\ , \tag{2.77}$$

where V_p is the particle volume. The first integral on the right-hand side represents the Newtonian fluid stress which is split into a pressure p_f and viscous stress contribution. The two last terms are commonly described as the "particle stress" $\sum_{ij}^{p}$:

$$\Sigma_{ij}^{p} = \frac{1}{V}\sum\int_{V_p}\sigma_{ij}dV - \frac{1}{V}\int\rho u_i^{'}u_j^{'}dV \tag{2.78}$$

where the first term is the stress inside the particle volumes and the second term is a stress contribution stemming from the particle velocity fluctuations $u^{'}$. Application of the divergence theorem leads to:

$$\frac{1}{V}\sum\int_{V_p}\sigma_{ij}dV = \frac{1}{V}\sum\int_{A_p}x_j\sigma_{ik}n_k dA - \frac{1}{V_p}\int\frac{\partial\sigma_{ij}}{\partial x_j}x_j dV \tag{2.79}$$

and with the particle acceleration $\mathbf{a}(\mathbf{r}) = \mathbf{a} + \boldsymbol{\alpha}\times\mathbf{r} + \boldsymbol{\omega}\times(\boldsymbol{\omega}\times\mathbf{r})$ at position $\mathbf{r}$ ($\mathbf{r}$ pointing from centre of mass to the point $\mathbf{r}$) inside of a particle for $\frac{\partial\sigma_{ij}}{\partial x_j} = \rho a_i$ where the constant fluid density is ρ is uniform in space, the particle stress reads:

$$\Sigma_{ij}^{p} = \frac{1}{V}\sum\int_{A_p}x_j\sigma_{ik}n_k dA - \frac{1}{V}\sum\int_{V_p}\rho x_j a_i dV - \frac{1}{V}\int\rho u_i^{'}u_j^{'}dV\ . \tag{2.80}$$

The first term on the right-hand side is the stresslet, the second term the acceleration stress and the last term is the Reynolds stress. The stresslet can be computed as

$$\sigma_{ij}^{stresslet} = \frac{1}{V}\sum\int_{A_p}x_j\sigma_{ik}n_k dA = \frac{1}{V}\sum\int_{A_p}\frac{1}{2}(\sigma_{ik}x_j + \sigma_{jk}x_i)n_k dA\ , \tag{2.81}$$

the acceleration stress as

$$\sigma_{ij}^{acceleration} = \frac{1}{V}\sum\int_{V_p}\rho x_j a_i dV = \frac{1}{V}\sum\int_{V_p}\left(\frac{1}{2}(a_i x_j + a_j x_i)\right)dV\ , \tag{2.82}$$

and the Reynolds stress as

$$\sigma_{ij}^{Reynolds} = \frac{1}{V}\int\rho u_i^{'}u_j^{'}dV = \frac{1}{V}\sum_i m_i u_i^{'}u_j^{'}\ . \tag{2.83}$$

Similar to Batchelor (1970), Nott et al. (2011) decomposed the bulk stress into a fluid and particle contribution in the suspension momentum equation (2.67). The fluid stress for an incompressible Newtonian fluid with rigid particles is

$$\varepsilon\langle\boldsymbol{\sigma}_\mathbf{f}\rangle = \int_{V_f}(-p\mathbf{I}+2\eta_f\mathbf{e})dV = -\varepsilon\langle p_f\rangle\mathbf{I}+2\eta_f\langle\mathbf{e}\rangle\ . \tag{2.84}$$

The stress for the solid phase is according to Nott et al. (2011):

$$\phi\langle\boldsymbol{\sigma}_\mathbf{s}\rangle = \sum_i g_i\int_{V_{p,i}}\boldsymbol{\sigma}dV - \boldsymbol{\nabla}\cdot\sum_i g_i\int_{V_{p,i}}\mathbf{y}'\boldsymbol{\sigma}dV+\dots\ , \tag{2.85}$$

where g_i is a weighting function at the centre of particle i with the property $\int gdV=1$ and $\mathbf{y}'=\mathbf{y}-\mathbf{y}_i$ with $\mathbf{y}$ being an unaveraged coordinate over space. Further simplifications, discussed by Nott et al. (2011), lead ultimately to:

$$\begin{aligned}\phi\langle\boldsymbol{\sigma}\rangle^s = \sum_i g_i\left(\overline{\mathbf{S}}_i-\frac{1}{2}\boldsymbol{\epsilon}\cdot\mathbf{T}_i+\int_{V_{p,i}}\mathbf{y}'\mathbf{F}'dV\right)\\ -\frac{1}{2}\boldsymbol{\nabla}\cdot\sum_i g_i\left(\mathbf{Q}_i-\frac{1}{5}V_p d_p^2\mathbf{I}\mathbf{f}_i+\int_{V_{p,i}}\mathbf{y}'\mathbf{y}'\mathbf{F}'dV\right)+\dots\ ,\end{aligned} \tag{2.86}$$

where $\mathbf{f}_i=\int_{S,i}\mathbf{n}\cdot\boldsymbol{\sigma}dS$ is the zeroth moment of surface traction, $\overline{\mathbf{S}}_i=\frac{1}{2}(\mathbf{S}_i+\mathbf{S}_i^T)$ is the first moment of the surface traction where $\mathbf{S}_i=\int_{S,i}\mathbf{y}'\mathbf{n}\cdot\sigma dS$, $\mathbf{Q}_i=\int_{S,i}\mathbf{y}'\mathbf{y}'\mathbf{n}\cdot\boldsymbol{\sigma}dS$ is the second moment of surface traction, $\mathbf{F}'$ is the deviation of the mean of $\mathbf{F}$, and $\mathbf{T}_i$ is the external torque on particle i with ε being the Levi-Cita symbol. Although the result is very similar to Batchelor (1970), especially when $g_i=\frac{1}{V}$ is chosen, a main difference in terms of an additional gradient, including a second moment of the surface traction, is obtained. The found additional terms are only observable for suspensions with a non-uniform stress state in the stress tensor elements as the gradients otherwise disappear.

2.3.3.2. Bulk stress and viscosity computation in simulations

The bulk stress contributions can be computed based on the theoretical work discussed in the previous section.

2.3.3.2.1. Stress for interparticle forces from DEM For incompressible rigid particles, the mean stress within a solid is not affected by the elastic properties and the stress can be straightforward computed from the interaction force on the corresponding interaction surface point. In case of interparticle forces, the stresslet computation can be performed according to Thompson et al. (2009), which is in accordance with Nott et al. (2011), for the contact force

$$\sigma^C = \frac{1}{V}\sum_i\sum_j r_{ij}\mathbf{F}_{ij}^C \tag{2.87}$$

and pair-wise lubrication forces

$$\sigma^L = \frac{1}{V} \sum_i \sum_j r_{ij} \mathbf{F}_{ij}^L \ . \tag{2.88}$$

2.3.3.2.2. Stress for fluid-solid interaction from LBM In case of non-interparticle forces, such as drag forces, computed in LBM simulations, the bulk stress can be computed by different approaches. Haddadi and Morris (2014) re-write the stresslet (2.81) to:

$$\frac{1}{V} \sum \int_{A_p} \frac{1}{2} (\sigma_{ik} x_j + \sigma_{jk} x_i) n_k dA = \frac{1}{V} \sum^{N_{particles}} \sum^{N_{nodes}} (\frac{1}{2} (f_{ik}^{LBM} x_j + f_{jk}^{LBM} x_i)) \ , \tag{2.89}$$

where the hydrodynamic force f^{LBM} on each particle covered lattice node is summed for the corresponding particle to obtain the particle stress value.

Krüger et al. (2011) compute for a LBM-IBM the particle stress contribution by relating the hydrodynamic lattice node force F_{jx}, where x is the shearing direction, to a plane which slices the simulation domain at position z, where z is the direction of the shearing gradient, i.e.:

$$\Sigma_{xz}^p(z,t) = \frac{1}{2A} \sum_j F_{jx}(t) sgn(z - Z_j) \ . \tag{2.90}$$

A is the surface of the intersecting plane at location z and Z_j is the lattice node coordinate in z direction at which the force F_{jx} is evaluated.

A more cumbersome stress computation is used by Shakib-Manesh et al. (2002) and Hyväluoma et al. (2005) who use the fluid-solid coupling proposed by Ladd (1994a) and Ladd (1994b). The hydrodynamic shear stress contribution τ_{fp} is computed from the spatial, time, and ensemble averaged fluid-particle force in shearing direction F_{fp}. Therefore, F_{fp} is related to an intersecting surface A_p between particle volume and a plane S_p slicing the simulation domain with its normal component parallel to the shearing gradient:

$$\tau_{fp} = \langle \frac{F_{fp}}{A_p} \rangle \ . \tag{2.91}$$

The fluid-particle force $\mathbf{F}_{fp}$ is determined for the particle volume above or below the intersecting plane S_p and reads exemplary for the lower intersected particle volume $\mathbf{F}_{fp} = -\mathbf{F}_{i,d} - \mathbf{F}_{o,d} + m_d \mathbf{a} + m_d \boldsymbol{\alpha} \times \mathbf{r}_d + m_d \omega^2 r_d \mathbf{e}_y$. The first two terms are hydrodynamic forces acting on the particle from inside the particle and outside the particle. The last terms are related to the particle acceleration $\mathbf{a}$ and particle rotations with angular velocity ω. $\mathbf{r}_d$ is the vector from particle centre to the centre-of mass of the particle volume below the intersecting plane S_p with the corresponding mass m_d.

2.3.3.2.3. Viscosity computation The viscosity of a suspension can be determined by summing the different stress computations, discussed in the previous sections, and relating the total bulk stress to the shear rate $\dot{\gamma}$, i.e.

$$\eta = \eta_f + \frac{\Sigma^p_{xy}}{\dot{\gamma}} \ , \tag{2.92}$$

where $\sum^p_{xy} = \sigma^C + \sigma^L + \sigma^{stresslet} + \sigma^{acceleration} + \sigma^{Reynolds}$ with contributions from the above equations.

Alternatively, the viscosity can be also determined from the dissipation in the sheared system. In molecular dynamic simulations, Andreotti et al. (2012) determine the viscosity by evaluation of

$$\eta = \frac{\Gamma}{\dot{\gamma}^{1+\nu_{bf}}} \ , \tag{2.93}$$

where Γ is the dissipation which is computed from viscous forces and particle velocity fluctuations as

$$\Gamma = \frac{1}{V}\left[\sum_i \mathbf{F}^{visc}_i \cdot [\mathbf{u}_{p,i} - \mathbf{u}_{flow}(\mathbf{x}_{p,i})]\right] \ . \tag{2.94}$$

Without providing here the details of the viscous force expression used by Andreotti et al. (2012), it shall be only remarked that the parameter ν_{bf} is part of the viscous force $\mathbf{F}^{visc}$ and describes the background fluid as Newtonian $\nu_{bf} = 1$ or non-Newtonian $\nu_{bf} \neq 1$.

According to Lishchuk et al. (2006) the dissipation in LBM simulations is

$$\Gamma = \frac{\eta_f}{2}\sum_V \left[\left(\frac{\partial u_\alpha}{\partial x_\beta} + \frac{\partial u_\beta}{\partial x_\alpha}\right)^2\right]_{V,t} \ , \tag{2.95}$$

where lattice nodes within particle volume are excluded in the volume V and velocity gradients can be evaluated by $\frac{\partial u_\alpha}{\partial x_\beta} = \frac{1}{c_s^2}\sum_i w_i u_\alpha(\mathbf{r} + \mathbf{c}_i)c_{i\beta} + \mathcal{O}(\mathbf{c}_i^3)$. The suspension viscosity η is then found by the relationship $\eta = \frac{\Gamma_{tot}}{\dot{\gamma}/2}$ where Γ_{tot} is the total dissipation in the system and $\dot{\gamma}$ is the imposed shear rate on the system.

2.3.3.3. Dimensional analysis of suspension systems

In the previous sections, it has been shown which microscale occurrences contribute to the overall suspension bulk stress and how these contributions can be calculated in simulations. However, development of constitutive models to find closures for the stress term can be simplified when the focus is set on specific flow regimes or parameter sets. Therefore, a simple sheared suspension system with its characteristic parameters is here discussed first to show basic rheology determining parameters in form of dimensionless

	ρ_f	ρ_p	$\dot{\gamma}$	η_f	d_i	c_i	σ	V_p	μ_r	f_h	k_n
M	1	1	0	1	0	0	1	0	-	0	1
L	-3	-3	0	-1	1	1	-1	3	-	1	0
T	0	0	-1	-1	0	0	-2	0	-	-2	-2

Tab. 2.1.: Buckingham matrix for a suspension

numbers. A comparison to dimensionless numbers in the literature is finally undertaken before the focus is shifted to constitutive modelling in the next section 2.3.3.4.

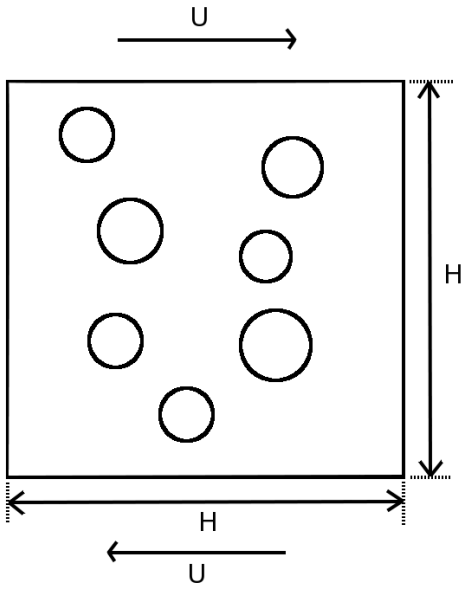

Fig. 2.4.: Sheared suspensions system

2.3.3.3.1. Buckingham analysis On the most fundamental level, a suspension can be studied under simple shear as depicted in figure 2.4. The suspension consists here of an incompressible Newtonian fluid of density ρ_f and dynamic viscosity η_f with rigid particles of density ρ_p, diameters d_i, and elastic stiffness k_n. Lubrication interactions between particles can occur for gap distances which are comparable in size of particle surface roughnesses and therefore, an inner cut-off distance c_i can be defined. Friction between particles is considered by a coefficient of friction μ_r and interaction between fluid and particles by a hydrodynamic volume force f_h, as in the above TFM. The whole suspension of fluid and N particles is sheared with a shear rate of $\dot{\gamma} = \frac{2U}{H}$ leading to a suspension stress σ. All parameters are summarised in a Buckingham matrix presented in table 2.1 which has the rank $r = 3$ with at least $n = 10$ parameters, i.e. leading to at least 7 dimensionless numbers. Simplifications can be undertaken by assuming a bidisperse system with a fixed particle diameter ratio so that $d = \frac{d_i d_j}{d_i + d_j}$ can be used to substitute the

various particle diameters d_i in table 2.1. Dimensionless numbers with $\dot{\gamma}$, d and η_f as the basis read then:

$$\pi_1 = \frac{\rho_f}{\frac{\eta_f}{\dot{\gamma} d^2}} = Re\,, \tag{2.96a}$$

$$\pi_2 = \frac{\rho_p}{\frac{\eta_f}{\dot{\gamma} d^2}} = St\,, \tag{2.96b}$$

$$\pi_3 = \frac{c_i}{d}\,, \tag{2.96c}$$

$$\pi_4 = \frac{V_p}{(\frac{H}{d} d)^3} = \phi\,, \tag{2.96d}$$

$$\pi_5 = \mu_r\,, \tag{2.96e}$$

$$\pi_6 = \frac{f_h d}{d^2 \dot{\gamma}^2} = \frac{f_h d}{U_0^2} = \frac{1}{Fr^2}\,, \tag{2.96f}$$

$$\pi_7 = \frac{k_n}{\eta_f \dot{\gamma} d} = k_n^*\,. \tag{2.96g}$$

$$\pi_8 = \frac{\sigma}{\eta_f \dot{\gamma}}\,. \tag{2.96h}$$

The characteristic velocity is here defined to be $U_0 = d\dot{\gamma}$ to make the connection between hydrodynamic force and commonly known Fr number, which represents the ratio between fluid inertial forces and body forces, apparent. Constitutive models for suspensions are constructed to find adequate closure expression for the stresses σ, i.e. of interest is the determination of a functional $\pi_8 = f(\pi_1, \pi_2, \pi_3, \pi_4, \pi_5, \pi_6, \pi_7)$ or

$$\frac{\sigma}{\eta_f \dot{\gamma}} = f(Re, St, \frac{c_i}{d}, \phi, \mu_r, Fr, k_n^*)\,. \tag{2.97}$$

The Stokes number and Reynolds number, which gives the ratio between fluid inertial forces and viscous forces, can be linked to each other by

$$St = \frac{\rho_p d^2 \dot{\gamma}}{\eta_f} \frac{\rho_f}{\rho_f} = \frac{\rho_p}{\rho_f} Re\,. \tag{2.98}$$

Under the assumption of $\rho_f = \rho_p = \rho$, i.e. for neutrally buoyant suspended particles, the Stokes number and Reynolds number are identical.

2.3.3.3.2. Comparison to literature Ancey et al. (1999) discuss a few dimensionless numbers to characterise fluid-solid flows and classify suspension regimes. The Stokes number St is a common characterisation giving the ratio of a particle inertia response time to a fluid convective time. Therefore, the Stokes number characterises the coupling between particle motion and fluid, i.e. $St << 1$ results in the fluid predominating and

hence the particle following the fluid flow, whereas on the contrary, independent particle motion from the fluid occurs for $St >> 1$. The Stokes number is expressed by Ancey et al. (1999) as:

$$St = \frac{\rho_p r_p^2 \dot{\gamma}}{\eta_f} , \tag{2.99}$$

which is virtually identical to the Stokes number $St = \frac{\rho_p}{\frac{\eta_f}{\dot{\gamma} d^2}}$ found by the Buckingham analysis in the previous section 2.3.3.3.1 except for the scaling with the particle radius r_p. Similarly to the Buckingham analysis above, Haddadi and Morris (2014) use a a virtually identical Reynolds number formulation (radius instead of diameter) and link in the very same way as in Eq. (2.98) the Stokes number with the Reynolds number.

According to Ancey et al. (1999), main suspension regimes can be classified with three dimensionless number which are obtained from setting different force contributions ratios, viz. the Bagnold number Ba, the Coulomb number Co and the Leighton number Le. The Bagnold number,

$$Ba = \frac{1}{ln(c_o/c_i)} \frac{\rho_p r_p^2 \dot{\gamma}}{\eta_f} , \tag{2.100}$$

describes the ratio of particle inertia to the work of normal lubrication forces.

The second dimensionless number, the Coulomb number,

$$Co = \frac{\rho_p r_p^2 \dot{\gamma}^2}{\Sigma^p} , \tag{2.101}$$

represents the ratio of collisional to frictional contacts where Σ^p is the particle stress.

The Leighton number,

$$Le = \frac{\eta_f r_p \dot{\gamma}}{c_i \Sigma^p} , \tag{2.102}$$

describes the ratio of frictional and lubrication forces. Ancey et al. (1999) show that the Leighton number is not independent of the Coulomb and Bagnold number, i.e. $Le \approx \frac{Cor_p}{c_i Ba}$. Based on the Bagnold, Coulomb, and Leighton number, Ancey et al. (1999) differentiate the suspension rheology into three regimes: Frictional regime ($Co << 1$ and $Le << 1$), collisional regime ($Co >> 1$ and $Ba >> 1$), and hydrodynamic regime ($Ba << 1$ and $Le >> 1$).

If additionally the thermal energy $k_B T$ is considered, where k_B is the Boltzmann constant and T is the temperature, another dimensionless number, the Peclet number, is found, e.g. Stickel and Powell (2005):

$$Pe = \frac{6\pi\eta_f r_p^3 \dot{\gamma}}{k_B T} . \tag{2.103}$$

The Peclet number is useful to classify between Brownian and non-Brownian regimes ($Pe \to \infty$). Moreover, Stickel and Powell (2005) show that depending on the Reynolds and Peclet number combination the rheological behaviour can be classified into Newtonian, shear-thinning, and shear-thickening regimes.

An additional important dimensionless number for dry granular media, which sets particle inertia in relation to confining stress, is given by Midi (2004):

$$I = \frac{\dot{\gamma} d}{\sqrt{p/\rho_p}}\,, \tag{2.104}$$

where p is the confining pressure of the system. The inertial number I, giving the ratio of inertial time of particle rearrangement on microscale to time of strain (macroscale), is however not valid for low Stokes numbers and systems should be described by a viscous number according to Cassar et al. (2005) or Boyer et al. (2011):

$$I_v = \frac{\eta_f \dot{\gamma}}{p}\,. \tag{2.105}$$

2.3.3.3.3. Conclusion of dimensional analysis The dimensionless numbers Le, Ba, Co are not independent to each other as shown by Ancey et al. (1999). Furthermore, Stokes number St and Bagnold number Ba are extremely similar. Moreover, Leighton number Le and viscous number I_v differ effectively only in the considered stress - particle stress or pressure. However, the dimensionless suspension stress is expressed as Buckingham functional. Hence in summary, taking all the previously elucidated dimensionless numbers and relations into account, the suspension stress might be generally expressed as the following functional:

$$\frac{\sigma}{\mu\dot{\gamma}} = f(Re, St, \frac{c_i}{d}, \phi, \mu_r, Fr, k_n^*, Pe, I_v)\,. \tag{2.106}$$

However, the dimensionless parameter list (2.106) is not extensive as many more parameters can, and should be, considered - particle size distributions, particle shape, particle deformability, cohesive forces, and turbulence to name but a few.

2.3.3.4. Constitutive equations

In section 2.3.3.1, the bulk stress is decomposed into a fluid and solid contribution. It is explained that the fluid bulk stress can be further decomposed into a pressure p_f and viscous stress $\boldsymbol{\tau}_f$ contribution:

$$\boldsymbol{\sigma}_f = -p_f \mathbf{I} + \boldsymbol{\tau}_f\,. \tag{2.107}$$

where $\mathbf{I}$ is the identity tensor. For an incompressible Newtonian fluid the shear stress can be expressed as

$$\tau^f_{\alpha\beta} = \eta_f \left(\frac{\partial u^f_\alpha}{\partial x^f_\beta} + \frac{\partial u^f_\beta}{\partial x^f_\alpha} \right) . \tag{2.108}$$

On this basis, the stress tensor for the solid phase could be analogously decomposed into an inter-particle pressure p_s and a solid shear stress component $\boldsymbol{\tau}_s$

$$\boldsymbol{\sigma}_s = -p_s \mathbf{I} + \boldsymbol{\tau}_s \, , \tag{2.109}$$

where the solid shear stress could be modelled similar to a Newtonian fluid, i.e.

$$\tau^s_{\alpha\beta} = \eta_s \left(\frac{\partial u^s_\alpha}{\partial u^s_\beta} + \frac{\partial u^s_\beta}{\partial x^s_\alpha} \right) . \tag{2.110}$$

However, in contrast to a Newtonian fluid, the solid phase pressure p_s is not isotropic and the viscosity η_s can be a complex function depending on the dimensionless parameters discussed in the previous section.

The suspension viscosity increases with increasing solid fraction. Einstein (1905) derived for very dilute suspension the relative viscosity $\eta_r = \frac{\eta_{suspension}}{\eta_f}$ relation

$$\eta_r = 1 + \phi \tag{2.111}$$

and Einstein (1911) published later an erratum to correct his derivation to

$$\eta_r = 1 + 2.5\phi \, . \tag{2.112}$$

Batchelor and Green (1972a) extended the solution to a higher order, i.e.

$$\eta_r = 1 + 2.5\phi + 7.6\phi^2 \, . \tag{2.113}$$

However, for a further increase of the solid fraction the analytical solutions differ tremendously from experimental findings. Eilers (1941) compared different formulas to determine the viscosity for any given solid fractions and concluded with the suggestion

$$\eta_r = \left(1 + \frac{2.5\phi}{2\left(1 - \frac{\phi}{0.74}\right)} \right)^2 , \tag{2.114}$$

where the expression in the numerator stems from the above Einstein correlation for dilute suspensions and the factor 0.74 in the denominator corresponded to a specific

maximum packing fraction in the system. Therefore, the correlation by Eilers (1941) is often generally expressed as

$$\eta_r = \left(1 + \frac{[\eta]\phi}{2\left(1 - \frac{\phi}{\phi_{max}}\right)}\right)^2 , \tag{2.115}$$

where $[\eta]$ is called an intrinsic viscosity, e.g. by Krieger and Dougherty (1959), and serves with the maximum packing fraction ϕ_{max} as fitting parameters. An alternative popular correlation between solid fraction and viscosity was semi-empirically determined by Krieger and Dougherty (1959):

$$\eta_r = \left(1 - \frac{\phi}{\phi_{max}}\right)^{-[\eta]\phi_{max}} , \tag{2.116}$$

where ϕ_{max} is a close packing fraction depending particle phase properties and $[\eta]$ is an intrinsic viscosity which depends on the suspension properties and is according to Krieger and Dougherty (1959) around $[\eta] = 2.5$. Although the above correlations are a function of the solid fraction, Jeffrey and Acrivos (1976) state after comparison of different experimental investigations that not only the solid fractions, but also other parameters, such as particle shape or particle size distributions, are important to consider.

As mentioned in the previous section 2.3.3.3.2, Midi (2004) found a dimensionless number, the inertial number I (2.104), to characterise granular flows and construct constitutive models. Therefore, the shear stress τ and solid fraction ϕ depends on the inertial number, i.e.

$$\tau = \mu_{eff}(I)p_s \tag{2.117a}$$

$$\phi = \phi(I) , \tag{2.117b}$$

where p_s is the particle pressure in the system and μ_{eff} is the effective friction coefficient and depends on the inertial number (2.104). Cassar et al. (2005) investigated submarine granular flows and accounting for the particle surrounding fluid, modified the inertial number for use in different flow regimes, such as viscous, inertial, or free fall regime. Boyer et al. (2011) used the modified inertial number for the viscous regime, the viscous number I_v by Cassar et al. (2005), to develop a constitutive modelling approach for suspensions which is similar to the constitutive models suggested by Midi (2004) for "dry" granular materials. The shear stress τ and particle pressure p_s in a suspension are then expressed as

$$\tau = \eta_s(\phi)\eta_f\dot{\gamma} \tag{2.118a}$$

$$p_s = \eta_n(\phi)\eta_f\dot{\gamma} \ . \tag{2.118b}$$

The effective shear and normal viscosities, η_s and η_n, respectively, are found by comparison of equations (2.118) with the viscous number (2.105) for the particle pressure and with equation (2.117) for the shear stress so that it follows:

$$\eta_s(\phi) = \frac{\mu[I_v(\phi)]}{I_v(\phi)} \tag{2.119a}$$

$$\eta_n(\phi) = \frac{1}{I_v(\phi)} \ . \tag{2.119b}$$

Boyer et al. (2011) suggest for modelling of μ_{eff} a combination of a contact contribution, which is similar to findings in "dry" granular materials, and a hydrodynamic part. Instead of giving the lengthy effective friction coefficient model and final viscosity expressions here, the reader is advised to consult the publication by Boyer et al. (2011). Further work, based on the I_v-modelling approach was performed by Ness and Sun (2015) who propose a constitutive model covering various suspension flow regimes by linking to a "dry" granular model proposed by Chialvo et al. (2012).

3 An analysis of two lattice Boltzmann partially saturated cell methods to simulate suspensions of solid particles

3.1 Introduction

Previous chapters elucidate that simulations can be employed to study in detail fluid-particle flows and various methodologies have been developed in the past. Methods for popular (and classic) finite difference (FDM) or finite volume methods (FVM) were developed, e.g. by Glowinski et al. (1999), Peskin (2002), Uhlmann (2005). However, computationally advantageous to FDM/FVM is the lattice Boltzmann method and different fluid-solid LBM coupling approaches, briefly discussed in a previous section 2.2.3.7, were proposed. One of the earliest and most used coupling approaches was developed by Ladd (1994a) and Ladd (1994b) which is based on a simple bounce back boundary condition on the particle surface. Improvements with regard to the momentum exchange were suggested by Aidun and Lu (1995) and Aidun et al. (1998). Nguyen and Ladd (2002) introduced explicit lubrication force corrections. Similar to the aforementioned FDM/FVM coupling approaches, also an immersed boundary method was developed for the LBM by Feng and Michaelides (2005).

An alternative approach, which is investigated with its applicability to suspension simulations in this thesis, was proposed by Noble and Torcyznski (1998) who extended the LBM by an additional collision term for the solid phase. The fluid and solid collision terms are appropriately weighted with a solid fraction weighting function describing the overlaps between lattice nodes and particle. Noble and Torcyznski (1998) proposed two different modelling approaches for the solid phase collision term, viz. a suggestion based on the non-equilibrium bounce back and a second suggestion described as superposition method. In general, the advantage of the partially saturated cell method (PSM) is its simplicity which conserves the locality of LB node computations. Hence, several studies showed in the past its validity for many different cases. Verification and validation with regard to the hydrodynamic force and torque calculations for particles were for example performed by Owen et al. (2011) and Seil (2016). Owen et al. (2011) simulated therefore various cases in $2D$ and $3D$ to assess the PSM. $2D$ simulations comprised flow around a cylinder as

well as a rectangular box for different Reynolds numbers, $0.5 \leq Re \leq 40$, and simulations results were compared to experimental and simulation results in the literature. For the cylinder, the obtained drag coefficient corresponds well to experimental findings for the investigated Reynolds number range except for low Reynolds numbers $Re \leq 1$. In contrast, the drag coefficient for the rectangular box was found to agree well for the whole investigated Reynolds number range. However, some small differences are found for the recirculation length of the fluid flow behind the rectangular box as well as in the transitions to symmetric flow vortices and unsteady wake behind the box compared to FVM and LBM simulation results from the literature. An additional $2D$ verification and validation case was performed by studying Couette flow realised by a rotating cylinder within larger hollow cylinder. Owen et al. (2011) show that the non-equilibrium bounce back method and the superposition method for the PSM can capture the developed velocity profile in the cylindrical Couette flow. The obtained torque has been shown to be more accurate for the non-equilibrium bounce back method, yet the error for the maximum velocity at the rotating cylinder surface is much smaller for the superposition method showing a contrasting accuracy behaviour. Cook et al. (2004b) performed very similar cylindrical Couette validation cases for the PSM, but only for the non-equilibrium bounce back method, which lead to comparable results to Owen et al. (2011). Further validation was undertaken by Owen et al. (2011) in $3D$ by simulating flow through a periodic array of a sphere, flow around a single sphere, and multiple particles settling in a fluid with the non-equilibrium bounce back method. The results for the former two cases agree with findings in the literature, but also show that the PSM is seemingly more accurate towards higher Reynolds numbers. For the latter multi-particle case, typical vortex structures are found which indicates the methodology's capability to simulate fluid-solid flows. Very similar verification and validation cases were carried out by Seil (2016) whose open-source coupling between the Palabos (LBM) and LIGGGHTS (DEM) solvers is used in this thesis with some minor modifications relevant to dense suspensions (e.g. particles overlapping on a same lattice node). Seil (2016) shows as well in $2D$ that the PSM can lead to correct drag coefficients for flows around single fixed spheres or torque calculations in cylindrical Couette flows as described above. In $3D$, Seil (2016) conducted simulations of a fixed sphere in sheared channel showing that drag, lift, and torque values are in agreement with results obtained from FVM simulations carried out with the commercial FLUENT code. Further $3D$ validation was performed by studying the settling behaviour of a single sphere in a closed container for different Reynolds numbers. Simulation results were compared to experimental findings in the literature and a good agreement is found for higher Reynolds numbers. But growing discrepancies are observed for decreasing Reynolds numbers, especially in the wall region before particle-wall collision.

A slight modification to the non-equilibrium bounce back solid phase collision term, cited frequently in the literature, was proposed by Holdych (2003). Holdych (2003) modified the non-equilibrium bounce back solid phase collision term by substitution

of the fluid velocity by the solid phase velocity to analyse momentum truncation error terms for one-dimensional steady flow for a fixed relaxation parameter $\tau = 1.0$ under the assumptions of a uniform solid velocity distribution and no-slip on the fluid-solid interface. However, numerical instability problems and non-convergence problems in two dimensional simulations are reported by Cook et al. (2004a) and by Wang et al. (2016), respectively. Moreover, Leonardi et al. (2016) state that the proposed modification by Holdych (2003) is only applicable for stationary particles. Strack and Cook (2007) contradict those findings by reporting of validation cases which include besides fixed spheres, freely settling particles for varied Reynolds numbers and simulations of the draft-kissing-tumbling case for two particles in $3D$. Yet, instability problems in $3D$-simulations for freely moving particles were found during work on this PhD thesis when employing the method suggested by Holdych (2003). The method proposed by Holdych (2003) was found to be only applicable for fixed particles. Thus, it is henceforth refrained from evaluating, discussing, and using the method by Holdych (2003). However, in appendix A a possible reason for instability issues is briefly described.

In another modification proposed by Zhou et al. (2011), the lattice node solid fraction is replaced by a normalised shortest distance between lattice node and particle surface. Thereby, Zhou et al. (2011) attempted to facilitate the lattice node solid fraction computation and improve the no-slip condition on solid covered nodes. Tests were performed in a two dimensional system with Lees-Edwards boundary conditions for single particles and dilute suspensions with solid fractions ϕ ranging from $0 < \phi < 0.25$. For the single particle simulations, the translational and angular momentum conservation for particles crossing the Lees-Edwards boundary conditions are investigated. For the sheared dilute suspensions, the apparent viscosity are determined and matched to the semi-empirical Krieger-Dougherty correlation. However, the method by Zhou et al. (2011) was implemented and tested during this PhD project. But similar to the method by Holdych (2003) only fixed particle simulations proofed to be successful wheareas instability issues rendered simulations of freely moving particles into a mere attempt. Considering that the method by Zhou et al. (2011) has not been used in another publication to the author's knowledge and moreover that stability problems were experienced during this PhD project, the proposed method by Zhou et al. (2011) is not considered in the remainder of this thesis.

The PSM was proposed by Noble and Torcyznski (1998) without any derivation or further theoretical analysis with regard to implications of introduced modification on the macroscale fluid mass or momentum conservation equations. In addition to a lacking fundamental theoretical understanding of the PSM, none of the aforementioned studies investigates in detail the slip velocity occurring on the particle surface and in the particle volume. Moreover, analysis and validation with regard to the stresslet computation have not been undertaken so far. Although the latter quantity is not necessary to compute particle motions, it is an important quantity for evaluation of

the total stress in a suspension system. Hence in this work, analysis of the fluid slip velocity and hydrodynamic forces over a particle volume with its implications on the stresslet computation are undertaken for the original proposed approaches by Noble and Torcyznski (1998). Furthermore in this chapter, the original proposed methods by Noble and Torcyznski (1998) are analytically analysed by means of a Chapman-Enskog analysis for the first time to the author's knowledge. Any of the modifications to the original method are not considered here because critical stability issues with above mentioned modifications were found.

Firstly the basics of the lattice Boltzmann method and the fluid-solid coupling are investigated here. Furthermore, the fluid-solid coupling is theoretically analysed by means of a Chapman-Enskog analysis. In subsequent sections, simulations of single and two particles between two parallel sheared walls are conducted to investigate the velocity and force profiles over the particle volume to assess the implications on the stresslet and torque computation. In the last part, the importance of the accurate computation of the stresslet is demonstrated by comparison of suspension viscosities obtained from simulations of suspensions with varying solid fractions under simple shear to the known semi-empirical Krieger-Dougherty correlation (Krieger and Dougherty (1959)).

3.2 Methodology

3.2.1 Lattice Boltzmann method

A fluid can be statistically described by summarising locally its fluid molecules into particle distribution functions $f(\mathbf{x}, \mathbf{u}, t)$ which represent the probability of a molecule with velocity $\mathbf{u}$ to be found at position $\mathbf{x}$ at time t. The dynamics of a fluid can then be determined by evaluating a transport equation, the Boltzmann equation, for the particle distribution function. The latttice Boltzmann method (LBM) is the evaluation of the discretised Boltzmann equation on a lattice. On each lattice node, a discrete particle distribution functions $f_i(\mathbf{x}, t)$ is subject to a collision and streaming step. During the collision step, the discrete particle distribution functions $f_i(\mathbf{x}, t)$ are relaxed towards an equilibrium distribution function $f_i^{eq}(\mathbf{x}, \mathbf{u}, t)$ where $\mathbf{u}$ is the macroscopic fluid velocity. In the simplest case, the Bhatnagar-Gross-Krook (BGK) collision (cf. Bhatnagar et al. (1954)), of which is made use of, the collision is described by a single relaxation parameter τ, i.e.

$$\Omega_i^{BGK} = \frac{\Delta t}{\tau}(f_i^{eq}(\mathbf{x}, \mathbf{u}, t) - f_i(\mathbf{x}, t)) \; . \tag{3.1}$$

After the collision step, each distribution is moved according to pre-defined lattice velocities $\mathbf{c}_i$ to adjacent lattice nodes during the streaming step. Streaming and BGK collision step can be summarised to the discrete lattice Boltzmann equation:

$$f_i(\mathbf{x} + \mathbf{c}_i \Delta t, t + \Delta t) = f_i(\mathbf{x}, t) + \Omega_i^{BGK} \,, \tag{3.2}$$

where the lattice velocities $\mathbf{c}_i$ are appropriately chosen to retrieve the equations for mass and momentum (Navier-Stokes equations) conservation and the relaxation parameter τ can be related to the fluid viscosity $\nu = (\tau - 0.5)/3$. Details of deriving the macroscopic conservation equations can be found for example in Succi (2001) or Chen and Doolen (1998). Macroscopic fluid density and velocity can be obtained by computing the zeroth and first moments of the particle distribution functions, i.e. $f_i(\mathbf{x}, t)$, i.e. $\rho = \sum_i f_i(\mathbf{x}, t)$ and $\rho \mathbf{u} = \sum_i f_i(\mathbf{x}, t) \mathbf{c}_i$.

3.2.2 Discrete element method

Each particle is tracked with a discrete element method (DEM) (cf. Cundall and Strack (1979)) by solving effectively Newton's second law for translational and angular motion with a velocity-Verlet algorithm. Determination of the particle motion in suspensions simulated with a LBM can include forces/torques to describe mechanical particle-particle interactions $\mathbf{F}^C/\mathbf{T}^C$ and hydrodynamic forces $\mathbf{F}^H/\mathbf{T}^H$ determined by the LBM. The resulting equations can be written as:

$$m_i \frac{\partial \mathbf{x}_i^2}{\partial^2 t} = \mathbf{F}_i = \mathbf{F}_i^C + \mathbf{F}_i^H \,, \tag{3.3}$$

for translation motion and similarly for the angular motion:

$$\mathbf{J}_i \frac{\partial \omega_i}{\partial t} = \mathbf{T}_i = \mathbf{T}_i^C + \mathbf{T}_i^H \,, \tag{3.4}$$

where mass, position, moment of inertia and angular velocity of particle i are described by m_i, $\mathbf{x}_i$, $\mathbf{J}_i$ and ω_i, respectively.

3.2.3 Fluid-solid coupling

3.2.3.1. Modified LBM equation

Noble and Torcyznski (1998) proposed that the presence of particles can be accounted for by including an additional collision term Ω^s and a weighting function $B(\mathbf{x}, \tau)$ for the solid fraction of the lattice node at $\mathbf{x}$ so that Eq. 3.2 reads:

$$f_i(\mathbf{x} + \mathbf{c}_i \Delta t, t + \Delta t) = f_i(\mathbf{x}, t) + (1 - B(\mathbf{x}, \tau))\Omega_i^{BGK} + B(\mathbf{x}, \tau)\Omega_i^s \,. \tag{3.5}$$

3.2.3.2. Solid phase collision terms and weighting functions

The focus is here on the two different collision terms for the solid phase Ω^s suggested by Noble and Torcyznski (1998). The first suggestion, which is widely used in the literature, reads:

$$\Omega_i^s = f_{-i}(\mathbf{x},t) - f_i(\mathbf{x},t) + f_i^{eq}(\mathbf{x},\mathbf{u}_s,t) - f_{-i}^{eq}(\mathbf{x},\mathbf{u},t) \ , \tag{3.6}$$

where velocity of fluid $\mathbf{u}$ and particle $\mathbf{u}_s$ are individually considered on each lattice node. Distribution functions denoted by f_{-i} stand for the opposite direction of f_i. Noble and Torcyznski (1998) describe Eq. (3.6) as being inspired by the non-equilibrium bounce back boundary condition. Hence, it is abbreviated in this work as BB method.

A second approach, suggested by Noble and Torcyznski (1998), reads:

$$\Omega_i^s = f_i^{eq}(\mathbf{x},\mathbf{u}_s,t) - f_i(\mathbf{x},t) + \left(1 - \frac{\Delta t}{\tau}(f_i(\mathbf{x},t) - f_i^{eq}\right)(\mathbf{x},\mathbf{u},t)) \ . \tag{3.7}$$

Described as superposition method by Noble and Torcyznski (1998), it is henceforth abbreviated as the SP method.

The weighting function can assume different forms. Two options were proposed by Noble and Torcyznski (1998), a linear relationship to the lattice node solid fraction,

$$B(\mathbf{x},\tau) = \varepsilon_s \ , \tag{3.8}$$

and a non-linear form,

$$B(\mathbf{x},\tau) = \frac{\varepsilon_s(\tau/\Delta t - 0.5)}{(1-\varepsilon_s) + (\tau/\Delta t - 0.5)} \ . \tag{3.9}$$

The solid fraction computation is based on a ”brute force“ approach as depicted in figure 3.1. For each lattice node, the lattice node itself acts as the centre of a surrounding cubic volume element of the size of a lattice volume cell. The cubic volume is equally divided into smaller cubes with N_{SGR} number of cubes in each coordinate direction, i.e. N_{SGR}^3 smaller cubes in total for a three dimensional system. The number of cubes within the particle volume related to the total number of cubes provides the lattice node solid fraction. An increase in this subgrid resolution (SGR) leads to a more accurate solid fraction computation, but also to an increased computational overhead.

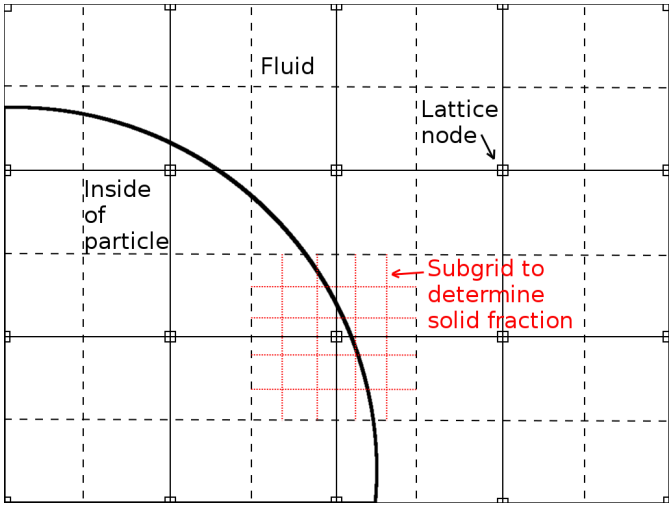

Fig. 3.1.: Solid fraction computation for the partially saturated cell method.

3.2.3.3. Hydrodynamic force and torque

The hydrodynamic force and torque acting on a particle can be computed by summing the product of Ω_i^s with the solid fraction weighting function B over all solid covered lattice nodes with a lattice spacing of h in d dimensions:

$$\mathbf{F}^H = \frac{h^d}{\Delta t} \sum_n B_n \sum_i \Omega_i^s \mathbf{c}_i \,, \tag{3.10}$$

$$\mathbf{T}^H = \frac{h^d}{\Delta t} \sum_n (\mathbf{x} - \mathbf{x}_s) \times \left(B_n \sum_i \Omega_i^s \mathbf{c}_i \right) = \sum_n (\mathbf{x} - \mathbf{x}_s) \times \mathbf{F}^H \,. \tag{3.11}$$

3.2.3.4. Stresslet

Batchelor (1970) derived a general formulation for the computation of the bulk stress in a suspension which has been used in previous LBM simulation, e.g. Haddadi and Morris (2014) or Daghoogi and Borazjani (2015). According to Batchelor (1970), the bulk stress can be computed as:

$$\Sigma_{ij} = \frac{1}{V} \int_V (\sigma_{ij} - \rho u_i' u_j') dV \,, \tag{3.12}$$

where V is the averaging volume. For a Newtonian fluid, Eq. (3.12) can be written as:

$$\Sigma_{ij} = \frac{1}{V} \int_{V - \sum V_p} \left[-p\delta_{ij} + \mu \left(\frac{\partial u_i}{\partial x_j} + \frac{\partial u_j}{\partial xi} \right) \right] dV + \frac{1}{V} \sum \int_{V_p} \sigma_{ij} dV - \frac{1}{V} \int_V \rho u_i' u_j' dV \,, \tag{3.13}$$

where V_p is the particle volume and V the total volume. The particle stress can be simplified by application of the divergence theorem (details are explained by Batchelor (1970) and Haddadi and Morris (2014)) and leads to three stress contributions, viz.

stresslet, acceleration stress and Reynolds stress. For low Reynolds numbers and no external couples imposed on the suspended particles, the particle stress, i.e. the last two terms in Eq. (3.13), reduces to the total stresslet divided by the averaging volume:

$$\sigma_{ij}^{P} = \frac{1}{V} S_{ij} = \frac{1}{V} \sum \frac{1}{2} \int_{A_p} (\sigma_{ik} x_j + \sigma_{jk} x_i) n_k dA \,. \tag{3.14}$$

The stress from the stresslet in LBM simulations can be computed from the hydrodynamic interaction lattice forces F^H (cf. eq (3.10)) by summing over all particle covered lattice nodes and particles:

$$\frac{1}{V} \sum \int_{A_p} \frac{1}{2} \left(\sigma_{ik} x_j + \sigma_{jk} x_i\right) n_k dA = \frac{1}{V} \sum^{N_{particles}} \sum^{N_{nodes}} \left(\frac{1}{2} (F_{ik}^H x_j + F_{jk}^H x_i) \right) \,, \tag{3.15}$$

where the vector x_i points for spherical particles from particle centre to lattice node on which F^H acts.

3.3 Results

3.3.1 Theoretical analysis of the LBDEM coupling

3.3.1.1. Hydrodynamic forces

The relation between hydrodynamic force $\mathbf{F}^H$, weighting function B, solid and fluid velocities $\mathbf{u}_s$ and $\mathbf{u}$ can be shown by substituting the collision terms into equation (3.10).

For simplicity, only the x-component of the hydrodynamic force on a $D2Q9$ lattice is considered here and Eq. (3.6) (BB method) is substituted into the sum over the collision term in Eq. (3.10) while dropping the function parameters $\mathbf{x}$ and t for readability reasons:

$$\begin{aligned} \sum_i \Omega_i^s c_i = (&-2(f_1 - f_3 + f_5 - f_7 + f_8 - f_6) + \\ &f_1^{eq}(u_{s,x}) + f_1^{eq}(u_x) - f_3^{eq}(u_{s,x}) - f_3^{eq}(u_x) + f_5^{eq}(u_{s,x}) + f_5^{eq}(u_x) - \\ &f_7^{eq}(u_{s,x}) - f_7^{eq}(u_x) + f_8^{eq}(u_{s,x}) + f_8^{eq}(u_x) - f_6^{eq}(u_{s,x}) - f_6^{eq}(u_x))c \end{aligned} \tag{3.16}$$

The momentum $\rho\mathbf{u} = \sum_i f_i \mathbf{c}_i$ in x-direction reads

$$\rho u_x = c(f_1 - f_3 + f_5 - f_6 + f_8 - f_7) \,. \tag{3.17}$$

The equilibrium function is

$$f_i^{eq}(\rho, \mathbf{u}) = w_i \rho \left[1 + 3 \left(\frac{\mathbf{c}_i \mathbf{u}}{c^2} \right) + \frac{9}{2} \left(\frac{\mathbf{c}_i \mathbf{u}}{c^2} \right)^2 - \frac{3}{2} \left(\frac{\mathbf{u}}{c} \right)^2 \right] , \tag{3.18}$$

where the lattice weighting functions are $w_0 = 4/9$, $w_{1,2,3,4} = 1/9$ and $w_{5,6,7,8} = 1/36$. It follows therefore for Eq. (3.16) with the momentum Eq. (3.17) and the equilibrium function Eq. (3.18) in x-direction:

$$\sum_i \Omega_i^s c_i = \rho(u_{s,x} - u_x) . \tag{3.19}$$

The force in direction α can be then written as:

$$F_{hyd,\alpha}^{BB} = \frac{h^d}{\Delta t} \sum_n B_n \rho(u_{s,\alpha} - u_\alpha) . \tag{3.20}$$

It is found that the hydrodynamic force is effectively based on the momentum difference between solid and fluid. Analogously for Eq. (3.7) (SP method), the hydrodynamic force in α-direction leads to the same result:

$$F_{hyd,\alpha}^{SP} = \frac{h^d}{\Delta t} \sum_n B_n \rho(u_{s,\alpha} - u_\alpha) . \tag{3.21}$$

3.3.1.2. Re-written fluid-solid coupled LBM equations

The modified LBM equation (3.5) can be re-written into a form of the basic LBM equation (3.2) with an additional term which represents, or can be interpreted as, a forcing term. For the collision term given by Eq. (3.6) (BB method), it is obtained:

$$\begin{aligned} f_i(\mathbf{x} + \mathbf{c}_i \Delta t, t + \Delta t) = f_i(\mathbf{x}, t) &+ \frac{\Delta t}{\tau} (f_i^{eq}(\mathbf{x}, \mathbf{u}, t) - f_i(\mathbf{x}, t)) \\ &+ B(\mathbf{x}, \tau) \Big(\frac{\Delta t}{\tau} \left[f_i(\mathbf{x}, t) - f_i^{eq}(\mathbf{x}, \mathbf{u}, t) \right] \\ &+ f_{-i}(\mathbf{x}, t) - f_i(\mathbf{x}, t) + f_i^{eq}(\mathbf{x}, \mathbf{u}_s, t) - f_{-i}^{eq}(\mathbf{x}, \mathbf{u}, t) \Big) \\ = f_i(\mathbf{x}, t) &+ \Omega_i^{BGK}(\mathbf{x}, \mathbf{u}, t) + F_i^{BB}(\mathbf{x}, \mathbf{u}, t) , \end{aligned} \tag{3.22}$$

where

$$\begin{aligned} F_i^{BB}(\mathbf{x}, t) = B(\mathbf{x}, \tau) \Big(&\frac{\Delta t}{\tau} \left[f_i(\mathbf{x}, t) - f_i^{eq}(\mathbf{x}, \mathbf{u}, t) \right] \\ &+ f_{-i}(\mathbf{x}, t) - f_i(\mathbf{x}, t) + f_i^{eq}(\mathbf{x}, \mathbf{u}_s, t) - f_{-i}^{eq}(\mathbf{x}, \mathbf{u}, t) \Big) . \end{aligned} \tag{3.23}$$

For the SP method, i.e. Eq. (3.7), it is found:

$$\begin{aligned} f_i(\mathbf{x}+\mathbf{c}_i\Delta t, t+\Delta t) &= f_i(\mathbf{x},t) + \frac{\Delta t}{\tau}(f_i^{eq}(\mathbf{x},\mathbf{u},t) - f_i(\mathbf{x},t)) \\ &\quad + B(\mathbf{x},\tau)(f_i^{eq}(\mathbf{x},\mathbf{u}_s,t) - f_i^{eq}(\mathbf{x},\mathbf{u},t)) \\ &= f_i(\mathbf{x},t) + \Omega_i^{BGK}(\mathbf{x},t) + F_i^{SP}(\mathbf{x},t)\ , \end{aligned} \tag{3.24}$$

where

$$F_i^{SP}(\mathbf{x},t) = B(\mathbf{x},\tau)\left(f_i^{eq}(\mathbf{x},\mathbf{u}_s,t) - f_i^{eq}(\mathbf{x},\mathbf{u},t)\right)\ . \tag{3.25}$$

The first moments of the external forcing terms (3.23) and (3.25), i.e. $\sum_i F_i^{BB/SP}\mathbf{c}_i$, are consistent with the hydrodynamic force evaluation from the solid phase collision term given by Eq. (3.10). For the forcing term given by Eq. (3.23), the same hydrodynamic force expression, Eq. (3.20), is obtained because the additional term to the non-equilibrium bounce back collision term, $\frac{\Delta t}{\tau}\left[f_i(\mathbf{x},t) - f_i^{eq}(\mathbf{x},\mathbf{u},t)\right]$, is the BGK collision term which conserves mass and momentum. Similar for the forcing term (3.25), expression (3.21) is obtained. This can be also seen by comparison to the re-written SP solid phase collision term (3.7) which results in $\Omega_i^{SP} = f_i^{eq}(\mathbf{u}_s) - f_i^{eq}(\mathbf{u}) - \frac{\Delta}{\tau}(f_i - f_i^{eq}(\mathbf{u}))$. The last term is again the BGK collision term which conserves mass and momentum and the remainder of the re-written SP solid phase collision term is identical to the external forcing term (3.25).

The re-written BB LB equation (3.22) highlights also the unusual formulation of a forcing term including particle distribution functions f_i and f_{-i}. This peculiar characteristic is part of the Chapman-Enskog discussion in the next section.

3.3.1.3. Chapman-Enskog analysis

The re-written PSM equations (3.22) and (3.24) have the same form:

$$f_i(\mathbf{x}+\mathbf{c}_i\Delta t, t+\Delta t) = f_i(\mathbf{x},t) + \Omega_{BGK}(\mathbf{x},\mathbf{u},t) + F_i(\mathbf{x},\mathbf{u},t)\ . \tag{3.26}$$

This equation is analysed by means of a Chapman-Enskog analysis to investigate the influence of the external BB and SP forcing terms on the macroscale conservation equations. Therefore, a Taylor approximation is applied on the term $f_i(\mathbf{x}+\mathbf{c}_i\Delta t, t+\Delta t)$.

The general Taylor approximation $\mathcal{T}$ of a function $f(x, y)$ with two variables around $(x, y) = (a, b)$ can be expressed up to an order of two by:

$$\mathcal{T}(x,y) = f(a,b) + (x-a)\frac{\partial f(a,b)}{\partial x} + (y-b)\frac{\partial f(a,b)}{\partial y} + \frac{1}{2!}\left[(x-a)^2\frac{\partial^2 f(a,b)}{\partial x^2} + 2(x-a)(y-b)\frac{\partial^2 f(a,b)}{\partial x \partial y} + (y-b)^2\frac{\partial^2 f(a,b)}{\partial y^2}\right] + \dots \quad . \tag{3.27}$$

Taylor expansion of $f_i(\mathbf{x} + \mathbf{c}_i\Delta t, t + \Delta t)$ leads for (3.26) to:

$$\Delta t\left[\frac{\partial}{\partial t} + \mathbf{c}_i\nabla\right] f_i(\mathbf{x},t) + \frac{\Delta t^2}{2}\left[\frac{\partial}{\partial t} + \mathbf{c}_i\nabla\right]^2 f_i(\mathbf{x},t) + \mathcal{O}(\Delta t^3) = \Omega_{BGK}(\mathbf{x},\mathbf{u},t) + F_i(\mathbf{x},\mathbf{u},t)\ . \tag{3.28}$$

For the remainder of the analysis, the Einstein notation is used and a shorter notation is introduced for the partial derivatives by expressing $\frac{\partial}{\partial x} = \partial_x$ and $\frac{\partial}{\partial t} = \partial_t$. Furthermore, the distribution function and equilibrium distribution functions are henceforth written as $f_i(\mathbf{x}, t) = f_i$ and $f_i^{eq}(x_\alpha, u_{s,\alpha}, t) = f_i^{eq}(u_{s,\alpha})$ for the sake of readability. By multiplying Eq. (3.28) with $\Delta t/2\,(\partial_t + c_{i,\alpha}\partial_\alpha)$ and subtracting the resulting Eq. from Eq. (3.28), it is obtained:

$$\Delta t\,(\partial_t + c_{i,\alpha}\partial_\alpha)\,f_i + \mathcal{O}(\Delta t^3) \;=\; \Omega_i^{BGK} + F_{i,\alpha} - \frac{\Delta t}{2}\,(\partial_t + c_{i,\alpha}\partial_\alpha)\left[\Omega_i^{BGK} + F_{i,\alpha}\right] \quad , \tag{3.29}$$

where terms of higher order than $\mathcal{O}(\Delta t^3)$ are neglected.

A perturbation ansatz is used for the particle distribution function

$$f_i = f_i^{(0)} + \epsilon f_i^{(1)} + \epsilon^2 f_i^{(2)} + \dots \tag{3.30}$$

and for the time and space derivatives

$$\partial_t = \epsilon\partial_t^{(1)} + \epsilon^2\partial_t^{(2)} + \epsilon^3\partial_t^{(3)} + \dots\ , \tag{3.31}$$

$$\partial_\alpha = \epsilon\partial_\alpha^{(1)}\ . \tag{3.32}$$

The external forcing term has to be also perturbed as shown by Buick and Greated (2000). However, particle distribution functions f_i are contained in the BB forcing term (3.23). A perturbation of the distribution function within the forcing term and the forcing term

itself results effectively in a second order perturbed forcing term. For example with the perturbation $f_i = f_i^{(0)} + \epsilon f_i^{(1)}$:

$$\begin{aligned} F_{i,\alpha}^{BB} &= \epsilon^1 F_{i,\alpha}^{BB,(1)} \\ &= \epsilon B\left[\frac{\Delta t}{\tau}\left(\epsilon^0 f_i^{(0)} + \epsilon^1 f_i^{(1)} - f_i^{eq}(u_\alpha)\right)\right. \\ &\quad \left. +\epsilon^0 f_{-i}^{(0)} + \epsilon^1 f_{-i}^{(1)} - \epsilon^0 f_i^{(0)} - \epsilon^1 f_i^{(1)} + f_i^{eq}(u_{s,\alpha}) - f_{-i}^{eq}(u_\alpha)\right] \\ &= \epsilon B\left[\frac{\Delta t}{\tau}\left(f_i^{(0)} - f_i^{eq}\right) + f_{-i}^{(0)} - f_i^{(0)} + f_i^{eq}(u_{s,\alpha}) - f_{-i}^{eq}(u_\alpha)\right] \\ &\quad + \epsilon^2 B\left[\frac{\Delta t}{\tau} f_i^{(1)} + f_{-i}^{(1)} - f_i^{(1)}\right]. \end{aligned} \tag{3.33}$$

Hence, similar to Halliday et al. (2001), the general ansatz for the forcing term is:

$$F_{i,\alpha} = \epsilon F_{i,\alpha}^{(1)} + \epsilon^2 F_{i,\alpha}^{(2)} \,. \tag{3.34}$$

Applying the perturbations (3.30), (3.31), and (3.32) on Eq. (3.29) yields

$$\mathcal{O}\left(\epsilon^0\right): \; f_i^{(0)} = f_i^{eq}(u_\alpha) \,. \tag{3.35}$$

Making use of the relation given by Eq. (3.35) at higher orders, it is moreover found:

$$\mathcal{O}\left(\epsilon^1\right): \; \left(\partial_t^{(1)} + c_{i,\alpha}\partial_\alpha^{(1)}\right) f_i^{(0)}(u_\alpha) = -\frac{1}{\tau} f^{(1)} + \frac{1}{\Delta t} F_{i,\alpha}^{(1)}, \tag{3.36}$$

$$\begin{aligned} \mathcal{O}\left(\epsilon^2\right): \; \partial_t^{(2)} f_i^{eq}(u_\alpha) + \left(\partial_t^{(1)} + c_{i,\alpha}\partial_\alpha^{(1)}\right)\left[1 - \frac{\Delta t}{2\tau}\right] f_i^{(1)} &= -\frac{1}{\tau} f^{(2)} + \frac{1}{\Delta t} F_{i,\alpha}^{(2)} \\ &\quad - \frac{1}{2}\left(\partial_t^{(1)} + c_{i,\alpha}\partial_\alpha^{(1)}\right) F_{i,\alpha}^{(1)} \,, \end{aligned} \tag{3.37}$$

and

$$\begin{aligned} \mathcal{O}\left(\epsilon^3\right): \; \partial_t^{(3)} f_i^{eq}(u_\alpha) + \partial_t^{(2)} f^{(1)} + \left(\partial_t^{(1)} + c_{i,\alpha}\partial_\alpha^{(1)}\right) f_i^{(2)} &= -\frac{1}{\tau} f_i^{(3)} + \frac{1}{\Delta t} \\ - \frac{1}{2}\partial_t^{(2)}\left(-\frac{\Delta t}{\tau} f_i^{(1)} + F_{i,\alpha}^{(1)}\right) - \frac{1}{2}\left(\partial_t^{(1)} + c_{i,\alpha}\partial_\alpha^{(1)}\right)\left[-\frac{\Delta t}{\tau} f_i^{(2)} + F_{i,\alpha}^{(2)}\right] \,. \end{aligned} \tag{3.38}$$

For further progression with the analysis, the zeroth to first moments of the above perturbed LB equations have to be taken. Therefore, the zeroth to second moments of the perturbed external forcing terms, listed in table 3.1, are discussed first. The results of the zeroth and first moments of the perturbed forcing terms are the same. The zeroth moments are zero for all perturbations which means that mass is conserved. Fluid momentum is affected by the forcing term as the first moment is non-zero. Expression

	$F_i^{SP,(1)}$	$F_i^{SP,(2)}$	$F_i^{BB,(1)}$	$F_i^{BB,(2)}$
$\sum_i F_{i,\alpha}^{(n)}$	0	0	0	0
$\sum_i F_{i,\alpha}^{(n)} c_{i,\alpha}$	$B\rho(u_{s,\alpha} - u_\alpha)$	0	$B\rho(u_{s,\alpha} - u_\alpha)$	0
$\sum_i F_{i,\alpha}^{(n)} c_{i,\alpha} c_{i,\beta}$	$B\rho(u_{s,\alpha}u_{s,\beta} - u_\alpha u_\beta)$	0	$B\rho(u_{s,\alpha}u_{s,\beta} - u_\alpha u_\beta)$	$B\frac{\Delta t}{\tau}\Pi_{\alpha\beta}^{(1)}$

Tab. 3.1.: Zeroth to second moments of perturbed external forcing terms, (3.23) and (3.23), from the non-equilibrium bounce back and superposition partially saturated methods where $\Pi_{\alpha\beta}^{(1)} = \sum_i f_i^{(1)} c_{i,\alpha} c_{i,\beta}$.

$B\rho(u_{s,\alpha} - u_\alpha)$ is directly related to the hydrodynamic force via Eq. (3.20) and can be therefore re-written by substitution to:

$$B\rho(u_{s,\alpha} - u_\alpha) = \frac{\Delta t}{h^d} F_{hyd,\alpha} \ . \tag{3.39}$$

Similar the expressions $B\rho(u_{s,\alpha}u_{s,\beta} - u_\alpha u_\beta)$, obtained from taking the second moments, can be expressed in dependency of fluid velocity and hydrodynamic force by substituting for $u_{s,\alpha}$ and $u_{s,\beta}$:

$$B\rho(u_{s,\alpha}u_{s,\beta} - u_\alpha u_\beta) = \left(u_\alpha F_{hyd,\beta} + u_\beta F_{hyd,\alpha} + \frac{\Delta t}{h^d} \frac{F_{hyd,\alpha} F_{hyd,\beta}}{B\rho} \right) \frac{\Delta t}{h^d} \ . \tag{3.40}$$

A difference between the perturbed forcing terms is found for the second moment at order $\mathcal{O}(\epsilon^2)$. In contrast to the SP method, the BB method leads to non-zero results, i.e. $\sum_i F_{i,\alpha}^{(2)} c_{i,\alpha} c_{i,\beta} = \sum_i f_i^{(1)} c_{i,\alpha} c_{i,\beta} = B\frac{\Delta t}{\tau}\Pi_{\alpha\beta}^{(1)}$. During the further Chapman-Enskog analysis below, it is shown that $\Pi_{\alpha\beta}^{(1)}$ is related to the viscous shear stresses. Investigation of the effect of $\sum_i F_{i,\alpha}^{(2)} c_{i,\alpha} c_{i,\beta}$ on the macroscale conservation equations and the resulting difference between the BB and SP methods requires that the Chapman-Enskog analysis of Eq. (3.29) is performed as above up to a order of $\mathcal{O}(\epsilon^3)$.

The zeroth and first moment of equation (3.35) lead to $\sum_i f_i^{(eq)}(u_\alpha) = \rho$ and $\sum_i f_i^{(eq)}(u_\alpha) c_{i,\alpha} = \rho u_\alpha$, respectively. Furthermore, it is $\rho = \sum_i f_i = \sum_i (f_i^{(0)} + \epsilon f_i^{(1)} + \epsilon^2 f_i^{(2)} + ...)$ and $\rho u_\alpha = \sum_i f_i c_{i,\alpha} = \sum_i (f_i^{(0)} c_{i,\alpha} + \epsilon f_i^{(1)} c_{i,\alpha} + \epsilon^2 f_i^{(2)} c_{i,\alpha} + ...)$. Thus, the following restrictions are found:

$$\sum_i f_i^{(n)} = 0 \ \text{ for } \ n \geq 1 \ , \tag{3.41a}$$

$$\sum_i f_i^{(n)} c_{i,\alpha} = 0 \ \text{ for } \ n \geq 1 \ . \tag{3.41b}$$

The zeroth moment of Eq. (3.36), (3.37), and (3.38) results with the restrictions (3.41) in

$$\partial_t^{(1)}\rho + \partial_\alpha^{(1)}\left(\rho u_\alpha\right) = \frac{1}{\Delta t}\sum_i F_{i,\alpha}^{(1)} \,, \tag{3.42}$$

$$\partial_t^{(2)}\rho = \frac{1}{\Delta t}\sum_i F_{i,\alpha}^{(2)} - \sum_i \frac{1}{2}\left(\partial_t^{(1)} + c_{i,\alpha}\partial_\alpha^{(1)}\right) F_{i,\alpha}^{(1)} \,, \tag{3.43}$$

and

$$\partial_t^{(3)}\rho = -\frac{1}{2}\partial_t^{(2)}\sum_i F_{i,\alpha}^{(1)} - \frac{1}{2}\partial_t^{(1)}\sum_i F_{i,\alpha}^{(2)} - \frac{1}{2}\partial_\alpha^{(1)}\sum_i F_{i,\alpha}^{(2)} c_{i,\alpha} \,, \tag{3.44}$$

respectively. Summation of Eqs. (3.42), (3.43), and (3.44) gives

$$\begin{aligned}\left(\epsilon\partial_t^{(1)} + \epsilon^2\partial_t^{(2)} + \epsilon^3\partial_t^{(3)}\right)\rho + \epsilon\partial_\alpha^{(1)}\left(\rho u_\alpha\right) \\ = \frac{1}{\Delta t}\left[\epsilon\sum_i F_{i,\alpha}^{(1)} + \epsilon^2\sum_i F_{i,\alpha}^{(2)}\right] - \frac{1}{2}\left[\epsilon\partial_t^{(1)} + \epsilon^2\partial_t^{(2)}\right]\epsilon\sum_i F_{i,\alpha}^{(1)} - \frac{1}{2}\epsilon^3\partial_t^{(1)}\sum_i F_{i,\alpha}^{(2)} \\ - \frac{1}{2}\epsilon\partial_\alpha^{(1)}\left[\epsilon\sum_i F_{i,\alpha}^{(1)} c_{i,\alpha} + \epsilon^2\sum_i F_{i,\alpha}^{(2)} c_{i,\alpha}\right] \,.\end{aligned} \tag{3.45}$$

Reversal of the moments of the perturbed forcing terms could be achieved by taking the corresponding moments of Eq. (3.34), e.g. $\sum_i F_{i,\alpha} = \epsilon\sum_i F_{i,\alpha}^{(1)} + \epsilon^2\sum_i F_{i,\alpha}^{(2)}$. Reversal of Eq. (3.45) leads to the mass conservation equation. However, reversal of all perturbations is postponed to the next sections when the specific BB and SP forcing term moments are inserted. At first, the derivation of the momentum conservation equation is undertaken. Therefore, the first moments of Eqs. (3.36), (3.37), and (3.38) are determined. For Eq. (3.36), it is obtained

$$\partial_t^{(1)}\left(\rho u_\alpha\right) + \partial_\beta^{(1)}\Pi_{\alpha\beta}^{(0)} = \frac{1}{\Delta t}\sum_i F_{i,\alpha}^{(1)} c_{i,\alpha} \,, \tag{3.46}$$

where

$$\Pi_{\alpha\beta}^{(0)} = \sum_i f_i^{(0)} c_{i,\alpha} c_{i,\beta} = \rho u_\alpha u_\beta + \rho c_s^2 \delta_{\alpha\beta} \tag{3.47}$$

and $c_s^2 = 1/3$. The first moment of equation (3.37) leads to

$$\begin{aligned}\partial_t^{(2)}\left(\rho u_\alpha\right) + \left[1 - \frac{\Delta t}{2\tau}\right]\partial_\beta^{(1)}\Pi_{\alpha\beta}^{(1)} = \frac{1}{\Delta t}\sum_i F_{i,\alpha}^{(2)} c_{i,\alpha} - \frac{1}{2}\partial_t^{(1)}\sum_i F_{i,\alpha}^{(1)} c_{i,\alpha} \\ - \frac{1}{2}\partial_\beta^{(1)}\sum_i F_{i,\alpha}^{(1)} c_{i,\alpha} c_{i,\beta}\end{aligned} \tag{3.48}$$

and the first moment of equation (3.38) yields

$$\partial_t^{(3)}\left(\rho u_\alpha\right) + \partial_\beta^{(1)}\Pi_{\alpha\beta}^{(2)}\left[1-\frac{\Delta t}{2\tau}\right] = -\frac{1}{2}\partial_t^{(2)}\sum_i F_{i,\alpha}^{(1)}c_{i,\alpha} - \frac{1}{2}\partial_t^{(1)}\sum_i F_{i,\alpha}^{(2)}c_{i,\alpha} - \frac{1}{2}\partial_\beta^{(1)}\sum_i F_{i,\alpha}^{(2)}c_{i,\alpha}c_{i,\beta}\,. \quad (3.49)$$

Summation of Eqs. (3.46), (3.48), and (3.49) results in

$$\begin{aligned}\left(\epsilon\partial_t^{(1)} + \epsilon^2\partial_t^{(2)} + \epsilon^3\partial_t^{(3)}\right)\left[\rho u_\alpha\right] + \epsilon\partial_\beta^{(1)}\Pi_{\alpha\beta}^{(0)} + \left[1-\frac{\Delta t}{2\tau}\right]\epsilon\partial_\beta^{(1)}\epsilon\Pi_{\alpha\beta}^{(1)} + \epsilon\partial_\beta^{(1)}\epsilon^2\Pi_{\alpha\beta}^{(2)}\left[1-\frac{\Delta t}{2\tau}\right] \\ = \frac{1}{\Delta t}\left[\epsilon\sum_i F_{i,\alpha}^{(1)}c_{i,\alpha} + \epsilon^2 F_{i,\alpha}^{(2)}c_{i,\alpha}\right] - \frac{1}{2}\left[\epsilon\partial_t^{(1)} + \epsilon^2\partial_t^{(2)}\right]\epsilon\sum_i F_{i,\alpha}^{(1)}c_{i,\alpha} \\ - \frac{1}{2}\epsilon\partial_t^{(1)}\epsilon^2\sum F_{i,\alpha}^{(2)}c_{i,\alpha} - \frac{1}{2}\epsilon\partial_\beta^{(1)}\left[\epsilon\sum_i F_{i,\alpha}^{(1)}c_{i,\alpha}c_{i,\beta} + \epsilon^2 F_{i,\alpha}^{(2)}c_{i,\alpha}c_{i,\beta}\right]\,. \quad (3.50)\end{aligned}$$

In the next step the unknown term $\Pi_{\alpha\beta}^{(1)}$ is determined. Therefore, the second moment of equation (3.36) is evaluated:

$$\Pi_{\alpha\beta}^{(1)} = \tau\left[-\partial_t^{(1)}\Pi_{\alpha\beta}^{(0)} - \partial_\gamma^{(1)}\Pi_{\alpha\beta\gamma}^{(0)} + \frac{1}{\Delta t}\sum_i F_{i,\alpha}^{(1)}c_{i,\alpha}c_{i,\beta}\right]\,. \quad (3.51)$$

The derivation of the time differential $\partial_t^{(1)}\Pi_{\alpha\beta}^{(0)}$ and space differential $\partial_\gamma^{(1)}\Pi_{\alpha\beta\gamma}^{(0)}$ for the case of no applied external force is explained in detail in the literature, e.g. Krüger et al. (2017). Analogously, the derivation of the derivatives, here with an imposed external forcing term, can be performed. The third moment of the equilibrium function is $\Pi_{\alpha\beta\gamma}^{(0)} = f_i^{(eq)}c_{i,\alpha}c_{i,\beta}c_{i,\gamma} = \rho c_s^2(u_\alpha\delta_{\beta\gamma} + u_\beta\delta_{\alpha\gamma} + u_\gamma\delta_{\alpha\beta})$ and the derivative can be written as:

$$\partial_\gamma^{(1)}\Pi_{\alpha\beta\gamma}^{(0)} = c_s^2\left(\partial_\beta^{(1)}(\rho u_\alpha) + \partial_\alpha^{(1)}(\rho u_\beta)\right) + c_s^2\delta_{\alpha\beta}\partial_\gamma^{(1)}(\rho u_\gamma)\,. \quad (3.52)$$

The expression $\partial_t^{(1)}\Pi_{\alpha\beta}^{(0)}$ can be evaluated by making use of the product rule, $\partial_*(abc) = a\partial_*(bc) + b\partial_*(ac) - ab\partial_* c$ and by rearranging equations (3.42) and (3.46) to:

$$\partial_t^{(1)}\rho = -\partial_\alpha^{(1)}(\rho u_\alpha) + \frac{1}{\Delta t}\sum_i F_{i,\alpha}^{(1)}\,, \quad (3.53a)$$

$$\partial_t^{(1)}(\rho u_\alpha) = -\partial_\beta^{(1)}\Pi_{\alpha\beta}^{(0)} + \frac{1}{\Delta t}\sum_i F_{i,\alpha}^{(1)}c_{i,\alpha}\,. \quad (3.53b)$$

It follows for $\partial_t^{(1)}\Pi_{\alpha\beta}^{(0)}$ with equation (3.47):

$$\begin{aligned}
\partial_t^{(1)}\Pi_{\alpha\beta}^{(0)} &= \partial_t^{(1)}\left(\rho u_\alpha u_\beta + \rho c_s^2\delta_{\alpha\beta}\right)\\
&= u_\alpha\partial_t^{(1)}(\rho u_\beta) + u_\beta\partial_t^{(1)}(\rho u_\alpha) - u_\alpha u_\beta\partial_t^{(1)}\rho + c_s^2\delta_{\alpha\beta}\partial_t^{(1)}\rho\\
&= -u_\alpha\partial_\gamma^{(1)}\left(\rho u_\beta u_\gamma + \rho c_s^2\delta_{\beta\gamma}\right) + u_\alpha\frac{1}{\Delta t}\sum_i F_{i,\beta}^{(1)}c_{i,\beta}\\
&\quad - u_\beta\partial_\gamma^{(1)}\left(\rho u_\alpha u_\gamma + \rho c_s^2\delta_{\alpha\gamma}\right) + u_\beta\frac{1}{\Delta t}\sum_i F_{i,\alpha}^{(1)}c_{i,\alpha}\\
&\quad + u_\alpha u_\beta\partial_\gamma^{(1)}(\rho u_\gamma) - u_\alpha u_\beta\frac{1}{\Delta t}\sum_i F_{i,\gamma}^{(1)}\\
&\quad - c_s^2\delta_{\alpha\beta}\partial_\gamma^{(1)}(\rho u_\gamma) + c_s^2\delta_{\alpha\beta}\frac{1}{\Delta t}\sum_i F_{i,\gamma}^{(1)}\\
&= -\left[u_\alpha\partial_\gamma^{(1)}(\rho u_\beta u_\gamma) + u_\beta\partial_\gamma^{(1)}(\rho u_\alpha u_\gamma) - u_\alpha u_\beta\partial_\gamma^{(1)}(\rho u_\gamma)\right]\\
&\quad + \frac{1}{\Delta t}\left[u_\alpha\sum_i F_{i,\beta}^{(1)}c_{i,\beta} + u_\beta\sum_i F_{i,\alpha}^{(1)}c_{i,\alpha} - u_\alpha u_\beta\sum_i F_{i,\gamma}^{(1)} + c_s^2\delta_{\alpha\beta}\sum_i F_{i,\gamma}^{(1)}\right]\\
&\quad - c_s^2\left[u_\alpha\partial_\beta^{(1)}\rho + u_\beta\partial_\alpha^{(1)}\rho\right] - c_s^2\delta_{\alpha\beta}\partial_\gamma^{(1)}(\rho u_\gamma)\\
&= -\partial_\gamma^{(1)}(u_\alpha u_\beta u_\gamma)\\
&\quad + \frac{1}{\Delta t}\left[u_\alpha\sum_i F_{i,\beta}^{(1)}c_{i,\beta} + u_\beta\sum_i F_{i,\alpha}^{(1)}c_{i,\alpha} - u_\alpha u_\beta\sum F_{i,\gamma}^{(1)} + c_s^2\delta_{\alpha\beta}\sum_i F_{i,\gamma}^{(1)}\right]\\
&\quad - c_s^2\left[u_\alpha\partial_\beta^{(1)}\rho + u_\beta\partial_\alpha^{(1)}\rho\right] - c_s^2\delta_{\alpha\beta}\partial_\gamma^{(1)}(\rho u_\gamma)
\end{aligned} \tag{3.54}$$

Substitution of Eq. (3.54) and Eq. (3.52) with $c_s^2(\partial_\beta^{(1)}(\rho u_\alpha) + \partial_\alpha^{(1)}(\rho u_\beta)) = c_s^2\rho(\partial_\beta^{(1)}u_\alpha + \partial_\alpha^{(1)}u_\beta) + c_s^2(u_\alpha\partial_\beta^{(1)}\rho + u_\beta\partial_\alpha^{(1)}\rho)$ into Eq. (3.51) gives finally:

$$\begin{aligned}
\Pi_{\alpha\beta}^{(1)} = -\tau\Bigg[&c_s^2\rho\left(\partial_\beta^{(1)}u_\alpha + \partial_\alpha^{(1)}u_\beta\right)\\
&- \partial_\gamma^{(1)}\left(u_\alpha u_\beta u_\gamma\right)\\
&+ \frac{1}{\Delta t}\left(u_\alpha\sum_i F_{i,\beta}^{(1)}c_{i,\beta} + u_\beta\sum_i F_{i,\alpha}^{(1)}c_{i,\alpha} - u_\alpha u_\beta\sum_i F_{i,\gamma}^{(1)} + c_s^2\delta_{\alpha\beta}\sum_i F_{i,\gamma}^{(1)}\right)\\
&-\frac{1}{\Delta t}\sum_i F_{i,\alpha}^{(1)}c_{i,\alpha}c_{i,\beta}\Bigg]
\end{aligned} \tag{3.55}$$

The term $\partial_\gamma^{(1)}\left(u_\alpha u_\beta u_\gamma\right)$ is in the remainder of this analysis neglected as it is assumed that $u^2 << c_s^2$, i.e. the Mach number is $Ma = \frac{u}{c_s} << 1$.

One unknown term is left in equation (3.50), namely $\Pi_{\alpha\beta}^{(2)}$. One could argue that only the two lowest orders, ϵ^0 and ϵ^1, are of interest and therefore neglect the term $\Pi_{\alpha\beta}^{(2)}$. However,

the $\Pi^{(2)}_{\alpha\beta}$ term is here considered to some extent. Therefore, the second moments of equations (3.36) and (3.37) are evaluated and the resulting equations are summed:

$$\begin{aligned}\left(\epsilon\partial_t^{(1)}+\epsilon^2\partial_t^{(2)}\right)\Pi^{(0)}_{\alpha\beta}+\epsilon\partial_\gamma^{(1)}\Pi^{(0)}_{\alpha\beta\gamma}+\epsilon^2\left(1-\frac{\Delta t}{2\tau}\right)\partial_t^{(1)}\Pi^{(1)}_{\alpha\beta}+\epsilon^2\left(1-\frac{\Delta t}{2\tau}\right)\partial_\gamma^{(1)}\Pi^{(1)}_{\alpha\beta\gamma}\\ =-\epsilon\frac{1}{\tau}\Pi^{(1)}_{\alpha\beta}-\epsilon^2\frac{1}{\tau}\Pi^{(2)}_{\alpha\beta}+\frac{1}{\Delta t}\left(\epsilon\sum_i F^{(1)}_{i,\alpha}c_{i,\alpha}c_{i,\beta}+\epsilon^2\sum_i F^{(2)}_{i,\alpha}c_{i,\alpha}c_{i,\beta}\right)\\ -\frac{\epsilon^2}{\Delta t}\partial_t^{(1)}\sum_i F^{(1)}_{i,\alpha}c_{i,\alpha}c_{i,\beta}-\frac{\epsilon^2}{\Delta t}\partial_\gamma^{(1)}\sum_i F^{(1)}_{i,\alpha}c_{i,\alpha}c_{i,\beta}c_{i,\gamma}\,. \qquad (3.56)\end{aligned}$$

The main aim of this Chapman-Enskog analysis is identification of the main differences between the BB and SP method. Normally, it is sufficient to perform the Chapman-Enskog analysis to the order of $\mathcal{O}(\epsilon^2)$ to obtain the macroscale conservation equations. It is shown above in table 3.1 that a difference between both methods is in the second moments of the $F^{(2)}_{i,\alpha}$ terms. Hence, this Chapman-Enskog analysis was extended to order of $\mathcal{O}(\epsilon^3)$. As the other moments in table 3.1 are identical and, again, the main interest is in determination of the main differences between BB and SP method, the $\Pi^{(2)}_{\alpha\beta}$ term is "simplified" by grouping of terms which would be identical between the BB and SP method when evaluated into one single term $\Re$. Thus, Eq. (3.56) can be re-written to:

$$\epsilon^2\Pi^{(2)}_{\alpha\beta}=\frac{\tau}{\Delta t}\left(\epsilon\sum_i F^{(1)}_{i,\alpha}c_{i,\alpha}c_{i,\beta}+\epsilon^2\sum_i F^{(2)}_{i,\alpha}c_{i,\alpha}c_{i,\beta}\right)+\Re\,. \qquad (3.57)$$

Substitution of equations (3.47), (3.55), and (3.57) into Eq. (3.50) yields the perturbed momentum conservation equation:

$$\begin{aligned}\left[\epsilon\partial_t^{(1)}+\epsilon^2\partial_t^{(2)}+\epsilon^3\partial_t^{(3)}\right](\rho u_\alpha)+\epsilon\partial_\beta^{(1)}\left(\rho u_\alpha u_\beta+p\delta_{\alpha\beta}\right)=\epsilon^2\partial_\beta^{(1)}\eta_f\left(\partial_\beta^{(1)}u_\alpha+\partial_\alpha^{(1)}u_\beta\right)\\ +\left(\tau-\frac{\Delta t}{2}\right)\epsilon^2\partial_\beta^{(1)}\frac{1}{\Delta t}\left[u_\alpha\sum_i F^{(1)}_{i,\beta}c_{i,\beta}+u_\beta\sum_i F^{(1)}_{i,\alpha}c_{i,\alpha}-u_\alpha u_\beta\sum_i F^{(1)}_{i,\gamma}-c_s^2\delta_{\alpha\beta}\sum_i F^{(1)}_{i,\gamma}\right]\\ -\left(\tau-\frac{\Delta t}{2}\right)\epsilon^2\partial_\beta^{(1)}\frac{1}{\Delta t}\sum_i F^{(1)}_{i,\alpha}c_{i,\alpha}c_{i,\beta}+\frac{1}{\Delta t}\left[\epsilon\sum_i F^{(1)}_{i,\alpha}c_{i,\alpha}+\epsilon^2\sum_i F^{(2)}_{i,\alpha}c_{i,\alpha}\right]\\ -\frac{1}{2}\left[\epsilon\partial_t^{(1)}+\epsilon^2\partial_t^{(2)}\right]\epsilon\sum_i F^{(1)}_{i,\alpha}c_{i,\alpha}-\frac{1}{2}\epsilon\partial_t^{(1)}\epsilon^2\sum_i F^{(2)}_{i,\alpha}c_{i,\alpha}\\ -\frac{1}{2}\epsilon\partial_\beta^{(1)}\left[\epsilon\sum_i F^{(1)}_{i,\alpha}c_{i,\alpha}c_{i,\beta}+\epsilon^2\sum_i F^{(2)}_{i,\alpha}c_{i,\alpha}c_{i,\beta}\right]\\ -\epsilon\partial_\beta^{(1)}\frac{\tau}{\Delta t}\left[\epsilon\sum_i F^{(1)}_{i,\alpha}c_{i,\alpha}c_{i,\beta}+\epsilon^2\sum_i F^{(2)}_{i,\alpha}c_{i,\alpha}c_{i,\beta}\right]\left[1-\frac{\Delta t}{2\tau}\right]\\ -\epsilon\partial_\beta^{(1)}\Re\left[1-\frac{\Delta t}{2\tau}\right]\,, \qquad (3.58)\end{aligned}$$

where $p=\rho c_s^2$ and $\eta_f=\left(\tau-\frac{\Delta t}{2}\right)\rho c_s^2$. In the next two sections, the perturbations are reversed. The method depending external forcing terms are substituted with the moments listed in table 3.1 in combination with equations (3.39) and (3.40).

3.3.1.3.1. Macroscale conservation equations for the superposition method

After some algebra, the mass conservation equation (3.45) for the SP method is:

$$\partial_t \rho + \partial_\alpha \left(\rho u_\alpha\right) = -\frac{1}{2}\frac{\Delta t}{h^d}\partial_\alpha F_{hyd,\alpha} \ . \tag{3.59}$$

The momentum conservation equation (3.58) is found to be:

$$\begin{aligned}\partial_t \left(\rho u_\alpha\right) + \partial_\beta \left(\rho u_\alpha u_\beta\right) = &-\partial_\alpha p + \partial_\beta \eta_f \left(\partial_\beta u_\alpha + \partial_\alpha u_\beta\right) + \frac{1}{h^d} F_{hyd,\alpha} \\ &- \frac{\Delta t}{2h^d}\left[\epsilon\partial_t^{(1)} + \epsilon^2\partial_t^{(2)}\right] F_{hyd,\alpha} - \left(2\tau - \frac{\Delta t}{2}\right)\partial_\beta \frac{\Delta t}{h^{2d}}\frac{F_{hyd,\alpha}F_{hyd,\beta}}{B\rho} \\ &- \frac{\tau}{h^d}\partial_\beta\left(u_\alpha F_{hyd,\beta} + u_\beta F_{hyd,\alpha}\right) - \partial_\beta \Re\left(1 - \frac{\Delta t}{2\tau}\right)\end{aligned} \tag{3.60}$$

3.3.1.3.2. Macroscale conservation equations for the non-equilibrium bounce back method

For the BB method, the mass conservation equation (3.45) reads:

$$\partial_t \rho + \partial_\alpha \left(\rho u_\alpha\right) = -\frac{1}{2}\frac{\Delta t}{h^d}\partial_\alpha F_{hyd,\alpha} \ . \tag{3.61}$$

The momentum conservation equation (3.58) is as follows:

$$\begin{aligned}\partial_t \left(\rho u_\alpha\right) + \partial_\beta \left(\rho u_\alpha u_\beta\right) = &-\partial_\alpha p + \partial_\beta \left[\eta_f + B\tau\rho c_s^2\right]\left(\partial_\beta u_\alpha + \partial_\alpha u_\beta\right) + \frac{1}{h^d} F_{hyd,\alpha} \\ &- \frac{\Delta t}{2h^d}\left[\epsilon\partial_t^{(1)} + \epsilon^2\partial_t^{(2)}\right] F_{hyd,\alpha} - \frac{\Delta t}{2h^d}\partial_\beta^{(1)}\left(u_\alpha F_{hyd,\beta} + u_\beta F_{hyd,\alpha}\right) \\ &- \frac{dt}{h^{2d}}\tau\frac{F_{hyd,\alpha}F_{hyd,\beta}}{\rho}\left(\frac{1}{B} + 1\right) - \frac{\epsilon}{\Delta t}\partial_\beta \sum_i F_{i,\alpha}^{(1)} c_{i,\alpha} c_{i,\beta} \\ &- \partial_\beta \Re\left(1 - \frac{\Delta t}{\tau}\right) \ .\end{aligned} \tag{3.62}$$

3.3.1.3.3. Discussion of theoretical analysis

It is found that on macroscale a few additional terms appear in the mass and momentum conservation equations. This is not particularly surprising if compared to external forcing terms in the literature. For that reason, a closer look at the F_i^{SP} forcing term is necessary. The term F_i^{SP} resembles an external forcing scheme proposed by Kupershtokh et al. (2009) which reads:

$$F_i = f_i^{eq}(\rho, \mathbf{u}^{eq} + \Delta\mathbf{u}) - f_i^{eq}(\rho, \mathbf{u}^{eq}) \ , \tag{3.63}$$

where $\Delta\mathbf{u} = \frac{\mathbf{F}\Delta t}{\rho}$, $\mathbf{u}^{eq} = \frac{1}{\rho}\sum_i f_i\mathbf{c}_i$ and the physical velocity is $\mathbf{u}^{physical} = \mathbf{u}^{eq} + \frac{\mathbf{F}\Delta t}{2\rho}$. If for evaluation of the velocity difference $\Delta\mathbf{u}$, the force $\mathbf{F}$ is determined according to $B_n\sum_i \Omega_i^s c_i$ (i.e. Eq. (3.21)), it can be written:

$$\mathbf{u}^{eq} + \Delta\mathbf{u} = \mathbf{u}^{eq} + \frac{B\rho(\mathbf{u}_s - \mathbf{u}^{eq})\Delta t}{\rho} = \mathbf{u}^{eq}(1 - B\Delta t) + B\mathbf{u}_s \ . \tag{3.64}$$

In the lattice system, the time-step $\Delta t = 1$ is commonly used and for a lattice cell completely covered by a particle, $B = 1$, the corrected velocity is found as:

$$\mathbf{u}^{eq} + \Delta\mathbf{u} = \mathbf{u}_s \ . \tag{3.65}$$

This means that Eq. (3.24) corresponds for $B = 1$ effectively to a LBM-BGK equation with an additional forcing term on basis of the suggestion by Kupershtokh et al. (2009).

An analysis of different external forcing terms was conducted by Huang et al. (2011). For the forcing term suggested by Kupershtokh et al. (2009) a non-linear force contribution is found which is similar to the finding here, i.e. the fifth term of the r.h.s of Eq. (3.60). Other terms, such as the time derivative of the external force or $u_\alpha F_\beta + u_\beta F_\alpha$ in the mass or momentum equations (3.59)-(3.62), appear due to a missing velocity correction and an appropriate formulation of the external force including a velocity correction as was shown by Guo et al. (2002). Avoidance of these unwanted terms could be possibly achieved by rewriting the external forcing to $F_i = BF_i^{Guo}$ where F_i^{Guo} would be the suggested external force formulation by Guo et al. (2002).

In the analysis, the fluid-solid coupled equations are re-written so that a BGK fluid collision term and an additional term, which is interpreted as an external force, are obtained. This leads to F_i^{BB} containing also the particle distribution function f_i. The Chapman-Enskog analysis for the BB method is the same as for the SP method to the order $\mathcal{O}(\epsilon^2)$ and differs for higher orders. This means that error terms on the macroscale due to external forcing are the same between the SP and BB method when only equations to the order of $\mathcal{O}(\epsilon^2)$ are considered. However, consideration of higher order equations lead to additional error terms where the most noticeable discrepancy between the BB and SP method leads to a modified stress tensor on solid covered lattice nodes, i.e. for the SP method the stress term $\eta_f\left[\partial_\beta u_\alpha + \partial_\alpha u_\beta\right]$ is found which compares to the BB method with $\partial_\beta\left[\eta_f + B\tau\rho c_s^2\right](\partial_\beta u_\alpha + \partial_\alpha u_\beta)$. The stress tensor is the expected stress tensor for a Newtonian fluid. However, the fluid stress tensor for the BB method is changed in particle proximity ($B \neq 0$) because the viscosity is artificially increased by $B\tau\rho c_s^2$. Even when the $\Pi_{\alpha\beta}^{(2)}$ term in the analysis is neglected, the viscosity is artificially increased. The result for the stress tensor, without giving a detailed derivation here, would read $\partial_\beta\left[\eta_f + B\frac{\Delta t}{2}\rho c_s^2\right](\partial_\beta u_\alpha + \partial_\alpha u_\beta)$ when neglecting $\Pi_{\alpha\beta}^{(2)}$ in the above analysis. In either way, an artificial increase of the viscosity is problematic. It affects possibly not only the fluid velocity computation in particle proximity due to an artificial increased resistance to

the fluid flow. But thereby also the hydrodynamic force calculation for a particle which is a effectively based on the difference between solid and fluid velocity according to Eq. (3.20).

The difference between SP and BB method due to the artificial changed fluid stress tensor for the BB method, should be best observable in fluid-particle flows which are dominated by shear stress contributions so that an influence of the pressure term is diminished. Therefore, fluid-particle simulations under simple shear are performed in the subsequent sections to verify and validate the stresslet and bulk stress computation.

3.3.2 Freely moving particle in sheared flow

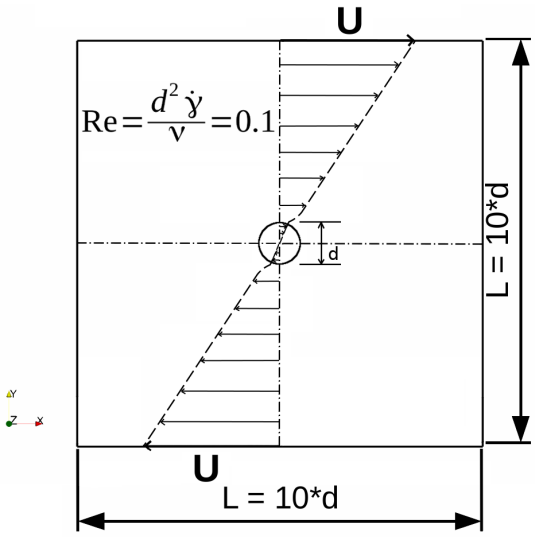

Fig. 3.2.: Setup of a single particle placed between two sheared walls to verify the stresslet computation. The sketch shows an expected fluid velocity profile.

In the simplest case, the stresslet computation can be verified by simulating a single particle in a sheared domain as illustrated in figure 3.2. The analytical solution for the single sphere stresslet in a low Reynolds number range is known and the stresslet is according to Guazzelli and Morris (2012):

$$S_{ij} = \frac{20}{3}\pi\eta_f r_p^3 E_{ij} \ , \tag{3.66}$$

where r_p is the particle radius, η_f the dynamic viscosity of the fluid and E_{ij} is the strain rate tensor. Moreoever, the fluid velocity field for one sphere in straining motions can be evaluated, according to Guazzelli and Morris (2012), by

$$u_i = u_i^\infty - \frac{5}{2}r_p^3\frac{x_i(x_j E_{jk} x_k)}{r^5} - \frac{r_p^5}{2}E_{jk}\left[\frac{\delta_{ij}x_k + \delta_{ik}x_j}{r^5} - \frac{5x_i x_j x_k}{r^7}\right] \ , \tag{3.67}$$

where $r = |x|$ is the distance from the particle centre and u_i^∞ is the undisturbed fluid velocity. Equation (3.67) can be simplified by placing particle and coordinate origin

in the middle of a domain which is sheared in x_1-directions over the height x_2, i.e $E_{12} = E_{21} = \frac{1}{2}\dot{\gamma}$ with the shear rate $\dot{\gamma}$. In particular, the interest is in the velocity u_1 along the direction x_2 which leads to $x_1 = 0$ and $r = |x| = x_2$ and $u_1^\infty = \dot{\gamma} x_2$. The simplified Eq. (3.67) reads then

$$u_1 = \dot{\gamma} x_2 \left(1 - \frac{r_p^5}{2x_2^5}\right) . \tag{3.68}$$

Additionally for a freely moving sphere in a sheared system, the spin rate in steady state is according to Bluemink et al. (2008):

$$\frac{\Omega_p}{\omega^\infty} = \frac{1}{2} , \tag{3.69}$$

where Ω_p is the particle's angular velocity and the fluid vorticity in a sheared system is $\omega^\infty = \frac{1}{2}(\nabla \times \mathbf{u}^\infty)$.

It is known that a BGK collision for the fluid results in slip velocities depending on the used boundary condition and relaxation time τ (e.g. He et al. (1997)). Thus, simulations for varying relaxation parameters $\tau = [0.6 - 1.4]$ with a fixed lattice resolution ($N = 10$ lattice cells over the particle diameter) in a domain of size $\left[\frac{L_1}{d_p} \times \frac{L_2}{d_p} \times \frac{L_3}{d_p}\right] = [10 \times 10 \times 10]$ with periodic boundary conditions in x/z-direction and sheared walls in y direction were performed. The sheared motion of the walls was realised by imposing a macroscale velocity through the non-equilibrium bounce back boundary condition proposed by Zou and He (1997). A single particle was placed in the middle of the domain so that its centre either collapsed exactly with a lattice node (henceforth the non-shifted lattice alignment is abbreviated by "NS") or that its centre was slightly shifted by $\delta = \frac{\Delta x}{2}$ in all directions with regard to the centre lattice node (henceforth the shifted lattice alignment is abbreviated by "S"). The solid fraction computation for each lattice node leads to a symmetric solid fraction distribution between each wall and particle centre for the NS lattice alignment. By shifting the particle location, the symmetric distribution is broken and the influence of the lattice on the simulation results can be thereby investigated. Considering this two lattice alignments, the lattice influence on moving particles which would undergo various lattice alignments during translational motion can be estimated.

The difference between simulation results and analytical solutions are presented for the BB and SP method for all combinations of weighting functions B (Eqs. (3.8) and (3.9)) and particle alignments ("NS" and "S") in figure 3.3. The differences of the angular velocities in steady state are extremely small over the whole relaxation parameter range for all investigated combinations of methods, solid fraction weighting functions, and lattice alignments. However, the stresslet values can significantly differ to the analytical solutions. The differences between the two different alignments "NS" and "S" are minor, but the chosen solid fraction weighting function and method have a major impact on the stresslet value. In all cases, a tendency of decreasing error with decreasing relaxation

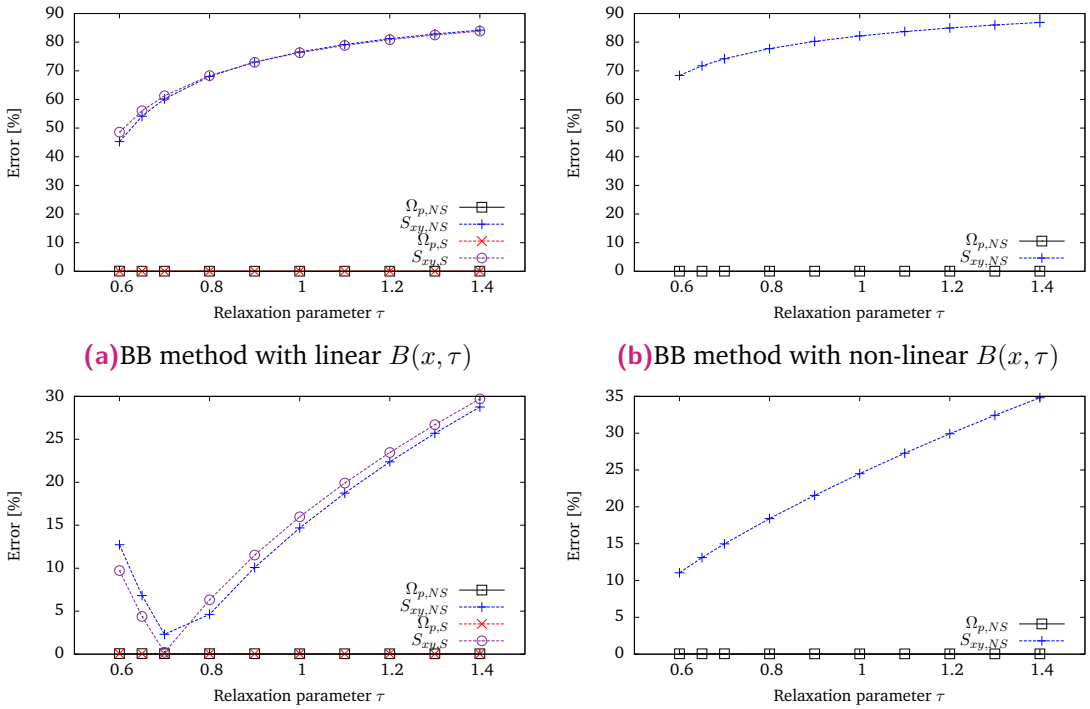

(a) BB method with linear $B(x,\tau)$

(b) BB method with non-linear $B(x,\tau)$

(c) SP method with linear $B(x,\tau)$

(d) SP method with non-linear $B(x,\tau)$

Fig. 3.3.: Single sphere stresslet S_{xy} and angular velocity errors Ω_p over τ for a freely moving particle and different lattice alignments NS and S. Piece-wise linear lines connecting the symbols are for visual guidance and not interpolation curves.

parameter is observed. For the BB method, however, the discrepancy to the analytical solution remains over 40% for the smallest τ value and is even further increased if the solid fraction weighting function is changed from the linear to the non-linear form. The SP Method shows for the nonlinear weighting function a minimum discrepancy of around 10% and might be even decreased for smaller relaxation parameters than $\tau < 0.6$. However, combining the SP method with the linear solid fraction weighting function results in a minimum error of around or less than five per cent for relaxation parameters choosen between $0.65 - 0.8$. For relaxtion parameters outside this range, a drastic stresslet error increase is observed.

The solid velocity profile and fluid velocity profiles of the analytical solution as well as from simulations with an optimal relaxation parameter of $\tau = 0.7$ are depicted in figure 3.4. The insets of figure 3.4 show the velocity profiles from the proximity of the particle surface, indicated by the horizontal green dashed line, to the upper channel wall. The velocity information from only every fourth lattice node is used for figure 3.4. The velocity profiles from the simulations show good agreement to the analytical solution for most of the lattice nodes between particle and wall. However, the velocity difference between simulations and analytical solution grows for decreasing lattice node distance to the particle. The SP method shows a slightly better agreement to the analtyical velocity profile in close particle proximity than the BB method. In contrast, inside of the particle

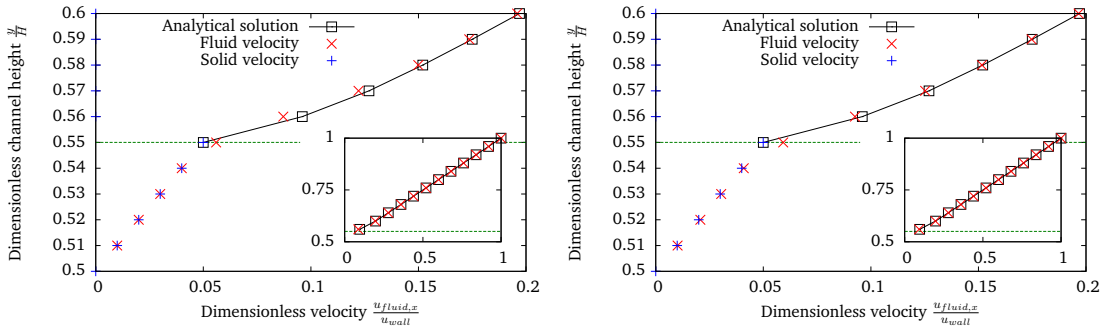

(a) BB method **(b)** SP method

Fig. 3.4.: Fluid velocity profiles of a free single particle in centre of sheared channel with $N = 10$ lattice nodes over the particle diameter and $\tau = 0.7$. Simulation results are compared to the analytical solution given by (3.68). The exact location of the particle surface is indicated by the horizontal, green, dashed line. Insets: Fluid velocity profile for the same simulations shown from particle surface to channel wall where only every fourth lattice node is plotted. Piece-wise linear lines connecting the symbols are for visual guidance and not interpolation curves.

volume, all nodes below the horizontal green dashed line, the BB method seems to fulfill the no-slip condition slightly better in comparison to the SP method.

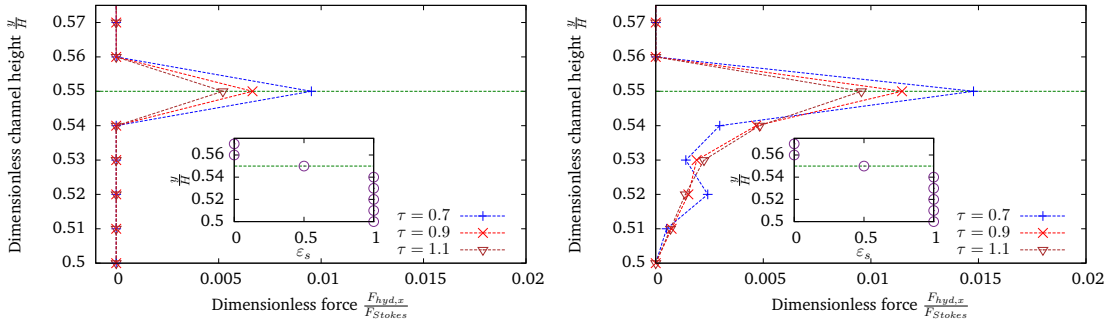

(a) BB method **(b)** SP method

Fig. 3.5.: Hydrodynamic force profiles of a free single particle in centre of sheared channel with $N = 10$ lattice nodes over the particle diameter for a varing relaxation parameter τ. The exact location of the particle surface is indicated by the horizontal, green, dashed line. Insets: Shown is the solid fraction over the dimensionless channel height. Piece-wise linear lines connecting the symbols are for visual guidance and not interpolation curves.

The implications of the slip velocities can be observed by examining the hydrodynamic forces on the lattice nodes covered by the particle. Therefore, the force distributions from simulations with $\tau = [0.7\ ;\ 0.9\ ;\ 1.1]$ are shown in figure 3.5 and the corresponding solid fraction is depicted in the insets of figure 3.5. Consideration of Eqs. (3.20) and (3.21), the hydrodynamic force is zero if the no-slip condition is pefectly fulfilled, i.e. $\mathbf{u} = \mathbf{u}_s$. It is observed that the no-slip condition is seemingly fulfilled by the BB method within the particle volume where the force is nearly zero for all τ on lattice nodes with a solid fraction of $\varepsilon_s = 1.0$. However, the SP method cannot apparently guarantee a perfect no-slip condition within the particle volume because the found force profiles are

non-zero and slightly changed for varied τ. On the particle surface, where $0 < \varepsilon_s < 1$, the hydrodynamic forces are larger for the SP method in comparison to the BB method for all relaxation parameters. Furthermore, it is observed that the forces on the particle surface increase with decreasing relaxation parameter.

The forces over the different particle parts, volume and surface, can be respectively integrated to obtain two stresslet contributions, a volume stresslet contribution $S_{xy,Volume}$ where the lattice node solid fraction is $\varepsilon_s = 1$ and a surface stresslet contribution $S_{xy,Surface}$ where the lattice node solid fraction is $\varepsilon_s < 1$. The two contributions, related to the analytical stresslet solution, are presented for both methods and specific relaxation parameters in table 3.2. It is found that the major contribution to the total stresslet is on the particle surface. For the BB method, the volume part is neglectable, but the surface contribution is unsufficent to obtain the correct stresslet value. In comparison, the volume part for the SP method is around 16% and the surface part slightly below 90% of the total stresslet. Considering that the change in the force profiles within the particle volume for a varying relaxation parameter is only minor, it can be concluded that the stresslet accuracy depends mostly on the hydrodynamic forces on the particle surface.

	$\frac{S_{xy,Volume}}{S_{xy,analytical}}$	$\frac{S_{xy,Surface}}{S_{xy,analytical}}$	$\frac{S_{xy}}{S_{xy,analytical}}$
BB method	1.9755e-7	0.3981	0.3981
SP method	0.1673	0.8559	1.0232

Tab. 3.2.: Integrated surface and volume stresslet parts over a freely moving sphere in sheared channel flow. Non-dimensionalised by the analytical stresslet value. Linear weighting function and relaxation parameter $\tau = 0.7$ are used for both methods, BB and SP.

	$0.5F_x d_y(d_y \geq 0)$	$0.5F_x d_y(d_y \leq 0)$	$0.5F_y d_x(d_x \geq 0)$	$0.5F_y d_x(d_x \leq 0)$	S_{xy}
BB method	0.0995	0.0995	0.0995	0.0995	0.398
SP method	0.2558	0.2558	0.2558	0.2558	1.0232

Tab. 3.3.: Integrated stresslet quadrants over a freely moving sphere in sheared channel flow. Non-dimensionalised by the analytical stresslet value. Linear weighting function and relaxation paramater $\tau = 0.7$ are used for both methods, BB and SP.

In addition, the different spatially integrated contributions, $0.5d_yF_x$ and $0.5d_yF_x$ over particle volume and surface for different particle quadrants are listed in table 3.3. Each method has equal contributions over the four different particle volumes to the total stresslet indicating a force-free (steady) state. As also seen from the force profiles and previous discussion about volume and surface stresslet contributions, the different spatial contributions of the BB method, which does not give the correct stresslet value, are much smaller than the contributions of the SP method which results in the correct stresslet value.

An influence of the boundary conditions can be excluded as a noteworthy change in the stresslet error for an altered domain size is not observed, cf. table 3.4.

$\left[\frac{L_x}{d_p} \times \frac{L_y}{d_p} \times \frac{L_z}{d_p}\right]$	$\tau = 0.7$	$\tau = 1.1$
$[10 \times 5 \times 10]$	3.64%	-
$[10 \times 10 \times 10]$	2.31%	18.74%
$[20 \times 20 \times 20]$	2.16%	18.85%

Tab. 3.4.: Stresslet error for different domain sizes for the SP method with a linear weighting function. Particle is freely rotating in a sheared channel flow.

Additionally, the lattice resolution influence was studied by refining the lattice with regard to the lattice numbers over particle diameter. The results are shown in figure 3.6(a) for method BB and SP. For a relaxation parameter of $\tau = 0.7$, the difference to the analytical solution does not change much for the SP method because the stresslet value is close to the analytical solution. Surprisingly, the error does not change much for the BB method. Hence, the same simulations with a relaxation parameter of $\tau = 1.1$ were performed because a larger discrepancy (around 20%) for a lattice resolution of $N = 10$ was also found for the SP method. The error for the SP method decreases with an increased lattice resolution as it would be expected. However, also for $\tau = 1.1$, the BB method results remain roughly similiar for an increased lattice resolution.

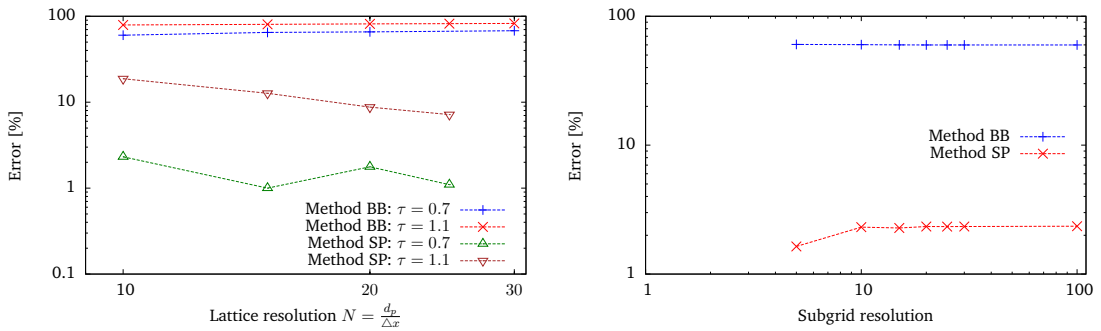

Fig. 3.6.: Stresslet error for varied lattice resolutions with a fixed subgrid resolution of $N_{SGR} = 10$ in (a) and varied subgrid resolution for fixed lattice resolution of $N = 10$ in (b). The domain size is $\left[\frac{L_x}{d_p} \times \frac{L_y}{d_p} \times \frac{L_z}{d_p}\right] = [10 \times 10 \times 10]$, the particle centre position is not shifted, and the weighting function for B is linear. Piece-wise linear lines connecting the symbols are for visual guidance and not interpolation curves.

A too coarse lattice resolution is detrimental to describe accurately the particle shape and transition from fluid to solid. Similarily, it is important to compute accurately the solid fraction at each lattice node. In figure 3.6(b), simulation results for the stresslet calculation obtained with a fixed lattice resolution of $N = 10$, a relaxation parameter $\tau = 0.7$, and varied subgrid resolution for the BB and SP method are depicted. The difference to the analytical solution is nearly unchanged and a subgrid resolution of $N_{SGR} = 10$ should give a good trade-off between accuracy and computational cost.

The differences in the simulation results between BB and SP method could be possibly explained by the findings from the analytical analysis in the previous section. According to the analytical analysis, the fluid viscosity is artificially increased on solid covered lattice nodes for the BB method. Thereby, an increased fluid flow resistance would be experienced in particle proximity which would in turn lead to decreased fluid velocities. Decreased fluid velocities are indeed found for the BB method in particle proximity as shown in figure 3.4. Moreover, the hydrodynamic force is essentially computed from the velocity difference between particle and fluid according to Eq. (3.20). The obtained forces are thereby smaller, as seen from Fig. 3.5, and thus smaller inaccurate stresslet values are obtained. The analytical analysis indicates furthermore that the introduced artificial viscosity depends on the relaxation parameter τ. Hence, a decrease of τ would lead to a decrease of the artificial viscosity which would explain the found decreasing stresslet error with decreasing relaxation parameter. Furthermore, the stresslet error independence from the lattice resolution could be possibly explained by the introduced artificial viscosity in that it is not caused by a numerical discretisation (scheme), but due to the peculiar formulation of the forcing term for the BB method. Thus, the stresslet error is roughly constant for varying lattice resolutions. In contrast, if an introduced artificial viscosity were introduced by a numerical discretisation scheme, then the error would be expected to decrease with an increasing lattice resolution.

3.3.3 Stresslet and torque for a fixed particle in sheared fluid flow

As mentioned in the introduction, the torque computation has been verified in the literature for the BB method. This is seemingly contradicting to the above stresslet findings considering that the stresslet is the symmetric part of the first moment of the surface traction and the torque is the antisymmetric part. The single sphere stresslet Eq. (3.66) depends on fluid viscosity, particle radius and strain rate tensor. Therefore, the above single sphere case was conducted for a fixed particle to demonstrate the difference in stresslet and torque computation. For such a case, the analytical solution for the particle torque is known and reads according to Guazzelli and Morris (2012):

$$T_i = 8\pi\eta_f r_p^3 \omega_i^\infty \ . \tag{3.70}$$

Similarily to the previous section, a domain size of $\left[\frac{L_1}{d_p} \times \frac{L_2}{d_p} \times \frac{L_3}{d_p}\right] = [10 \times 10 \times 10]$ with periodic boundary conditions in x/z-direction and sheared walls in y direction with a single particle placed exactly in the middle of the domain were carried out. The lattice resolution was chosen on basis of the lattice resolution study in the previous section to be $N = 10$ lattice nodes over the particle diameter and the relaxation parameter was varied between $\tau = [0.6 - 1.4]$.

The simulations results are presented in figure 3.7. As in the previous case, the stresslet discrepancy to the analytical solution decreases mostly with decreasing relaxation pa-

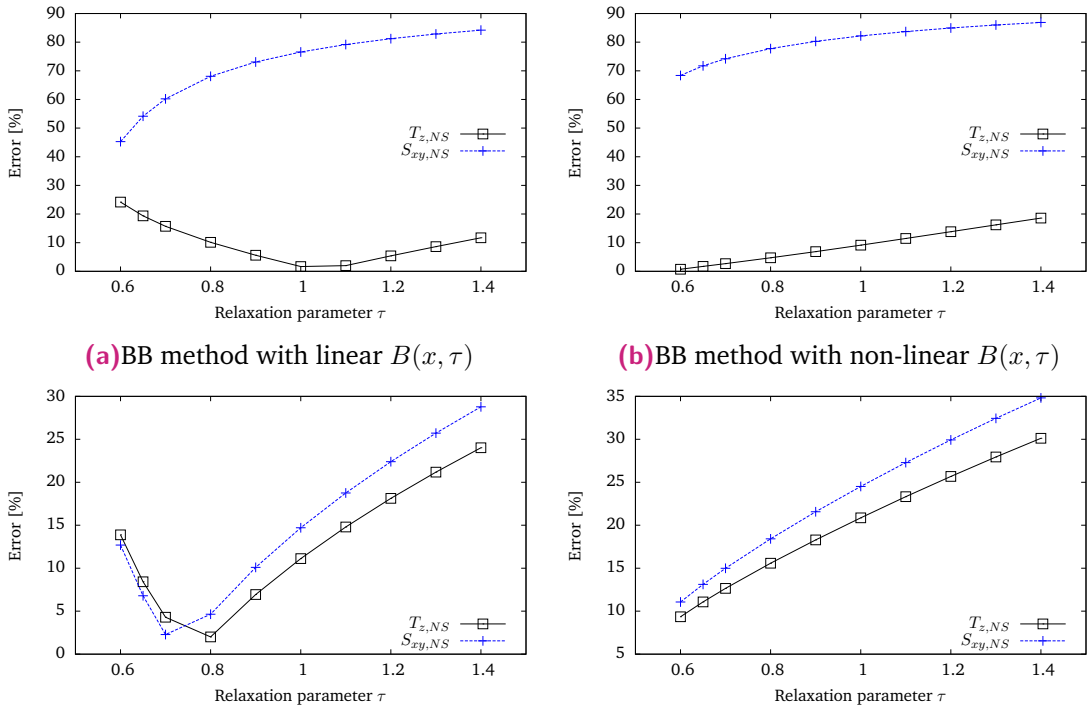

(a) BB method with linear $B(x, \tau)$

(b) BB method with non-linear $B(x, \tau)$

(c) SP method with linear $B(x, \tau)$

(d) SP method with non-linear $B(x, \tau)$

Fig. 3.7.: Single sphere stresslet and torque errors for varied τ for a fixed particle. Piece-wise linear lines connecting the symbols are for visual guidance and not interpolation curves.

rameter. The stresslet results with the BB method for both solid fraction weighting functions are similar to the previous results for which the stresslet could not be accurately computed. Employing the SP method, a drastic decrease for a decreasing relaxation parameter is found for a non-linear weighting function although the discrepancy remains somewhat large, around 10%, for the smallest relaxation parameter. Applying the SP method with a linear weighting function, a minimum for the stresslet error is found in the parameter range of $\tau = [0.65 - 0.8]$.

Although the stresslet results compare to the previous results, the torque results are different. For the SP method, the trends and accuracy of the torque calculation are comparable to the stresslet computation leading to an optimal relaxation parameter range of $\tau = [0.65 - 0.8]$ when a linear weighting function is applied. In contrast, the BB method, which cannot accurately compute the stresslet, can yield the correct torque values. The error in the torque calculation is reduced for smaller relaxation parameters when a non-linear weighting function is used and provides acceptable results. A minimum error in the torque calculation is found in the approximate range $\tau = [0.9 - 1.1]$ when a linear weighting function is applied.

To understand the different outcomes in the accuracy for the stresslet and torque accuracies, the hydrodynamic force profiles in x and y directions for BB and SP methods whilst

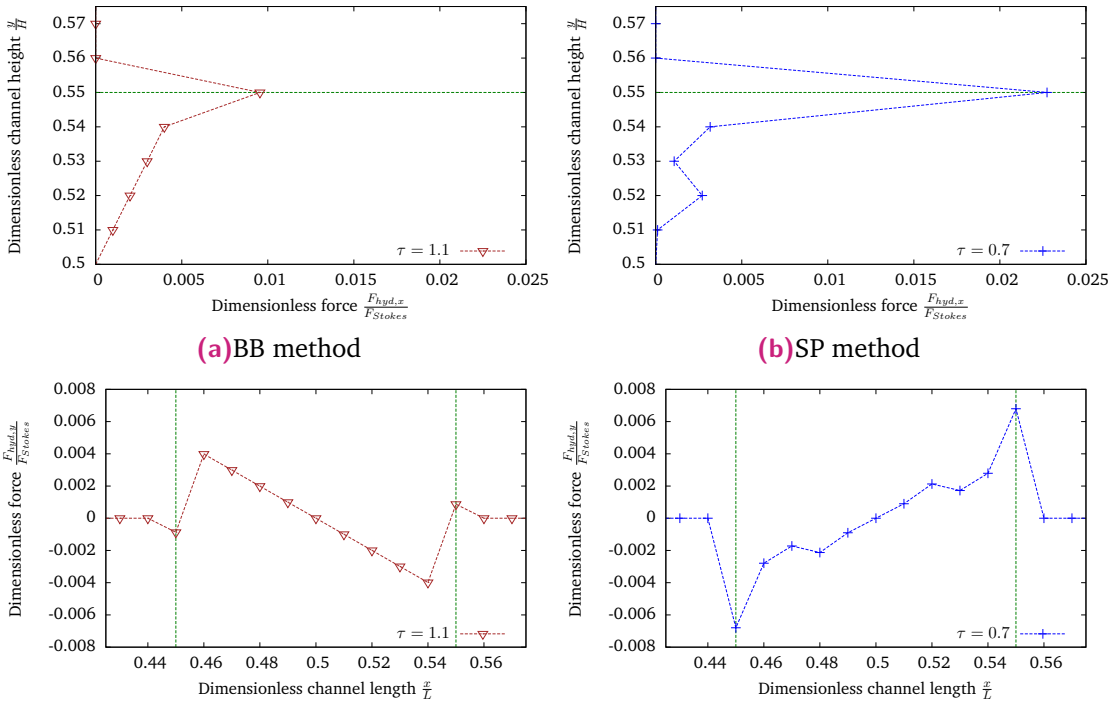

(a)BB method **(b)**SP method

(c)BB method **(d)**SP method

Fig. 3.8.: Hydrodynamic force profiles for a fixed particle in centre of a sheared channel with $N = 10$ lattice nodes over the diameter. The exact location of the particle surface is indicated by the green, dashed lines. The force profiles are shown for BB and SP methods combined with a linear solid fraction weighting function along the x and y direction. The relaxation parameter is chosen so that the torque error is minimised. Piece-wise linear lines connecting the symbols are for visual guidance and not interpolation curves.

applying a linear weighting function with different relaxation parameters are shown in figure 3.8. For both methods, the force profiles in x direction along the y axis, cf. Fig. 3.8 (a)/(b), are comparable to the force profiles obtained in simulations of the freely rotating sphere (Fig. 3.5). However, the surface forces are somewhat larger in the fixed sphere case. For the forces in y direction along the x axis, Fig. 3.8 (c)/(d), the surface forces for BB and SP methods are smaller in magnitude than the surface forces in x direction along the y axis. For the SP method, it is observed that the forces on lattice nodes within the particle volume have the same direction as the surface forces on the closest surface. However, the opposite is found for the BB method where the force direction is changed within the particle volume.

The main difference between the stresslet and torque calculation can be seen by comparison of the stresslet and torque formulas. Evaluation of Eq. (3.11) for the z-component leads to:

$$T_z = \sum^{N_{nodes}} (F_y d_x - F_x d_y) \, . \tag{3.71}$$

The stresslet S_{xy} is then according to Eq. (3.15):

$$S_{xy} = \sum^{N_{nodes}} \left(\frac{1}{2}(F_x d_y + F_y d_x) \right) . \tag{3.72}$$

Comparison of equations (3.71) and (3.72) shows that the difference is an addition and subtraction between different $\mathbf{F} \otimes \mathbf{r}$ contributions. Therefore, integrated $\mathbf{F} \otimes \mathbf{r}$ contributions over specific parts of the particle volume are listed in table 3.5. For the SP method, all $\mathbf{F} \otimes \mathbf{r}$ contributions are positive. In contrast, the BB methods results in positive $F_x d_y$ contributions, but negative $F_y d_x$ contributions. Between the SP and BB method, the $F_y d_x$ contributions are comparable in magnitude. However, the $F_x d_y$ contributions obtained from the SP method are approximately twice as large as from the BB method. The stresslet is determined by addition of all contributions according to equation (3.72). This leads for the SP method to a total stresslet value which is in agreement with the analytical solution. However, the BB method results in a drastically underestimated total stresslet value because the $F_x d_y$ contributions are much smaller than the corresponding SP method contributions. Additionally, the $F_y d_x$ contributions are negative leading to a further reduction of the total stresslet value. The torque calculation is a subtraction of $F_x d_y$ contributions from the $F_y d_x$ contributions according to equation (3.71). For the SP method, the large $F_x d_y$ contribution would overestimate the torque when considered as only contribution. However, it is subtracted from the smaller $F_y d_x$ contributions, which has the same sign, and thereby resulting in an accurate total torque computation. An accurate total torque is also obtained with the BB method. Yet, the accurate torque calculation is not achieved due to a subtraction like for the SP method. The $F_y d_x$ contributions are negative whereas the $F_x d_y$ contributions are positive. This change of the sign leads effectively to a summation of the contributions according to the torque calculation (3.71). Thereby, the total $F_x d_y$ torque contribution, which would underestimate the total torque calculation when considered as only contribution, is compensated by the additional $F_y d_x$ contributions.

	$0.5F_x d_y(d_y \geq 0)$	$0.5F_x d_y(d_y \leq 0)$	$0.5F_y d_x(d_x \geq 0)$	$0.5F_y d_x(d_x \leq 0)$	S_{xy}	T_z
BB method	0.212	0.212	-0.093	-0.093	0.238	-1.22
SP method	0.423	0.423	0.102	0.102	1.05	-1.284

Tab. 3.5.: Integrated $\mathbf{F} \otimes \mathbf{r}$ stresslet parts over parts of a fixed sphere in a sheared channel flow. Non-dimensionalised by the analytical stresslet value. $S_{xy} = \sum 0.5(F_x d_y + F_y d_x)$ and $T_z = \sum(F_y d_x - F_x d_y)$ where $\frac{T_{analytical}}{S_{analytical}} = 1.2$.

3.3.4 Stresslet for two fixed particles in sheared fluid flow

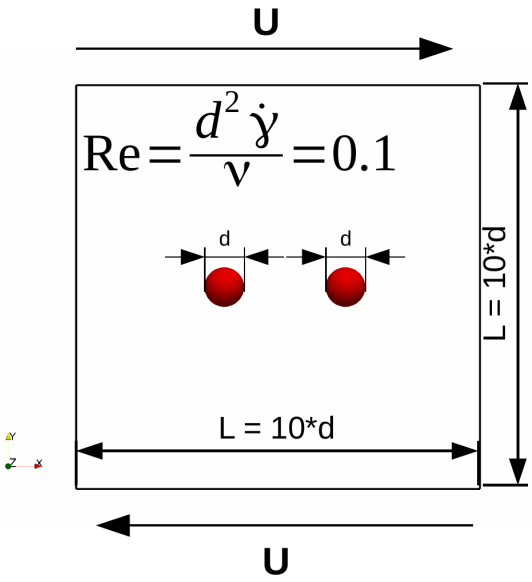

Fig. 3.9.: Simulation setup of two particles placed between two sheared walls to verify the stresslet computation.

Similar to the previous section, the particle stresslet was determined in a sheared system of the same size, but for two particles as illustrated in figure 3.9. Both particles had the same size and a lattice resolution of $N = 10$ lattice nodes over the particle diameter was chosen. The system was sheared so that a Reynolds number of $Re = 0.1$ was obtained. The analytical solution for a stresslet in a two particle system with particles of radii $r_{p,1}$ and $r_{p,2}$ was derived by Batchelor and Green (1972b):

$$\begin{aligned} S'_{ij} = \frac{20}{3}\pi r_{p,1}^3 \eta_f \Bigg(& E_{ij}(1+K') + E_{kl}\left(\frac{r_i r_k \delta_{jl} + r_j r_k \delta_{il}}{r^2} - \frac{r_k r_l}{r^2}\frac{2}{3}\delta_{ij}\right) L' \\ & + E_{kl}\frac{r_k r_l}{r^2}\left(\frac{r_i r_j}{r^2} - \frac{1}{3}\delta_{ij}\right) M' \Bigg) \end{aligned} \tag{3.73}$$

where

$$K' = -\frac{r_{p,2}^3 (r_{p,1}^2 + r_{p,2}^2)}{r^5} + \mathcal{O}\left(\frac{(r_{p,1}+r_{p,2})^6}{r^6}\right), \tag{3.74}$$

$$L' = -\frac{5r_{p,2}^3}{2r^3} + \frac{5r_{p,2}^3 (r_{p,1}^2 + r_{p,2}^2)}{r^5} + 25\frac{r_{p,1}^3 r_{p,2}^3}{4r^6} + \mathcal{O}\left(\frac{(r_{p,1}+r_{p,2})^6}{r^6}\right), \tag{3.75}$$

$$M' = -\frac{25r_{p,2}^3}{2r^3} + \frac{35r_{p,2}^3 (r_{p,1}^2 + r_{p,2}^2)}{r^5} + 25\frac{r_{p,1}^3 r_{p,2}^3}{4r^6} + \mathcal{O}\left(\frac{(r_{p,1}+r_{p,2})^6}{r^6}\right), \tag{3.76}$$

and $\mathbf{r}$ is the vector between the particle-particle-centres. With the same conditions and simplifcations as in the previous section, namely a shearing motion in x_1 direction (i.e $E_{12} = E_{21} = \frac{1}{2}\dot{\gamma}$), the stresslet for $i = 1$ and $j = 2$ reads:

$$S'_{12} = \frac{20}{3}\pi r_{p,1}^3 \eta_f \left(\frac{1}{2}\dot{\gamma}(1 + K') + \frac{1}{2}\dot{\gamma}\frac{r_1 r_1 + r_2 r_2}{r^2} L' + \dot{\gamma}\left(\frac{r_1 r_2}{r^2}\right)^2 M' \right) . \tag{3.77}$$

The relaxation parameter was varied between $\tau = 0.6 - 1.4$ and the difference between simulation results and analytical solution are shown in figure 3.10. The obtained results are very similar to the single particle case. For the BB method, the discrepancy decreases with decreasing relaxation parameter for all weighting function combinations. Although the discrepancy is larger when using a non-linear weighting function. The BB Method cannot reproduce the stresslet and shows a minimum discrepancy of more than 40% with the linear solid fraction weighting function.

In contrast, the SP method can also yield the stresslet in the two particle case correctly when a linear function for the solid fraction is considered and the relaxation parameter range lies between around $\tau = 0.65 - 0.8$. Non-linear weighting of the solid fraction results similarly to the single sphere case in an increased difference to the analytical solution.

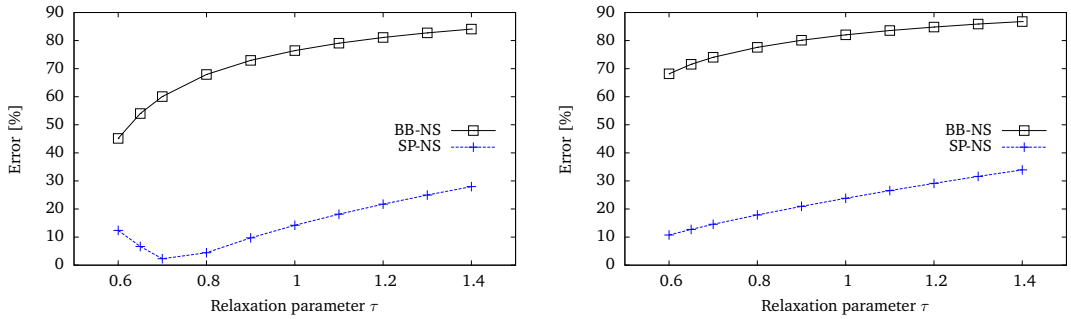

(a) Linear $B(x, \tau)$.

(b) Non-linear $B(x, \tau)$.

Fig. 3.10.: Stresslet error of two freely rotating particles in shear flow ($Re = 0.1$) for a varied relaxation parameter τ with a lattice resolution of $N = 10$ lattice cells over a particle diameter for methods BB and SP with different weighting functions B. Piece-wise linear lines connecting the symbols are for visual guidance and not interpolation curves.

3.3.5 Stresslet contribution in sheared suspensions

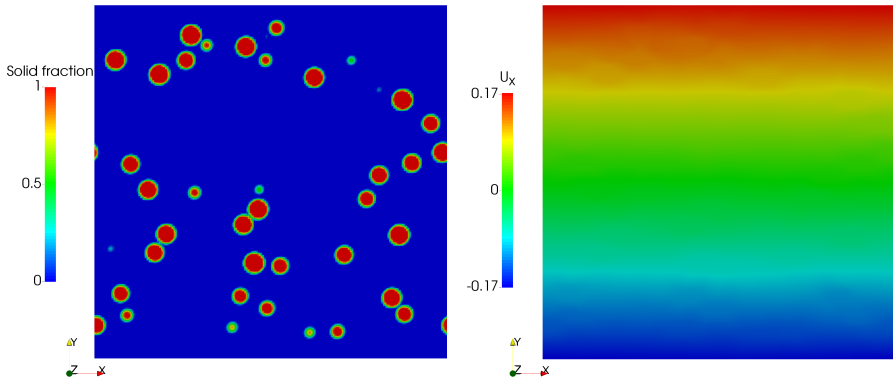

Fig. 3.11.: 3D simulation setup of a sheared suspension illustrated on a slice through the domain. The particle distribution is shown on the left and the fluid velocity component in horizontal direction on the right.

Hitherto, the computation of the stresslet has been analysed on a particle scale. In this section, the effect of the stresslet computation for the BB and SP methods on the suspension viscosity and stress contributions on a bulk scale are investigated. Therefore, simulations in a shear cell under simple shear were performed with an imposed shear rate resulting in a low Reynolds number regime, i.e. $Re = \frac{d_p^2 \dot{\gamma}}{\nu} < 1$. The shear cell was realised by imposing a combination of DEM boundary conditions which are conceptually equivalent to Lees-Edwards boundary conditions (LEbc), cf. Lees and Edwards (1972), and LEbc for LBM, cf. Wagner and Pagonabarraga (2002), on a three dimensional periodic simulation domain The simulation setup with particle distribution and fluid velocity is exemplarily illustrated on a slice through the simulation domain in figure 3.11. Around 500 neutrally buoyant frictionless mono-disperse particles were suspended in a Newtonian fluid. Different solid fractions were obtained by varying the domain size under the restriction of having a minimum size of at least $\left[\frac{L_1}{d_p} \times \frac{L_2}{d_p} \times \frac{L_3}{d_p}\right] \geq [10 \times 10 \times 10]$. Moreover, the lattice resolution was chosen so that $N = 10$ lattice nodes cover a particle diameter. The focus was on the stresslet contribution to the total stress. Hence, the solid fraction range was limited to $\phi_{max} = 0.25$ to minimise particle-particle interactions and thereby avoid lubrication force modelling. In the case of particle collisions, a Hooke spring contact model was employed and resulting stress contributions from the mechanical contact were computed according to Thompson et al. (2009).

The divergence of the suspension viscosity with increasing solid fraction can be described by the semi-empirical Krieger-Dougherty correlation, Krieger and Dougherty (1959), i.e.:

$$\eta_s = \left(1 - \frac{\phi}{\phi_{max,mono}}\right)^{-[\eta]\phi_{max,mono}} , \tag{3.78}$$

where the intrinsic viscosity $[\eta]$ and maximum packing fraction $\phi_{max,mono}$ have to be determined by comparison to experiments. According to Debbas and Rumpf (1966) and Haughey and Beveridge (1969), the close random packing for mono-sized spheres is in a range of around $0.615 \leq \phi_{max,mono} \leq 0.641$ which is also in accordance to experimental investigations carried out by Werff and Kruif (1989). Werff and Kruif (1989) determine, besides the maximum packing fraction $\phi_{max,mono} = 0.63$, furthermore the exponent $[\eta]\phi_{max,mono} = 2$ for the Krieger-Dougherty correlation. The experimental findings of Werff and Kruif (1989) are adopted for comparison to the simulation results obtained with the BB and SP method. An additional Krieger-Dougherty correlation (3.78) with the parameters $[\eta]\phi_{max,mono} = 1.8$ and $\phi_{max,mono} = 0.64$ was determined by fitting to the SP simulation results.

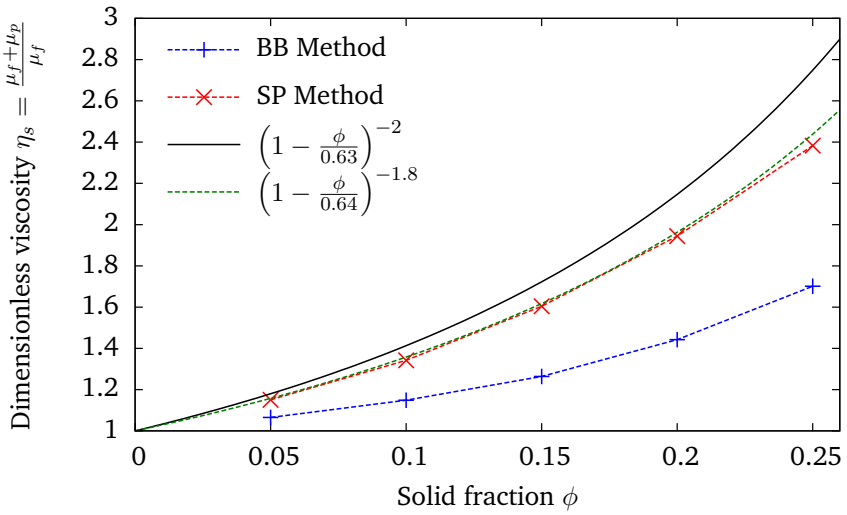

Fig. 3.12.: Apparent viscosity for varied solid fractions of sheared frictionless mono-disperse suspensions. Piece-wise linear lines connecting the symbols are for visual guidance and not interpolation curves.

The Krieger-Dougherty correlations and simulation results are shown in figure 3.12. For both methods, an increase of the suspension viscosity is found for higher solid fractions. However, the BB method shows a large discrepancy to the Krieger-Dougherty correlations. The SP method, in contrast, captures relatively accurately the viscosity increase. The differences to the findings of Werff and Kruif (1989), which grow with increasing solid fraction, could be explained by a missing lubrication force correction when particles are in close contact.

The different stress contributions to the particle stress η_p for the different solid fractions are presented for the BB and SP method in figures 3.13(a) and (b), respectively. The stress, non-dimensionalised by the fluid stress $\eta_f\dot{\gamma}$, is dominated by the stresslet contribution for both methods. The contact stress contributions are much smaller for low solid fractions and increase for higher solid fractions due to a growing probability of colliding particles, but remain well below the stresslet values. Although the qualitative trend of the stress

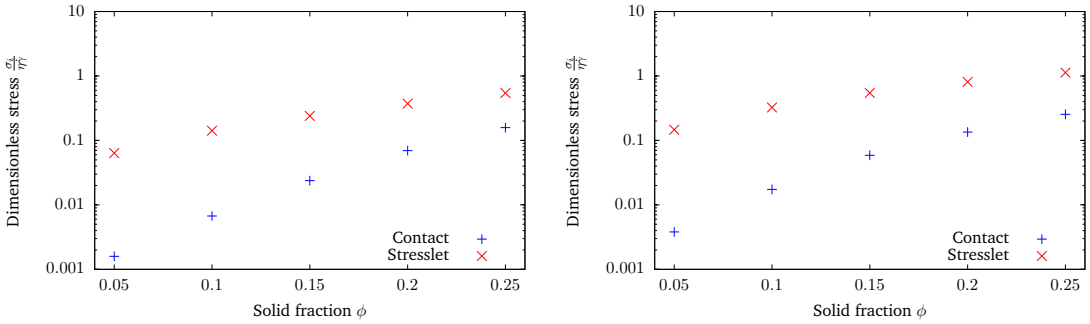

(a)BB method **(b)**SP method

Fig. 3.13.: Dimensionless stress contributions for varying solid fractions for methods BB and SP.

contributions between the BB and SP methods are similar, quantitatively the contributions between both methods differ. Especially, the stresslet contribution for all solid fractions are larger for the SP method in comparison to the BB method. Thus, the accuracy of the stresslet computation on particle scale, as discussed in the previous sections, affects also the stresslet value on bulk scale and ultimately, the stresslet difference leads to the large viscosity discrepancy found in figure 3.12. Therefore, an accurate stresslet computation is of paramount importance. It is here found that only the SP method leads to realistic values on particle and bulk scale.

Furthemore, it shall be remarked that a stress contribution from a lubrication force correction would be expected to fall between the stresslet and contact stress contributions. Thereby, leading to increased suspension viscosities and hence better agreement between simulation results and the experimental findings of Werff and Kruif (1989). An inclusion of a lubrication force correction shall however be subject in subsequent chapters as the focus was here on a correct stresslet computation.

3.4 Conclusions

Two different solid phase collision terms for the immersed moving boundary method in LBM were evaluated theoretically and numerically with regard to the accuracy to compute the stresslet. One solid collision term, abbreviated as BB method, was inspired by the non-equilibrium bounce back. The other solid collision term is abbreviated as SP method according to the method's name (superposition method). Numerical studies were conducted on particle scale for single and two particles in a sheared domain as well as for bulk suspensions under simple shear. Stresslet simulation results on particle scale were compared to analytical solutions and the influence of the single relaxation parameter for the fluid phase collision term on the stresslet accuracy was investigated. Bulk suspension viscosities were compared to the semi-empirical Krieger-Dougherty correlation and the various stress contributions were compared.

The theoretical analysis demonstrates that the partially saturated cell method can be re-written to the common LB notation with an external force. In case of the SP method, the external force can be interpreted as Kuperstokh external force whereas the complexity of the BB method lacks interpretation. The re-written LB equation has been analysed and it has been shown that the SP method leads to additional error terms on macroscale. The BB method, which is more complex, results in similar additional error terms. However, the BB method affects also moreover the stress tensor by an artificial increase of the viscosity on solid covered lattice nodes. The additional artificial viscosity depends on the solid fraction of the lattice nodes, single relaxation parameter, density, and speed of sound.

For the single sphere case, it has been shown that variation of the single relaxation parameter changes slip velocities between particle and fluid velocities and thus hydrodynamic interaction forces. Only the SP method achieves an accurate computation of the stresslet for a relaxation parameter in the range of around $\tau = [0.65 - 0.8]$. The BB method results in discrepancies of at least 40% compared to the analytical solution. Similarly, only the SP method leads to accurate stresslet computations for a two particle case in contrast to the BB method.

Moreover, the correct torque calculation, but failing stresslet calculation, has been explained by examining sheared flow around a fixed particle. Analysis of force profiles over the particle for the BB and SP methods revealed flipped force directions along the shearing axis for the BB method in comparison to the SP method. Thereby, leading to incorrect stresslet calculations, but correct torque calculations for the BB method. In contrast, force profiles over the particle for the SP method are consistent for all directions and thus lead to accurate torque as well as stresslet computations.

For sheared suspensions consisting of hundreds of particles, large viscosity discrepancies for the investigated solid fraction range $\phi \leq 0.25$ between the BB and SP method are found. The SP method leads to accurate viscosity values when compared to a Krieger-Dougherty correlation, whereas the BB method significantly underestimates the viscosity values. The inaccurate stresslet computation on particle scale, which in turn leads to smaller bulk stresslet values for the BB method in comparison to the SP method, has hence a direct effect on the resulting viscosity values.

It is advised for future LBDEM simulations with a partially saturated cell method that the SP method is used instead of the BB method.

4

Lubrication force calibration of a partially saturated cell method for the lattice Boltzmann method

4.1 Introduction

A variety of fluid-solid coupling approaches were proposed and commonly used are methods which solve the fluid flow on a fixed Eulerian lattice and track particles in a Lagrangian framework, e.g. Ladd (1994a) and Ladd (1994b), Noble and Torcyznski (1998), or Feng and Michaelides (2005). However, no matter which approach, computational expenses lead to limitations with regard to the fluid flow resolution. A fine lattice resolution to resolve very small gap distances and arising lubrication forces between particles is thus impossible. Yet, lubrication forces are important to consider to describe properly the microscale suspension physics. A remedy was proposed by Nguyen and Ladd (2002) by introducing lubrication force corrections to model hydrodynamic solid-solid interactions for unresolved small gap distances.

In this chapter it is shown that the proposed lubrication force correction, which was developed for the methodology proposed by Ladd (1994a) and Ladd (1994b), can also be used to some extent, and after some calibration, in combination with the partially saturated cell method suggested by Noble and Torcyznski (1998). Therefore, the applied methodology and the lubrication force correction is discussed firstly. Thereafter, close range hydrodynamic interactions between two particles, subject to the lattice resolution, are simulated. On this basis, recommendations for the single relaxation parameter choice, which affects the slip velocities and hence forces between fluid and particles, are provided. Furthermore, the applicability of the aforementioned lubrication force corrections is investigated with calibration recommendations to minimise discrepancies between simulation results and known analytical solutions.

4.2 Methodology

4.2.1 Discrete element method

A discrete element method (DEM), e.g. Cundall and Strack (1979), is used to solve Newton's second law for translational and angular motion with a velocity-Verlet algorithm for each particle. The total force and torque acting on a particle can be split into particle-particle contacts $\mathbf{F}^C$ and $\mathbf{T}^C$, hydrodynamic interactions $\mathbf{F}^H$ and $\mathbf{T}^H$ determined by the LBM and an imposed lubrication force correction $\mathbf{F}^L$ and $\mathbf{T}^L$ for short particle-particle gap distances which cannot be resolved by the LBM. The translational motion can be expressed as:

$$m_i \frac{\partial \mathbf{x}_i^2}{\partial^2 t} = \mathbf{F}_i = \mathbf{F}_i^C + \mathbf{F}_i^H + \mathbf{F}_i^L \ . \tag{4.1}$$

Similarly for the angular motion, it can be written:

$$\mathbf{J}_i \frac{\partial \omega_i}{\partial t} = \mathbf{T}_i = \mathbf{T}_i^C + \mathbf{T}_i^H + \mathbf{T}_i^L \ . \tag{4.2}$$

Mass, position, moment of inertia and angular velocity of particle i are described by m_i, $\mathbf{x}_i$, $\mathbf{J}_i$ and ω_i, respectively.

4.2.2 Lattice Boltzmann method

Fluid dynamics can be described by the Boltzmann equation which is a transport equation for a particle distribution function. In a particle distribution function $f(\mathbf{x}, \mathbf{u}, t)$, the fluid molecules are statistically summarised in a six dimensional space divided in a velocity space $\mathbf{u}$ at position $\mathbf{x}$ at time t. Discretisation of the Boltzmann equation leads to the lattice Boltzmann method (LBM). The discretised system consists of a numerical mesh, the lattice, and on each lattice node discrete particle distribution functions $f_i(\mathbf{x}, t)$ undergo a collision and streaming step. The discrete particle distribution functions $f_i(\mathbf{x}, t)$ are relaxed towards an equilibrium distribution function $f_i^{eq}(\mathbf{x}, \mathbf{u}, t)$ during the collision step where $\mathbf{u}$ is the macroscopic fluid velocity. In the simplest case, the collision occurs via a single relaxation parameter τ, known as the Bhatnagar-Gross-Krook (BGK) collision according to Bhatnagar et al. (1954):

$$\Omega_i^{BGK} = \frac{\Delta t}{\tau}(f_i^{eq}(\mathbf{x}, \mathbf{u}, t) - f_i(\mathbf{x}, t)) \ . \tag{4.3}$$

During the streaming step, each distribution is moved according to pre-defined lattice velocities $\mathbf{c}_i$ to adjacent lattice nodes. Streaming and BGK collision step can be summarised to the discrete lattice Boltzmann equation:

$$f_i(\mathbf{x} + \mathbf{c}_i \Delta t, t + \Delta t) = f_i(\mathbf{x}, t) + \Omega_i^{BGK} \ , \tag{4.4}$$

where the lattice velocities $\mathbf{c}_i$ are chosen so that macroscale conservation equations for mass and momentum (Navier-Stokes equations) are obtained. The relaxation parameter

τ is related to the fluid viscosity $\nu = (\tau - 0.5)/3$. Details of deriving the macroscopic conservation equations can be found for example in Succi (2001) and Krüger et al. (2017). Macroscopic fluid density and velocity can be obtained by computing the zeroth and first moments of the particle distribution functions, i.e. $\rho = \sum_i f_i(\mathbf{x}, t)$ and $\rho\mathbf{u} = \sum_i f_i(\mathbf{x}, t)\mathbf{c}_i$.

4.2.3 Fluid-solid coupling

Noble and Torcyznski (1998) proposed that the presence of particles can be accounted for by including an additional collision term Ω^s and a weighting function $B(\mathbf{x}, \tau)$ for the solid phase so that Eq. 4.4 reads:

$$f_i(\mathbf{x} + \mathbf{c}_i\Delta t, t + \Delta t) = f_i(\mathbf{x}, t) + \left(1 - \sum_s B(\mathbf{x}, \tau)\right)\Omega_i^{BGK} + \sum_s B(\mathbf{x}, \tau)\Omega_i^s \,. \tag{4.5}$$

If two particles overlap on one lattice cell, the weighting function $B(\mathbf{x}, \tau)$ for solid fractions was modified to $B_1 = \frac{B_1}{B_1+B_2}$ and $B_2 = \frac{B_2}{B_1+B_2}$ for each particle contribution.

As shown in the previous chapter, choice of the solid phase collision term, weighting function and relaxation parameter are not straightforward. Thus, the previous chapter's recommendation was followed and the following solid phase collision term was used:

$$\Omega_i^s = f_i^{eq}(\mathbf{u_s}) - f_i(\mathbf{x}, t) + \left(1 - \frac{\Delta t}{\tau}(f_i(\mathbf{x}, t) - f_i^{eq}(\mathbf{u})\right) \,. \tag{4.6}$$

A linear relationship to the lattice node solid fraction,

$$B(\mathbf{x}, \tau) = \varepsilon_s \,, \tag{4.7}$$

was chosen and the single relaxation parameter choice is studied with regard to the resolution of lubrication force between two particles in a later section.

The hydrodynamic force and torque from the fluid phase on the particle can be computed by summing the product between solid phase collision term Ω_i^s, solid fraction weighting function B, and lattice velocities $\mathbf{c}_i$, over all solid covered lattice nodes with a lattice spacing of h in d dimensions:

$$\mathbf{F}^H = \frac{h^d}{\Delta t}\sum_n B_n \sum_i \Omega_i^s \mathbf{c}_i \,, \tag{4.8}$$

$$\mathbf{T}^H = \frac{h^d}{\Delta t}\sum_n (\mathbf{x} - \mathbf{x}_s) \times \left(B_n \sum_i \Omega_i^s \mathbf{c}_i\right) = \frac{h^d}{\Delta t}\sum_n (\mathbf{x} - \mathbf{x}_s) \times \mathbf{F}^H \,. \tag{4.9}$$

4.2.4 Lubrication force corrections

The fluid flow resolution is limited by the lattice resolution. Considering two approaching particles, the lubrication forces can be in theory resolved down to a gap distance of one lattice cell width. For smaller gap distances, Nguyen and Ladd (2002) proposed a lubrication force correction on basis of the analytical solution for pairwise lubrication forces between particles. The idea is that the lubrication force is ideally resolved to a certain gap distance between particles, around the size of one lattice cell width. For smaller gap distances, the analytical solution is evaluated at two points: At the resolution limit and the current gap distance. The difference between both forces is the lubrication force correction which can be added to the DEM procedure as an additional particle force as expressed in Eqs. (4.1) and (4.2).

Lubrication forces between particles have been extensively studied and a comprehensive overview is provided by Jeffrey and Onishi (1984), Jeffrey (1992) and Kim and Karrila (2005). Arising lubrication interactions between two particles can be expressed in a grand-resistance-matrix notation:

$$\begin{pmatrix} F_1 \\ F_2 \\ T_1 \\ T_2 \\ S_1 \\ S_2 \end{pmatrix} = \eta_f \begin{pmatrix} A_{11} & A_{12} & \tilde{B}_{11} & \tilde{B}_{12} & \tilde{G}_{11} & \tilde{G}_{12} \\ A_{21} & A_{22} & \tilde{B}_{21} & \tilde{B}_{22} & \tilde{G}_{21} & \tilde{G}_{22} \\ B_{11} & B_{12} & C_{11} & C_{12} & \tilde{H}_{11} & \tilde{H}_{12} \\ B_{21} & B_{22} & C_{21} & C_{22} & \tilde{H}_{11} & \tilde{H}_{12} \\ G_{11} & G_{12} & H_{11} & H_{12} & M_{11} & M_{12} \\ G_{21} & G_{22} & H_{21} & H_{22} & M_{21} & M_{22} \end{pmatrix} \begin{pmatrix} v^{\infty}(x_1) - U_1 \\ v^{\infty}(x_2) - U_2 \\ \Omega^{\infty} - \omega_1 \\ \Omega^{\infty} - \omega_2 \\ E^{\infty} \\ E^{\infty} \end{pmatrix} . \tag{4.10}$$

The subscripts of tensor elements in the resistance matrix, e.g. in general $P_{\alpha\beta}$, describe force, torque, and stresslet of particle α while taking into account the motion of particle β. The focus is here only on the forces and torques. The stresslet and stress computation was studied in the previous chapter. The lubrication interaction on particle α with a particle diameter ratio γ to particle β and dimensionless particle-particle gap distance $\xi = \frac{h_{gap}}{r_\alpha}$ can then be generally expressed as:

$$\mathbf{F}^L_\alpha(\gamma, \xi) = \eta_f(\mathbf{P}_{\alpha\alpha}(\gamma, \xi)\mathbf{U}_\alpha + \mathbf{P}_{\alpha\beta}(\gamma, \xi)\mathbf{U}_\beta) \, . \tag{4.11}$$

According to Nguyen and Ladd (2002), consideration of only the leading order terms in the resistance terms, allow to use only the particle velocities. The correction for small gap distances reads then:

$$\mathbf{F}^L_{\alpha,correction}(\gamma, \xi) = \mathbf{F}^L_\alpha(\gamma, \xi) - \mathbf{F}^L_\alpha(\gamma, \xi_N) \, , \tag{4.12}$$

where ξ_N is the minimal resolvable gap distance, e.g. $\xi_N = h_{lattice}$.

4.3 Results

4.3.1 Lubrication force resolution

4.3.1.1. Normal lubrication force

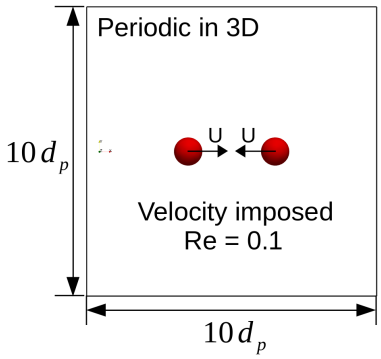

Fig. 4.1.: Simulation set-up to study normal lubrication forces between two particles.

At first, the methodology's capability to resolve the lubrication force without any correction was studied in a three dimensional periodic system in which the simulation domain lengths L_i corresponded to $\left[\frac{L_x}{d_p} \times \frac{L_y}{d_p} \times \frac{L_z}{d_p}\right] = [10 \times 10 \times 10]$. As illustrated in figure 4.1, a constant velocity was imposed on two particles of diameter d_p so that they approach each other with a low Reynolds number of $Re = \frac{d_p U}{\nu} = 0.1$ along the centre-to-centre line. A lattice resolution of $N = 10$ lattice cells over the particle diameter d_p was chosen and the relaxation parameter τ was varied.

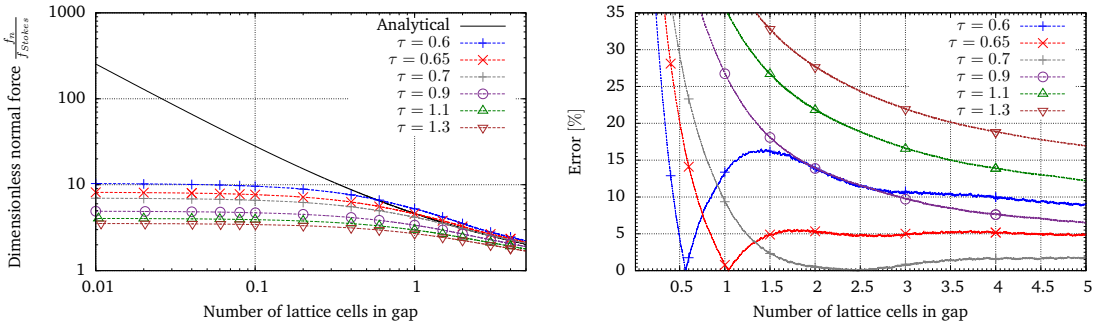

Fig. 4.2.: Dimensionless normal lubrication force (a) and percent difference to the analytical solution (b) over the gap distance. Dashed lines represent actual simulation results where the corresponding symbols represent selective data points for visual guidance.

The obtained hydrodynamic forces are non-dimensionalised by the Stokes force $F_{Stokes} = 3\pi\eta_f r_p \Delta U_{relative}$, where η_f is the dynamic viscosity and r_p the particle radius, and are depicted as a function of the dimensionless gap distance $\xi = \frac{h_{gap}}{r_p}$ in figure 4.2a. The

simulation results are compared to the analytical solution derived by Jeffrey (1982) which reads for monodisperse particles in dimensionless form:

$$\frac{f_n}{f_{Stokes}} = \frac{1}{2\xi} - \frac{9}{20} log(\xi) + 1.3456 - \frac{3}{56}\xi log(\xi) + 0.19\xi \; . \tag{4.13}$$

The obtained hydrodynamic forces from the simulations depend on the relaxation parameter τ which is rather unsurprising considering that slip velocities are caused by a single relaxation parameter scheme as demonstrated by for example He et al. (1997). Larger relaxation parameter values underestimate the lubrication force. A decrease of the relaxation parameter results in an increase of the obtained lubrication force from LBM simulations to the point that a further decrease leads to an overestimation. The deviation in per cent between analytical solution and simulation results over the gap distance is shown in figure 4.2b. For far distances, discrepancies of over 5% are found for larger relaxation parameters, $\tau \geq 0.9$, and a small relaxation parameter $\tau = 0.6$. Furthermore, for these relaxation parameters the error increases for decreasing gap distances. However, intermediate relaxation parameter values, in the narrow range of $\tau = 0.65 - 0.7$, lead to acceptable accuracies for larger gap distances with an adequate lubrication force resolution down to small gap distances. Furthermore, the hydrodynamic force is not instantly constant when particles start to overlap, but increases to a constant value at gap distances smaller than the theoretical resolvable limit of one lattice cell width.

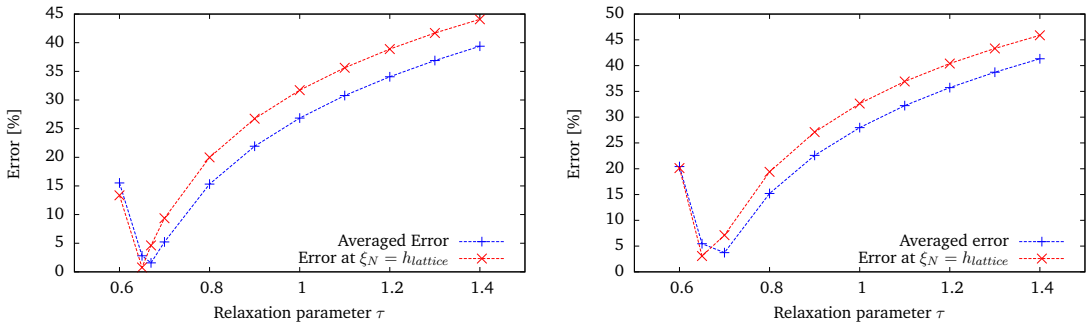

Fig. 4.3.: Normal lubrication force errors for particle motion aligned to lattice grid (a) and diagonal to the lattice (b). Piece-wise linear lines connecting the symbols are for visual guidance and not interpolation curves.

The results were quantified by two measures. Firstly, differences at a gap distance of one lattice cell width, $h_{gap} = h_{lattice}$, were evaluated. Secondly, an artificial increase in the hydrodynamic force is observed for a small relaxation parameter of $\tau = 0.6$. This lead to computation of the averaged discrepancy for gap distances between one and one-half times the lattice width, i.e. $1.0 h_{lattice} < h_{gap} < 1.5 h_{lattice}$ as an additional measure. The results for both accuracy measures for varying relaxation parameters and two different simulation set-ups are presented in figure 4.3a and 4.3b. In figure 4.3a, the particle set-up and motion is as illustrated in figure 4.1. Both particles' motion is aligned to the lattice structure. In the second case, the particles are placed towards the upper right and

lower left corners of the simulation domain so that the normal relative motion occurs diagonally to the lattice grid. In both cases, the two discrepancy measures follow the same trends and the values differ only slightly. The error decreases from larger relaxation parameter values to a minimum around the relaxation parameter range $\tau = [0.65 - 0.7]$ and increases then again drastically for smaller values.

4.3.1.2. Lubrication interactions due to relative tangential motion

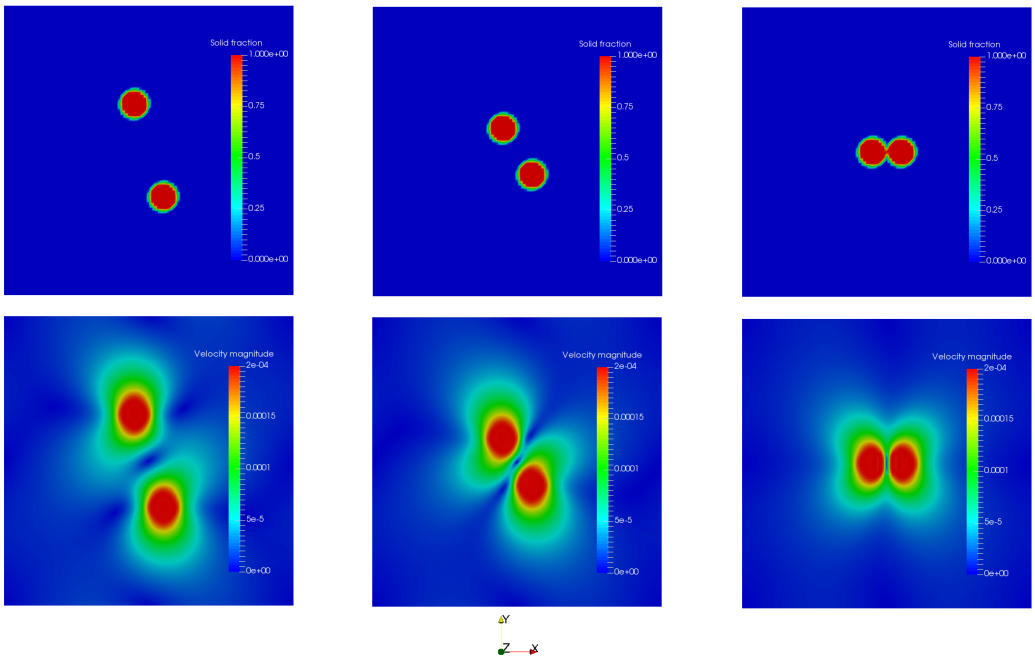

Fig. 4.4.: Particle location and the magnitude of the fluid velocity field for two particles undergoing relative tangential motion.

The lubrication force and torque contribution from relative tangential motion between particles can be similarly probed as the normal lubrication force component. In a simulation domain of the size $\left[\frac{L_x}{d_p} \times \frac{L_y}{d_p} \times \frac{L_z}{d_p}\right] = [10 \times 10 \times 10]$, two particles, whose centre were offset to the y-axis, were moved with a constant velocity parallel to the y-axis as depicted in figure 4.4 for three different points in time. The imposed velocities were chosen so that a low Reynolds number $Re = 0.1$ was obtained and the lattice resolution was fixed to $N = 10$ lattice points over a particle diameter. In the previous section, the normal lubrication force could be relatively accurately captured for a relaxation parameter range of $\tau = [0.65 - 0.7]$. Thus, the relaxation parameter was henceforth fixed to $\tau = 0.65$.

Three different contributions can be extracted, viz. normal and tangential forces as well as a torque. The dimensionless lubrication contributions and differences to the known analytical solutions in per cent are shown in figures 4.5, 4.6, and 4.7. The result for the normal lubrication force contribution, presented in Fig. 4.5, is similar to previous results.

Except that a small increase of the error towards a gap distance of one lattice cell width is found. This is also discussed in the next paragraph.

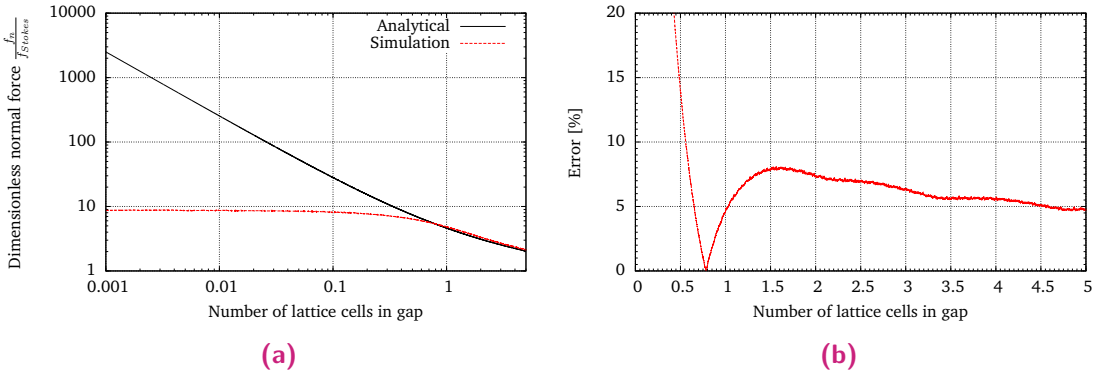

Fig. 4.5.: Normal lubrication force for tangentially passing particles.

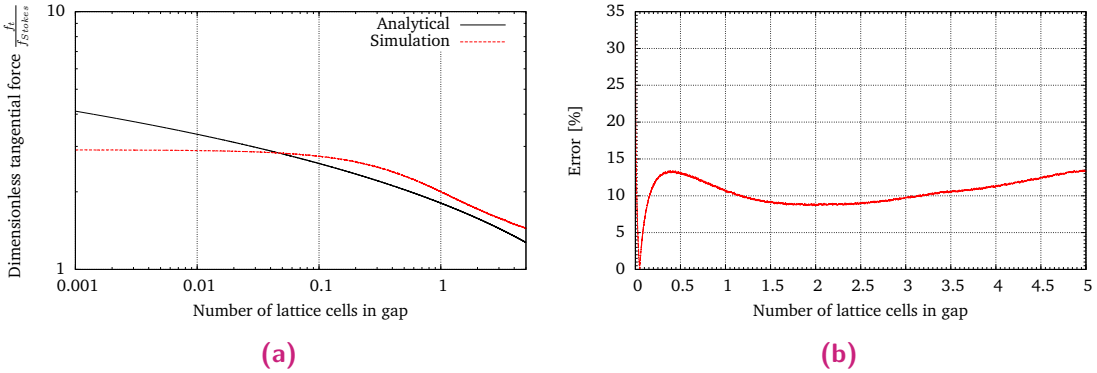

Fig. 4.6.: Tangential lubrication force for tangentially passing particles.

The dimensionless tangential force component over particle-particle gap distance is presented in figure 4.6a. The tangential lubrication force found from the simulation shows a qualitative same increase as the analytical solution for a reducing distance between the particles. However, for gap distances smaller than the theoretical resolution limit of one lattice cell width, it can be observed that the simulation result shows a slightly steeper increase in the hydrodynamic force for a decreasing gap distance to a point where it assumes a constant value. This is visible as a “bump” in the error plot 4.6b and could be explained with a significantly increased overlap between the particles as it is illustrated in the last timestep of figure 4.4. The overlap results in changed flow patterns because the particle-particle gap is closed due to an increased solid fraction and hence, resulting in an increased hydrodynamic interaction force. Furthermore, larger gap distances lead seemingly to an increased discrepancy which could be however explained with the validity of the analytical solution for only small gap distances. Overall, for the tangential force component in Fig. 4.6, a small overestimation of the force, around 10%, is found.

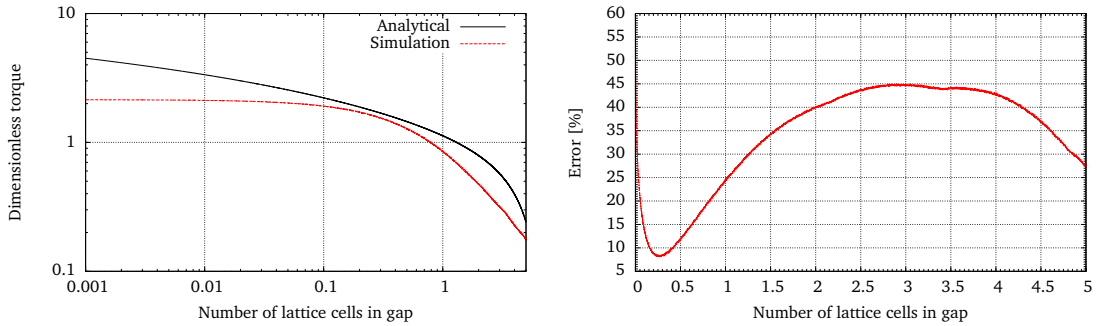

(a) (b)

Fig. 4.7.: Lubrication torque for tangentially passing particles.

A relative tangential motion between particles leads also to a torque contribution, which is presented in figure 4.7. Figure 4.7a shows the dimensionless torque, obtained by relating the simulation result to $\frac{T_{simulation}}{2\pi\eta_f r_p^2 U_{relative}}$, over the gap distance. Although the hydrodynamic torque grows with a decreasing gap distance, it is obvious that the simulation result differs in its magnitude from the analytical solution. The discrepancy, shown in figure 4.7b, is a difference of up to 45 per cent. In contrast to the force contributions, the torque simulation result reveals a large percentage discrepancy to the analytical solution.

4.3.1.3. Rotational lubrication interactions

Hydrodynamic force and torque acting on the particles can not only arise from translational motion, but also due to rotating particles. Therefore, the same simulations which were performed to study normal lubrication forces between particles, as described in section 4.3.1.1 and illustrated in figure 4.1, were conducted. However, in addition to the translational motion along the particle-particle centre line in a domain of size $\left[\frac{L_x}{d_p} \times \frac{L_y}{d_p} \times \frac{L_z}{d_p}\right] = [10 \times 10 \times 10]$, a constant angular velocity of the same magnitude was imposed on each particle. The particles rotated into the same direction and the obtained Reynolds number was as before $Re < 1.0$. The lattice resolution was chosen so that $N = 10$ lattice cells over the particle diameter d_p were obtained and the relaxation parameter is chosen according to the results from the normal lubrication force study, i.e. $\tau = 0.65$.

The normal lubrication force, shown in figure 4.8, does not differ to the previous results and thus, the focus is set on the force and torque stemming from the particle rotation which are presented in figures 4.9 and 4.10, respectively.

The analytical force and force from simulation, non-dimensionalised by $4\pi r_p^2 \eta_f \Omega_p$, over particle-particle gap distance are shown in Fig. 4.9a. For larger gap distances, the analytical solution shows a singular force spike indicating that it is only valid for very short gap distances. For short gap distances, the analytical and numerical solution

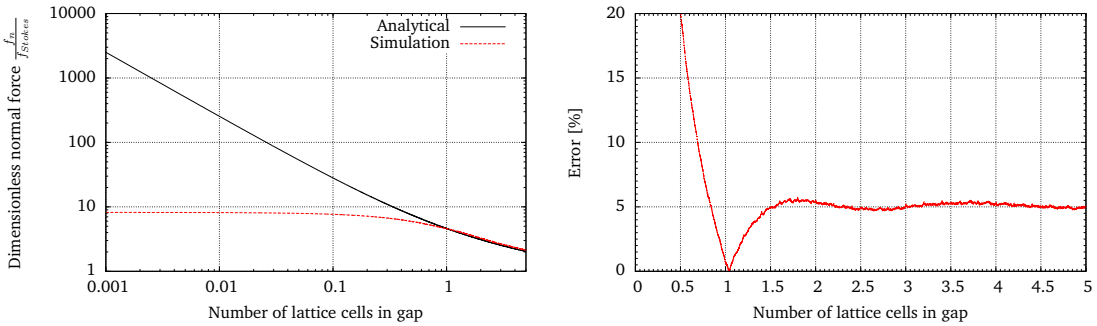

Fig. 4.8.: Normal lubrication force for the case of rotating particles approaching each other along the centre-to-centre line.

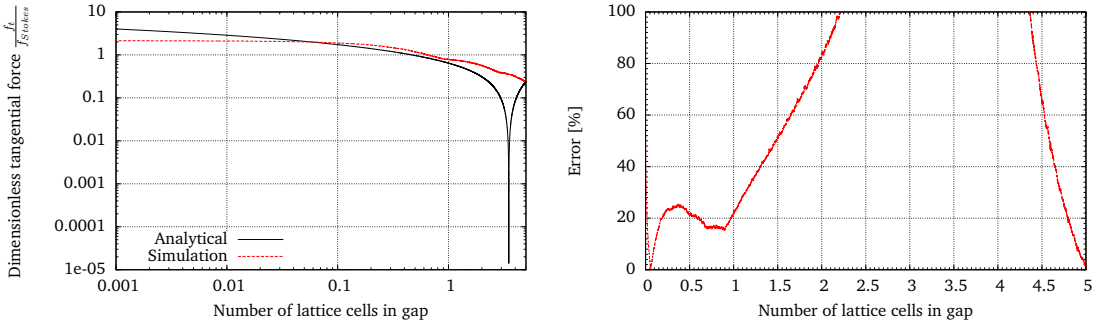

Fig. 4.9.: Lubrication force resulting from the particle rotation of rotating particles approaching each other along the centre-to-centre line.

show the same tendency in increasing force for decreasing gap distances. However, a quantitative comparison shows a rather large difference in per cent between simulation and analytical solution (cf. Fig. 4.9b). Furthermore, below the theoretical resolution limit, i.e. gap distances smaller than one lattice cell width, an increase of the force to a constant value is found. Thereby, the hydrodynamic force is increasingly overestimated for very small gap distances of around $[0.05 - 1.0]$ of a lattice cell width. This is visible as a "bump" in the error figure 4.9b and could be explained, as in the previous section for particles undergoing relative tangential motion, with a significantly increased overlap between the particles.

A similar result is found for the torque contribution which is shown in figure 4.10a. The torque, which is non-dimensionalised by the factor $8\pi r_p^3 \eta_f \Omega_p$, shows the same trend for a decreasing short gap distance as the analytical solution. The difference in per cent, depicted in 4.10b, indicates a similar error behaviour, albeit reduced in its quantity, in comparison to the previously discussed lubrication force arising from rotation. The difference to the analytical solution decreases for decreasing gap distances and shows an increase in the hydrodynamic torque to a constant value for gap distances smaller than one lattice cell width.

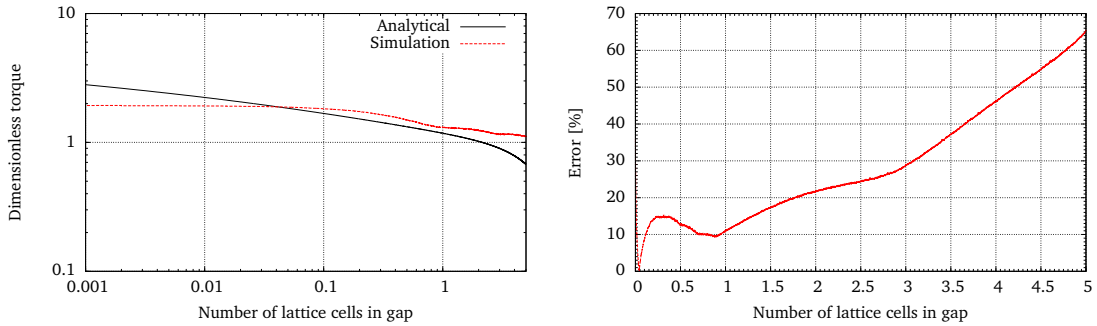

(a) (b)

Fig. 4.10.: Lubrication torque resulting from rotating particles approaching each other along the centre-to-centre line.

4.3.2 Corrections for lubrication interactions

The hydrodynamic lubrication contributions due to relative tangential motion or rotation between particles are extremely small compared to the normal lubrication force. Depending on the gap distance, the difference to the normal lubrication force contribution can be of several magnitudes. An accurate modelling of the normal lubrication force seems therefore much more important than the contributions due to relative tangential or rotational motion. Thus, a rough approximation of other contributions than the normal lubrication force could be justified.

4.3.2.1. Normal lubrication force correction

Simulations of colliding particles in normal directions as described in section 4.3.1.1 were repeated. However, the relaxation parameter was fixed to $\tau = 0.65$ and the lubrication force correction described in section 4.2.4 was applied. The discrepancy to the analytical solution over the gap distance is depicted as black solid line, legend entry $\delta_{cut} = 1.0$, in figure 4.11. The lubrication force is drastically overestimated due to the further increase of the hydrodynamic force for gap distances smaller than one lattice cell width. Taking this effect into account, the lubrication force correction, Eq. (4.12), is slightly modified by shifting the outer cut-off distance to smaller gap distances than one lattice cell width, i.e.

$$\mathbf{F}^L_{\alpha,correction}(\gamma,\xi) = \mathbf{F}^L_{\alpha}(\gamma,\xi) - \mathbf{F}^L_{\alpha}(\gamma,\delta_{cut}\xi_N)\ ,\ \text{for}\ \xi \leq \delta_{cut}\xi_N = \delta_{cut}h_{lattice}\ , \qquad (4.14)$$

where δ_{cut} is a calibration parameter for the lubrication force correction.

Shifting the outer cut-off marginally by a factor of $\delta_{cut} = 0.85$ leads to an initial improvement, but for further decreasing gap distances an overestimation of the normal lubrication forces remains. The overestimation at small gap distances can be diminished

by reducing the outer cut-off to smaller values. In doing so, the lubrication force is then however increasingly underestimated for gap distances close to the cut-off. Therefore, it seems that there exists an optimum for the cut-off in the range $\delta_{cut} = [0.75 - 0.8]$.

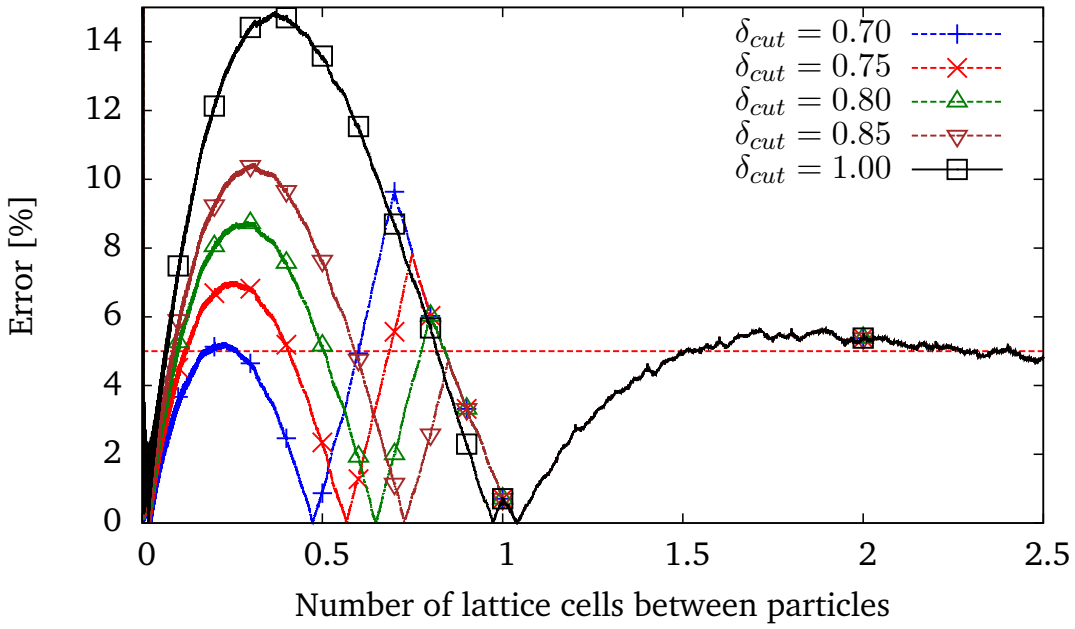

Fig. 4.11.: Normal lubrication force errors with corrections for different outer cut-offs.

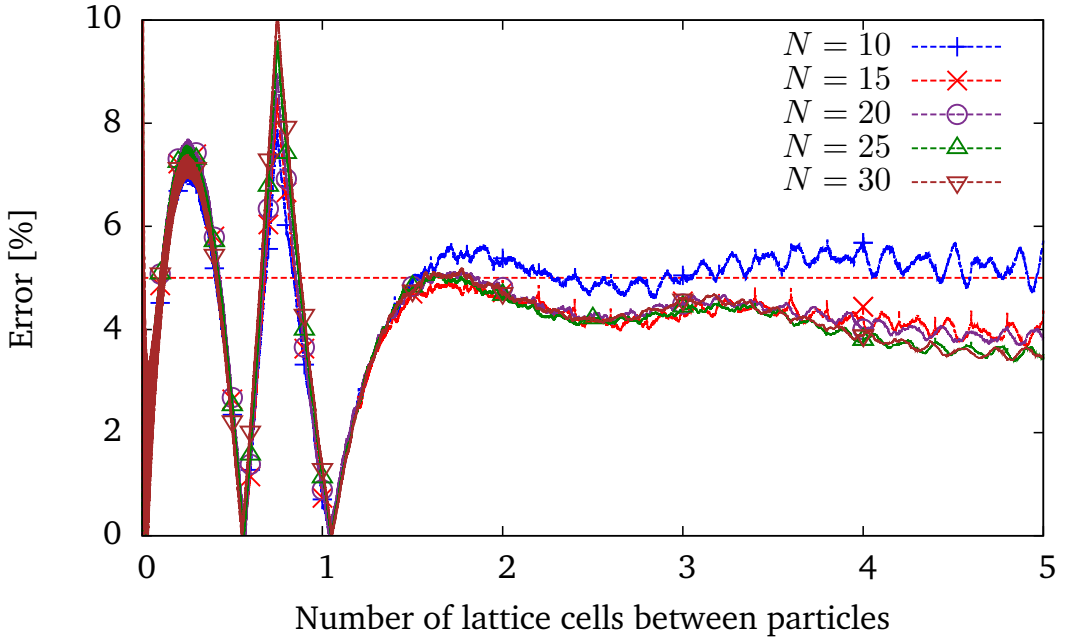

Fig. 4.12.: Normal lubrication force errors with cut-off corrections $\delta_{cut} = 0.75$ for different lattice resolutions. Dashed lines represent actual simulation results where the corresponding symbols represent selective data points for visual guidance.

After determination of an optimal cut-off range, a value of $\delta_{cut} = 0.75$ was applied to simulations with varying lattice resolutions. The lattice resolution was gradually increased from $N = 10$ to $N = 30$ lattice cells over a particle diameter. An increase in the lattice cell number leads to an increase of the lubrication force resolution towards smaller gap distances. The error is presented in 4.12 which illustrates only a minor change in the obtained combination of lubrication force and imposed lubrication force correction. As an increase in the lattice resolution has only a small effect on the lubrication force correction, the lattice resolution could be fixed to $N = 10$ lattice cells over a particle diameter for following simulations.

4.3.2.2. Corrections for lubrication interactions due to relative tangential motion

Although comparison of the lubrication components in section 4.3.1.2 was problematic, a correction, as given by Eq. (4.14), was employed. For the same case as in section 4.3.1.2 with $\tau = 0.65$, particles passed each other on parallel lines. The lattice resolution was fixed to $N = 10$ lattice cells over a particle diameter as the lattice influence on the correction in normal collision direction was minor as shown in the above discussion. The tangential force component over the gap distance and the discrepancy to the analytical solution are shown in figure 4.13a and 4.13b, respectively. A cut-off size corresponding to one lattice cell width leads to an overestimation of the tangential component. Therefore, the cut-off is incrementally reduced to limit the divergence from the analytical solution and thereby leading to a relatively small value of $\delta_{cut} = 0.05$. Likewise for the torque, the cut-off distance for a correction as Eq. (4.14) is stepwise decreased. The torque over gap distance is plotted in figure 4.14a. For a calibration parameter close to $\delta_{cut} = 1$, the torque is significantly overestimated and the discrepancy can be as large as over 35 per cent (cf. 4.14b). A reduction of the calibration parameter results in an improved modeling and an optimal value of around $\delta_{cut} = 0.1$ is found.

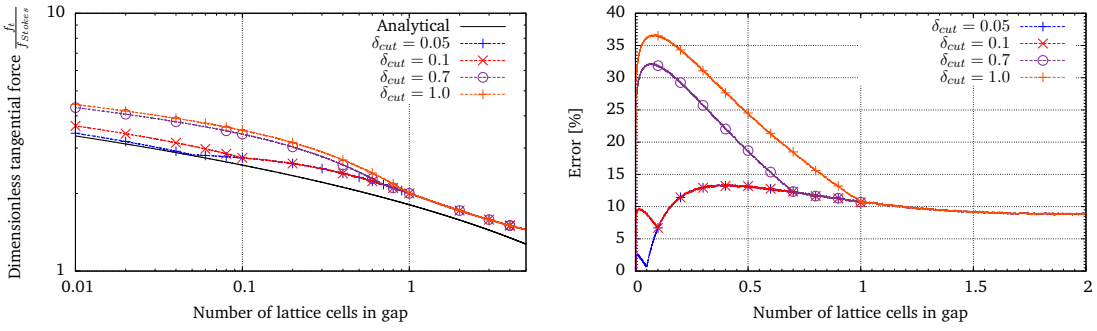

Fig. 4.13.: Modified tangential lubrication force correction. Dashed lines represent actual simulation results where the corresponding symbols represent selective data points for visual guidance.

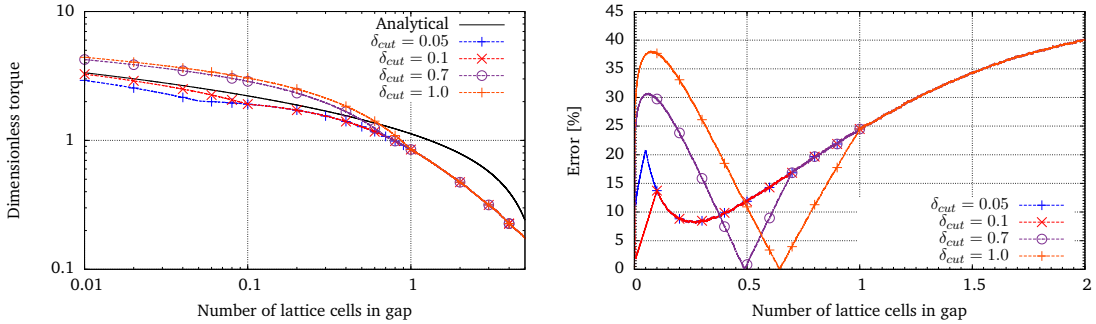

Fig. 4.14.: Modified torque due to sheared motion of particles. Dashed lines represent actual simulation results where the corresponding symbols represent selective data points for visual guidance.

4.3.2.3. Corrections for rotational interactions

The very same simulation setup as described in section 4.3.1.3 with $\tau = 0.65$ and $N = 10$ lattice cells over a particle diameter was used to calibrate a modified lubrication correction Eq. (4.14) for hydrodynamic force and torque arising due to the rotation of particles.

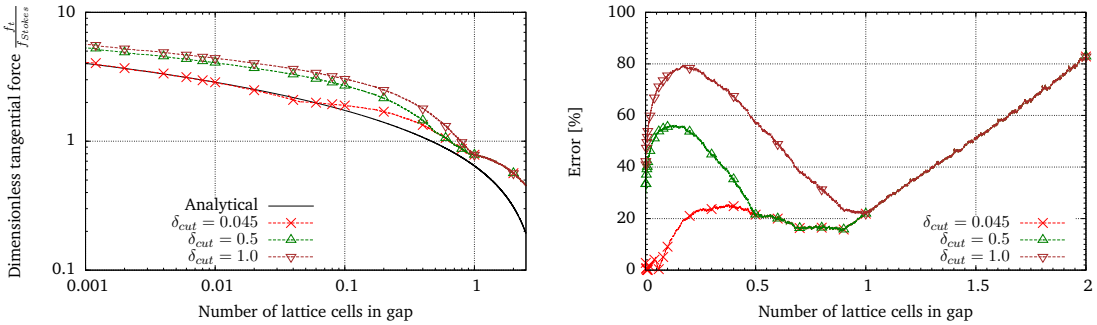

Fig. 4.15.: Modified lubrication force correction for rotational interactions. Dashed lines represent actual simulation results where the corresponding symbols represent selective data points for visual guidance.

In figure 4.15a, the force over the gap distance is depicted for a varied calibration cut-off parameter δ_{cut}. Similar to the correction for interactions due to relative tangential motion, a calibration parameter close to $\delta_{cut} = 1$ leads to a huge overestimation of the lubrication force, i.e. nearly 80% in the worst case (cf. Fig. 4.15b). A tremendously smaller cut-off has to be choosen to obtain a more accurate lubrication description for small gap distances, i.e. $\delta_{cut} \approx 0.045$.

Very similar for a torque correction, depicted in figure 4.16a for torque over gap distance and in figure 4.16b as difference to the analytical solution in per cent, larger cut-offs

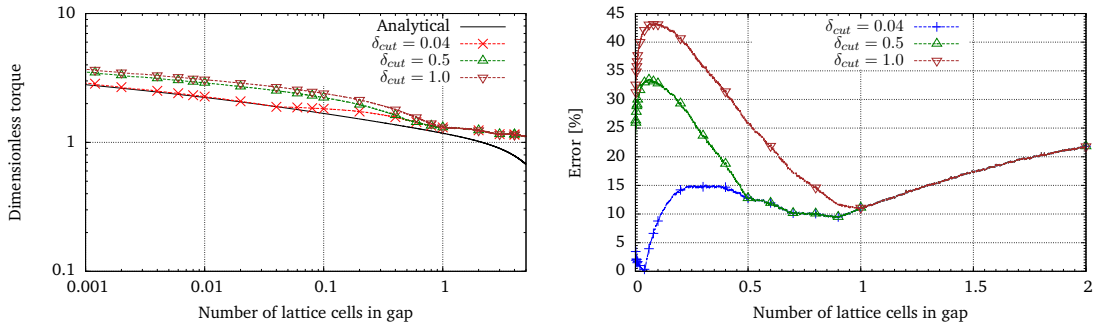

(a) (b)

Fig. 4.16.: Modified lubrication torque correction for rotational interactions. Dashed lines represent actual simulation results where the corresponding symbols represent selective data points for visual guidance.

results in huge discrepancies and a very small calibration parameter of $\delta_{cut} \approx 0.04$ leads to small discrepancies for small gap distances.

4.4 Conclusions

Analytical solutions for the lubrication force contributions can be used to determine a lubrication correction for resolved LBM when gap distances are too small to properly resolve the interstitial fluid flow. The lubrication force correction, the difference between analytical solution and hydrodynamic interaction force obtained for the smallest resolvable gap distance, is imposed on the particles as an additional force. The applicability of such a lubrication correction for a partially saturated cell method is investigated.

It is found that accurate simulation of the lubricated interactions between two particles depends on the chosen single relaxation parameter. For the investigated methodology, the optimal relaxation parameter range lies between $\tau = [0.65 - 0.7]$ to reduce discrepancies to the analytical solution of the normal lubrication force contribution. Other lubrication contributions, force and torque due to tangential relative motion between the particles, are difficult to study and determined discrepancies to the analytical solutions seem to be larger than for the normal contribution. However, the normal lubrication force contribution is of several orders in magnitude larger than other contributions. Hence, an accurate lubrication force model for the normal lubrication force contribution is of higher significance and a rough modeling approach for other contributions could be thus justified.

Employment of aforementioned lubrication force correction shows significant overestimations of the normal lubrication forces. Modification of the lubrication force correction by slightly shifting the outer cut-off to smaller values than a gap distance of one lattice cell width leads to an improvement in modelling the normal lubrication

force. However, careful calibration of the shifted cut-off distance is required. Similarly, the lubrication correction for the lubrication force and torque due tangential relative or rotational motion of the particles can be modified to obtain an improved lubrication force model.

5 A comparison study between DEM and LBDEM for simulation of dense suspensions

5.1 Introduction

Kulkarni and Morris (2008) and Haddadi and Morris (2014) performed simulations of suspensions under simple shear with a coupled LBDEM approach, proposed by Ladd (1994a) and Ladd (1994b), to study inertial effects on the suspension rheology and microstructure. The suspensions of low solid fractions, $\phi \leq 0.35$, were sheared for varying Reynolds numbers between $0.005 \leq Re \leq 5$. Kulkarni and Morris (2008) and Haddadi and Morris (2014) show that with increasing Reynolds number, i.e. increasing inertia, the microstructure, characterised by a pair distribution function, changes although the effect of inertia is diminished for higher solid fractions. Furthermore, it is shown by Haddadi and Morris (2014) that for low Reynolds number flows the stresslet contribution is the largest bulk stress contribution whereas the other contributions, Reynolds and acceleration stresses, become important for Reynolds number of $\mathcal{O}(Re \geq 1)$.

However, simulations employing a LBDEM coupling to simulate suspensions are expensive. Hence, some studies applied therefore only a DEM solver with additional models to imitate hydrodynamic and lubrication interactions without any coupling to a fluid resolving solver, e.g Andreotti et al. (2012), Ness and Sun (2015) and Trulsson et al. (2017). Although LBDEM simulations by Kulkarni and Morris (2008) and Haddadi and Morris (2014) indicate that inertia, and hence avoidance of a coupling, could be avoided for low Reynolds number flows, especially for high solid fractions, only Gallier et al. (2018) compared very recently DEM simulations to simulations employing a fictitious domain method (FDM) to solve for Stokes equations describing the fluid flow around suspended particles. Gallier et al. (2018) found that obtained suspension viscosities between both modelling approaches are effectively the same. However, it is moreover shown that the underlying microstructures between DEM and FDM differs for pair correlation functions, velocity correlations, and diffusion coefficients for lower solid fractions. Yet, for higher solid fractions, found microstructures are very similar.

In this chapter, intermediate to dense suspensions in a low Reynolds number regime are simulated with the LBDEM coupling, extensively discussed in the previous chapter, and

with DEM employing additional models for hydrodynamic fluid-solid drag and lubrication interactions. At first, two lubrication model formulations are compared with regard to obtained viscosities and stress contributions. Thereafter, results obtained with one of the lubrication force modelling approaches are compared to LBDEM simulation results. Comparison between DEM and LBDEM is performed for viscosities, stress contributions, normal stress differences, and velocity profiles.

5.2 Methodology

5.2.1 Discrete element method

By employing a discrete element method (DEM), e.g. Cundall and Strack (1979), the motion of a particle is determined by solving Newton's second law. A velocity-Verlet algorithm is used to determine the translational and angular velocities as well as the location of a particle. Various particle-particle interactions can be considered in the total force acting on the particle. Thereby, the equation describing the translational motion reads here:

$$m_i \frac{\partial \mathbf{x}_i^2}{\partial^2 t} = \mathbf{F}_i = \mathbf{F}_i^C + \mathbf{F}_i^H + \mathbf{F}_i^L \ . \tag{5.1}$$

Similarly for the angular motion:

$$\mathbf{J}_i \frac{\partial \omega_i}{\partial t} = \mathbf{T}_i = \mathbf{T}_i^C + \mathbf{T}_i^H + \mathbf{T}_i^L \ , \tag{5.2}$$

where mass, position, moment of inertia and angular velocity of particle i are described by m_i, $\mathbf{x}_i$, $\mathbf{J}_i$ and ω_i, respectively. The included forces $\mathbf{F}$ and torques $\mathbf{T}$ on a particle consist of a mechanical contact when particles overlap ($\mathbf{F}^C$ and $\mathbf{T}^C$), a lubrication interaction when particles are in close proximity to each other resulting in a mutual influence through the surrounding fluid ($\mathbf{F}^L$ and $\mathbf{T}^L$), and a hydrodynamic interaction between particle and fluid ($\mathbf{F}^H$ and $\mathbf{T}^H$).

5.2.1.1. Mechanical contact

The basic mechanical contact between particles is modelled through a spring-dashpot model in normal as well as tangential contact direction. A multitude of models, such as a Hooke or Hertz model, exist to describe the particle-particle contact, e.g. Luding (1998) and Herrmann and Luding (1998). A Hooke model is chosen which leads in normal contact direction between particles with the relative velocity $\mathbf{u}$ to the force

$$\mathbf{F}_n^C = k_n \boldsymbol{\delta}_n + \gamma_n \mathbf{u}_{rel,n} \tag{5.3}$$

and in tangential direction with a history dependent tangential overlap $\boldsymbol{\delta}_t$ to

$$\mathbf{F}_t^C = k_t \boldsymbol{\delta}_t + \gamma_t \mathbf{u}_{rel,t} \; . \tag{5.4}$$

The spring stiffness in normal and tangential direction is k_n and k_t, respectively. The damping coefficient in normal direction is expressed as γ_n and in tangential direction as γ_t. The damping coefficients are chosen to be $\gamma_n = \gamma_t = 0$ due to the already existing dissipation caused by lubrication interactions between particles. The tangential spring stiffness is chosen in dependence of the normal spring stiffness, $k_t = \frac{2}{7} k_n$, according to Schäfer et al. (1996).

Additional to the elastic-dissipative mechanical contact, friction between particles can be considered on basis of a Coulomb friction criterion. A variety of Coulomb-based friction criteria exist, e.g. Cundall and Strack (1979), Herrmann and Luding (1998) and Schäfer et al. (1996). Each of the suggestions link friction, normal and tangential force via a Coulomb criteria differently. However, for a contact without a dashpot model, as it is here by setting the damping coefficients to zero, the different friction models lead to the same criterion which reads then:

$$|\mathbf{F}_t^C| \leq |\mu_r \mathbf{F}_n^C| \; , \tag{5.5}$$

where the force tangential to the particle-particle contact, is limited by the product of coefficient of friction μ_r and absolute contact normal force.

5.2.1.2. Hydrodynamic interactions in DEM

Particles immersed in a fluid can have a mutual influence on their motion through hydrodynamic forces due to relative velocities between the particles itself and betweem the particles and fluid. A vast amount of work has been carried out to understand and describe lubrication interactions between particles, e.g. Jeffrey and Onishi (1984), Jeffrey (1992) and Kim and Karrila (2005).

Instead of considering all possible lubrication interactions for all particles, as it is performed for Stokesian dynamics, lubrication effects are introduced as a pure two-particle-particle interaction when the gap distances between both interacting particles falls below a predefined threshold, henceforth described as outer cut-off $\delta_{c,o}$. Therefore, the lubrication interaction between two particles can be expressed in a grand-resistance-matrix

(GRM) notation, e.g. Jeffrey and Onishi (1984), Jeffrey (1992) and Kim and Karrila (2005), as:

$$\begin{pmatrix} \mathbf{F}_1 \\ \mathbf{F}_2 \\ \mathbf{T}_1 \\ \mathbf{T}_2 \\ \mathbf{S}_1 \\ \mathbf{S}_2 \end{pmatrix} = \eta_f \begin{pmatrix} \mathbf{A}_{11} & \mathbf{A}_{12} & \tilde{\mathbf{B}}_{11} & \tilde{\mathbf{B}}_{12} & \tilde{\mathbf{G}}_{11} & \tilde{\mathbf{G}}_{12} \\ \mathbf{A}_{21} & \mathbf{A}_{22} & \tilde{\mathbf{B}}_{21} & \tilde{\mathbf{B}}_{22} & \tilde{\mathbf{G}}_{21} & \tilde{\mathbf{G}}_{22} \\ \mathbf{B}_{11} & \mathbf{B}_{12} & \mathbf{C}_{11} & \mathbf{C}_{12} & \tilde{\mathbf{H}}_{11} & \tilde{\mathbf{H}}_{12} \\ \mathbf{B}_{21} & \mathbf{B}_{22} & \mathbf{C}_{21} & \mathbf{C}_{22} & \tilde{\mathbf{H}}_{11} & \tilde{\mathbf{H}}_{12} \\ \mathbf{G}_{11} & \mathbf{G}_{12} & \mathbf{H}_{11} & \mathbf{H}_{12} & \mathbf{M}_{11} & \mathbf{M}_{12} \\ \mathbf{G}_{21} & \mathbf{G}_{22} & \mathbf{H}_{21} & \mathbf{H}_{22} & \mathbf{M}_{21} & \mathbf{M}_{22} \end{pmatrix} \begin{pmatrix} \mathbf{v}^{\infty}(\mathbf{x}_1) - \mathbf{u}_{p,1} \\ \mathbf{v}^{\infty}(\mathbf{x}_2) - \mathbf{u}_{p,2} \\ \boldsymbol{\omega}^{\infty} - \boldsymbol{\omega}_{p,1} \\ \boldsymbol{\omega}^{\infty} - \boldsymbol{\omega}_{p,2} \\ \mathbf{E}^{\infty} \\ \mathbf{E}^{\infty} \end{pmatrix} . \tag{5.6}$$

The tensor elements in the resistance matrix determine the force on one particle in dependence of itself and the other particle. Hence, the tensor notation of the resistance elements, such as $\mathbf{A}_{11}$ or $\mathbf{A}_{12}$, have to be understood that the first subscript gives the particle on which force, torque, or stresslet act in dependence of the particle stated by the second subscript. Here only force and torque on two interacting particles are evaluated with the GRM. Instead of determining the separate stresslet values $\mathbf{S}_1$ and $\mathbf{S}_2$ via lengthy GRM computations to evaluate the particle stress, the particle stress can be determined from the forces itself as is discussed in the subsequent section 5.2.1.3.

Computation of the lubrication interactions with the GRM and resistance matrices provided by Kim and Karrila (2005) lead to force and torque contributions arising from translational and angular relative velocities between particles and fluid as well as a contribution from the strain rate tensor. The details of the GRM evaluation and the final expressions for force and torque, which were implemented into LIGGGHTS, can be found in the appendix B. However, the GRM can be also re-written by substituting all relevant resistance matrices and simplifying lengthy expressions under the assumption that for close gap distances between particles the fluid velocities on the closest particle surfaces are approximately the same. Thereby, the GRM reduces to lubrication expressions based only on the relative velocity between two interacting particles and without background fluid velocity components or explicit strain rate contributions. Fluid or strain components are indirectly considered within the simplified expressions for forces due to normal collision, relative tangential and angular velocities as well as torques due to relative tangential and angular velocities. The simplifications were deduced by my colleague Rangarajan Radhakrishnan and implemented into LAMMPS. Both, deductions and code were made publicly available by Radhakrishnan (2018). I implemented the above GRM model (5.6) into LIGGGHTS. My contributions with regard to the simplified GRM work was limited to LAMMPS coding support, code verification support, and conversion of the LAMMPS code files for use with LIGGGHTS. The simplified expressions read for the force on a particle:

$$\mathbf{F} = \eta_f \Big[X_A^{11} \mathbf{u}_{p,rel,n} + Y_A^{11} \left(\mathbf{u}_{p,rel,t} - (r_{p,1} + r_{p,2})(\boldsymbol{\omega}_s \times \mathbf{e}) \right) + \frac{1 - \gamma(1+4\gamma)}{4+\gamma} Y_B^{11} \left(\boldsymbol{\omega}_d \times \mathbf{e} \right) \Big] , \tag{5.7}$$

where $\boldsymbol{\omega}_s = (\boldsymbol{\omega}_{p,1} + \boldsymbol{\omega}_{p,2})/2$, $\mathbf{w}_d = (\boldsymbol{\omega}_{p,1} - \boldsymbol{\omega}_{p,2})/2$, and $\mathbf{u}_{p,rel,n}$ and $\mathbf{u}_{p,rel,t}$ are the normal and tangential component of the relative velocity $\mathbf{u}_{p,rel} = \mathbf{u}_{p,2} - \mathbf{u}_{p,1}$ between particles 1 and 2. γ describes the particle size ratio between particles 1 and 2. In Eq. (5.7), the first term describes lubrication forces in normal collision direction, the second term is due to relative tangential shearing motion of two particles and the last term represent the lubricated interactions due to particle rotation. The simplified lubrication torque expression can be written as:

$$\mathbf{T} = \eta_f \Big[Y_B^{11} \left(\mathbf{u}_{p,rel} \times \mathbf{e}\right) + (r_{p,1} + r_{p,2})(\boldsymbol{\omega}_s - (\boldsymbol{\omega}_s \cdot \mathbf{e})\mathbf{e}) \\ + Y_C^{12} \left(1 - \frac{4}{\gamma}\right) (\boldsymbol{\omega}_d - (\boldsymbol{\omega}_d \cdot \mathbf{e})\mathbf{e}) \Big] , \quad (5.8)$$

where the first term arises due to shearing motion between particle surfaces and the second term stems from particle rotations. The resistance functions X_A^{11}, Y_A^{11}, Y_B^{11}, and Y_C^{12} are taken to the order of $log(\xi^{-1})$ with $\xi = \frac{h_{gap}}{r_p}$ from Kim and Karrila (2005).

In both cases, GRM and simplified GRM lubrication computation, only hydrodynamic interactions between particles are considered. A simple model to incorporate additionally a drag force from the relative fluid and particle motion can be based on the Stokes single sphere drag law so that it can be written for the hydrodynamic force

$$\mathbf{F}_{Stokes} = 6\pi\eta_f r_p (\mathbf{u}_f^{\infty}(\mathbf{x}_p) - \mathbf{u}_p) \quad (5.9)$$

and moreover for the hydrodynamic torque

$$\mathbf{T}_{Stokes} = 8\pi\eta_f r_p (\boldsymbol{\omega}_f^{\infty}(\mathbf{x}_p) - \boldsymbol{\omega}_p) \, . \quad (5.10)$$

The fluid rotation is $\boldsymbol{\omega}_f^{\infty}(\mathbf{x}_p) = \frac{1}{2}\left(\nabla \times \mathbf{u}_f^{\infty}(\mathbf{x}_p)\right)$ and for a sheared system, a linear velocity profile for the fluid velocity can be assumed, i.e. the only non-zero components for the strain rate tensor are $E_{xy} = E_{yx} = \frac{1}{2}\dot{\gamma}$.

5.2.1.3. Stress evaluation

The total bulk stress is decomposed into different contributions: Mechanical particle-particle contact stress σ^C and contributions based on the lubrication force σ^L. For interparticle forces, such as contact forces or lubrication forces, the stress computation can be performed for rigid particles according to Thompson et al. (2009) as:

$$\sigma^C = \frac{1}{V} \sum_i \sum_j r_{ij} \mathbf{F}_{ij}^C \quad (5.11)$$

and

$$\sigma^L = \frac{1}{V} \sum_i \sum_j r_{ij} \mathbf{F}_{ij}^L \,, \tag{5.12}$$

where $\mathbf{r}$ is the connecting vector between the interacting particles while pointing from particle j to i. A single sphere Stokes drag force, as discussed in the previous section, should be also considered in the stress evaluation for which the stresslet could be expressed according to the single sphere stresslet (e.g. Guazzelli and Morris (2012)):

$$S_{ij} = -\frac{20}{3} \pi \eta_f r_p^3 E_{ij}^{\infty} \,. \tag{5.13}$$

5.2.2 Lattice Boltzmann method

As discussed above, a single sphere Stokes drag force can be imposed in pure DEM simulations employing a pairwise lubrication model. However, it is not entirely clear how this modelling approach affects sheared simulations of dense suspensions and how it is justified. Therefore, the goal is to resolve the fluid flow around the particles by means of a lattice Boltzmann method (LBM) which is coupled to DEM for comparison.

In the LBM, fluid molecules are statistically described by a particle distribution function $f(\mathbf{x}, \mathbf{u}, t)$ which gives the fluid molecules with velocity $\mathbf{u}$ at the location $\mathbf{x}$ at time t. The spatial and temporal evolution of the distribution function is described by the Boltzmann equation and a discretisation with regard to velocities, space and time leads to the lattice Boltzmann method. The discrete distribution function $f_i(\mathbf{x}, t))$ is subject to a collision on the lattice nodes, i.e. relaxation towards a local equilibrium function $f_i^{eq}(\mathbf{x}, \mathbf{u}, t)$, and a streaming step at which the distribution functions are moved along pre-defined paths with the velocities $\mathbf{c}_i$ towards neighbouring lattice nodes.

The simplest collision step, Bhatnagar-Gross-Krook (BGK) collision after Bhatnagar et al. (1954), relaxes the distribution function towards an equilibrium distribution function f_i^{eq} over a single relaxation parameter τ:

$$\Omega_i^{BGK} = \frac{\Delta t}{\tau} (f_i^{eq}(\mathbf{x}, \mathbf{u}, t) - f_i(\mathbf{x}, t)) \,. \tag{5.14}$$

Combination of the streaming and BGK collision step leads to the lattice Boltzmann equation:

$$f_i(\mathbf{x} + \mathbf{c}_i \Delta t, t + \Delta t) = f_i(\mathbf{x}, t) + \Omega_i^{BGK} \,. \tag{5.15}$$

Taking the zeroth and first moments of the distribution functions yields macroscopic fluid density $\rho = \sum_i f_i(\mathbf{x}, t)$ and fluid momentum $\rho \mathbf{u} = \sum_i f_i(\mathbf{x}, t) \mathbf{c}_i$. The macroscale conservation equations, inter alia the Navier-Stokes equations, can be obtained from the lattice Boltzmann equation (5.15). The detailed derivation can be found elsewhere, e.g.

Succi (2001) and Krüger et al. (2017), and it shall be here only noted that the relaxation parameter τ is linked in this process to the fluid viscosity by $\nu = (\tau - 0.5)/3$.

5.2.2.1. Fluid-solid coupling

The hydrodynamic interaction between fluid and particles can be achieved by various methods. Here, a fluid-solid coupling proposed by Noble and Torcyznski (1998), which is analysed in the previous chapters 3 and 4, is used.

In essence, an additional collision term Ω^s is introduced to consider interactions between particle distribution functions and a particle on a lattice node. The fluid and solid phase are differentiated by a weighting function for the solid phase which leads to the modified LBM equation:

$$f_i(\mathbf{x} + \mathbf{c}_i\Delta t, t + \Delta t) = f_i(\mathbf{x}, t) + \left(1 - \sum_s B(\mathbf{x}, \tau)\right) \Omega_i^{BGK} + \sum_s B(\mathbf{x}, \tau)\Omega_i^s \,. \tag{5.16}$$

The solid collision term reads:

$$\Omega_i^s = f_i^{eq}(\mathbf{u_s}) - f_i + \left(1 - \frac{\Delta t}{\tau}(f_i - f_i^{eq}(\mathbf{u})\right) \,. \tag{5.17}$$

For the weighting function, a linear relationship to the lattice node solid fraction ε_s, describing the overlap between particle and lattice node, is chosen:

$$B(\mathbf{x}, \tau) = \varepsilon_s \,. \tag{5.18}$$

The hydrodynamic force and torque on a particle can be obtained by summation of the solid phase collision term multiplied by the lattice velocities over all lattice nodes covered by a particle, i.e.:

$$\mathbf{F}^H = \frac{h^d}{\Delta t} \sum_n B_n \sum_i \Omega_i^s \mathbf{c}_i \,, \tag{5.19}$$

and

$$\mathbf{T}^H = \frac{h^d}{\Delta t} \sum_n (\mathbf{x} - \mathbf{x}_s) \times \left(B_n \sum_i \Omega_i^s \mathbf{c}_i\right) = \frac{h^d}{\Delta t} \sum_n (\mathbf{x} - \mathbf{x}_s) \times \mathbf{F}^H \,, \tag{5.20}$$

where h is the lattice spacing in d dimensions.

5.2.2.2. Lubrication correction

The LBM has a limited fluid flow resolution due to the lattice size which means that lubrication forces between particles can be only resolved to particle-particle gap distances

of around one lattice cell width. For smaller gap distances a lubrication force correction is necessary to model the hydrodynamic particle-particle interactions. Therefore the lubrication force correction discussed in the previous chapter in employed. The correction is limited to normal lubrication forces and neglects other contributions due to their small overall contribution in comparison to normal lubrication forces as shown in the previous chapter 4. The normal lubrication force correction from previous chapter, which is added to equation (5.1), reads:

$$\mathbf{F}^{L}_{\alpha,correction}(\gamma,\xi) = \mathbf{F}^{L}_{\alpha}(\gamma,\xi) - \mathbf{F}^{L}_{\alpha}(\gamma,\delta_{cut}\xi_N)\ ,\ \text{for}\ \xi \leq \delta_{cut}\xi_N = \delta_{cut}h_{lattice}\ , \tag{5.21}$$

where γ is the particle size ratio, $\xi = \frac{h_{gap}}{r_p}$ the dimensionless gap distance and $\delta_{cut} = 0.75$ is a cut-off calibration parameter for the lubrication force correction based on the findings in the previous chapter.

5.2.2.3. Stresslet calculation

As shown in chapter 3, the stresslet in LBM can be computed from the hydrodynamic lattice forces F^{LBM} (cf. eq (5.19)) by summing over all particle covered lattice nodes and particles:

$$\begin{aligned}\sigma_{ij,stresslet} &= -\frac{1}{V}\sum\int_{A_p}\frac{1}{2}\left(\sigma_{ik}x_j + \sigma_{jk}x_i\right)n_k dA \\ &= -\frac{1}{V}\sum^{N_{particles}}\sum^{N_{nodes}}\left(\frac{1}{2}(F^{LBM}_{ik}x_j + F^{LBM}_{jk}x_i)\right)\ ,\end{aligned} \tag{5.22}$$

where the vector x_i points from particle centre to the lattice node on which F^{LBM} acts. The negative sign is chosen to make the stresslet computation consistent to the stresses stemming from particle-particle interactions as in Eqs. (5.11) and (5.12).

5.3 Results

A comparison study between the aformentioned LBDEM coupling and different DEM models to simulate dense suspensions under simple shear was carried out. Lees-Edwards boundary conditions (LEbc) for LBM, cf. Wagner and Pagonabarraga (2002), and for DEM conceptually equivalent boundary conditions to LEbc, cf. Lees and Edwards (1972), were imposed on a three dimensional periodic domain as it is depicted on a slice on the x-y-plane through the simulation domain in figure 5.1. The fluid velocity component in sheared direction $u_{f,x}$ is depicted in the right illustration in figure 5.1 with the corresponding particle distribution in the left illustration. The particle distribution was bi-disperse with a diameter ratio of $\frac{d_{p,2}}{d_{p,1}} = 1.4$, which is commonly used in the literature to avoid crystallisation, and a volume ratio of $\frac{V_{p,2,tot}}{V_{p,1,tot}} = 1$. In comparison to a mono-disperse

system, a bi-disperse particle system is expected to have a jamming point at higher solid fractions due to geometrical constraints. The total particle number was fixed and different solid fractions were obtained by varying the domain size where for the maximum studied solid fraction $\phi_{max} = 0.65$ a minimum domain size of $\left[\frac{L_x}{d_{p,2}} \times \frac{L_y}{d_{p,2}} \times \frac{L_z}{d_{p,2}}\right] = [10 \times 10 \times 10]$ was chosen to minimise boundary condition effects and thereby resulting in over 2000 total particles. The applied shear rate was determined so that a low-Reynolds number regime $Re = \frac{\dot{\gamma} d_{p,1}^2}{\nu_f} = 0.1$ was obtained. The particles were neutrally buoyant due to equal fluid and particle density, thereby resulting in the Stokes number being identical to the Reynolds number.

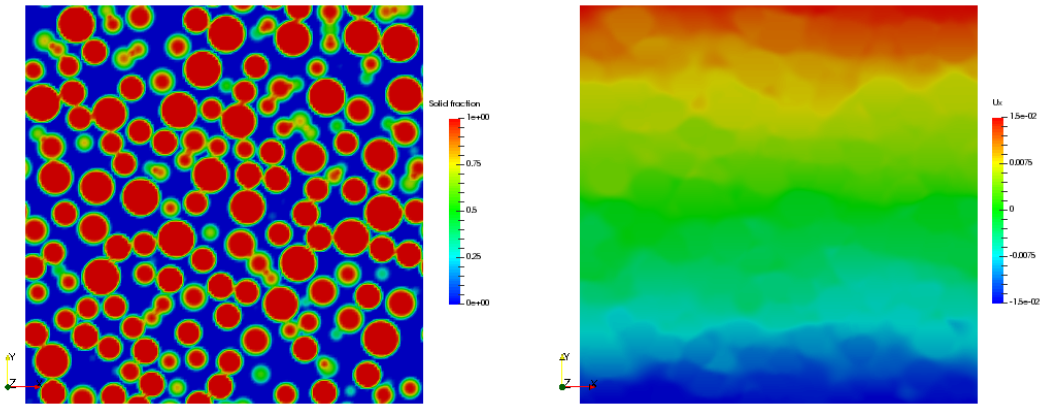

Fig. 5.1.: Slice through a LBDEM simulation of a sheared suspension with Lees-Edwards boundary conditions showing particle distribution on the left with $\phi = 0.5$ and corresponding fluid velocity in sheared direction for $Re = 0.1$ on the right.

5.3.1 Lubrication force modelling and cut-off choice

Davis et al. (2003) show that particle contacts due to particle surface roughness influence suspension dynamics. The inner cut-off $\delta_{c,i}$ of the lubrication models could be interpreted as a particle property parameter describing particle surface asperities leading to a breakdown of the lubrication force increase due to solid-solid particle contact when gap distances are comparable to the surface asperities. Thus, the inner lubrication cut-off could be chosen according to typical asperity sizes which were for example determined by Smart and Leighton Jr. (1989) who found asperities to be the size of 10^{-2} to 10^{-3} particle radii. Although asperity sizes are material dependent, the values provided by Smart and Leighton Jr. (1989) are used as an orientation to choose cut-off distances. Therefore, the simplified GRM model was used with varied inner and outer cut-offs to estimate the influence on the suspension rheology. The cut-off values lay between $0.0001 d_{eff}$ and $0.01 d_{eff}$ where $d_{eff} = \frac{d_1 d_2}{d_1 + d_2}$. The obtained suspension viscosities for varied cut-offs are shown in figure 5.2 over a solid fraction range $0.475 \leq \phi \leq 0.65$ for frictionless particles. For an altered outer lubrication cut-off $\delta_{c,o}$ the obtained viscosities

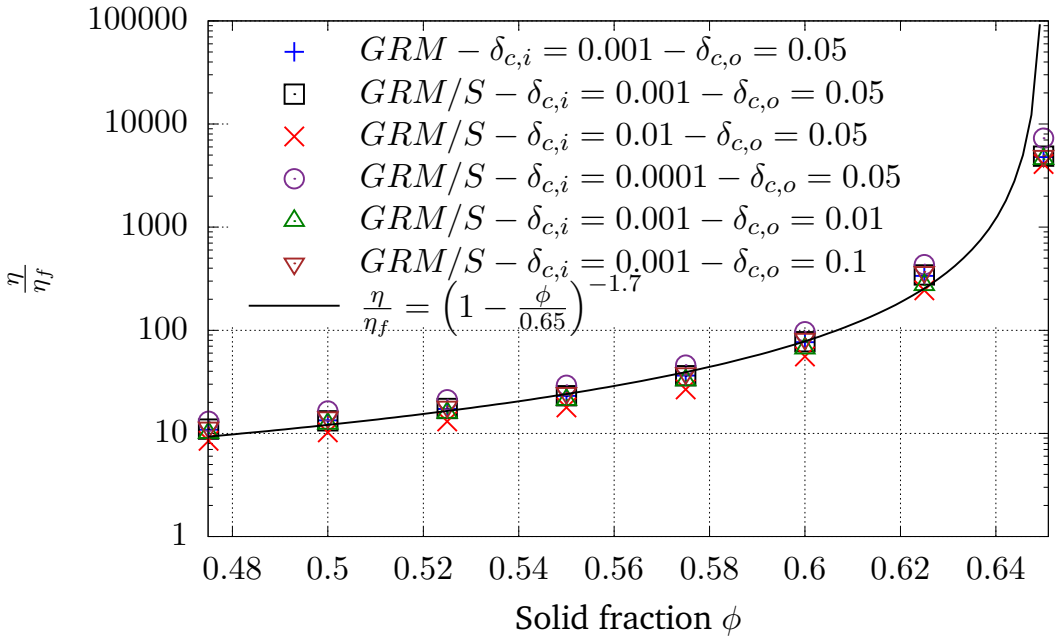

Fig. 5.2.: Comparison of suspension viscosities for different solid fractions between GRM and simplified GRM models with different lubrication cutoff choices for low Reynolds number sheared dense suspensions.

differ barely as the lubrication interactions change only marginal. However, a change in the inner cut-off leads to somewhat larger variations in the obtained suspension viscosities. An increase in the inner cut-off, limiting the lubrication forces towards larger gap distances, yields decreased suspension viscosities in comparison to a decrease of the inner cut-off which leads to observable higher viscosity values. The results are compared to the Krieger-Dougherty correlation $\frac{\eta}{\eta_f} = \left(1 + \frac{\phi}{0.65}\right)^{-1.7}$ where maximum packing fraction is set to $\phi_{max} = 0.65$ and the exponent is interpolated from the results obtained with the simplified GRM model where $\delta_{c,o} = 0.05$ and $\delta_{c,i} = 0.001$.

The GRM and simplified GRM model lead for the same cut-off distances, $\delta_{c,o} = 0.05 d_{eff}$ and $\delta_{c,i} = 0.001 d_{eff}$, to effectively the same viscosities as shown in Fig. 5.2. Differences between the models can be seen by comparison of separate stress contributions over the same solid fraction range. The separated contributions, non-dimensionalised by the Newtonian fluid stress, are shown in figure 5.3a for the GRM model and in figure 5.3b for the simplified GRM model. In both figures, the various stress contributions are a product of relative particle-particle motion in normal and tangential direction as well as relative rotational motion. Furthermore, a stresslet contribution, Eq. (5.13), is included due to the imposed Stokes drag. For the GRM model an additional strain contribution, stemming from the strain rate tensor in Eq. (5.6), is considered. The simplified GRM model contains implicitly the strain contribution in the other lubrication force formulations, such as for the normal, tangential, or rotational contribution, due to the simplifications. All obtained contributions from the simplified GRM model are negative. The contact stress increases

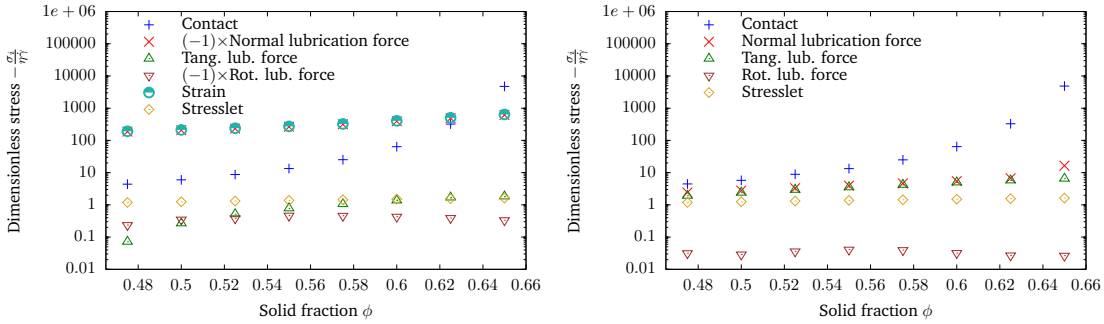

(a)GRM **(b)**GRM/S

Fig. 5.3.: Stress contributions obtained from the GRM, (a), and simplified GRM models, (b), from corresponding simulations in Fig. 5.2.

and turns into the dominating contribution with increasing solid fraction whereas the normal and tangential lubrication contributions, which are comparable to each other in magnitude for all solid fractions, increase only slightly. The stresslet contribution is similar in its magnitude to the normal and tangential contribution for lower solid fraction values, but is nearly unchanged for varying solid fractions. The rotational lubrication stress contribution is much smaller than all other contributions for the whole investigated solid fraction range.

In comparison to the simplified GRM model, contributions from the GRM model are different in two aspects for all solid fractions - namely the changed sign of the stresses for the normal as well as the rotational lubrication component, indicated by the multiplication with (-1) in the legend, and futhermore, the huge difference in the magnitude of the normal lubrication stress contribution between GRM and simplified GRM.

The opposite sign of the normal lubrication stress contributions between the GRM and simplified GRM model could be explained by the different reference points in both models. Therefore, a closer look at the contact stress contribution is helpful because the contact forces in the simulations here are always repulsive due to pure repulsive elastic force. As above mentioned, the contact stress is here for a positive shear direction and steady-state always negative. By definition of the stress in Eq. (5.11), the particle-particle connecting vector $\mathbf{r}$ points towards the centre of the currently considered particle for which the stress is computed. Thus, the product of $r_x F_y^C$ giving the shear stress σ_{xy}^C is always negative. Yet, lubrication forces depend also on the particle and fluid velocities in contrast to the contact model which depends only on the stiffness and particle overlaps. Comparison of the lubrication force models, Eqs. (5.6) and (5.7), shows that the difference between the lubrication models is mostly in the considered velocities. In the simplified GRM model, only the relative particle-particle velocities are considered, i.e. $\mathbf{u}_{p,rel} = \mathbf{u}_{p,2} - \mathbf{u}_{p,1}$. For the GRM model however, the fluid velocity is also part of the force fomula, i.e. $\mathbf{v}^{\infty}(\mathbf{x}_1) - \mathbf{u}_{p,1}$ and $\mathbf{v}^{\infty}(\mathbf{x}_2) - \mathbf{u}_{p,2}$. This leads to two different reference points. The reference frame for the simplified GRM model is locally with the particles whereas the global system

is the reference frame in the GRM model. Hence, the normal lubrication force of the simplified GRM model corresponds basically to the sum of the normal lubrication force and a strain rate force of the GRM model. In fact, in the derivation of the simplified expressions of the lubrication interactions, Radhakrishnan (2018) combined the strain rate contributions with all other contributions to obtain the final equations in (5.7) and (5.8). With regard to the obtained shear stress contributions from simulations employing the GRM model, the stress magnitude of the strain contribution is slightly larger than the normal lubrication force contribution of the GRM model. It could be shown that the summation of both contributions obtained from the simulations leads to very similar (negative) values obtained by the simplified GRM model for the normal lubrication stress contribution.

The huge magnitude of the normal lubrication contribution and strain rate contribution obtained with the GRM model could be also understood by the aforementioned explanation. As mentioned above, for the simplified GRM model the normal lubrication force corresponds to the sum of the normal lubrication force and force due to strain rate of the the GRM model. However, in the GRM force formulations of both components, normal lubrication force and force caused due to a strain rate tensor, the forces increase with $\frac{1}{\xi}$ in the leading order term over the dimensionless particle-particle gap distance ξ. In comparison, other lubrication contributions increase only with $log(\xi^{-1})$ in the leading order terms. This difference leads to the huge observed stress magnitudes when using the GRM model.

For high solid fractions, the particle-particle contact stress is the dominating contribution. Hence, it could be possibly argued that the linear Hooke contact model is too simple as particle asperity contact modelling might rather require a non-linear contact model (cf. Otsubo et al. (2017)). However, in the performed simulations the particles are assumed to be rigid and stiff by appropriate particle stiffness choice resulting in marginal particle overlaps. Moreover, it cannot only be separately looked at the mechanical particle-particle contact, but the fluid between particles should be additionally considered for low Stokes numbers, i.e. the actual combination of linear Hooke contact model and above lubrication interaction models results in a more complex contact model attempting to recreate elastohydrodynamic particle contacts.

5.3.2 Viscosity and stress contributions in low-Reynolds sheared suspensions

Similar to the above sheared suspension simulations at a low Reynolds number of $Re = 0.1$ were performed with the above described LBDEM coupling. Results are compared to DEM simulations for which henceforth only the simplified GRM model was

employed because no large overall differences in stress and viscosity values were found when compared to the GRM model.

5.3.2.1. Frictionless particles

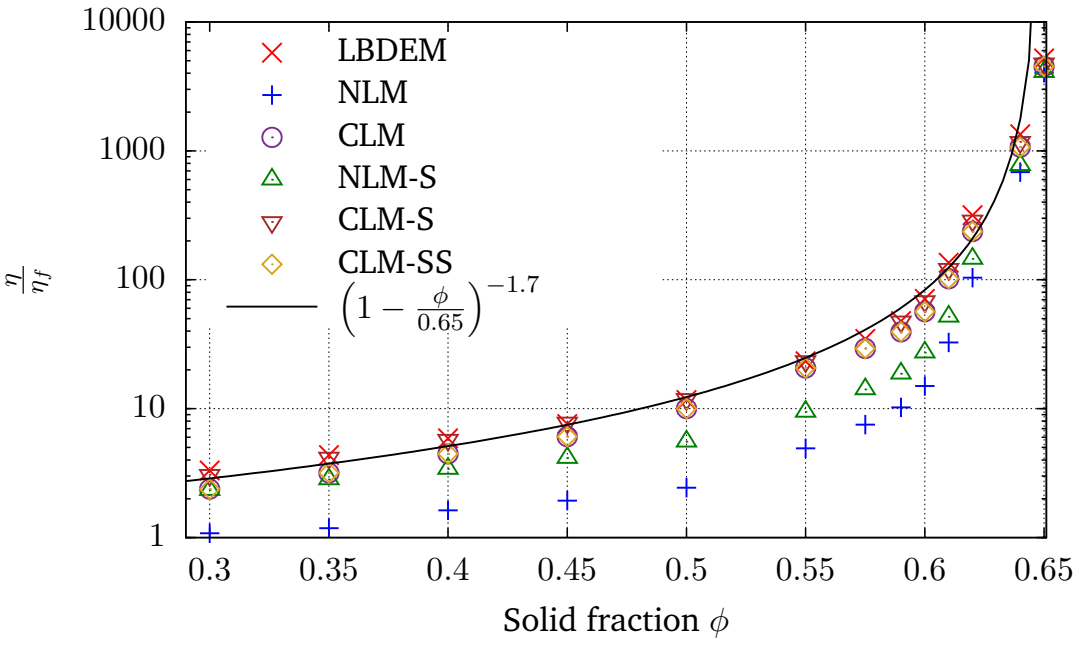

Fig. 5.4.: Frictionless suspension viscosity values for different solid fraction obtained from low Reynolds number sheared LBDEM and DEM simulations.

Initially, simulations without friction, i.e. Eq. (5.5) with $\mu_r = 0$, were conducted and the obtained suspension viscosities for varied solid fractions are shown in figure 5.4. The simulation results are compared to a semi-empirical Krieger-Dougherty correlation, Krieger and Dougherty (1959), i.e.:

$$\eta_s = \left(1 - \frac{\phi}{\phi_{max}}\right)^{-[\eta]\phi_{max}} , \tag{5.23}$$

where the exponent is usually around $[\eta]\phi_{max} \approx 2$, e.g. Krieger and Dougherty (1959) and Werff and Kruif (1989). The maximum solid fraction value $\phi_{max,frictionless} = 0.65$ and exponent $[\eta]\phi_{max} = 1.7$ by fitting to the LBM simulation results were determined. The fitted exponent $[\eta]\phi_{max} = 1.7$ is slightly lower than the usual mentioned $[\eta]\phi_{max} \approx 2$ exponents found in the literature. However, the fitting parameters, intrinsic viscosity and maximum solid fractions, can vary between experiments of different fluid or particle materials. Krieger and Dougherty (1959) report values of the intrinsic viscosity of $2.58 \leq [\eta] \leq 3.44$ which can lead with the here interpolated maximum packing fraction $\phi_{max,frictionless} = 0.65$ to exponents of $[\eta]\phi_{max} = 1.7$.

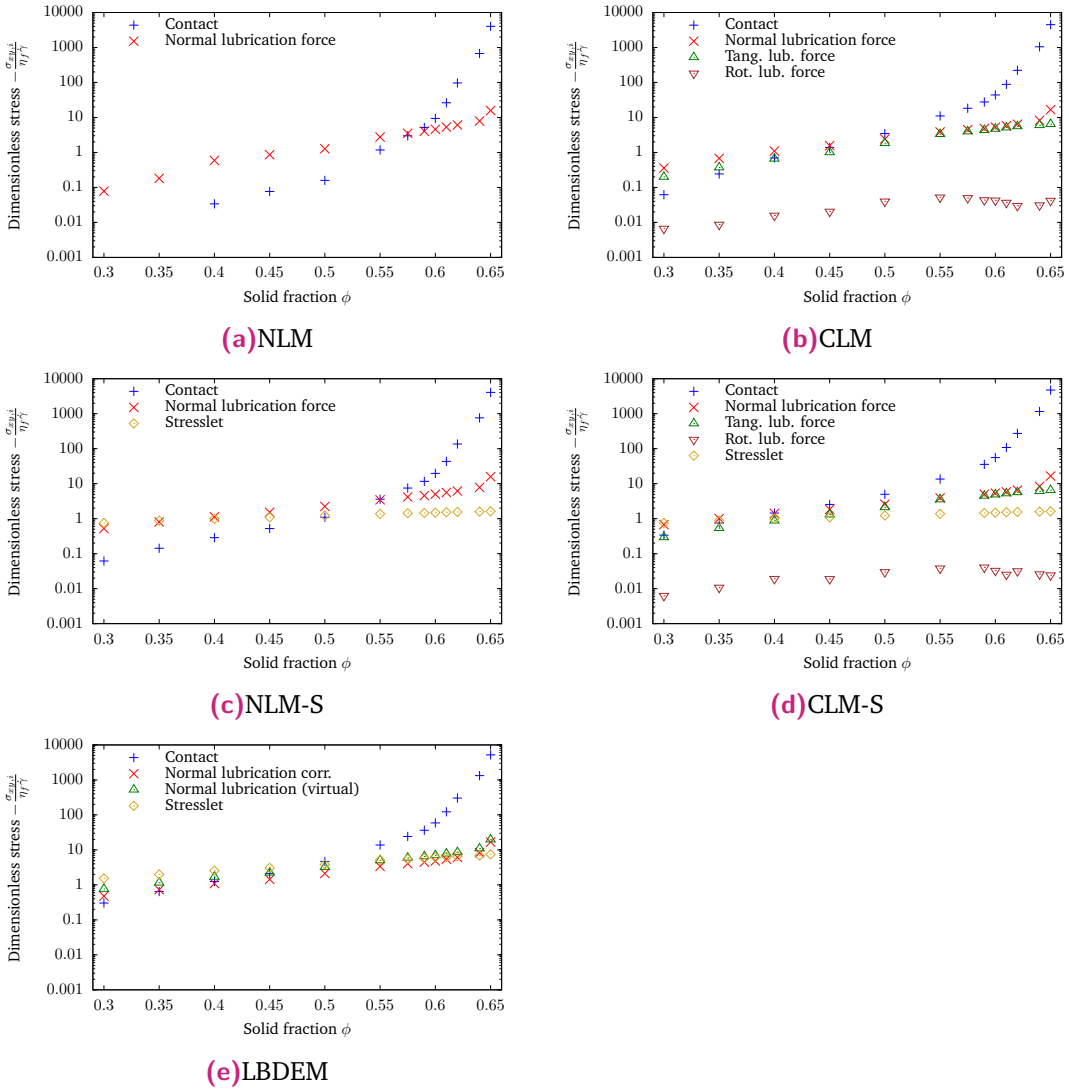

Fig. 5.5.: Various stress contributions from the different frictionless LBDEM and DEM simulations corresponding to Fig. 5.4.

The LBM simulations were performed with an additional correction for the lubrication force in normal direction of colliding particles as discussed in section 5.2.2.2. As discussed in the introduction section, various implementations of lubrication models exist in the literature. Hence, for comparison reasons to the LBDEM simulations and for assessement of different hydrodynamic modelling strategies, DEM simulations with different included hydrodynamic force components were performed. On one hand, only lubrication forces in normal collision direction without an additional Stokes drag (NLM) or with additional Stokes drag (NLM-S) were considered. On the other hand, a complete lubrication modelling approach, i.e. including all lubrication contributions, without Stokes drag (CLM) or with Stokes drag (CLM-S) were employed.

Employing only a normal lubrication force model for DEM (NLM), the obtained viscosities differ significantly to the LBM simulations for the whole investigated solid fraction range.

If the complete lubrication model (CLM), i.e. additional lubrication interactions for tangential and relative particle-particle motion, were employed , a drastic increase for all obtained viscosities is observed. However, a difference to the LBM simulation, especially large for the lower solid fraction range $0.3 \leq \phi \leq 0.45$, is found.

Performing the same simulations with an additional single sphere Stokes drag, Eqs. (5.9) and (5.10), and consideration of the single sphere stresslet, Eq. (5.13), for every particle, an improvement in the viscosity values for lower solid fractions is found. In particular for the complete lubrication force model including a Stokes drag (CLM-S), the obtained viscosity values fall nearly together with the LBM simulations which is in contrast to using only lubrication forces in normal directions of the particle-particle collisions with Stokes drag (NLM-S). Especially for higher solid fractions, a discrepancy between the partial NLM-S and complete CLM-S lubrication model are found where CLM-S leads to effectively the same viscosities as the LBM simulations.

Moreover, simulations were conducted for which all lubrication interactions without any Stokes drag model were considered, but the single sphere stresslet (5.13) was separately added to the total stress results (CLM-SS). A slight difference to the CLM-S and the LBM simulations is found for lower solid fractions, indicating a minor effect of the drag force model on the rheology. However, a greater agreement between the simulations results is observed for high solid fractions which is likely caused due to increased particle-particle interactions and hence less importance of accurate drag force modelling efforts.

The effect of the fluid drag and particle-particle interactions can be studied by examining the different stress contributions $\sigma_{xy,i}$ to the suspension viscosity which are presented in figure 5.5 for the various employed modelling combinations. The stress contributions, non-dimensionalised by the fluid stress, are separated into a contact stress, lubrication stress from different components (e.g. lubrication force in normal direction of particle-particle collisions), and stresslet. Lubrication interactions occur only for particles in close proximity and thus, the stresslet could be interpreted as a quantity arising from the drag force acting on the particles. As observed in the previous section, for all modelling approaches, DEM as well as LBDEM, the contact contribution grows with increasing solid fraction and is the dominating contribution for high solid fractions whereas lubrication interactions are of considerable significance for lower solid fractions.

However, employing a lubrication interaction in only normal collision direction (NLM and NLM-S model in Fig. 5.5a and 5.5c, respectively) in comparison to the complete lubrication description (CLM and CLM-S model in Fig. 5.5b and 5.5d, respectively) leads to quantitative differences in the stress contributions resulting in different viscosities. Interestingly, the inclusion of a Stokes drag for DEM modelling lead to seemingly increased contact and normal lubrication contributions, especially for the NLM model for low solid fractions where $\phi \leq 0.35$. This possibly indicates an enforced change in the

particle-particle interaction microstructure due to the imposed Stokes drag force. The effect of increased stress contributions due to introduction of a Stokes drag is found to be more pronounced for NLM than CLM modelling.

The Stokes drag force introduced in the DEM cases was considered as an additional stresslet contribution which is especially important for lower solid fractions. In fact, the viscosity difference for lower solid fractions in Fig. 5.4 is mostly a cause of the missing drag force and stresslet contribution. The minor stresslet change for varied solid fractions in the DEM case is a result of changed domain sizes which lead to slightly changed shear rates to obtain the same Reynolds number over the investigated solid fraction range.

In contrast to the DEM cases, the stresslet obtained from the LBM simulations is larger for the same solid fractions and a slightly steeper increase is found for an increasing solid fraction. The stresslet difference between DEM and LBDEM simulations is a result of the calibrated outer cut-off gap distances at which the lubrication force corrections for the LBM fluid-solid coupling are triggered. As it is discussed in chapter 4 for the LBDEM coupling, the resolution limit of the lubrication forces is theoretically around the size of one lattice cell, but for lubrication corrections for relative tangential and rotational motion between particles, the correction was shifted towards much smaller particle-particle gap distances. Due to the varying lubrication cut-offs, lubrication interactions from DEM do not necessarily convey the same information as the lubrication corrections from LBDEM simulations and some stress which would belong to the lubrication stresses in DEM are part of the stresslet in LBDEM simulations. Thus, in addition to the stress contribution from the normal lubrication force correction for LBDEM simulations, a "virtual" normal lubrication stress state was computed. "Virtual" means here that based on the particle dynamics in the LBDEM simulations, normal lubrication forces between particles were evaluated according to the simplified GRM model without actual consideration in the motion equation of the particles. Thereby, information about a normal lubrication stress state, corresponding to the simplified GRM model with the same cut-off choices as in the DEM simulations, could be obtained. Comparison between figures 5.5d and 5.5e as well as comparison of the normal lubrication correction and "virtual" normal lubrication stress state show that the stress from normal lubrication forces in LBDEM simulations is indeed slightly smaller than the stress from normal lubrication forces in DEM simulations.

Other lubrication interactions than the normal lubrication force in CLM-S simulations are contributions from relative tangential and rotational motion between particles. Albeit rotation of particles lead to no significant contributions, relative tangential motions produce stress contributions which are only marginable smaller than normal lubrication contributions. The LBDEM simulations here are not subject to relative tangential motion induced lubrication corrections because the calibrated corrections would be initiated at very small gap distances. Moreover, with regard to the inner cut-off, which limits the lubrication interactions, would lead to only small separate stress contributions

linked directly to the tangential corrections. However, a large part of the tangential lubrication contribution is indirectly accounted for in the LBDEM stresslet computation which ultimately leads to the observed larger stresslet values in LBDEM than in CLM-S simulations.

5.3.2.2. Frictional particles

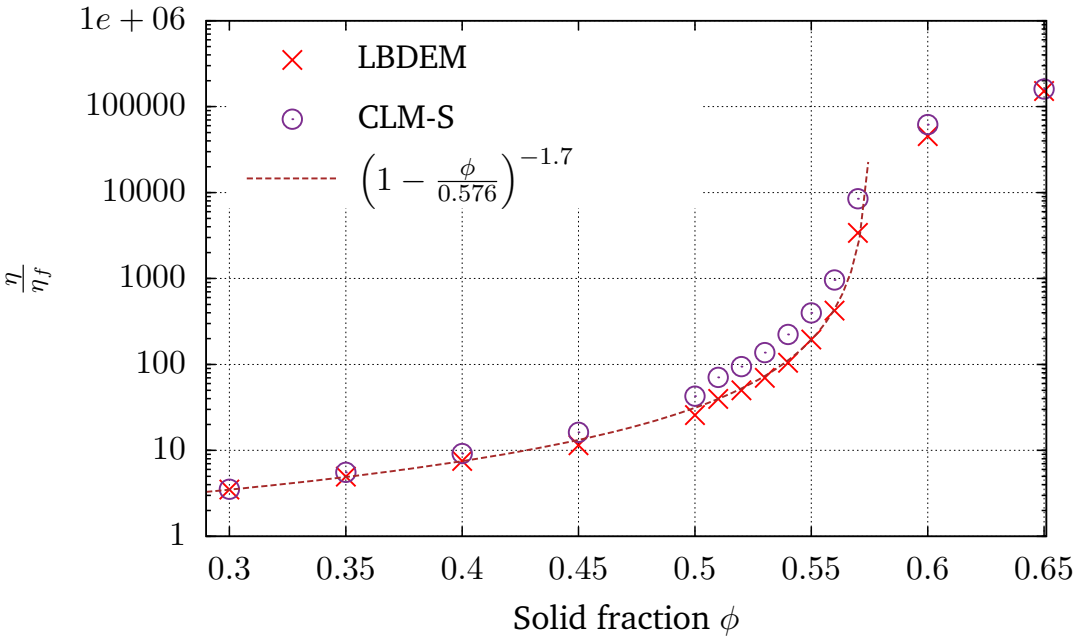

Fig. 5.6.: Frictional ($\mu_r = 1$) suspension viscosity values for different solid fraction obtained from low Reynolds number sheared LBDEM and DEM simulations.

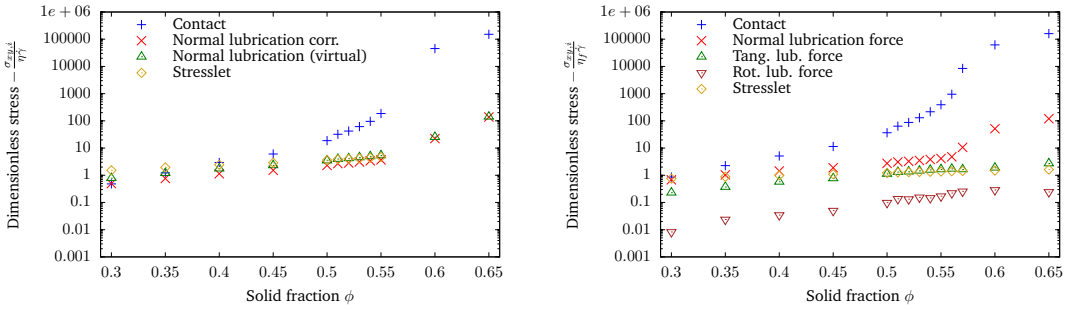

(a) LBDEM with $\mu_r = 1.0$ **(b)** DEM with $\mu_r = 1.0$

Fig. 5.7.: Various stress contributions from the different frictional LBDEM and DEM simulations corresponding to Fig. 5.6.

Particles in contact can undergo also frictional contacts and hence, simulations with friction were carried out for varied solid fractions. As DEM and LBDEM are compared to each other, the other extreme compared to a frictionless system was investigated. Therefore, a friction coefficient of $\mu_r = 1.0$ was chosen. The simulation setup was identical to the previous subsection 5.3.2.1. In figure 5.6, the obtained suspension

viscosities are shown. Frictional DEM simulations were exclusively performed with the CLM-S approach because it was shown for the frictionless case (cf. section 5.3.2.1) that LBDEM and CLM-S simulation results are alike.

The exponent in the Krieger-Dougherty correlation in the frictionless case was determined to be $[\eta]\phi_{max} = 1.7$. For the sake of comparability the same exponent is chosen for the frictional system and $\phi_{max,friction} = 0.576$ was determined by fitting over the solid fraction range $0.3 \leq \phi \leq 0.55$ of the LBDEM data. Although the determined Krieger-Dougherty correlation for the frictionless and frictional case have the same exponent, the fitted closest packing parameter is smaller for the frictional than frictionless particles. A shift of the jamming state to smaller closest packing fractions is expected for increasing friction between particles, e.g. Silbert (2010).

The obtained viscosities from frictional LBDEM and CLM-S simulations are similar. However, for higher solid fractions, around $\phi > 0.45$, a growing deviation between the two approaches for increasing solid fractions is observed. Thus, in addition to the suspension viscosities, the different stress contributions are shown for different solid fractions in figure 5.7. The qualitative results as well as the trend of a transition from lubrication to contact stress dominated suspensions towards higher solid fractions are similar to the frictionless case. Stresslet, normal and tangential lubrication interactions dominate for lower solid fractions and are surpassed by contact contributions for increased solid fractions. The hydrodynamic contributions between LBDEM and CLM-S agree mostly very well over the investigated solid fraction range. As in the previous section for frictionless particles, small discrepancies between the stresslet and the normal lubrication contribution from CLM-S and normal lubrication correction contributions from LBDEM are found. Therefore, “virtual” normal lubrication stress contributions, based on the simplified GRM model for DEM, were determined analogously to the frictionless case. The found minor differences between “virtual” stress contribution and the stress from the lubrication correction indicate only a small effect of the different cut-off choices on the separate hydrodynamic stress contributions between CLM-S and LBDEM. Interestingly however, the contact stress is somewhat larger for CLM-S than for LBDEM simulations for frictional particles. The difference in the contact stress would therefore explain the small differences in the obtained suspension viscosities in figure 5.6. Similarly, Gallier et al. (2018) report also of overestimated contact stresses due to molecular dynamics in comparison to a FDM. Yet, Gallier et al. (2018) observe furthermore underestimated hydrodynamic contributions in contrast to the findings here. A reason for differences in the contact stress contributions has unfortunately not been found and would require further investigations.

In comparison to the frictionless case, the contact stresses from LBDEM and DEM simulations are not only found to be larger over the whole investigated solid fraction range, but the contact contribution increases also more rapidly for increasing packing fraction.

Despite tremendous differences in the stress values between frictional and frictionless particles at specific solid fractions, comparison between frictional and frictionless case can be achieved by plotting the dimensionless viscosity values against $\phi_{max} - \phi$ instead only ϕ. The jamming point ϕ_{max} was determined above by fitting of the Krieger-Dougherty correlation to the simulation results. Thereby, the contact stresses presented in figure 5.8(a) are comparable except for packing fractions close to jamming and beyond. An even better agreement between frictional and frictional simulation results is found with regard to the normal lubrication force contribution for which the corresponding stress contributions collapse for solid fractions up to the jamming point as it is shown in figure 5.8(b).

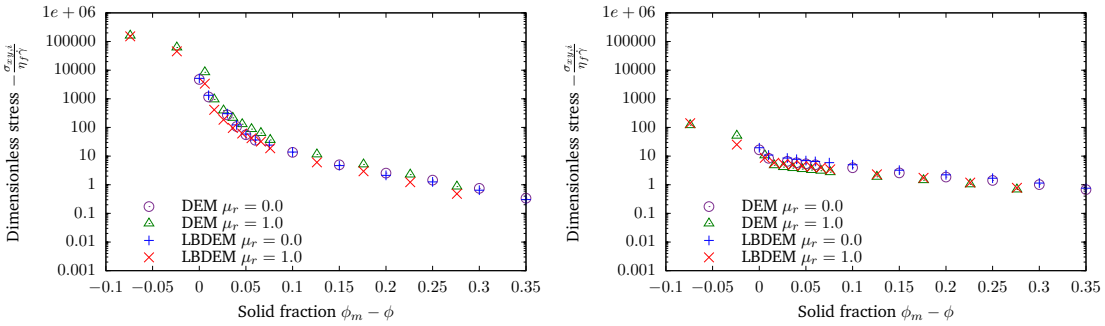

(a) Contact stresses **(b)** Normal lubrication force stresses

Fig. 5.8.: Contact and lubrication stress comparisons between LBDEM and DEM simulations for frictionless and frictional particle results.

5.3.2.3. Normal stresses

Besides the suspension viscosity, normal stress differences in sheared suspensions are another important quantity. Therefore, the normal stress differences $N_1 = \sigma_{xx} - \sigma_{yy}$ and $N_2 = \sigma_{yy} - \sigma_{zz}$ obtained from LBDEM and DEM simulations are compared. The normal stress difference results for DEM (CLM-S) as well as LBDEM simulations with frictionless and frictional particle contacts for varying solid fractions undergoing low Reynolds number ($Re = 0.1$) shearing motion are shown in figure 5.9.

For frictionless particles, shown in figures 5.9a and 5.9b, the normal stress differences are positive for the DEM and LBDEM simulations in the investigated solid fraction range except N_1 at jamming point for which the data points are not depicted. Both normal stresses, N_1 and N_2, obtained from the simulations grow with increasing solid fraction. The N_1 stresses are found to be larger than the N_2 stresses for LBDEM simulations for solid fractions below $\phi \approx 0.55$ and smaller for higher solid fractions. Surprisingly, the N_2 normal stress differences are larger than the N_1 normal stress differences for the DEM simulations in the whole solid fraction range. Hence, DEM results contradict LBDEM findings for solid fractions below $\phi \approx 0.55$. Results for the N_2 stresses at higher

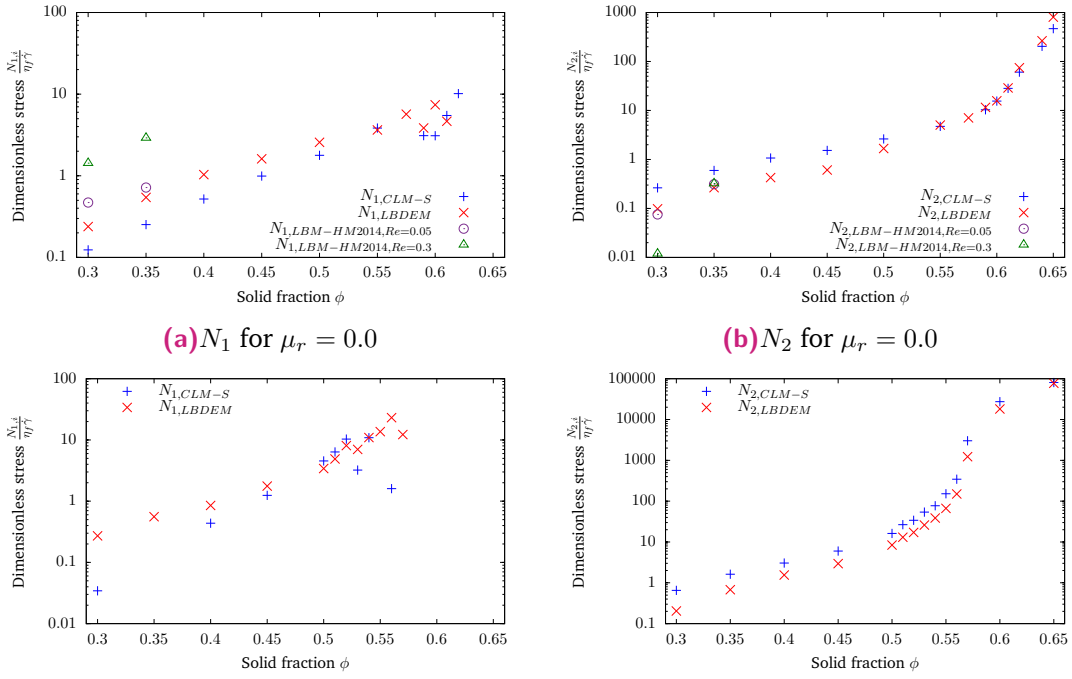

(a) N_1 for $\mu_r = 0.0$ **(b)** N_2 for $\mu_r = 0.0$

(c) N_1 for $\mu_r = 1.0$ **(d)** N_2 for $\mu_r = 1.0$

Fig. 5.9.: Normal stress differences N_1 and N_2 from the corresponding LBDEM and DEM simulations in Fig. 5.6. Additional data from Haddadi and Morris (2014), abbreviated as HM2014 in the legend, is included for the frictionless case for comparison purposes.

solid fractions are in somewhat better agreement between LBDEM and DEM. However, discrepancies between the N_1 stresses are found.

Due to the contradicting findings, normal stresses obtained by Haddadi and Morris (2014) from LBM simulations for two different low Reynolds numbers, $Re = 0.05$ and $Re = 0.3$, at low solid fractions are depicted. It shall be remarked that Haddadi and Morris (2014) define for the stress computation the vector direction from the particle centre of mass to the point on which the force acts. This corresponds to an opposite definition of the sign convention used in Eq. (5.22) and definitions in section 5.2.1.3. This means that in the publication by Haddadi and Morris (2014), obtained negative (normal) stresses correspond to positive (normal) stresses here. The Reynolds number $Re = 0.05$ results by Haddadi and Morris (2014) are comparable to the obtained LBDEM findings at a Reynolds number $Re = 0.1$. The found normal stress differences at $Re = 0.3$ by Haddadi and Morris (2014) differ strongly, especially for the first normal stress differences, due to somewhat increased particle inertia. For both Reynolds numbers however, the qualitative results show a larger first normal stress difference than the second normal stress difference. This corroborates the obtained LBDEM findings.

Inclusion of friction leads qualitatively to a simular outcome for the first and second normal stress differences obtained with DEM and LBDEM as shown in figures 5.9c and 5.9d. All normal stress differences are found to be positive except at solid fractions at the

jamming point and higher. Furthermore, N_2 stresses which were determined with DEM are larger than the N_1 stresses. In comparison, N_2 stresses from LBDEM simulations are larger than N_1 stresses for solid fractions above $\phi \gtrsim 0.35$. At a low solid fraction of $\phi = 0.3$, the first normal stress difference is found to be larger than the second normal stress difference for LBDEM simulations. This is similar to the frictionless case albeit the transition at which the second normal stress difference surpasses the first normal stress differences occurs at much lower solid fractions. This could be caused by the introduced friction which also leads to smaller maximum packing fractions as shown in the previous section by the changed viscosity divergence towards lower solid fractions for frictional particle contacts.

Therefore, analogously to the σ_{xy} stress contributions in the previous section, the normal stress differences were divided into different parts stemming from particle contact, lubrication interaction, or stresslet. The separated contributions for frictionless and frictional particles obtained from LBDEM and DEM (CLM-S) simulations are shown in figure 5.10.

For frictionless particles, the obtained contributions to first normal stress difference from LBDEM simulations are for the most part positive except for the contact contribution at the lowest and highest studied solid fractions (cf. Fig. 5.10a). The contact contribution is much smaller than the contribution from the normal lubrication force corrections at lower solid fractions. However, the contact contribution increases stronger than the lubrication contribution and surpasses it at a solid fraction of around $\phi \approx 0.55$. The found stresslet contribution is for the whole investigated solid fraction range by nearly one order smaller than the lubrication contribution. Thus, the major contributions to the first normal stress difference are regulated by particle-particle lubrication interactions at lower solid fractions and contact interactions at higher solid fractions. The separated contributions to the second normal stress differences are shown in figure 5.10b. In contrast to the first normal stress differences, only the contact contributions are positive whereas the contributions from the normal lubrication force correction and stresslet are negative for most of the solid fractions except for very high solid fraction above $\phi \geq 0.6$. Furthermore, the magnitude of the contact contributions is larger than the lubrication contributions and differences between both contribution grow with increasing solid fraction. The magnitude of the stresslet contribution is similar to the N_1 stresses much smaller than the normal lubrication contributions. In contrast to the first normal stress differences, the second normal stress differences are dominated by contact interactions between particles and lubrication interactions might be only of importance at lower solid fractions.

Results for frictionless particles obtained from DEM simulations are presented in figures 5.10e and 5.10f, respectively. The first normal stress differences are separated into similar contributions as for the LBDEM coupling. However, additional contributions from lubrication interactions due to relative tangential and rotational motion are considered.

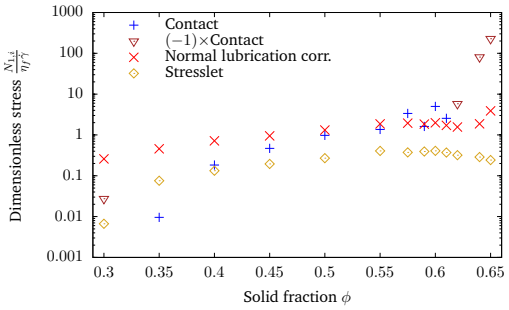

(a) LBDEM $\mu_r = 0.0$. Different contributions to N_1.

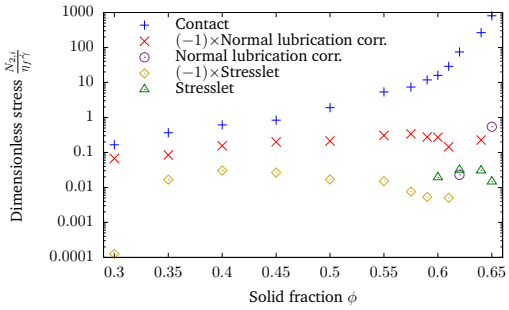

(b) LBDEM $\mu_r = 0.0$. Different contributions to N_2.

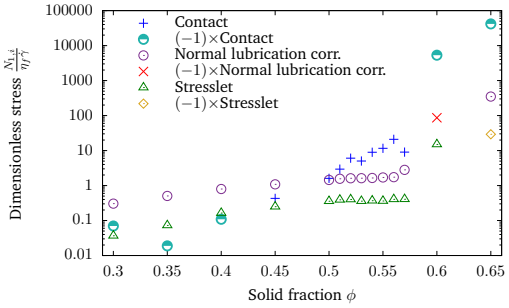

(c) LBDEM $\mu_r = 1.0$. Different contributions to N_1.

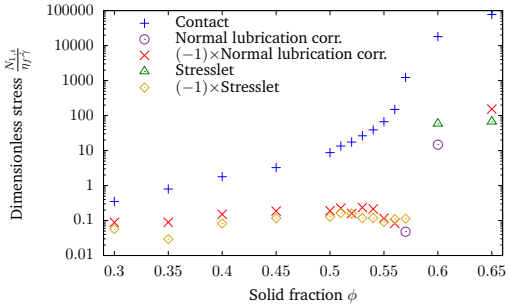

(d) LBDEM $\mu_r = 1.0$. Different contributions to N_2.

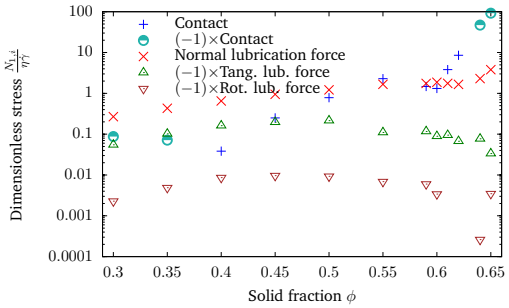

(e) CLM-S $\mu_r = 0.0$. Different contributions to N_1.

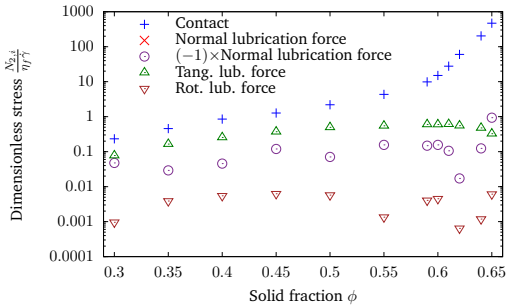

(f) CLM-S $\mu_r = 0.0$. Different contributions to N_2.

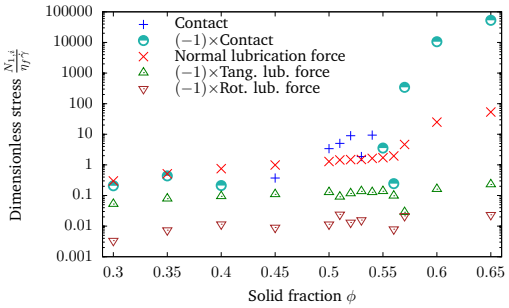

(g) CLM-S $\mu_r = 1.0$. Different contributions to N_1.

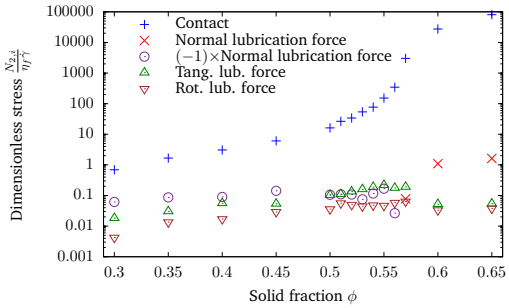

(h) CLM-S $\mu_r = 1.0$. Different contributions to N_2.

Fig. 5.10.: Different contributions to N_1 and N_2 normal stress differences obtained from CLM-S and LBDEM where both include or exclude friction.

The stresslet was computed on basis of the single sphere stresslet which leads to only a $\sigma_{xy,stresslet}$ stress contribution. Any other possible stresslet tensor contributions were

hence neglected. In comparison to the LBDEM coupling results, the contributions from the normal lubrication force interactions are comparable in magnitude and sign of stress. However, normal stress differences from particle contacts are in contrast not always positive and found results indicate negative contact first normal stress differences for lower solid fractions as well as at the jamming point. Moreover, the additional contributions from lubricated tangential and rotational interactions are negative. Hence, the summation of all contributions leads to total first normal stress differences which are smaller than N_1 stresses obtained from LBDEM simulations. For second normal stress differences shown in figure 5.10f, the contact contributions are very similar to the LBDEM results, cf. Fig. 5.10b, in magnitude as well as for the sign of the normal stresses. Besides similarites between the contact contributions between DEM and LBDEM, further agreement is found between DEM and LBDEM for contributions from normal lubrication interactions. However, additional tangential and rotational lubrication interactions lead to positive contributions. Although the rotational lubrication components result in neglectable second normal stress differences for all solid fractions, N_2 contributions from tangential lubricated particle-particle interactions are comparable, if not larger, than contributions from normal lubrication forces between particles. Hence, tangential lubrication contributions counteract normal lubrication contributions. Thus, the only relevant mechanism to the second normal stress differences in DEM simulations are mechanical particle contacts and thereby the found total N_2 stresses are larger than the obtained total N_1 stresses.

As discussed above, the total first normal stress differences from LBDEM simulations and LBM simulations conducted by Haddadi and Morris (2014) were found to be larger than the total second normal stress differences for solid fractions below $\phi \approx 0.55$ which is contradicting to the DEM simulation results. The contradicting findings could be however explained by the different lubrication contributions to the normal stress differences. The LBDEM simulations in this work and performed by Haddadi and Morris (2014) consider only a correction to the normal lubrication forces between colliding particles and corrections to the tangential or rotational lubrication components are not included. However, it is indicated by the outcome of the DEM simulations, which include all possible lubrication interactions, that the normal stress difference contributions from tangential lubrication interactions can be important. Some parts of the tangential lubrication forces are implicitly comprised in the stresslet. Yet, a change in the LBDEM simulation results, and thereby agreement to DEM simulations, might be obtained by consideration of additional corrections for tangential and rotational lubrication contributions.

The normal stress difference results for frictional particles are shown for LBDEM simulations in figures 5.10c and 5.10d and for DEM simulations in figures 5.10g and 5.10h. The results between frictionless and frictional particles are different in that the contact contributions are increased for the same solid fractions which are below the jamming point The hydrodynamic contributions, such as from normal lubrication forces or the stresslet

contribution, are mostly unchanged. Results at or above the jamming point are found to have a possibly flipped sign in the normal stress difference results. However, simulations of dense suspensions at or above jamming point are intrinsically difficult to simulate and findings in this high solid fraction regions are probably rather to be discarded. Similar to the findings for frictionless particles, contributions from tangential or rotational lubrication interactions are not considered in the LBDEM simulations. Neglect of additional lubrication corrections could explain the observed total differences between the normal stress differences obtained from LBDEM and DEM simulations because contributions from contact and normal lubrication interactions are comparable between LBDEM and DEM simulations. However, tangential lubrication forces between particles can lead to normal stress difference contributions which are of similar magnitude as contributions from normal lubrication forces. Thus, the aforementioned suggestion for frictionless particles to include lubrication corrections complementary to normal lubrication forces can be here only reiterated.

5.3.2.4. Particle and velocity profiles

Having shown that an imposed single sphere Stokes drag force results in similar viscosity and stress values as obtained from LBDEM simulations in previous sections, the velocity profiles in shearing direction are investigated here. In figures 5.11, 5.12, and 5.13 the time and space averaged velocity profiles for the frictionless particle phase with respective solid fractions of $\phi = 0.3$, $\phi = 0.45$, and $\phi = 0.6$ are shown. For coupled LBDEM simulations the fluid velocity profile is determined by averaging over all lattice cells on x-z-planes along the y-axis over time in steady state. For the DEM case where a drag model is used, the imposed velocity profile is drawn.

The fluid velocity profile from the coupled LBDEM simulations is linear for all solid fractions. Hence, imposition of a linear fluid velocity profile over the simulation domain for DEM simulations seems reasonable. In addition, the particle velocity profile is for LBDEM and CLM-S linear for all solid fractions. The slight velocity overestimation towards the LEbc could be possibly explained by the averaging process for the particle phase. The particle properties, i.e. velocities, are averaged in specific bins, here 10 bins over the simulation domain. Thereby, it could be possible that a higher number of particles with higher velocity values than the fluid velocities are considered in an averaging bin leading to a marginal increased particle phase velocity in comparison to the fluid phase.

For DEM simulations without an imposed drag force (CLM) linear particle phase velocity profiles are obtained for moderately to high packing fractions which are comparable to DEM simulations with drag force (CLM-S) and LBDEM simulations. However, a decrease

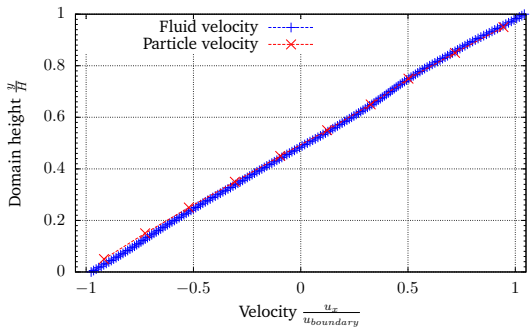

(a)LBM $\phi = 0.30$

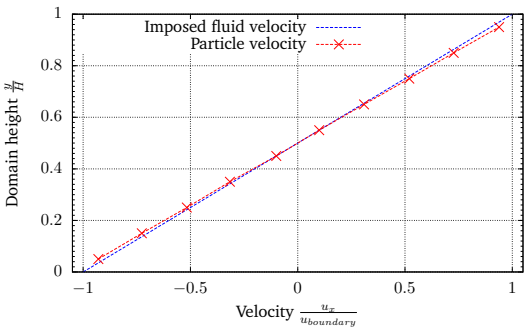

(b)CLM-S $\phi = 0.30$

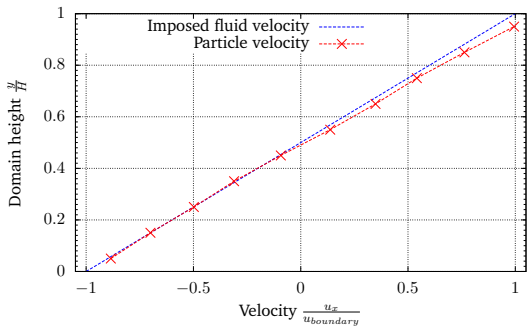

(c)CLM $\phi = 0.30$

Fig. 5.11.: Fluid and particle velocity profiles of frictionless suspensions under simple shear at a low Reynolds number $Re = 0.1$ and at a solid fraction $\phi = 0.3$.

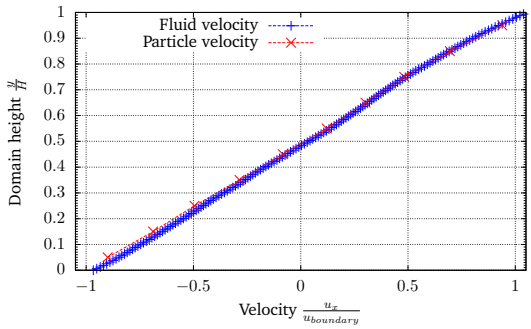

(a)LBM $\phi = 0.45$

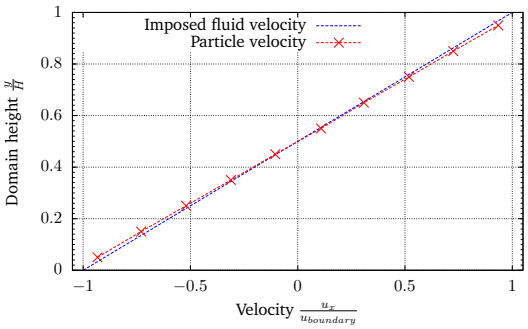

(b)CLM-S $\phi = 0.45$

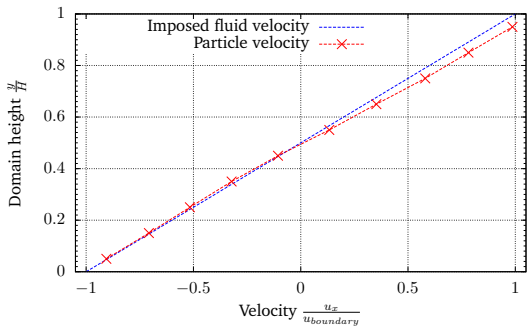

(c)CLM $\phi = 0.45$

Fig. 5.12.: Fluid and particle velocity profiles of frictionless suspensions under simple shear at a low Reynolds number $Re = 0.1$ and at a solid fraction $\phi = 0.45$.

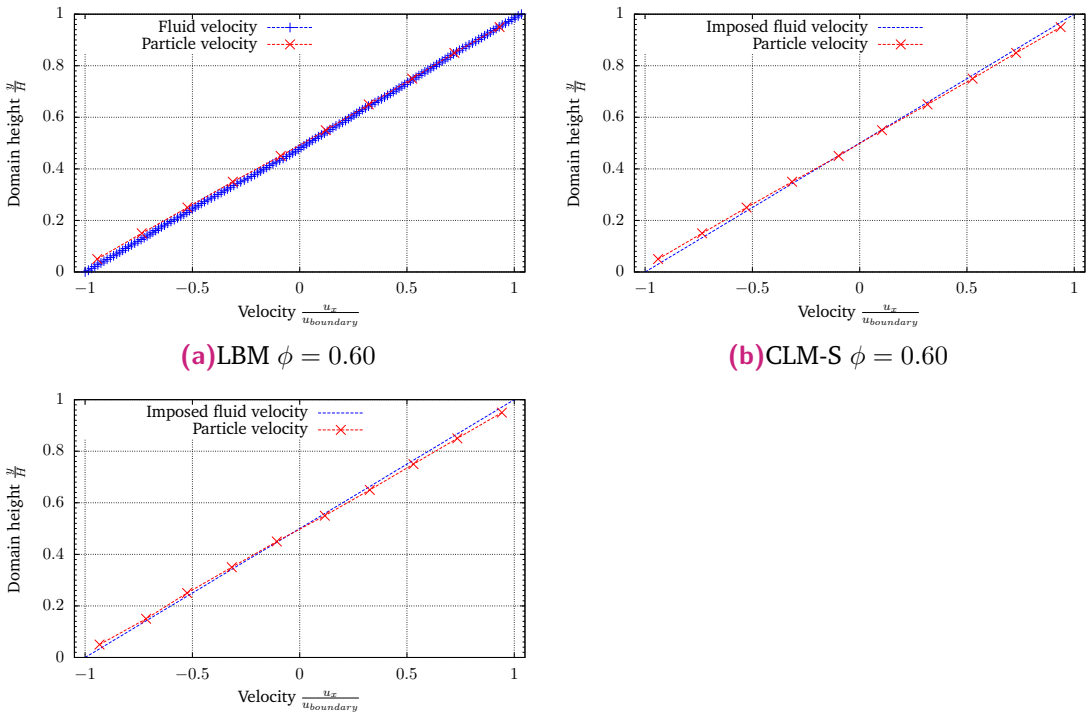

(a) LBM $\phi = 0.60$ **(b)** CLM-S $\phi = 0.60$

(c) CLM $\phi = 0.60$

Fig. 5.13.: Fluid and particle velocity profiles of frictionless suspensions under simple shear at a low Reynolds number $Re = 0.1$ and at a solid fraction $\phi = 0.6$.

in the packing fraction leads to a somewhat increased difference to the linear LBM and CLM-S profiles, cf. Fig. 5.11c and 5.12c.

The similarity or differences in the velocity profiles could explain similar or differing viscosity and stress values as it leads to slightly changed microstructural interactions. DEM simulations with a drag force model lead to similar viscosity and stress contributions as LBDEM simulations. Both, approaches show also very similar velocity profiles. In contrast, DEM simulations without additional drag force modelling lead to viscosity and stress values similar to the aforementioned simulation approaches for high packing fractions, where the velocity profiles are similar, but for lower packing fractions, where the velocity profiles differ to LBDEM or DEM with drag force model simulations, discrepancies in viscosity and stress contributions are found as discussed in previous sections.

5.4 Conclusions

A comparison study between a coupled LBDEM approach and a DEM with two particle-particle pairwise interactions approaches for low Reynolds sheared dense suspensions with frictional and frictionless particles has been conducted. The lubrication force models are based on the grand-resistance matrix formulation where one was considerably simplified in its formulation so that only the particle velocities without the background fluid

velocities or strain rate components have to be considered. Both employed lubrication models lead to the same suspension viscosities, which agree to the Krieger-Dougherty correlation, and overall same lubrication stress contributions. Although the simplified formulation cannot yield lubrication stress information from the applied strain on the suspension as the force and torque computation contains implicitly this contributions due to simplifications in the formulation.

As the two lubrication interaction modelling approaches gave the same overall results, the simplified formulation was compared to coupled LBDEM simulations. The findings with regard to the suspension viscosities show that a DEM approach can lead to similar results as LBDEM simulations when the employed lubrication model comprise forces and torques from relative motion between particles in normal direction, tangential direction, and rotation, as well as from an imposed single sphere Stokes drag force on each particle. Especially for low and intermediate solid fraction ranges, it is observed that the single sphere Stokes drag force and resulting single sphere stresslet have a great influence. For lower solid fractions, minor differences in the obtained suspension viscosities between DEM and LBDEM simulations are found. However, simulations results between the LBDEM and DEM approaches are very similar for high solid fractions due to increasing importance of mechanical particle-particle contacts and close-range lubrication interactions in comparison to a receding effect of long range forces as the stresslet contribution diminishes in comparison to other contributions for high solid fractions. It is furthermore shown that normal stress differences N_1 and N_2 obtained from LBDEM and DEM with a simplified lubrication model are alike to some extent. Found discrepancies are a likely result of not included lubrication force corrections in LBDEM simulations. As the imposed single sphere Stokes drag in the DEM simulations is based on a linear fluid velocity profile caused by the shearing motion, the fluid velocity obtained from the LBDEM simulations was evaluated. It is found that a linear velocity profile is justified as modelling approach for low Reynolds numbers as the obtained fluid velocity and particle velocity profile agree excellently between LBDEM and DEM simulations.

In conclusion, for low Reynolds sheared suspensions, especially at high solid fractions, a pure DEM simulation approach employing a single sphere Stokes drag force based on a linear fluid velocity profile in combination with a lubrication model describing forces and torques in a pairwise fashion due to normal, tangential, and rotational relative motions between particles is justified as the results are in very good agreement compared to a coupled LBDEM approach.

6 Linking contact stress and lubrication dissipation to the viscosity divergence in dense suspensions

6.1 Introduction

Interest in an increase and divergence of suspension viscosities with increasing solid fraction has had a long history. Einstein (1905) and Einstein (1911), who wanted to find an approach to determine the dimensions of molecules, linked analytically for dilute suspensions the fluid stress on particle surfaces to an expression describing performed work of the fluid on the particles which in turn could be related to the suspension mixture viscosity - or expressed in other words, Einstein (1905) and Einstein (1911) linked the viscous dissipation to the suspension mixture viscosity in a dilute regime. An extension towards very dense suspensions was undertaken by Frankel and Acrivos (1967) who deduced analytically a viscosity correlation from viscous dissipation caused by lubrication forces between particles. Frankel and Acrivos (1967) concluded with the claim that the viscosity divergence at high solid fraction is a result from lubricated interactions. Andreotti et al. (2012) show by simulating suspensions under simple shear that different computational models lead to similar viscosities, which are computed from the viscous dissipation, and that similar particle fluctuations are obtained for differently employed models. Andreotti et al. (2012) hypothesize that due to similarities in the microscale dynamics, a link between suspension flows and underlying geometrical microscale structures could exist.

For this chapter, simulations of sheared suspensions under simple shear were performed. Contact models were changed while the suspension viscosities were computed from the bulk stresses as well as from viscous dissipation caused by lubricated particle-particle interactions. Furthermore, relative particle-particle velocities were analysed. The results corroborate previous findings and claims on viscosity divergence (cf. Frankel and Acrivos (1967) and Andreotti et al. (2012)) by using a different numerical method. It is further demonstrated that the divergence behaviour does not depend on the details of lubrication.

6.2 Methodology & simulation setup

As shown in the previous chapter, it can be justified to use a discrete element method with an additional model for lubrication interactions to simulate sheared dense suspensions in a steady-state low Reynolds number regime.

6.2.1 Discrete element method

A discrete element method (DEM) (cf. Cundall and Strack (1979)) on open-source basis (cf. Plimpton (1995) and Kloss et al. (2012)) was employed to simulate particle dynamics by solving with a velocity-Verlet algorithm for the translational motion

$$m_i \frac{\partial \mathbf{x}_i^2}{\partial^2 t} = \mathbf{F}_i = \mathbf{F}_i^C + \mathbf{F}_i^L \,, \tag{6.1}$$

and similarly for the angular motion

$$\mathbf{J}_i \frac{\partial \boldsymbol{\omega}_i}{\partial t} = \mathbf{T}_i = \mathbf{T}_i^C + \mathbf{T}_i^L \,. \tag{6.2}$$

Mass, position, moment of inertia and angular velocity of particle i are described by m_i, $\mathbf{x}_i$, $\mathbf{J}_i$ and $\boldsymbol{\omega}_i$, respectively. The total force and torque on a particle can be split here into two different contributions, namely particle-particle contacts, $\mathbf{F}^C$ and $\mathbf{T}^C$, and particle-particle lubrication interactions, $\mathbf{F}^L$ and $\mathbf{T}^L$.

6.2.2 Lubrication and contact interactions

Lubrication interactions between particles are modelled pairwise between two particles on basis of simplified equations, cf. previous chapter, of the grand-resistance matrix (GRM) formulation given by for example Jeffrey and Onishi (1984), Jeffrey (1992) and Kim and Karrila (2005). Lubrication interactions are imposed on particles when the gap distance between particles is below a defined outer cut-off value $\delta_{c,o}$. For gap distances below an inner cut-off value of $\delta_{c,i}$, comparable in its size to particle asperities as explained in the previous chapter, the lubrication interactions remain constant. The lubrication force on a particle reads:

$$\mathbf{F}^L = \mu \Big[X_A^{11} \mathbf{u}_{p,rel,n} + Y_A^{11} \left(\mathbf{u}_{p,rel,t} - (r_{p,1} + r_{p,2})(\boldsymbol{\omega}_s \times \mathbf{e}) \right) + \frac{1-\gamma(1+4\gamma)}{4+\gamma} Y_B^{11} \left(\boldsymbol{\omega}_d \times \mathbf{e} \right) \Big] \,, \tag{6.3}$$

where $\boldsymbol{\omega}_s = (\boldsymbol{\omega}_{p,1} + \boldsymbol{\omega}_{p,2})/2$, $\mathbf{w}_d = (\boldsymbol{\omega}_{p,1} - \boldsymbol{\omega}_{p,2})/2$, and $\mathbf{u}_{p,rel,n}$ and $\mathbf{u}_{p,rel,t}$ are the normal and tangential component of the relative velocity $\mathbf{u}_{p,rel} = \mathbf{u}_{p,2} - \mathbf{u}_{p,1}$ between particles

1 and 2. γ describes the particle size ratio between particles 1 and 2. The lubrication torque expression can be written as:

$$\mathbf{T}^L = \mu\Big[Y_B^{11}\left(\mathbf{u}_{p,rel}\times\mathbf{e}\right) + (r_{p,1}+r_{p,2})(\boldsymbol{\omega}_s - (\boldsymbol{\omega}_s\cdot\mathbf{e})\mathbf{e}) \\ + Y_C^{12}\left(1-\frac{4}{\gamma}\right)(\boldsymbol{\omega}_d - (\boldsymbol{\omega}_d\cdot\mathbf{e})\mathbf{e})\Big] \ . \quad (6.4)$$

The resistance functions X_A^{11}, Y_A^{11}, Y_B^{11}, and Y_C^{12} are taken to the order of $log(\xi^{-1})$ with $\xi = \frac{h_{gap}}{r_p}$ from Kim and Karrila (2005).

Although it has been shown that an additional drag model based on the single sphere stresslet lead to more accurate stress and viscosity values in a suspension, it was refrained from imposition of such a drag model. The here intented focus is on discussion of the viscosity divergence in suspensions on a qualitative basis. Therefore, it was preferred to employ the simplest possible hydrodynamic models allowing to clearly differentiate between microscale effects.

For overlapping particles, a Hooke and Hertz model were used, e.g. Luding (1998) and Herrmann and Luding (1998). The contact according to the Hooke model can be expressed as:

$$\mathbf{F}^{C,Hooke} = (k_n\boldsymbol{\delta}_n + \gamma_n\mathbf{u}_{p,rel,n}) - (k_t\boldsymbol{\delta}_t + \gamma_t\mathbf{u}_{p,rel,t}) \ . \quad (6.5)$$

The spring stiffness in normal and tangential direction are k_n and k_t, respectively. The damping coefficient in normal direction is expressed as γ_n and in tangential direction as γ_t. The Hertz model can be expressed as:

$$\mathbf{F}^{C,Hertz} = \sqrt{\frac{\delta_n}{r_{eff}}}\mathbf{F}_{C,Hooke} \ , \quad (6.6)$$

where the effective particle radius is $r_{eff} = \frac{r_i r_j}{r_i+r_j}$. The tangential spring stiffness is chosen for the Hooke and Hertz model in dependence of the normal spring stiffness, $k_t = \frac{2}{7}k_n$, according to Schäfer et al. (1996). Moreover, the damping coefficients for the Hooke and Hertz model are chosen to be $\gamma_n = \gamma_t = 0$ due to the already existing dissipation caused by lubrication interactions between particles.

6.2.3 Viscosity and stress calculation

Andreotti et al. (2012) compute the suspension viscosity from the dissipation Γ caused by viscous forces as

$$\eta = \frac{\Gamma}{\dot{\gamma}^2} \ , \quad (6.7)$$

for a Newtonian background fluid where $\dot{\gamma}$ is the shear rate. The dissipation from translational motion was here computed as:

$$\Gamma^F = \frac{1}{2}\frac{1}{V}\sum_i \sum_{i \neq j} [\mathbf{F}_{ij}^L \cdot \mathbf{u}_{p,rel,ij}] \ , \tag{6.8}$$

where $\mathbf{u}_{p,rel,ij} = \mathbf{u}_{p,i} - \mathbf{u}_{p,j}$ is the relative velocity between two particles. According to Trulsson et al. (2017), the rotational dissipation can be computed analogously from the lubrication torque and relative particle angular velocities, i.e. $\boldsymbol{\omega}_{rel,p,ij} = \boldsymbol{\omega}_{p,i} - \boldsymbol{\omega}_{p,j}$, as

$$\Gamma^T = \frac{1}{2}\frac{1}{V}\sum_i \sum_{i \neq j} [\mathbf{T}_{ij}^L \cdot \boldsymbol{\omega}_{rel,p,ij}] \ . \tag{6.9}$$

The total dissipation follows then from $\Gamma = \Gamma^F + \Gamma^T$.

The viscosity of the suspension can be also evaluated from the fluid viscosity and total particle stress in shearing direction, i.e.

$$\eta = \eta_f + \frac{|\sigma_{xy}^P|}{\dot{\gamma}} \ . \tag{6.10}$$

The total particle stress $\boldsymbol{\sigma}^P$ consists of a contact and lubrication stress contribution:

$$\boldsymbol{\sigma}^C = \frac{1}{V}\sum_i \sum_j \mathbf{r}_{ij}\mathbf{F}_{ij}^C \ , \tag{6.11a}$$

$$\boldsymbol{\sigma}^L = \frac{1}{V}\sum_i \sum_j \mathbf{r}_{ij}\mathbf{F}_{ij}^L \ , \tag{6.11b}$$

where $\mathbf{r}_{ij}$ is a vector between two interacting particles i and j and points along the centre-to-centre line from particle j to i.

6.2.4 Simulation setup

Dense suspensions of frictionless, rigid, bi-disperse particle assemblies of slightly more than $N = 2000$ particles of same density ρ, a size ratio of $\frac{d_{p,2}}{d_{p,1}} = 1.4$ and total volume ratio of $\frac{V_{p,2}}{V_{p,1}} = 1$ to avoid clustering under simple shear were studied. Simple shear was realised by imposition of boundary conditions which are conceptually equivalent to Lees-Edwards boundary conditions, cf. Lees and Edwards (1972), on a three dimensional periodic domain. The solid fraction in the system was changed by keeping the particle number constant and varying the domain size under the restriction of a minimum domain size of at least $\left[\frac{d_{p,1}}{L_x} \times \frac{d_{p,1}}{L_y} \times \frac{d_{p,1}}{L_z}\right] = [10 \times 10 \times 10]$. The applied shear rate was determined according to the required Stokes number St, i.e. $\dot{\gamma} = \frac{\eta_f St}{\rho d_{p,1}^2}$, and the suspension was sheared to a strain of 10 to obtain a steady-state sheared suspension

which allows for sufficient time averaging, from strain 5 to 10, of the volume averaged stress, viscosity, and particle fluctuations. The values for the outer cut-off $\delta_{c,o} = 0.05 d_{eff}$ and inner cut-off $\delta_{c,i} = 0.001 d_{eff}$, where $d_{eff} = \frac{d_i d_j}{d_i + d_j}$, for the lubrication force model were chosen according to the previous chapter. The spring stiffness of the aforementioned contact models was varied. Therefore, the spring stiffness is non-dimensionalised by $k_n^* = \frac{k_n / d_{p,1}}{\eta_f \dot{\gamma}} = k_n \frac{\rho d_{p,1}}{St \eta_f^2}$ for presentation of the results.

6.3 Results

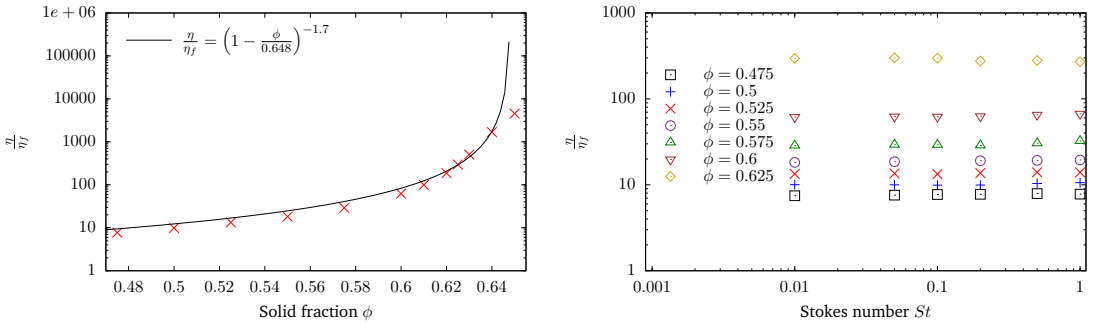

(a) (b)

Fig. 6.1.: (a): Dimensionless suspension viscosities obtained from frictionless simulations employing a Hooke contact model with $k_n^* = 2.5 \cdot 10^5$ at $St = 0.1$. Viscosity values are computed from the bulk stress according to Eq. (6.10) and compared to a Krieger-Dougherty correlation. (b): Dimensionless viscosity values for different St numbers from simulations with a Hooke contact model with $k_n^* = 2.5 \cdot 10^5$.

In figure 6.1a, the suspension viscosity is shown in dependence of the solid fraction for simulations with a Hooke contact model and a dimensionless contact stiffness of $k_n^* = 2.5 \cdot 10^5$. The viscosities are determined from the bulk stress (6.10) at a low Stokes number $St = 0.1$. The viscosity diverges with increasing solid fraction as it has been shown in the previous chapter as well in literature, e.g Krieger and Dougherty (1959). The results are obtained in a quasi-Newtonian regime, which can be identified from Fig. 6.1b, for which nearly unchanged viscosity values for varied low Stokes numbers are obtained.

In the previous chapter, the different stress contributions to the total stress, and hence viscosity, for low Reynolds number sheared suspensions for varying solid fractions are presented and discussed. As those results are also relevant here, a brief recap is provided by separating analogously the stress contributions for the simulations conducted in this chapter. The separated stress contributions are depicted in figures 6.2a and 6.2b for a Hooke and Hertz contact model, respectively, at a low Stokes number $St = 0.1$. The found contributions are very similar between both contact models. For a smaller solid fraction of around $\phi = 0.475$, the total lubrication interaction, separated into normal, tangential, and rotational contributions, is comparable to the contact stress. However, the

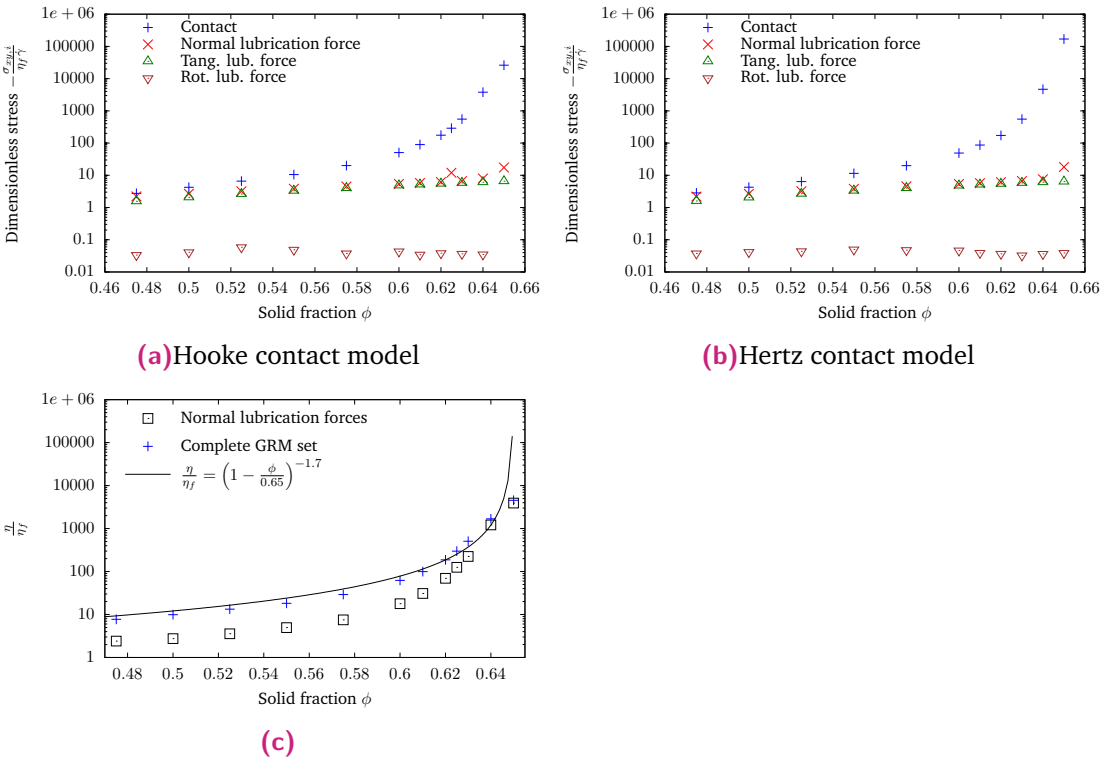

Fig. 6.2.: (a)/(b): Dimensionless stress contributions at different solid fractions obtained from sheared simulations with a Hooke model, where $k_n^* = 2.5 \cdot 10^6$, and a Hertz model, where $k_n^* = 3.6458 \cdot 10^8$, at $St = 0.1$. (c): Dimensionless relationships between viscosity and solid fraction for the complete lubrication interaction model and a model considering only lubrication forces in normal collision direction.

contact stress increases drastically with increasing solid fraction and is the dominating contribution for high solid fractions close to jamming. The lubrication contributions increase only slightly. The normal and tangential lubrication interactions lead to very similar contributions whereas the rotational contribution is negligible in comparison to the other contributions. A difference between the results obtained from simulations with a Hooke and Hertz model is found for values beyond the jamming point. This difference could be explained by the limitations of the used numerical method in that the acceptable particle overlap is violated when the particle stiffness is too small. However, the extreme similarity between the results obtained with two different contact modelling approaches prompts the question of the underlying interplay between mechanical particle contacts and lubricated particle interactions. Therefore at first, the above simulations with an employed Hooke contact model at a Stokes number $St = 0.1$ were repeated while tangential and rotational lubrications were neglected to study the effect of the removed contributions on the viscosity divergence. Especially because the tangential lubrication interactions lead to comparable stress contributions as lubrication forces in normal particle-particle collision directions. Removal of the tangential and rotational lubrication interactions results in lower viscosity values, but leads still to a viscosity divergence for increasing solid fractions as shown in figure 6.2c. Furthermore, the

maximum packing fraction at which the viscosity diverges remains unchanged when lubrication contributions apart from the normal lubrication interaction are neglected due to the dominating role of mechanical particle-particle contacts at high solid fractions.

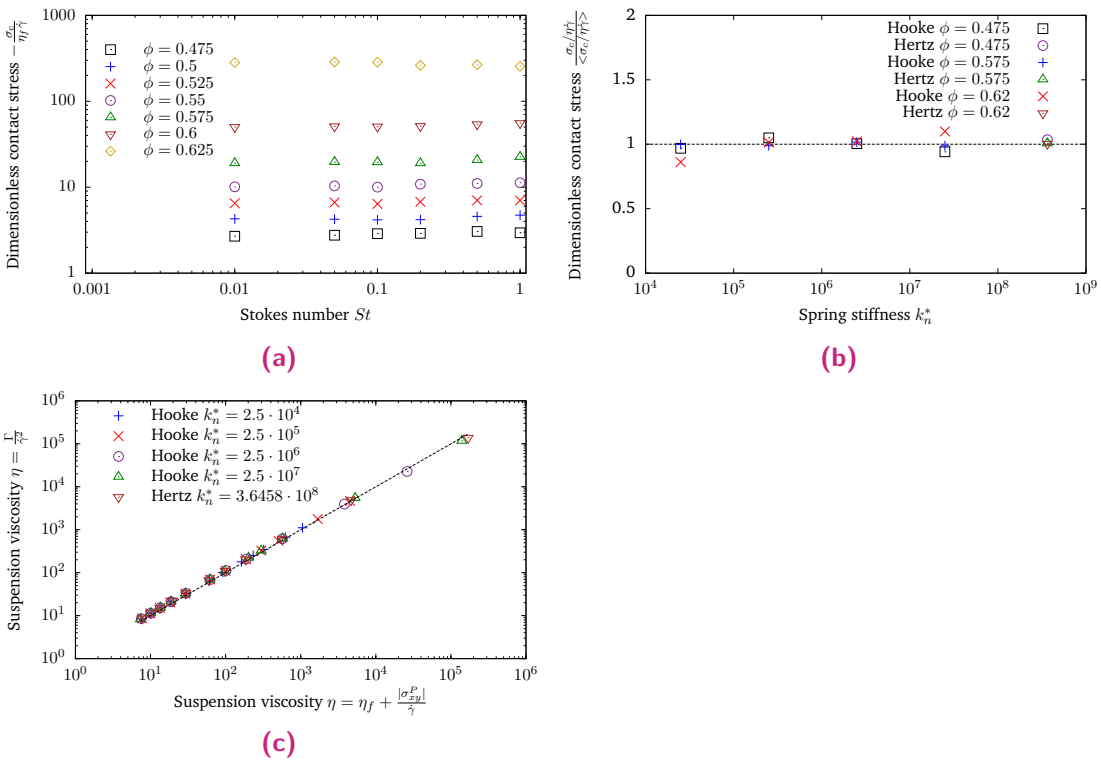

Fig. 6.3.: (a): Dimensionless contact stress for varied St numbers obtained from simulations with a Hooke contact model where $k_n = 2.5 \cdot 10^5$. (b): Dimensionless contact stress contributions for varied spring stiffnesses k_n^* and changed contact models at $St = 0.1$. (c): Parity plot of viscosities computed according to Eqs. (6.7) and (6.10) for different contact models at $St = 0.1$.

In the investigated quasi-Newtonian suspension regime, the suspension viscosity remains constant for a changed shear rate. This means that the total stress should scale linearly with the shear rate. Furthermore, Bagnold (1954) introduced a classification into two different regimes, namely an inertia and viscous regime according to the proportionality of the measured stress to the shear rate in form of $\sigma \propto \dot{\gamma}^2$ and $\sigma \propto \dot{\gamma}$, respectively. Thus, the contact stress contributions, non-dimensionalised by the fluid stress, for different solid fractions and varied Stokes number, i.e. varied shear rates, are presented in figure 6.3a for a Hooke contact model with $k_n^* = 2.5 \cdot 10^5$. It is found that the contact stress scales linearly with the Stokes number as the dimensionless stress is reduced to approximately constant values $c(\phi)$ stemming from $\frac{\sigma_c}{\sigma_f} = \frac{c(\phi)\eta_f\dot{\gamma}}{\eta_f\dot{\gamma}} = c(\phi)$. Observation of this viscous regime for the conducted simulations could imply that the obtained contact stress is not a collisional contribution (collisional stress), but a result from viscous interactions. As a consequence of such a theorised link between viscous interactions and contact stress, as well as consideration of the above explained similarities in stress contributions from two different contact models, cf. fig 6.2, contact stress contributions from simulations

with different contact modelling approaches are shown in figure 6.3b. It is found that the contact stress, related to the mean value of obtained contact stresses, is independent of the contact model because the contact stresses from different simulations remain nearly constant when the contact stiffness or the contact model is changed. The contact model independence can be understood by comparison between the viscosity computations from dissipation, Eq. (6.7), and total stress, Eq. (6.10). Viscosities, evaluated by both aforementioned methods, are presented for all above performed simulations in figure 6.3c. Very minor differences are found between both viscosity evaluations. Differences in the viscosities between different contact models are only found for very high viscosity values. This can be explained by the very high solid fractions at or beyond jamming point, $\phi \gtrapprox 0.64$, which results in larger particle overlaps for smaller stiffness values and thereby violation of the numerical method. It is, however, shown that the obtained viscosities below and close jamming point are not affected by the contact model choice and moreover, in particular, the viscous dissipation leads to the same viscosities as the bulk stresses. This means that the microscale interactions must be alike.

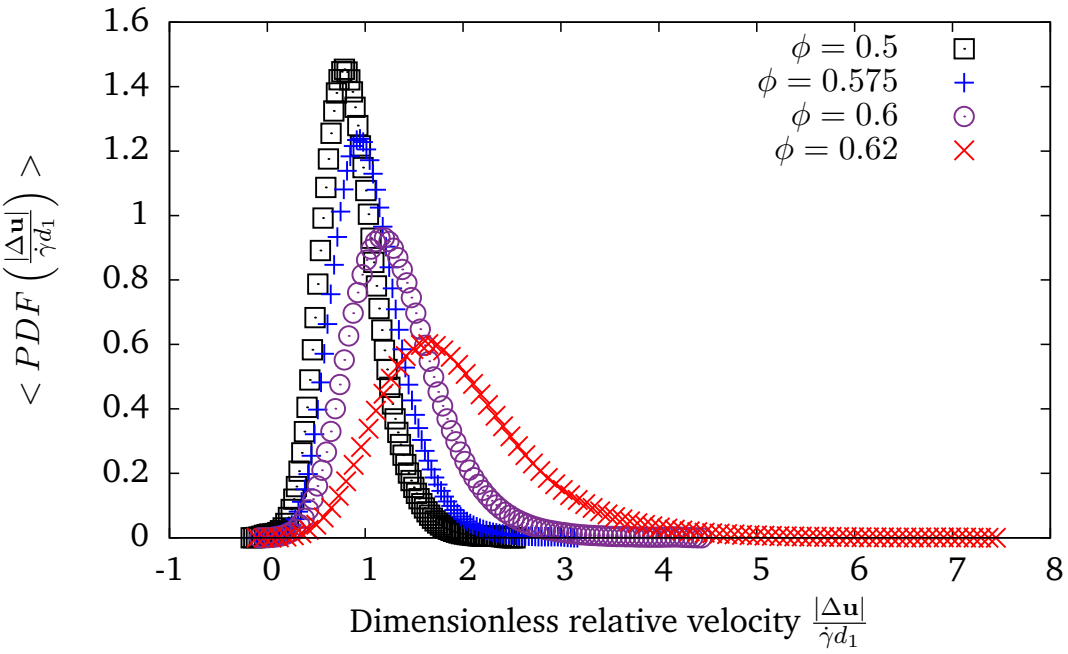

Fig. 6.4.: Probability density functions of dimensionless relative particle-particle velocities at different solid fractions obtained with a Hooke contact model with $k_n^* = 2.5 \cdot 10^5$ at $St = 0.1$.

As the dissipation is calculated from the product of relative particle-particle velocities and lubrication interactions, which depend besides the gap distances also on the relative velocities, the relative velocities can provide some information about the dynamic microscale structure. Therefore at first, the probability density functions (PDF) of the relative particle-particle velocities obtained from simulations with a Hooke contact model where $k_n^* = 2.5 \cdot 10^5$ for different solid fractions at a low Stokes number of $St = 0.1$ are shown in figure 6.4. For lower solid fractions, the distributions are narrow and the

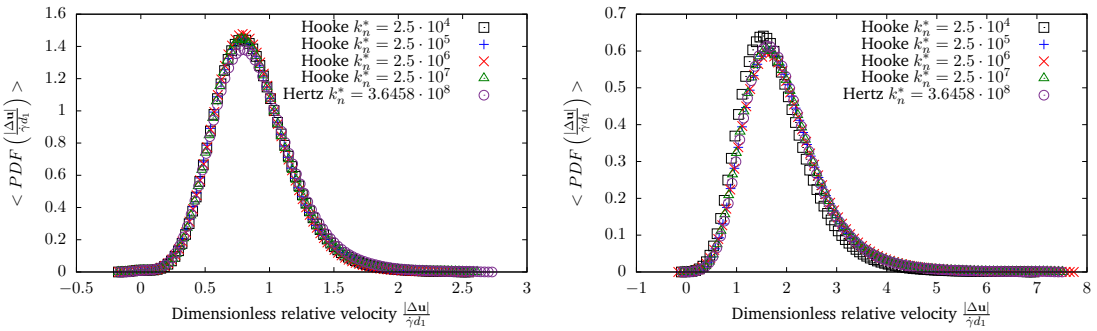

Fig. 6.5.: Probability density functions of dimensionless relative particle-particle velocities obtained from different contact modelling approaches at $St = 0.1$ and solid fractions $\phi = 0.5$ shown in (a) and $\phi = 0.62$ presented in (b).

mean is found to be at lower relative particle-particle velocities. Higher solid fractions lead to a widened spectrum of relative velocities around a mean value at higher relative particle-particle velocities. An increased dissipation, and thereby increased viscosity, is the result of shifted distribution mean values towards higher relative velocities and widened distributions for increasing solid fractions. Although the PDFs of the relative particle-particle velocities are different between varying solid fractions, the PDFs obtained from simulations with different contact models would need to be similar at the same solid fractions. Otherwise, different viscosity values would be found due to different obtained dissipation values which would contradict above presented results in figure 6.1a. Hence, for a low Stokes number, $St = 0.1$, at the solid fraction $\phi = 0.5$ and $\phi = 0.62$, relative velocity fluctuations are summarised into PDFs for different contact models and are shown in figure 6.5a and 6.5b, respectively. The PDFs of the different simulations for the same solid fraction collapse in large parts, i.e. the similarity of the microscale kinematics demonstrates indeed the contact model independence which, for rigid hard particles, is a result from the viscous dissipation. Similarities in PDFs of particle velocity fluctuations in dense suspensions obtained with different simulation methods are also reported by Andreotti et al. (2012) who theorise that particle trajectories and viscous dissipation can be possibly decoupled due to the modelling independence.

6.4 Conclusions

Sheared dense suspensions, consisting of neutrally buoyant and rigid particles, were simulated in a low Stokes number regime, i.e. quasi-Newtonian suspension regime, with DEM employing different contact models, Hooke and Hertz, and an additional lubrication interaction model. Suspension viscosity, stress contributions, and probability density functions of relative particle velocities were calculated. The same viscosity values below and close to the jamming point were obtained for different contact models and the contact stress was observed to be the dominating stress contribution at high packing

fractions. However, the contact stress was also found to be independent of the contact modelling approach with evidence provided from the microscale dynamics leading to same viscosities as when calculated from the macroscopic stress. Similarities between the microscale dynamics, which ultimately lead to the same dissipation and thereby viscosities, were found for relative particle velocity probability distribution functions obtained with different contact models.

7 Summary, conclusion, and future work

7.1 Summary and conclusion

This thesis consists of four parts: Firstly, work on a methodology analysis of a coupled lattice Boltzmann discrete element method (LBDEM) to simulate sheared suspensions. Secondly, an adaption of a lubrication force correction for aforementioned LBDEM coupling. Thirdly, comparison between the LBDEM coupling and a DEM with a particle pairwise lubrication interaction model to simulate suspensions under simple shear. Finally, a study on the viscosity divergence in dense suspensions by investigation of the underlying physical microscale interactions between particles by employing the foregoing DEM with a lubrication force model.

In the first part, an evaluation of two partially saturated methods, a non-equilibrium bounce-back and superposition method, to couple LBM and DEM to simulate fluid-particle flows, specifically sheared suspensions, was undertaken. Both methods were assessed by simulating one, two, and several hundred particles under simple shear. Results were assessed with regard to the obtained velocity profiles as well as the stress state, in particular the stresslet, by comparison to analytical known solutions or the semi-empirical Krieger-Dougherty correlation describing the suspension viscosity in dependence of the solid fraction. Accurate results were only obtained by employing the superposition method under the restriction of an appropriate single relaxation parameter choice to reduce slip velocity effects. A performed theoretical analysis of both methods revealed that inclusion of higher order terms leads for the non-equilibrium bounce-back method to additional terms affecting the stress state in contrast to the superposition method. Based on the outcome of the methodology analysis, the superposition method was therefore used for the remainder of the work. An existing correction for lubrication interactions, which are limited by the numerical mesh resolution, was slightly modified by extension of a method specific calibration. Calibration of the superposition method, while restrained by the previously found ideal single relaxation parameter to reduce slip velocities, was performed and recommendations for the LBDEM parameter choice have been provided. Although LBDEM simulations provide great detail and insights into suspensions flows, drastic simplifications by introduction of a lubrication interaction model into DEM, which significantly reduces the computational effort, could be justified to simulate dense, steady-state, low Reynolds number suspensions under simple shear. Hence, the LBDEM coupling

was compared to DEM with an additional lubrication interaction model to simulate dense suspensions under simple shear. It was found that the drastic simplifications by using DEM were justified as obtained suspension viscosities, stress contributions, normal stress differences, and velocity profiles agree well for dense suspensions. In the last part, the DEM capabilities to simulate dense suspensions was used to conduct sheared simulations to investigate the viscosity divergence for increasing solid fractions in a quasi-Newtonian regime. The contact stress contributions were observed to be the dominating stress contributions at high solid fractions. Yet, it was also found that the results were independent of the contact model. Furthermore, it was shown that the obtained viscosities were the same if computed from the suspension bulk stresses or dissipation caused due to lubrication interactions on microscale. The obtained relative particle velocity fluctuations were in accordance with the other findings due to high similarities in corresponding distribution functions between simulation results obtained with different contact models. Thereby indicating that the contact model independence is a result from the viscous dissipation.

In conclusion, this work proves through a careful assessment of partially saturated LBDEM couplings and corresponding calibration of a lubrication force correction that simulations of suspensions under simple shear can be accurately performed. In addition, LBDEM parameter choices to simulate accurately dense suspensions are provided in this work. Moreover, it has been shown that dense suspensions simulations can be drastically simplified by use of DEM with an additional lubrication force. This tremendously simpler and computationally cheaper DEM approach has been employed to study physical processes in dense suspensions.

7.2 Suggestions for future work

A multitude of different in-house PSM-LBM codes between different research groups exist:

- It could be therefore perhaps advantageous to benchmark the variety of codes against each other for predefined and discussed cases. A benchmark published in collaboration between several research groups, using different codes, could establish a common ground and function as a standard for future work on PSM.

The LBDEM coupling, which is investigated and discussed in this thesis, can be employed to simulate dense suspensions. However, it is shown that due to use of a single relaxation scheme the coupling is limited to a fixed relaxation parameter range τ to reduce slip velocity effects. A necessary fixed relaxation parameter is troublesome because on one hand the fluid viscosity cannot be changed freely anymore. On the other hand the simulation timestep choice can be then only influenced by changing the lattice resolution

which itself is mostly restricted due to limited computational power. Moreover, it is thereby difficult to change the Reynolds number regime as a possible change is only achieved by variation of other parameters such as the characteristic velocity. However, changing the characteristic velocity comes with its own problems as the LB error increases by $\mathcal{O}(Ma^2)$ and hence leading to a lattice velocity restriction of $Ma < 0.2$. Furthermore, the theoretical analysis of the LBDEM coupling reveals error terms on macroscale caused by the hydrodynamic fluid-solid interaction force occur. Remedy of both problems could be solved in future by:

1. Substitution of the external hydrodynamic forcing term in Eq. (3.24) by an external forcing according to Guo et al. (2002) to remove additional error terms on the macroscale, i.e. $F_{ext} = \left(1 - \frac{1}{2\tau}\right) \omega_i \left[\frac{\mathbf{e}_i - \mathbf{u}}{c_s^2} + \frac{\mathbf{e}_i \cdot \mathbf{u}}{c_s^4}\mathbf{e}_i\right] \cdot \mathbf{F}_{hyd}$. The external hydrodynamic force $\mathbf{F}_{hyd} = B(\mathbf{x}, \tau)\rho(\mathbf{u}_s - \mathbf{u})$ could be similarly modelled to equation (3.21) on basis of the particle-fluid velocity differences and consideration of the lattice node solid fraction in $B(\mathbf{x}, \tau)$.

2. Substitution of the BGK collision term for the fluid phase by a TRT or MRT scheme to obtain greater flexibility in the parameter choice and to keep slip-velocities under control. Additionally, a MRT scheme could also lead to a more stable algorithm when simulating high Reynolds number flows. "Calibration" of the various introduced relaxation parameters could be either achieved by theoretical analysis of slip velocities in a channel flow setup, as it has been performed for IBM in the literature (e.g. Seta et al. (2014)). Alternatively, calibration could be achieved by empirically determination of a relaxation parameter correlation for any (or all) of the above studied cases (e.g. normal particle-particle collision to study lubrication forces).

Assessment of above suggestions could be achieved by simulation of the same cases in chapter 3 and 4.

Further work to study the physics of suspensions could be carried out on the following topics:

1. Comparison of a DEM employing a lubrication interaction model to LBDEM showed that viscosities are somewhat overestimated for frictional particles. An investigation of the observed viscosity difference and a probable explanation is outstanding.

2. Continuation of the work in last chapter on linking contact stress and viscous dissipation by inclusion of friction between particles.

3. Further post-processing of the simulations in the last chapter with regard to PDFs of particle-particle gap distances. Combination of the PDFs of particle-particle gap distances and relative particle-particle velocities could possibly lead to new mod-

elling approaches which allow for decoupling of particle kinematics and microscale structures. In that case, or rather for the latter case, the gulf between the porous media and rheology community could possibly bridged by an attempt to utilise existent pore space or simplified hydraulic radius models.

4. The LBDEM coupling allows for simulation of neutrally buoyant particles which is not straightforward to achieve with other fluid-solid coupling. The feature of a less restricted density difference could prove advantageous for studying the influence of particle inertia on suspension rheology.

5. Consideration of non-spherical particles. A superquadric shape feature has been implemented into the LBDEM code. However, numerical instabilities for moving particles leading to simulation crashes were experienced. Further tests and analysis of the problem would be necessary before the superquadric feature could be extensively used.

A

Modified non-equilibrium bounce back solid phase collision term for PSM

In chapter 3 is mentioned a modification by Holdych (2003) to the non-equilibrium bounce back solid phase collision term (3.6) suggested by Noble and Torcyznski (1998). Holdych (2003) substituted the fluid velocity by the particle velocity, i.e. Eq. (3.6) is re-written as:

$$\Omega_i^s = f_{-i} - f_i + f_i^{eq}(\mathbf{u}_s) - f_{-i}^{eq}(\mathbf{u}_s) \; . \tag{A.1}$$

However, instability issues are not only reported in the literature as explained in section 3.1, but were also found during work in this PhD project. A possible explanation for found instabilities is given here. Therefore, the solid phase collision term (A.1) is substituted into the hydrodynamic force expression (3.10) analogously to the analysis of the unmodified solid phase collision terms in section 3.3.1.1. The resulting hydrodynamic force, obtained on a $D2Q9$ lattice, reads then:

$$F_{hyd,\alpha}^{Holdych} = \frac{h^d}{\Delta t} \sum_n B_n \cdot 2 \cdot \rho(u_{s,\alpha} - u_\alpha) \; . \tag{A.2}$$

Equation (A.2) is apart from a factor of 2 identical to the previously found hydrodynamic force equations (3.20) and (3.21). This means that the hydrodynamic force acting on particles is twice as large for the proposed modification by Holdych (2003) in comparison to the original suggestions by Noble and Torcyznski (1998). It was found that simulations of fixed particles can be conducted with the modified non-equilibrium bounce back method (A.1). For freely moving particles however, the doubled hydrodynamic forces and torques on the particles could be reason for the found simulation instabilities due to exaggerated particle dynamics. In fact, if equation (A.1) is multiplied by a factor of 0.5, i.e.

$$\Omega_i^s = 0.5 \left[f_{-i} - f_i + f_i^{eq}(\mathbf{u}_s) - f_{-i}^{eq}(\mathbf{u}_s) \right] \; , \tag{A.3}$$

the resulting hydrodynamic force expression does not contain the factor of 2 and simulations of freely moving particles are found to be seemingly stable.

B

Grand-resistance matrix implementiation

For evaluation of the lubrication interactions with the GRM Eq. (5.6), the resistance tensors have the following properties:

$$A_{ij}^{(\alpha\beta)} = A_{ji}^{(\beta\alpha)} \,, \tag{B.1}$$

$$B_{ij}^{(\alpha\beta)} = \tilde{B}_{ji}^{(\beta\alpha)} \,, \tag{B.2}$$

$$C_{ij}^{(\alpha\beta)} = C_{ji}^{(\beta\alpha)} \,, \tag{B.3}$$

$$G_{ijk}^{(\alpha\beta)} = \tilde{G}_{kji}^{(\beta\alpha)} \,, \tag{B.4}$$

$$H_{ijk}^{(\alpha\beta)} = \tilde{H}_{kji}^{(\beta\alpha)} \,. \tag{B.5}$$

Defining the unit vector $\mathbf{e}$ along the line of centres, it can be written:

$$A_{ij}^{(\alpha\beta)} = X_{\alpha\beta}^{A} e_i e_j + Y_{\alpha\beta}^{A}(\delta_{ij} - e_i e_j) \,, \tag{B.6}$$

$$B_{ij}^{(\alpha\beta)} = \tilde{B}_{ji}^{(\beta\alpha)} = Y_{\alpha\beta}^{B} \epsilon_{ijk} e_k \,, \tag{B.7}$$

$$C_{ij}^{(\alpha\beta)} = X_{\alpha\beta}^{C} e_i e_j + Y_{\alpha\beta}^{C}(\delta_{ij} - e_i e_j) \,, \tag{B.8}$$

$$G_{ijk}^{(\alpha\beta)} = X_{\alpha\beta}^{G}(e_i e_j - \frac{1}{3}\delta ij) + Y_{\alpha\beta}^{G}(e_i \delta_{jk} + e_j \delta_{ik} - 2 e_i e_j e_k) \,, \tag{B.9}$$

$$H_{ijk}^{(\alpha\beta)} = Y_{\alpha\beta}^{H}(\epsilon_{ikl} e_l e_j + \epsilon_{jkl} e_l e_i) \,. \tag{B.10}$$

The grand-resistance matrix (5.6) consists of different lubrication interactions:

- Squeezing force in normal direction: $X_{\alpha\beta}^{A} e_i e_j$
- Shearing force in tangential direction: $Y_{\alpha\beta}^{A}(\delta_{ij} - e_i e_j)$

- Force due to particle rotation: $Y^B_{\alpha\beta}\epsilon_{ijk}e_k$
- Torque due to tangential relative motion: $Y^B_{\alpha\beta}\epsilon_{ijk}e_k$
- Torque due to particle rotation (twisting excluded): $Y^C_{\alpha\beta}(\delta_{ij} - e_ie_j)$
- Torque due to twisting motion: $X^C_{\alpha\beta}e_ie_j$
- Force and torque due to a straining motion $G^{(\alpha\beta)}_{ijk}$ and $H^{(\alpha\beta)}_{ijk}$, respectively.

Except for the second-last contribution (twisting terms), all the contributions have been implemented in LAMMPS/LIGGGHTS. The twisting contribution has been omitted because its contribution to the overall lubrication interaction is neglectable and additionally would require expensive computations of coefficients in the $X^C_{\alpha\beta}$ terms.

B.1 Geometrical and kinematic properties

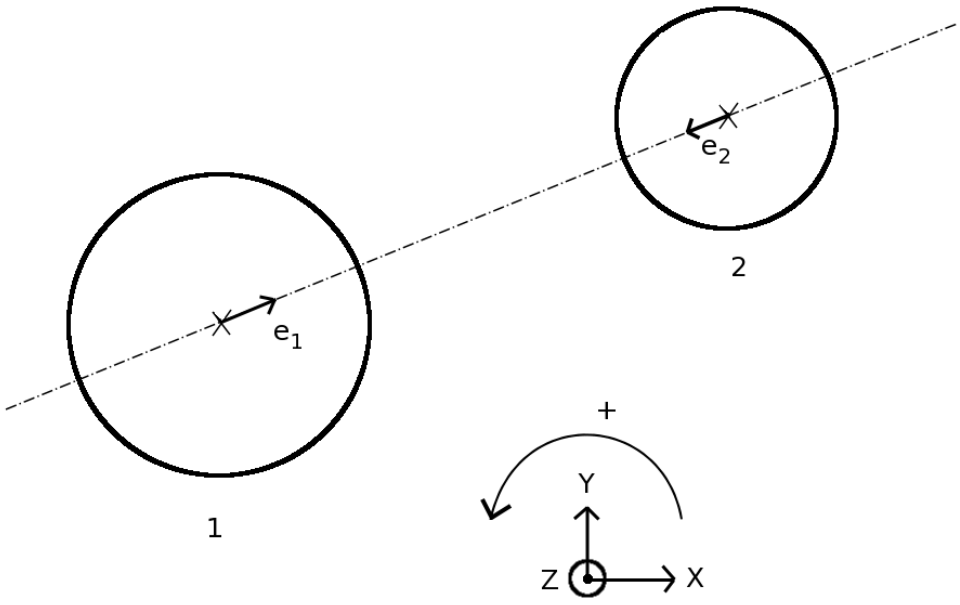

Fig. B.1.: Illustration of the main coordinate system, which follows the right-hand rule, and the unit vector e pointing away from the particle for which lubrication forces and torques are calculated.

A particle i has a linear and angular velocity, given by $\mathbf{U}_i$ and $\mathbf{\Omega}_i$, respectively. The particle positions for particle 1 and particle 2 are defined in the main coordinate system

x-y-z by $\mathbf{x}_1$ and $\mathbf{x}_2$, respectively. The particle centre-to-centre direction can be described by

$$\mathbf{x}_{12} = \mathbf{x}_2 - \mathbf{x}_1 \tag{B.11}$$

and the particle centre-to-centre distance is

$$|\mathbf{x}_{12}| = \sqrt{\mathbf{x}_{12}^2} \, . \tag{B.12}$$

The normal velocity components between the particles can be determined by projecting the particle velocity onto the particle centre-to-centre line. Therefore, a unit vector $\mathbf{e}$ pointing away from the particle as depicted in figure B.1 is defined:

$$\mathbf{e} = \frac{\mathbf{x}_{12}}{|\mathbf{x}_{12}|} \, . \tag{B.13}$$

It follows for the normal velocity components

$$\mathbf{U}_{1,n} = (\mathbf{U}_1 \cdot \mathbf{e})\mathbf{e} \, , \tag{B.14a}$$

$$\mathbf{U}_{2,n} = (\mathbf{U}_2 \cdot \mathbf{e})\mathbf{e} \, . \tag{B.14b}$$

The tangential velocity components read:

$$\mathbf{U}_{1,t} = \mathbf{U}_1 - \mathbf{U}_{1,n} \, , \tag{B.15a}$$

$$\mathbf{U}_{2,t} = \mathbf{U}_2 - \mathbf{U}_{2,n} \, . \tag{B.15b}$$

Similarly, the different components for the angular velocities can be obtained:

$$\boldsymbol{\Omega}_{1,n} = (\boldsymbol{\Omega}_1 \cdot \mathbf{e})\mathbf{e} \, , \tag{B.16a}$$

$$\boldsymbol{\Omega}_{2,n} = (\boldsymbol{\Omega}_2 \cdot \mathbf{e})\mathbf{e} \, . \tag{B.16b}$$

The tangential angular velocity components are:

$$\boldsymbol{\Omega}_{1,t} = \boldsymbol{\Omega}_1 - \boldsymbol{\Omega}_{1,n} \, , \tag{B.17a}$$

$$\boldsymbol{\Omega}_{2,t} = \boldsymbol{\Omega}_2 - \boldsymbol{\Omega}_{2,n} \, . \tag{B.17b}$$

The expressions $e_i e_j$ and $\delta_{ij} - e_i e_j$ in the above equations (B.6)-(B.10) describe normal and tangential contributions. The Levi-Cita symbol is defined in the three-dimensional case as:

$$\epsilon_{ijk} = \begin{cases} +1 \text{ , if } (ijk) \text{ is } (1,2,3),(2,3,1),(3,1,2) \\ -1 \text{ , if } (ijk) \text{ is } (3,2,1),(1,3,2),(2,1,3) \\ 0 \text{ , if } i=j \text{ or } j=k \text{ or } k=i \end{cases} \tag{B.18}$$

Hence, the expression $\epsilon_{ijk} e_k$ in Eqs. (B.6)-(B.10) describes the cross-product between the particle unit vector and another vector, e.g. linear or angular velocity vector. For example, here demonstrated for $\mathbf{T}_1$ under the assumption that $\mathbf{U}_2 = \mathbf{0}$, $\mathbf{\Omega}_1 = \mathbf{0}$, $\mathbf{\Omega}_2 = \mathbf{0}$, and quiescent fluid field:

$$\begin{pmatrix} T_{1_1} \\ T_{1_2} \\ T_{1_3} \end{pmatrix}_{k=1} = \eta_f Y_{11}^B \begin{pmatrix} \epsilon_{111} & \epsilon_{121} & \epsilon_{131} \\ \epsilon_{211} & \epsilon_{221} & \epsilon_{231} \\ \epsilon_{311} & \epsilon_{321} & \epsilon_{331} \end{pmatrix} e_1 \begin{pmatrix} U_{1_1} \\ U_{1_2} \\ U_{1_3} \end{pmatrix} = \eta_f Y_{11}^B \begin{pmatrix} 0 \\ U_{1_3} e_{1_1} \\ -U_{1_2} e_{1_1} \end{pmatrix}, \tag{B.19a}$$

$$\begin{pmatrix} T_{1_1} \\ T_{1_2} \\ T_{1_3} \end{pmatrix}_{k=2} = \eta_f Y_{11}^B \begin{pmatrix} \epsilon_{112} & \epsilon_{122} & \epsilon_{132} \\ \epsilon_{212} & \epsilon_{222} & \epsilon_{232} \\ \epsilon_{312} & \epsilon_{322} & \epsilon_{332} \end{pmatrix} e_2 \begin{pmatrix} U_{1_1} \\ U_{1_2} \\ U_{1_3} \end{pmatrix} = \eta_f Y_{11}^B \begin{pmatrix} -U_{1_3} e_{1_3} \\ 0 \\ U_{1_2} e_{1_2} \end{pmatrix}, \tag{B.19b}$$

$$\begin{pmatrix} T_{1_1} \\ T_{1_2} \\ T_{1_3} \end{pmatrix}_{k=3} = \eta_f Y_{11}^B \begin{pmatrix} \epsilon_{113} & \epsilon_{123} & \epsilon_{133} \\ \epsilon_{213} & \epsilon_{223} & \epsilon_{233} \\ \epsilon_{313} & \epsilon_{323} & \epsilon_{333} \end{pmatrix} e_3 \begin{pmatrix} U_{1_1} \\ U_{1_2} \\ U_{1_3} \end{pmatrix} = \eta_f Y_{11}^B \begin{pmatrix} U_{1_2} e_{1_3} \\ -U_{1_1} e_{1_3} \\ 0 \end{pmatrix}. \tag{B.19c}$$

Summing up the different k components (B.19a)-(B.19c), the final result for the torque reads

$$\begin{pmatrix} T_{1_1} \\ T_{1_2} \\ T_{1_3} \end{pmatrix} = \eta_f Y_{11}^B \begin{pmatrix} U_{1_2} e_3 - U_{1_3} e_2 \\ U_{1_3} e_1 - U_{1_1} e_3 \\ U_{1_1} e_2 - U_{1_2} e_1 \end{pmatrix} \tag{B.20}$$

which is equivalent to the cross-product between $\mathbf{U}_1$ and $\mathbf{e}_1$: $\mathbf{T}_1 = \eta_f Y_{11}^B (\mathbf{U}_1 \times \mathbf{e}_1)$. Generally expressed it is $\epsilon_{ijk} e_k x_i = \mathbf{x} \times \mathbf{e}$ and it follows that for the B_{ij} and $\tilde{B}_{ji}$ terms $\mathbf{U} \times \mathbf{e}$ and $\mathbf{e} \times \boldsymbol{\omega}$ have to be evaluated, respectively.

For the expressions (B.6)-(B.10) which are multiplied by a symmetric strain rate tensor E^∞ can be expressed as:

$$\begin{aligned} &(e_j e_k E_{jk} - \frac{1}{3}\delta_{jk} E_{jk}) d_i = \\ &(e_1 e_1 E_{11} + e_2 e_2 E_{22} + e_3 e_3 E_{33} + 2e_1 e_2 E_{12} + 2e_1 e_3 E_{13} + 2e_2 e_3 E_{23}) e_i - \frac{1}{3}(E_{11} + E_{22} + E_{33}) e_i \\ &= \{[\mathbf{E} \cdot \mathbf{e}] \cdot \mathbf{e} - \frac{1}{3} tr(\mathbf{E})\} \mathbf{e} \,, \end{aligned} \tag{B.21}$$

$$(e_j\delta_{ki} + e_k\delta_{ji} - 2e_je_ke_i)E_{jk} = 2(\mathbf{E}\cdot\mathbf{e}) - 2([\mathbf{E}\cdot\mathbf{e}]\cdot\mathbf{e})\cdot\mathbf{e}\ , \tag{B.22}$$

and

$$(\epsilon_{jil}e_le_k + \epsilon_{kil}e_le_j)E_{jk} = -2((\mathbf{E}\cdot\mathbf{e})\times\mathbf{e})\ . \tag{B.23}$$

B.2 Pairwise lubrication forces

For the sake of concisness, the velocity terms here contain also the background fluid velocity (which is not explicitly written out) as in Eq. (5.6), i.e. $\mathbf{U} = \mathbf{v}^{\infty}(\mathbf{x}_1) - \mathbf{U}_1$.

B.2.1 Squeezing force / normal force

$$\mathbf{F}_{normal} = \eta_f(\mathbf{A}_{11}\mathbf{U}_1 + \mathbf{A}_{12}\mathbf{U}_2) = \eta_f(X^A_{11}\mathbf{U}_{1,n} + X^A_{12}\mathbf{U}_{2,n}) \tag{B.24}$$

B.2.2 Shearing force / tangential force

$$\mathbf{F}_{tangtenial} = \eta_f(\mathbf{A}_{11}\mathbf{U}_1 + \mathbf{A}_{12}\mathbf{U}_2) = \eta_f(Y^A_{11}\mathbf{U}_{1,t} + Y^A_{12}\mathbf{U}_{2,t}) \tag{B.25}$$

B.2.3 Force due to rotating particles

$$\mathbf{F}_{rotational} = \eta_f(\tilde{\mathbf{B}}_{11}\boldsymbol{\Omega}_1 + \tilde{\mathbf{B}}_{12}\boldsymbol{\Omega}_2) = \eta_f(Y^B_{11}(\mathbf{e}\times\boldsymbol{\omega}_1) + Y^B_{21}(\mathbf{e}\times\boldsymbol{\omega}_2)) \tag{B.26}$$

B.2.4 Torque due to tangential relative motion

$$\mathbf{T}_{tangential} = \eta_f(\mathbf{B}_{11}\mathbf{U}_1 + \mathbf{B}_{12}\mathbf{U}_2) = \eta_f(Y^B_{11}(\mathbf{U}_1\times\mathbf{e}) + Y^B_{12}(\mathbf{U}_1\times\mathbf{e})) \tag{B.27}$$

B.2.5 Torque due to rotating particles

$$\mathbf{T}_{rotational} = \eta_f(\mathbf{C}_{11}\boldsymbol{\Omega}_1 + \mathbf{C}_{12}\boldsymbol{\Omega}_2) = \eta_f(Y^C_{11}\boldsymbol{\Omega}_{1,t} + Y^C_{12}\boldsymbol{\Omega}_{2,t}) \tag{B.28}$$

B.2.6 Force due to strain rate tensor

$$\begin{aligned}\mathbf{F}_{strain} &= \eta_f(\tilde{\mathbf{G}}_{11}\mathbf{E}^{\infty} + \tilde{\mathbf{G}}_{12}\mathbf{E}^{\infty}) \\ &= \eta_f(X_{11}^G + X_{12}^G)\{[\mathbf{E}\cdot\mathbf{e}]\cdot\mathbf{e} - \frac{1}{3}tr(\mathbf{E})\}\mathbf{e} + \eta_f(Y_{11}^G + Y_{12}^G)[2(\mathbf{E}\cdot\mathbf{e}) - 2([\mathbf{E}\cdot\mathbf{e}]\cdot\mathbf{e})\cdot\mathbf{e}]\end{aligned} \tag{B.29}$$

B.2.7 Torque due to strain rate tensor

$$\mathbf{T}_{strain} = \eta_f(\tilde{\mathbf{H}}_{11}\mathbf{E}^{\infty} + \tilde{\mathbf{H}}_{12}\mathbf{E}^{\infty}) = \eta_f(Y_{11}^H + Y_{12}^H)[-2((\mathbf{E}\cdot\mathbf{e})\times\mathbf{e})] \tag{B.30}$$

B.2.8 Resistance functions

The resistance functions, $X_{\alpha\beta}^A$, $Y_{\alpha\beta}^A$, $Y_{\alpha\beta}^B$, $Y_{\alpha\beta}^C$, $X_{\alpha\beta}^G$, $Y_{\alpha\beta}^G$, $Y_{\alpha\beta}^H$ are evaluated to the order of $\mathcal{O}\left(log(\xi^{-1})\right)$ according to Kim and Karrila (2005) who list comprehensively the resistance functions and symmetry relations in chapter 11 of their book.

Bibliography

Ai, Jun, Jian-Fei Chen, J. Michael Rotter and Jin Y. Ooi (2011). „Assessment of rolling resistance models in discrete elements simulations“. In: *Powder Technology* 206, pp. 269–282 (cit. on p. 12).

Aidun, Cyrus K. and Jonathan R. Clausen (2010). „Lattice-Boltzmann Method for Complex Flows“. In: *Annual Review of Fluid Mechanics* 42, pp. 439–472 (cit. on p. 26).

Aidun, Cyrus K. and Yannan Lu (1995). „Lattice Boltzmann Simulation of Solid Particles Suspended in Fluid“. In: *Journal of Statistical Physics* 81.1/2, pp. 49–61 (cit. on p. 49).

Aidun, Cyrus K., Yannan Lu and E.-Jiang Ding (1998). „Direct Analysis of particulate suspensions with inertia using the discrete Boltzmann equation“. In: *Journal of Fluid Mechanics* 373, pp. 287–311 (cit. on pp. 27, 49).

Ancey, Christoph, Philippe Coussot and Pierre Evesque (1999). „A theoretical framework for granular suspensions in a steady simple shear flow“. In: *Journal of Rheology* 43.6, pp. 1673–1699 (cit. on pp. 42–44).

Anderson, T. B. and R. Jackson (1967). „A fluid mechanical description of fluidized beds. Equations of motion“. In: *Industrial & Engineering Chemistry Fundamentals* 6.4, pp. 527–539 (cit. on pp. 4, 8, 32).

Andreotti, B., Y. Forterre and O. Pouliquen (2013). *Granular Media: Between Fluid and Solid*. Cambridge University Press (cit. on p. 9).

Andreotti, Bruno, Jean-Louis Barrat and Claus Heussinger (2012). „Shear flow of non-Brownian suspensions close to jamming“. In: *Physical Review Letters* 109.10, p. 105901 (cit. on pp. 40, 101, 129, 131, 137).

Bagnold, R. A. (1954). „Experiments on a Gravity-Free Dispersion of Large Solid Spheres in a Newtonian Fluid under Shear“. In: *Proceedings of the Royal Society of London. Series A, Mathematical and Physical* 225.1160, pp. 49–63 (cit. on p. 135).

Batchelor, G. K (1970). „The stress system in a suspension of force-free particles“. In: *Journal of Fluid Mechanics* 41.3, pp. 545–570 (cit. on pp. 36, 38, 55).

Batchelor, G. K. (1976). „Brownian diffusion of particles with hydrodynamic interaction“. In: *Journal of Fluid Mechanics* 74.1, pp. 1–29 (cit. on p. 13).

Batchelor, G. K and J. T. Green (1972a). „The determination of the bulk stress in a suspension of spherical particles to order c^2“. In: *Journal of Fluid Mechanics* 56.3, pp. 401–427 (cit. on p. 45).

Batchelor, G. K and J. T. Green (1972b). „The hydrodynamic interaction of two small freely-moving spheres in a linear flow field“. In: *Journal of Fluid Mechanics* 56.2, pp. 375–400 (cit. on p. 78).

Beetstra, R., M. A. van der Hoef and J. A. M. Kuipers (2007a). „Drag Force of Intermediate Reynolds Number Flow Past Mono- and Bidisperse Arrays of Spheres“. In: *AIChE Journal* 53.2, pp. 489–501 (cit. on pp. 23, 34, 35).

– (2007b). „Erratum“. In: *AIChE Journal* 53, p. 3020 (cit. on p. 35).

– (2007c). „Numerical study of segregation using a new drag force correlation for polydisperse systems derived from lattice-Boltzmann simulations“. In: *Chemical Engineering Science* 62, pp. 246–255 (cit. on pp. 23, 34).

Benyahia, Sofiane, Nadhava Syamlal and Thomas J. O'Brien (2006). „Extension of Hill-Koch-Ladd drag correlation over all ranges of Reynolds number and solid volume fraction“. In: *Powder Technology* 162, pp. 166–174 (cit. on p. 34).

Bhatnagar, P.L., E. P. Gross and M. Krook (1954). „A Model for Collision Processes in Gases. I. Small Amplitude Processes in Charged and Neutral One-Component Systems“. In: *Physical Review* 94.3, pp. 511–525 (cit. on pp. 17, 52, 86, 106).

Bluemink, J. J., D. Lohse, A. Prosperetti and L. Van Wijngaarden (2008). „A sphere in a uniformly rotating or shearing flow“. In: *Journal of Fluid Mechanics* 600, pp. 201–233 (cit. on p. 69).

Boltzmann, Ludwig (1872). „Weitere Studien über das Wärmegleichgewicht unter Gasmolekülen“. In: *Sitzungsberichte der kaiserlichen Akademie der Wissenschaften: LXVI. Band* (cit. on pp. 15, 16).

Bossis, G. and John F. Brady (1984). „Dynamic simulation of sheared suspensions. I. General method“. In: *The Journal of Chemical Physics* 80.10, pp. 5141–5154 (cit. on p. 13).

Boyer, Francois, Elisabeth Guazelli and Olivier Pouliquen (2011). „Unifying suspension and granular rheology“. In: *Physical Review Letters* 107.18, p. 188301 (cit. on pp. 44, 46, 47).

Brady, John F. and Georges Bossis (1988). „Stokesian Dynamics“. In: *Annual Review of Fluid Mechanics* 20, pp. 111–157 (cit. on p. 13).

Brenner, Howard (1961). „The slow motion of a sphere through a viscous fluid towards a plane surface“. In: *Chemical Engineering Science* 16, pp. 242–251 (cit. on p. 12).

Brenner, Howard and Michael E. O'Neill (1972). „On the Stokes resistance of multiparticle systems in a linear shear field“. In: *Chemical Engineering Science* 27, pp. 1421–1439 (cit. on p. 13).

Buick, J. M. and C. A. Greated (2000). „Gravity in a lattice Boltzmann model“. In: *Physical Review E* 61.5, pp. 5307–5320 (cit. on p. 59).

Cassar, C., M. Nicolas and O. Pouliquen (2005). „Submarine granular flows down inclined planes“. In: *Physics of Fluids* 17.10, p. 103301 (cit. on pp. 44, 46).

Chalamala, Babu R., Thiagarajan Soundappan, Graham R. Fisher et al. (2014). „Redox Flow Batteries: An Engineering Perspective“. In: *Proceedings of the IEEE* 102.6, pp. 976–999 (cit. on pp. 1, 2).

Chen, Shiyi and Gary D. Doolen (1998). „Lattice Boltzmann method for fluid flows“. In: *Annual Review of Fluid Mechanics* 30, pp. 329–364 (cit. on pp. 21, 26, 53).

Chialvo, Sebastian, Jin Sun and Sankaran Sundaresan (2012). „Bridging the rheology of granular flows in three regimes“. In: *Physical Review E* 85.2, p. 021305 (cit. on p. 47).

Coetzee, C. J. (2017). „Review: Calibration of the discrete element method“. In: *Powder Technology* 310, pp. 104–142 (cit. on p. 12).

Cook, B. K., D. F. Bout, O. E. Strack, J. R. Williams and S. M. Johnson (2004a). „DEM-fluid model development for near-wellbore mechanics“. In: *Numerical Modeling Micromechanics via Particle Methods - 2004 Proceedings of the 2nd International PFC Symposium, Kyoto, Japan*. Ed. by Y. Shimizu, R. Hart and Peter Cundall. CRC Press. Chap. 37, pp. 301–309 (cit. on p. 51).

Cook, Benjamin K., David R. Noble and John R. Williams (2004b). „A direct simulation method for particle-fluid systems“. In: *Engineering Computations* 21.2/3/4, pp. 151–168 (cit. on p. 50).

Cooley, M. D. A. and M. E. O'Neill (1969). „On the slow motion generated in a viscous fluid by the approach of a sphere to a plane wall or stationary sphere“. In: *Mathematika* 16, pp. 37–49 (cit. on p. 13).

Cox, R. G. (1974). „The motion of suspended particles almost in contact“. In: *Internation Journal of Multiphase Flow* 1, pp. 343–371 (cit. on p. 13).

Cox, Raymond G. and Howard Brenner (1967). „The slow motion of a sphere through a viscous fluid towards a plane surface - II Small gap widths, including inertial effects“. In: *Chemical Engineering Science* 22, pp. 1753–1777 (cit. on pp. 12, 13).

CRED (n.d.). *Economic damage caused by mudslides worldwide from 1900 to 2016* (in 1,000 U.S. dollars)*. Statista - The Statistics Portal: https://www.statista.com/statistics/267837/economic-damage-caused-by-mudslides/ (accessed 9th May 2018). *Figures are as of 17th November 2016 (cit. on p. 2).

Cundall, P. A. (1988). „Formulation of a Three-dimensional Distinct Element Model - Part I. A Scheme to Detect and Represent Contacts in a System Composed of Many Polyhedral Blocks“. In: *International Journal of Rock Mechanics and Mining Sciences & Geomechanics Abstracts* 25.3, pp. 107–116 (cit. on p. 12).

Cundall, P. A. and O. D. L. Strack (1979). „A discrete numerical model for granular assemblies“. In: *Geotechnique* 29.1, pp. 47–65 (cit. on pp. 10, 11, 53, 86, 102, 103, 130).

D'Humières, Dominique and Irina Ginzburg (2009). „Viscosity independent numerical errors for lattice Boltzmann models: From recurrence equations to "magic" collision numbers“. In: *Computers and Mathematics with Applications* 58, pp. 823–840 (cit. on pp. 25, 26).

D'Humières, Dominique, Irina Ginzburg, Manfred Krafczyk, Pierre Lallemand and Li-Shi Luo (2002). „Multiple-relaxation time lattice Boltzmann models in three dimensions“. In: *Phil. Trans. R. Soc. Lond. A* 360, pp. 437–457 (cit. on pp. 24, 25).

Da Cunha, F. R. and E. J. Hinch (1996). „Shear-induced dispersion in a dilute suspension of rough spheres“. In: *Journal of Fluid Mechanics* 309, pp. 211–223 (cit. on p. 14).

Daghoogi, Mohsen and Iman Borazjani (2015). „The influence of inertia on the rheology of a periodic suspension of neutrally buoyant rigid ellipsoids“. In: *Journal of Fluid Mechanics* 781, pp. 506–549 (cit. on p. 55).

Davis, Robert H., Jean-Marc Serayssol and E. J. Hinch (1986). „The elastohydrodynamic collision of two spheres“. In: *Journal of Fluid Mechanics* 163, pp. 479–497 (cit. on p. 14).

Davis, Robert H., Yu Zhao, Kevin P. Galvin and Helen J. Wilson (2003). „Solid-solid contacts due to surface roughness and their effects on suspension behaviour“. In: *Philosophical Transactions: Mathematical, Physical and Engineering Sciences* 361.1806, pp. 871–894 (cit. on pp. 14, 109).

Debbas, S. and H. Rumpf (1966). „On the randomness of beds packed with spheres or irregular shaped particles“. In: *Chemical Engineering Science* 21, pp. 583–607 (cit. on p. 81).

Deen, N. G. and J. A. M. Kuipers (2014). „Direct Numerical Simulation (DNS) of mass, momentum and heat transfer in dense fluid-particle systems“. In: *Current Opinion in Chemical Engineering* 5, pp. 84–89 (cit. on p. 5).

Deen, Niels G., Sebastian H. L. Kriebitzsch, Martin A. van der Hoef and J. A. M. Kuipers (2012). „Direct numerical simulation of flow and heat transfer in dense fluid-particle systems“. In: *Chemical Engineering Science* 81, pp. 329–344 (cit. on p. 5).

Derksen, J. J. and S. Sundaresan (2007). „Direct numerical simulation of dense Suspensions: Wave instabilities in liquid-fluidized beds“. In: *Journal of Fluid Mechanics* 587, pp. 303–336 (cit. on p. 5).

Di Felice, R. (1994). „The voidage function for fluid-particle interaction systems“. In: *International Journal for Multiphase Flow* 20.1, pp. 153–159 (cit. on p. 35).

Ding, E.-Jiang and Cyrus K. Aidun (2003). „Extension of the Lattice-Boltzmann Method for Direct Simulation of Suspended Particles Near Contact“. In: *Journal of Statistical Physics* 112.3/4, pp. 685–708 (cit. on pp. 29, 30).

Drew, D. A. (1983). „Mathematical modelling of two-phase flow“. In: *Annual Review of Fluid Mechanics* 15, pp. 261–291 (cit. on pp. 7, 8).

Duduta, Mihai, Bryan Ho, Vanessa C. Wood et al. (2011). „Semi-Solid Lithium Rechargeable Flow Battery“. In: *Advanced Energy Materials* 1.4, pp. 511–516 (cit. on p. 1).

Eilers, H. (1941). „Die Viskosität von Emulsionen hochviskoser Stoffe als Funktion der Konzentration“. In: *Kolloid-Zeitschrift* 97.3, pp. 313–321 (cit. on pp. 45, 46).

Einstein, Albert (1905). „Eine neue Bestimmung der Moleküldimensionen“. PhD thesis. Universität Zürich (cit. on pp. 45, 129).

– (1911). „Berichtigung zu meiner Arbeit: "Eine neue Bestimmung der Moleküldimensionen"“. In: *Annalen der Physik* 14.1, pp. 406–407 (cit. on pp. 45, 129).

Enwald, H., E. Peirano and A.-E. Almstedt (1996). „Eulerian Two-Phase Flow Theory Applied To Fluidization“. In: *International Journal for Multiphase Flow* 22, pp. 21–66 (cit. on pp. 3, 7, 8, 33).

Ergun, S. (1952). „Fluid flow through packed columns“. In: *Chemical Engineering Progress* 48, pp. 89–94 (cit. on p. 34).

European Commision (May 2009). *The economics of climate change adaption in EU coastal areas*. Summary report. Study done on behalf of the European Commission (Directorate-General for Maritime Affairs and Fisheries) by Policy Research Corporation (in association with MRAG) (cit. on p. 1).

Favier, J. F., M. H. Abbaspour-Fard, M. Kremmer and A. O. Raji (1999). „Shape representation of axi-symmetrical, non-spherical particles in discrete element simulation using multi-element model particles“. In: *Engineering Computations* 16.4, pp. 467–480 (cit. on p. 12).

Feng, Zhi-Gang and Efstathios E. Michaelides (2004). „The immersed boundary-lattice Boltzmann method for solving fluid-particles interaction problems“. In: *Journal of Computational Physics* 195, pp. 602–628 (cit. on p. 27).

– (2005). „Proteus: A direct forcing method in the simulations of particulate flows“. In: *Journal of Computational Physics* 202, pp. 20–51 (cit. on pp. 27, 49, 85).

Ferziger, Joel H. and Milovan Perić (2002). *Computational Methods for Fluid Dynamics*. 3rd rev. Springer-Verlag (cit. on pp. 19, 30).

Frankel, N. A. and Andreas Acrivos (1967). „On the viscosity of a concentrated suspension of solid spheres“. In: *Chemical Engineering Science* 22, pp. 847–853 (cit. on p. 129).

Frisch, U., B. Hasslacher and Y. Pomeau (1986). „Lattice-gas automata for the Navier-Stokes equation“. In: *Physical Review Letters* 56.14, pp. 1505–1508 (cit. on pp. 15, 16).

Gallier, Stany, Francois Peters and Laurent Lobry (2018). „Simulations of sheared dense noncolloidal suspensions: Evaluation of the role of long-range hydrodynamics“. In: *Physical Review Fluids* 3.4, p. 042301 (cit. on pp. 101, 118).

Gibson, Ian, David Rosen and Brent Stucker (2015). *Additive Manufacturing Technologies: 3D Printing, Rapid Prototyping, and Direct Digital Manufacturing*. Springer (cit. on p. 2).

Ginzburg, Irina (2005). „Equilibrium-type and link-type lattice Boltzmann models for generic advection and anisotropic-dispersion equation“. In: *Advances in Water Resources* 28, pp. 1171–1195 (cit. on p. 25).

Glowinski, R., T.-W. Pan, T. I. Hesla and D. D. Joseph (1999). „A distributed Lagrange multiplier/fictitious domain method for particulate flows“. In: *International Journal for Multiphase Flow* 25, pp. 755–794 (cit. on pp. 30, 49).

Glowinski, R., T.W. Pan and J. Périaux (1998). „Distributed Lagrange multiplier methods for incompressible viscous flow around moving rigid bodies“. In: *Computer Methods in Applied Mechanics and Engineering* 151, pp. 181–194 (cit. on p. 30).

Goldman, A. J., R. G. Cox and H. Brenner (1967a). „Slow viscous motion of a sphere parallel to a plane wall - I Motion through a quiescent fluid“. In: *Chemical Engineering Science* 22, pp. 637–651 (cit. on p. 12).

– (1967b). „Slow viscous motion of a sphere parallel to a plane wall - II Couette Flow“. In: *Chemical Engineering Science* 22, pp. 653–660 (cit. on p. 12).

Gombosi, Tamas I. (1994). *Gaskinetic Theory*. Cambridge Atmospheric and Space Science Series. Cambridge University Press (cit. on p. 3).

Gondret, P., M. Lance and L. Petit (2002). „Bouncing motion of spherical particles in fluids“. In: *Physics of Fluids* 14.2, pp. 643–652 (cit. on p. 14).

Guazzelli, Élisabeth and Jeffrey Morris (2012). *A physical introduction to suspension dynamics*. Cambridge Texts in Applied Mathematics (Book 45). Cambridge University Press (cit. on pp. 68, 74, 106).

Guo, Zhaoli, Chuguang Zheng and Baochang Shi (2002). „Discrete lattice effects on the forcing term in the lattice Boltzmann method“. In: *Physical Review E* 65.4, p. 046308 (cit. on pp. 23, 67, 141).

Haddadi, Hamed and Jeffrey F. Morris (2014). „Microstructure and rheology of finite inertia neutrally buoyant suspensions“. In: *Journal of Fluid Mechanics* 749, pp. 431–459 (cit. on pp. 27, 39, 43, 55, 101, 120, 123).

Haeri, S. and J. S. Shrimpton (2012). „On the application of immersed boundary, fictitious domain and body-conformal mesh methods to many particle multiphase flows“. In: *International Journal for Multiphase Flow* 40, pp. 38–55 (cit. on p. 30).

Halliday, I., L. A. Hammond, C. M. Care, K. Good and A. Stevens (2001). „Lattice Boltzmann equation hydrodynamics“. In: *Physical Review E* 64.1, p. 011208 (cit. on p. 60).

Hansford, Robert E. (1970). „On converging solid spheres in a highly viscous fluid“. In: *Mathematika* 17, pp. 250–254 (cit. on p. 13).

Hatzell, Kelsey B., Muhammad Boota and Yury Gogotsi (2015). „Materials for suspension (semi-solid) electrodes for energy and water technologies“. In: *Chemical Society Reviews* 44, pp. 8664–8687 (cit. on p. 1).

Haughey, D. P. and G. S. G. Beveridge (1969). „Structural Properties of Packed Beds - A Review“. In: *The Canadian Journal of Chemical Engineering* 47, pp. 130–140 (cit. on p. 81).

He, Xiaoyi, Qisu Zou, li-Shi Luo and Micah Dembo (1997). „Analytic Solutions of Simple Flows and Analysis of Nonslip Boundary Conditions for the Lattice Boltzmann BGK model“. In: *Journal of Statistical Physics* 87.1/2, pp. 115–136 (cit. on pp. 21, 23–25, 69, 90).

Herrmann, H. J . and S. Luding (1998). „Modeling granular media on the computer“. In: *Continuum Mechanics and Thermodynamics* 10.4, pp. 189–231 (cit. on pp. 9–11, 102, 103, 131).

Hill, R. J., D. L. Koch and A. J. C. Ladd (2001). „Moderate Reynolds number flows in ordered and random arrays of spheres“. In: *Journal of Fluid Mechanics* 448, pp. 243–278 (cit. on p. 34).

Hoef, M. A. van der, R. Beetstra and J. A. M. Kuipers (2005). „Lattice-Boltzmann simulations of low-Reynolds-number flow past mono- and bidisperse arrays of spheres: Results for the permeability and drag force“. In: *Journal of Fluid Mechanics* 528, pp. 233–254 (cit. on pp. 23, 34, 35).

Hoef, M. A. van der, M. van Sint Annaland, N. G. Deen and J. A. M. Kuipers (2008). „Numerical Simulation of Dense Gas-Solid Fluidized Beds: A Multiscale Modeling Strategy“. In: *The Annual Review of Fluid Mechanics* 40, pp. 47–70 (cit. on pp. 3–5, 33).

Hoef, M.A. van der, M. Ye, M. van Sint Annaland et al. (2006). „Multiscale Modeling of Gas-Fluidized Beds“. In: *Advances in Chemical Engineering* 31, pp. 65–149 (cit. on pp. 3, 4).

Holdych, David James (2003). „Lattice Boltzmann methods for diffuse and mobile interfaces“. PhD thesis. Graduate College of the University of Illinois (cit. on pp. 28, 50, 51, 143).

Holloway, William, Xiaolong Yin and Sankaran Sundaresan (2010). „Fluid-Particle Drag in Inertial Polydisperse Gas-Solid Suspensions“. In: *AIChE Journal* 56.8, pp. 1995–2003 (cit. on p. 36).

Huang, Haibo, Manfred Krafczyk and Xiyun Lu (2011). „Forcing term in single-phase and Shan-Chen-type multiphase Boltzmann models“. In: *Physical Review E* 84.4, p. 046710 (cit. on pp. 24, 67).

Hyväluoma, J, P. Raiskinmäki, A. Koponen, M. Kataja and J. Timonen (2005). „Lattice-Boltzmann Simulation of Particle Suspensions in Shear Flow“. In: *Journal of Statistical Physics* 121.1/2, pp. 149–161 (cit. on pp. 27, 39).

Inamuro, Takaji, Masato Yoshino and Fumimaru Ogino (1995). „A non-slip boundary condition for lattice Boltzmann simulations“. In: *Physics of Fluids* 7.12, pp. 2928–2930 (cit. on p. 22).

Jeffrey, D. J. (1982). „Low-Reynolds-Number Flow Between Converging Spheres“. In: *Mathematika* 29, pp. 58–66 (cit. on pp. 13, 90).

– (1992). „The Calculation of the low Reynolds number resistance functions for two unequal spheres“. In: *Physics of Fluids A: Fluid Dynamics* 4.1, pp. 16–29 (cit. on pp. 13, 88, 103, 104, 130).

Jeffrey, D. J. and Andreas Acrivos (1976). „The Rheological Properties of Suspensions of Rigid Particles“. In: *AIChE Journal* 22.3, pp. 417–432 (cit. on p. 46).

Jeffrey, D. J. and Y. Onishi (1984). „Calculation of the resistance and mobility functions for two unequal rigid spheres in low-Reynolds-number flow“. In: *Journal of Fluid Mechanics* 139, pp. 261–290 (cit. on pp. 13, 88, 103, 104, 130).

Jensen, Richard P., Peter J. Bosscher, Michael E. Plesha and Tuncer B. Edil (1999). „DEM simulation of granular media - Structure interface: Effects of surface roughness and particle shape“. In: *International Journal for Numerical and Analytical Methods in Geomechanics* 23, pp. 531–547 (cit. on p. 12).

Joseph, G. G., R. Zenit, M. L. Hunt and A. M. Rosenwinkel (2001). „Particle-wall collisions in a viscous fluid“. In: *Journal of Fluid Mechanics* 433, pp. 329–346 (cit. on p. 14).

Kidanemariam, Aman G. and Markus Uhlmann (2014). „Direct numerical Simulation of pattern formation in subaqueous sediment“. In: *Journal of Fluid Mechanics* 750, R2-1–R2-13 (cit. on pp. 5, 31).

Kim, S. and S. J. Karrila (2005). *Microhydrodynamics: Principles and selected applications*. Butterworth - Heinemann series in chemical engineering. Dover Publications (cit. on pp. 13, 88, 103–105, 130, 131, 150).

Kloss, Christoph, Christoph Goniva, Alice Hager, Stefan Amberger and Stefan Pirker (2012). „Models, algorithms and validation for opensource DEM and CFD-DEM“. In: *Progress in Computational Fluid Dynamics* 12.2/3, pp. 140–152 (cit. on p. 130).

Krieger, Irvin M. and Thomas J. Dougherty (1959). „A Mechanism for Non-Newtonian Flow in Suspensions of Rigid Spheres“. In: *Transactions of the Society of Rheology* 3, pp. 137–152 (cit. on pp. 46, 52, 80, 113, 133).

Krüger, T., F. Varnik and D. Raabe (2011). „Particle stress in suspensions of soft objects“. In: *Philosophical Transactions of the Royal Society A* 369, pp. 2414–2421 (cit. on p. 39).

Krüger, Timm, Halim Kusumaatmaja, Alexandr Kuzmin et al. (2017). *The Lattice Boltzmann Method - Principles and Practice*. Springer International Publishing (cit. on pp. 17, 63, 87, 107).

Kulkarni, Pandurang M. and J. F. Morris (2008). „Suspension properties at finite Reynolds number from simulated flow“. In: *Physics of Fluids* 20.4, p. 040602 (cit. on pp. 27, 101).

Kupershtokh, A. L., D. A. Medvedev and D. I. Karpov (2009). „On equations of state in a lattice Boltzmann method“. In: *Computers and Mathematics with Applications* 58, pp. 965–974 (cit. on pp. 24, 66, 67).

Ladd, A. J. C. and R. Verberg (2001). „Lattice-Boltzmann Simulations of Particle-Fluid Suspensions“. In: *Journal of Statistical Physics* 104.5/6, pp. 1191–1251 (cit. on p. 26).

Ladd, Anthony J. C. (1994a). „Numerical simulation of particulate suspensions via a discretized Boltzmann equation. Part 1. Theoretical foundation“. In: *Journal of Fluid Mechanics* 271, pp. 285–309 (cit. on pp. 26, 27, 39, 49, 85, 101).

– (1994b). „Numerical simulations of particulate suspensions via a discretized Boltzmann equation. Part 2. Numerical results“. In: *Journal of Fluid Mechanics* 271, pp. 311–339 (cit. on pp. 26, 39, 49, 85, 101).

Lallemand, Pierre and Li-Shi Luo (2000). „Theory of the lattice Boltzmann method: Dispersion, dissipation, isotropy, Galilean invariance, and stability“. In: *Physical Review E* 61.6, pp. 6546–6562 (cit. on pp. 24, 25).

Latt, Jonas, Bastien Chopard, Orestis Malaspinas, Michel Deville and Andreas Michler (2008). „Straight velocity boundaries in the lattice Boltzmann method“. In: *Physical Review E* 77.5, p. 056703 (cit. on p. 22).

Lees, A. W. and S. F. Edwards (1972). „The computer study of transport processes under extreme conditions“. In: *Journal of Physics C: Solid State Physics* 5, pp. 1921–1929 (cit. on pp. 22, 80, 108, 132).

Leonardi, Christopher R., Jon W. S. McCullogh, Bruce D. Jones and John R. Williams (2016). „Electromagnetic excitation of particle suspensions in hydraulic fractures using a coupled lattice Boltzmann-discrete element model“. In: *Computational Particle Mechanics* 3.2, pp. 125–140 (cit. on p. 51).

Lieberman, Michael A. and Allan J. Lichtenberg (2005). *Principles of plasma discharges and materials processing*. John Wiley & Sons, Inc. (cit. on pp. 16, 17).

Lishchuk, S. V., I. Halliday and C. M. Care (2006). „Shear viscosity of bulk suspensions at low Reynolds number with three-dimensional lattice Boltzmann method“. In: *Physical Review E* 74.1, p. 017701 (cit. on p. 40).

Lorenz, Eric, Alfonso Caiazzo and Alfons G. Hoekstra (2009a). „Corrected momentum exchange method for lattice Boltzmann simulations of suspension flow“. In: *Physical Review E* 79.3, p. 036705 (cit. on p. 27).

Lorenz, Eric, Alfons G. Hoekstra and Alfonso Caiazzo (2009b). „Lees-Edwards boundary conditions for lattice Boltzmann suspensions simulations“. In: *Physical Review E* 79, p. 036706 (cit. on p. 27).

Lu, G., J. R. Third and C. R. Müller (2015). „Discrete elements models for non-spherical particle systems: From theoretical developments to applications“. In: *Chemical Engineering Science* 127, pp. 425–465 (cit. on p. 12).

Lu, Jianhu, Haifeng Han, Baochang Shi and Zhaoli Guo (2012). „Immersed boundary lattice Boltzmann model based on multiple relaxation times“. In: *Physical Review E* 85.1, p. 016711 (cit. on pp. 25, 28).

Luding, S. (1998). „Physics of Dry Granular Media“. In: ed. by H.J. Hermann, JP. Hovi and S. (eds) Luding. Vol. 350. NATO ASI Series (Series E: Applied Sciences). Springer, Dordrecht. Chap. Collision & Contacts between Two Particles, pp. 285–304 (cit. on pp. 10, 102, 131).

– (2005). „Shear flow modeling of cohesive and frictional fine powder“. In: *Powder Technology* 158, pp. 45–50 (cit. on p. 12).

Luding, Stefan (2004). „The Physics of Granular Media“. In: ed. by Haye Hinrichsen and Dietrich E. Wolf. Wiley-VCH. Chap. 13: Molecular Dynamics Simulations of Granular Materials, pp. 299–324 (cit. on p. 9).

Majumdar, Samir R. and Michael E. O'Neill (1972). „On the Stokes resistance of two equal spheres in contact in a linear shear field“. In: *Chemical Engineering Science* 27, pp. 2017–2028 (cit. on p. 13).

McNamara, Guy R. and Gianluigi Zanetti (1988). „Use of the Boltzmann equation to simulate lattice-gas automata“. In: *Physical Review Letters* 61.20, pp. 2332–2335 (cit. on p. 15).

Midi, G. D. R. (2004). „On dense granular flows“. In: *The European Physical Journal E* 14.4, pp. 341–365 (cit. on pp. 44, 46).

Ness, Christopher and Jin Sun (2015). „Flow regime transitions in dense non-Brownian suspensions: Rheology, microstructural characterisation and constitutive modelling“. In: *Physical Review E* 91.1, p. 012201 (cit. on pp. 47, 101).

Nguyen, N.-Q. and A. J. C. Ladd (2002). „Lubrication corrections for lattice-Boltzmann simulations of particle suspensions“. In: *Physical Review E* 66.4, p. 046708 (cit. on pp. 29, 30, 49, 85, 88).

Noble, D. R. and J. R. Torcyznski (1998). „A lattice-Boltzmann method for partially saturated computational cells“. In: *International Journal of Modern Physics* 9.8, pp. 1189–1201 (cit. on pp. 28, 29, 49, 51–54, 85, 87, 107, 143).

Nott, Prabhu R., Elisabeth Guazelli and Olivier Pouliquen (2011). „The suspension balance model revisited“. In: *Physics of Fluids* 23.4, p. 043304 (cit. on pp. 32, 38).

O'Neill, M. E. and K. Stewartson (1967). „On the slow motion of a sphere parallel to a nearby plane wall“. In: *Journal of Fluid Mechanics* 27.4, pp. 705–724 (cit. on p. 12).

Otsubo, M., C. O'Sullivan, K. J. Hanley and W. W. Sim (2017). „The influence of particle surface roughness on elastic stiffness and dynamic response“. In: *Géotechnique* 67.5, pp. 452–459 (cit. on p. 112).

Owen, D. R. J., C. R. Leonardi and Y. T. Feng (2011). „An efficient framework for fluid-structure interaction using lattice Boltzmann method and immersed moving boundaries“. In: *International Journal for Numerical Methods in Engineering* 87, pp. 66–95 (cit. on pp. 29, 49, 50).

Pan, C., L. S. Luo and C. T. Miller (2004). „An Evaluation of lattice Boltzmann equation methods for simulating flow through porous media“. In: *Developments in Water Science* 55.PART 1, pp. 95–106 (cit. on p. 26).

Pan, Chongxun, Li-Shi Luo and Cass T. Miller (2006). „An evaluation of lattice Boltzmann schemes for porous medium flow simulation“. In: *Computer and Fluids* 35, pp. 898–909 (cit. on p. 26).

Peskin, Charles S. (2002). „The immersed boundary method“. In: *Acta Numerica* 11, pp. 479–517 (cit. on pp. 27, 30, 49).

Plimpton, Steve (1995). „Fast Parallel Algorithms for Short-Range Molecular Dynamics“. In: *Journal of Computational Physics* 117, pp. 1–19 (cit. on p. 130).

Pope, Stephen B. (2000). *Turbulent Flows*. 9th. Cambridge University Press (cit. on pp. 7, 8).

Pöschel, Thorsten and Thomas Schwager (2005). *Computational Granular Dynamics: Models and algorithms*. Springer (cit. on pp. 9, 10).

Qian, Y. H., D. D'Humières and P. Lallemand (1992). „Lattice BGK Model for Navier-Stokes Equation“. In: *Europhysics Letters* 17.6, pp. 479–484 (cit. on p. 24).

Radhakrishnan, Rangarajan (Jan. 2018). *rangrisme/lubrication: Lubrication force (Version v1.0.0)*. Zenodo. http://doi.org/10.5281/zenodo.1137305 (cit. on pp. 104, 112).

Sarkar, S, M. A. van der Hoef and J. A. M. Kuipers (2009). „Fluid-particle interaction from lattice Boltzmann simulations for flow through polydisperse random arrays of spheres“. In: *Chemical Engineering Science* 64, pp. 2683–2691 (cit. on p. 35).

Schäfer, J., S. Dippel and D. E. Wolf (1996). „Force Schemes in Simulation of Granular Materials“. In: *Journal de Physique I* 6.1, pp. 5–20 (cit. on pp. 11, 103, 131).

Seil, Philippe (2016). „LBDEMcoupling: Implementation, Validation, and Applications of a Coupled Open-Source Solver for Fluid-Particle Systems“. PhD thesis. Department for Particulate Flow Modelling, Johannes Kepler Universität Linz (cit. on pp. 49, 50).

Seta, Takeshi, Roberto Rojas, Kosuke Hayashi and Akio Tomiyama (2014). „Implicit-correction-based immersed boundary-lattice Boltzmann method with two relaxation times“. In: *Physical Review E* 89.2, p. 023307 (cit. on pp. 25, 28, 141).

Shakib-Manesh, A., P. Raiskinmäki, A. Koponen, M. Kataja and J. Timonen (2002). „Shear Stress in a Couette Flow of Liquid-Particle Suspensions“. In: *Journal of Statistical Physics* 107.1/2, pp. 67–84 (cit. on p. 39).

Shan, Xiaowen and Hudong Chen (1993). „Lattice Boltzmann model for simulating flows with multiple phases and components“. In: *Physical Review E* 47.3, pp. 1815–1820 (cit. on p. 24).

Silbert, Leonardo E. (2010). „Jamming of frictional spheres and random loose packing“. In: *Soft Matter* 6.13, pp. 2918–2924 (cit. on p. 118).

Skordos, P. A. (1993). „Initial and boundary conditions for the lattice Boltzmann method“. In: *Physical Review E* 48.6, pp. 4823–4842 (cit. on p. 22).

Smart, Jeffrey R. and David T. Leighton Jr. (1989). „Measurement of the hydrodynamic surface roughness of noncolloidal spheres“. In: *Physics of Fluids A* 1.1, pp. 52–60 (cit. on pp. 14, 109).

Stickel, Jonathan J. and Robert L. Powell (2005). „Fluid Mechanics and Rheology of Dense Suspensions“. In: *Annual Review of Fluid Mechanics* 37, pp. 129–149 (cit. on pp. 43, 44).

Strack, O. Erik and Benjamin K. Cook (2007). „Three dimensional immersed boundary conditions for moving solids in the lattice-Boltzmann method“. In: *International Journal for Numerical Methods in Fluids* 55, pp. 103–125 (cit. on p. 51).

Succi, Sauro (2001). *The Lattice Boltzmann Equation: For Fluid Dynamics and Beyond*. Numerical Mathematics and Scientific Computation. Clarendon Press (cit. on pp. 17, 53, 87, 107).

Sun, Rui and Heng Xiao (2015). „Diffusion-Based Coarse Graining in Hybrid Continuum-Discrete Solvers: Theoretical Formulation and A Priori Tests“. In: *International Journal of Multiphase Flow* 72. Department of Aerospace and Ocean Engineering, Virginia Tech, pp. 233–247 (cit. on p. 9).

Syamlal, Madhava, William Rogers and Thomas J. O'Brien (1993). *MFIX Documentation Theory Guide*. Tech. rep. Technical report, Morgantown Energy Technology Center, U.S. Department of Energy (cit. on p. 34).

Tagawa, Kazuo and Ralph J. Brodd (2009). „Lithium-Ion Batteries: Science and Technologies“. In: ed. by Masaki Yoshio, Ralph J. Brodd and Akiya Kozawa. Springer. Chap. Production Processes for Fabrication of Lithium-Ion Batteries, pp. 181–194 (cit. on p. 2).

Tanner, Roger I. and Shaocong Dai (2016). „Particle roughness and rheology in noncolloidal suspensions“. In: *Journal of Rheology* 60.4, pp. 809–818 (cit. on p. 14).

Thakur, Subhash, John P. Morrissey, Jin Sun, J. F. Chen and J. Y. Ooi (2014). „Micromechanical analysis of cohesive granular materials using the discrete element method with an Adhesive elasto-plastic contact model“. In: *Granular Matter* 16, pp. 383–400 (cit. on p. 12).

Thompson, Aidan P., Steven J. Plimpton and William Mattson (2009). „General formulation of pressure and stress tensor for arbitrary many-body interaction potentials under periodic boundary conditions“. In: *The Journal of Chemical Physics* 131, p. 154107 (cit. on pp. 38, 80, 105).

Thornton, Colin, Sharen J. Cummins and Paul W. Cleary (2011). „An investigation of the comparative behaviour of alternative contact force models during elastic collisions“. In: *Powder Technology* 210.3, pp. 189–197 (cit. on p. 11).

Trulsson, M., E. DeGiuli and M. Wyart (2017). „Effect of friction on dense suspension flows of hard particles“. In: *Physical Review E* 95.1, p. 012605 (cit. on pp. 101, 132).

Uhlmann, Markus (2005). „An immersed boundary method with direct forcing for the simulation of particulate flows“. In: *Journal of Computational Physics* 209, pp. 448–476 (cit. on pp. 31, 49).

Wachs, Anthony (2009). „A DEM-DLM/FD method for direct numerical simulation of particulate flows: Sedimentation of polygonal isometric particles in a Newtonian fluid with collisions“. In: *Computers & Fluids* 38, pp. 1608–1628 (cit. on p. 31).

Wagner, Alexander J. and Ignacio Pagonabarraga (2002). „Lees-Edwards Boundary Conditions for Lattice Boltzmann“. In: *Journal of Statistical Physics* 107.1/2, pp. 521–537 (cit. on pp. 22, 80, 108).

Wang, Min, Y. T. Feng and C. Y. Wang (2016). „Coupled bonded particle and lattice Boltzmann method for modelling fluid-solid interaction“. In: *International Journal for Numerical and Analytical Methods in Geomechanics* 40, pp. 1383–1401 (cit. on p. 51).

Wen, C. Y. and Y. H. Yu (1966). „Mechanics of fluidiszation“. In: *Chemical Engineering Progress Symposium Series* 62, pp. 100–111 (cit. on p. 34).

Werff, J. C. van der and C. G. de Kruif (1989). „Hard-sphere Colloidal Dispersion: The Scaling of Rheological Properties with Particle Size, Volume Fraction, and Shear Rate“. In: *Journal of Rheology* 33.3, pp. 421–454 (cit. on pp. 81, 82, 113).

Williams, John R. and Alex P. Pentland (1992). „Superquadrics and modal dynamics for discrete elements in interactive design“. In: *Engineering Computations* 9.2, pp. 115–127 (cit. on p. 12).

Winter, Mike G., Barbara Shearer, Derek Palmer et al. (2016). „The Economic Impact of Landslides and Floods on the Road Network“. In: *Procedia Engineering* 143. Advances in Transportation Geotechnics III, pp. 1425–1434 (cit. on p. 1).

Wolf-Gladrow, Dieter A. (2000). *Lattice-Gas Cellular Automata and Lattice Boltzmann Model - An Introduction*. Springer-Verlag Berlin Heidelberg (cit. on p. 17).

Xiao, H. and J. Sun (2011). „Algorithms in a Robust Hybrid CFD-DEM Solver for Particle-Laden Flows“. In: *Communications in computational physics* 9, pp. 297–323 (cit. on p. 33).

Yang, Fu-Ling (2006). „Interaction law for a collision between two solid particles in a viscous liquid“. PhD thesis. California Institute of Technology (cit. on p. 15).

Yin, Xiaolong and Sankaran Sundaresan (2009a). „Drag Law for Bidisperse Gas-Solid Suspensions Containing Equally Sized Spheres“. In: *Industrial & Engineering Chemistry Research* 48.1, pp. 227–241 (cit. on p. 36).

– (2009b). „Fluid-Particle Drag in Low-Reynolds-Number Polydisperse Gas-Solid Suspensions“. In: *American Institute of Chemical Engineers Journal* 55.6, pp. 1352–1368 (cit. on p. 36).

Zhou, Guofeng, Limin Wang, Xiaowei Wang and Wei Ge (2011). „Galilean-invariant algorithm coupling immersed moving boundary conditions and Lees-Edwards boundary conditions“. In: *Physical Review E* 84.6, p. 066701 (cit. on pp. 29, 51).

Zhu, H. P., Z. Y. Zhou, R. Y. Yang and A. B. Yu (2007). „Discrete particle simulation of particulate systems: Theoretical developments“. In: *Chemical Engineering Science* 62, pp. 3378–3396 (cit. on p. 12).

Zou, Qisu and Xiaoyi He (1997). „On pressure and velocity boundary conditions for the lattice Boltzmann BGK model“. In: *Physics of Fluids* 9.6, pp. 1591–1598 (cit. on pp. 22, 69).